INVESTIGATION OF TRANSIENT PHASE CHANGE PHENOMENA OF WATER DROPLETS FOR MARINE ICING APPLICATIONS

by

© Kaniz Ronak Sultana

A thesis submitted to the School of Graduate Studies in partial fulfillment of the requirements for the degree of

Doctor of Philosophy

Faculty of Engineering and Applied Science

Memorial University of Newfoundland

July 2019

St. John's Newfoundlan

Abstract

Icing reduces the stability, reliability, productivity and safe operation of offshore exploration vessels, icebreakers and marine structures. A better understanding of the fundamentals of ice accumulation on variable surfaces will be helpful for developing solutions to reduce or prevent ice accretion on offshore vessels and marine structures. The main way that ice accretes on vessels and offshore structures is the solidification of wave-generated saltwater spray. Additionally, in cold climate conditions, vessels and offshore structures can also experience atmospheric or fresh water icing. This research investigates the primary cause of both ice accretion processes. Results were analyzed in terms of pre-impact and post-impact processes.

The pre-impact results of a single water droplet suggest the droplet is not in thermal equilibrium with ambient air. Additionally, the nucleation process can occur at higher temperatures than its equilibrium freezing point. Furthermore, it predicts that the nucleation temperature is controlled by the droplet's volume and the atmospheric temperature. Larger sized droplets have a higher nucleation temperature than smaller sized droplets. Moreover, internal circulation can enhance heat transfer from the droplet to the surrounding air and can accelerate nucleation in cold environmental conditions, as well as influence the fragmentation process. It was observed that the drag force is not only a function of droplet size, but also of ambient temperature and internal circulation.

The post-impact results show that for a droplet impacting on a semi-infinite medium, the thermal penetrated depth is minimal. Therefore, during the post-impact study, the substrate can be considered as an isothermal surface. Furthermore, the droplet

solidification process is primarily affected by droplet size, spreading area, surface temperature and pre-impact velocity. The lower the object temperature, the faster the cooling rate. Additionally; the larger the droplet size, the more time it takes to solidify.

Experimental studies on droplet impact behaviour on both bare and coated substrates were analyzed. The experiments suggest that a lower spreading and longer freezing time occur more frequently on coated substrates than on uncoated substrates. The main reasons for this are surface roughness, contact angle hysteresis, surface energy, surface properties, the thickness of the coatings and droplet-substrate surface tension. The new experimental data and numerical predictions presented in this thesis will help to develop superior and more accurate ice prediction and prevention models.

Acknowledgements

I would like to express my sincere gratitude and appreciation to my supervisors, Dr. Kevin Pope and Dr. Yuri Muzychka, who have the attitude and substance of great mentors. Without their insightful advice, guidance and financial support, this research would not have been possible.

I would like to acknowledge Dr. Lisa Lam, a postdoctoral fellow at Memorial University for her continuous support in the experimental setup design and preparation of tests in the setup. David Snook, Robert J Murphy and Mark from Technical Services (Mechanical Division) are acknowledged for their help in developing my experimental setup. I am also grateful to Craig Mitchell and Matthew Curtis from MUN's Fluids lab for their continuous support during my cold room experiment. I am also thankful to Adam Taylor from Procurement and Facilities Coordinator, and Kelly Greenfield from the Writing Center.

The financial support of Statoil, Mitacs, Petroleum Research Newfoundland and Labrador (PRNL) and School of Graduate Studies of Memorial University is gratefully acknowledged.

Most importantly, I would like to thank my beloved parents, this work could not have been possible without their continuous support and encouragement. Last but not least, I would like to thank my sister, husband, in-laws and my friends at the Memorial University of Newfoundland for providing me continuous inspiration during my study.

Table of Contents

Abstract……ii

Acknowledgements iv

Table of Contents v

List of Tables..... viii

List of Figures x

Nomenclature xiii

CHAPTER 1 LITERATURE REVIEW.....1

1.1 Introduction 1

1.2 Fundamentals of Icing 3

1.3 Bulk Water Flux Modelling of Ice Accretion for Marine Aspects 9

1.3.1 Empirical modelling 9

1.3.2 Analytical modelling 11

1.3.3 Computer modelling.....14

1.4 Thesis Objectives.....25

1.5 Thesis Outline.....27

CHAPTER 2 RESEARCH METHODOLOGY 30

2.1 Introduction 30

2.2 General Phase Change Formulation.....31

2.3 Numerical Techniques for Solving Phase Change Problem 33

2.3.1 Variable grid methods 34

2.3.2 Fixed grid method 41

2.4 Computational Methodology 53

2.4.1 Fluid flow conservation equation 54

2.4.2 Volume of Fluid (VOF).....60

2.5 Experimental Design and Methodology 63

2.5.1 Test substrate 63

2.5.2 Determination of surface roughness and coating thickness 64

2.5.3 Experimental set-up 65

2.6 Summary 70

CHAPTER 3, PRE-IMPACT PROCESS-ii: SPRAY OR DROPLET MOVEMENT IN AIR 71

3.1 Introduction 71

3.2 Scaling Analysis of Freezing Process of a Free Falling Droplet 74

3.3 Numerical Model and Methodology 76

3.4 Results and Discussion 80

3.5 Conclusions 93

CHAPTER 4 POST IMPACT PROCESS-i: NUMERICAL MODELLING OF DROPLET IMPACT AND FREEZING ONTO AN ISOTHERMAL SUBSTRATE 95

4.1 Introduction 95

4.2 Numerical Model and Methodology 100

4.3 Scaling Analysis of Sensible and Latent Energy Change During Solidification of Post-Impact Droplet 103

4.4 Results and Discussion 106

4.5 Conclusions 118

CHAPTER 5 POST-IMPACT PROCESS-i: NUMERICAL INVESTIGATION OF DROPLET SPREADING AND HEAT TRANSFER ON COLD SUBSTRATE 120

5.1 Introduction 120

5.2 Numerical Model and Methodology 121

5.3 Results and Discussion 124

5.4 Conclusions 130

CHAPTER 6 POST-IMPACT PROCESS- i: EXPERIMENTAL RESULTS OF DROPLETS DYNAMICS AND FREEZING PROCESS 132

6.1 Introduction 132

6.2 Contact Angle Measurements 136

6.3 Droplet Dynamics 143
6.4 Dimensionless Analysis on Droplet Dynamics 148
6.5 Determination of Thermophysical Properties 152
6.6 Normal Freezing Process 154
6.7 Supercooling Effect 157
6.8 Dimensionless Analysis on Droplet Freezing 162
6.9 Conclusions 180
CHAPTER 7 DISCUSSION AND RECOMMENDATIONS 181
7.1 Discussion 181
7.2 Main Contributions 182
7.3 Recommendations 184
References 186

List of Tables

Table 1.1 Causes of vessel icing (Kato, 2012; Zakrzewski, 1987). 6

Table 1.2 Meteorological conditions causing vessel ice accretion (Efimov, 2012). 7

Table 1.3 Characteristics of icing sources in an atmospheric surface layer. 8

Table 1.4 Analysis of existing marine icing models. 15

Table 1.5 Classification of ice modelling. 26

Table 2.1 Evolution of enthalpy formulation categorized by applied factors for both conduction and convection problems. 52

Table 2.2 Details of substrate dimensions. 63

Table 2.3 Test surfaces. 64

Table 2.4 Details of surface roughness. 65

Table 2.5 Details of coating thickness. 65

Table 2.6 Details of test fluid. 70

Table 2.7 Details of test conditions. 70

Table 3.1 Details of the numerical grid. 77

Table 3.2 Parameters to study droplet freezing in air. 78

Table 3.3 Physical properties of air and water. 79

Table 3.4 Thermophysical properties of water at several temperatures. 80

Table 3.5 Sensible and latent energy for fresh water droplets. 80

Table 4.1 Details of the numerical grid for zero substrate thickness. 101

Table 4.2 Initial boundary conditions. 102

Table 4.3 Thermophysical properties of water (constant). 102

Table 4.4 Temperature dependent thermophysical properties for fresh water. 102

Table 4.5 Mesh analysis test. 109

Table 4.6 Sensible and latent energy. 116

Table 5.1 Details of the numerical grid for a thicker substrate. 122

Table 5.2 Input parameters used in the computed predictions. 123

Table 5.3 Thermophysical properties of material used in this study (Oukach et al., 2012). 123

Table 5.4 Temperature dependent thermophysical properties for fresh water. 123

Table 6.1 Details of static contact angles on test substrates. 139

Table 6.2 Details of advancing and receding contact angles on test substrates. 142

Table 6.3 Details of pre-impact velocities. Reynolds and Weber numbers. 143

Table 6.4 Dimensionless time, pre-impact Reynolds number, drag coefficient and velocity for fresh water droplets in air at -15 and -18°C. 151

Table 6.5 Dimensionless time, pre-impact Reynolds number, drag coefficient and velocity for salt water droplets in air at -15 and -18°C. 151

Table 6.6 Details of thermophysical properties of test substrates. 153

Table 6.7 Thermophysical properties of ice and salt water ice (Cox and Weeks, 1975; Dehghani et al., 2018; Weeks, 2010).....154

Table 6.8 Latent energy released during solidification. 175

List of Figures

Fig. 1.1 Ice accretion (a) atmospheric (Hållén, 2015) and (b) sea spray (Ice Sight). 4

Fig. 1.2 Typical water spray generation process (Ryerson, 1992). 25

Fig. 2.1 Schematic diagram of a two-phase Stefan problem (Hu and Argyropoulos, 1996). 32

Fig. 2.2 Schematic of experimental set-up. 66

Fig. 2.3 Photographs of top surfaces. 68

Fig. 3.1 Effect of internal circulation and air drag on a free falling droplet. 73

Fig. 3.2 Computational domain for numerical predictions of gas-liquid phase change. 77

Fig. 3.3 Phase change and transient temperature of a free falling droplet. 82

Fig. 3.4 Comparison of nucleation temperature for different sized droplets. 84

Fig. 3.5 Grid independency test for fresh water droplets at an ambient temperature of -18 °C. 85

Fig. 3.6 Average volume fraction and air entrapment of a free falling water droplet. 87

Fig. 3.7 Dimensionless analysis incorporating the effects of internal circulation and mixing. 88

Fig. 3.8 Internal motion of a free falling droplet for different residence times. 89

Fig. 3.9 Comparison of numerical predictions with the available experimental data. 91

Fig. 3.10 Average drag coefficient at different atmospheric temperatures. 92

Fig. 4.1 Schematic of droplet impact and spreading on a solid substrate. 96

Fig. 4.2 Schematic of computational domain. 100

Fig. 4.3 Schematic of disk-shaped droplet. 104

Fig. 4.4 Internal temperature distribution of various sized droplets on an isothermal surface. 107

Fig. 4.5 Temperature variation of a water droplet during the impact on an isothermal substrate. 108

Fig. 4.6 Mesh independency study. 110

Fig. 4.7 Comparison of dimensionless freezing times for different sized droplets. 111

Fig. 4.8 Spread factor a function of droplet diameter. 112

Fig. 4.9 Impact and spreading characteristics of a 2 mm diameter water droplet. 114

Fig. 4.10 Impact and spreading velocities of a 5 mm diameter water droplet. 115

Fig. 4.11 Scaled thermal, experimental and numerical resistance for substrate of -20 °C. 116

Fig. 4.12 Scaled thermal, experimental and numerical resistance for substrate of -25 °C. 117

Fig. 4.13 Dimensionless resistance plotted against dimensionless ΔT/L. 118

Fig. 5.1 Schematic of computational domain. 122

Fig. 5.2 Temperature contour inside the substrate at different spreading times of droplet. 125

Fig. 5.3 Transient temperature history in the droplet-substrate interface region. 126

Fig. 5.4 Mesh independent study on a substrate temperature of -25 °C. 127

Fig. 5.5 Effect of ambient temperature on droplet-substrate interface region. 128

Fig. 5.6 Time evolution of the shape of the impinging droplet and the velocity field. 129

Fig. 6.1 Experimental set-up of contact angle measurement. 138

Fig. 6.2 Sample of static contact angle test of a salt water droplet. 139

Fig. 6.3 History of static contact angle measurements. 140

Fig. 6.4 Sample of dynamic contact angle test of a salt water droplet. 141

Fig. 6.5 Contact angle hysteresis of a salt water droplet. 141

Fig. 6.6 Sequential images of droplet dynamics onto an epoxy coated substrate. 144

Fig. 6.7 Sequential images of droplet dynamics onto a bare aluminum substrate. 146

Fig. 6.8 Experimental results of final droplet shape on various cold substrates. 147

Fig. 6.9 Plot of exact solution and asymptotes for free falling body. 149

Fig. 6.10 Thermal images of a 3 mm fresh water droplet. 155

Fig. 6.11 Normal freezing curve of a 3 mm fresh water droplet. 156

Fig. 6.12 Thermal images of a supercooled 5 mm salt water droplet. 158

Fig. 6.13 Supercooling freezing curve of a 5 mm salt water droplet. 159

Fig. 6.14 Summary of the supercooling effect of salt water on various substrates. 162

Fig. 6.15 Simplified schematic of thermal resistance network. 164

Fig. 6.16 Blended model of dimensionless heat flux from a circular source into a half space (Yovanovich et al., 1995). 170

Fig. 6.17 Dimensionless transient constriction resistance in a half-space with a disk-shaped isothermal source (Yovanovich et al., 1995).....171

Fig. 6.18 Dimensionless time to freeze though the drop and uncoated substrates.....176

Fig. 6.19 Dimensionless time to freeze through the drop and primer coated substrates.....177

Fig. 6.20 Dimensionless time to freeze through the drop, primers, and coatings.....178

Fig. 6.21 Dimensionless time to freeze through the drop, primers, and coatings for both coated and uncoated surfaces. 179

Nomenclature

A	Contact area between the droplet and surface	(m^2)
A_{mush}	Mushy constant	(-)
A_p	Projected area	(m^2)
A_s	Surface area of the droplet	(mm^2)
A	Acceleration of the droplet	(ms^{-2})
C_D	Drag coefficient	(-)
C_{Davg}	Average drag coefficient	(-)
C_{in}	Specific heat at the solid-liquid interface	(-)
C_2	Scale factor	(-)
C_3	Scaling coefficient	(-)
C_l	Specific heat of liquid	($J.kg^{-1}.K^{-1}$)
C_p	Specific heat	($J.kg^{-1}.K^{-1}$)
C_{pw}	Average specific heat of water	($J.kg^{-1}.K^{-1}$)
C_s	Specific heat of solid	($J.kg^{-1}.K^{-1}$)
D	Final droplet diameter along the substrate after impact	(mm)
D	Droplet diameter	(mm)
E_s	Sensible energy change	(-)
E_l	Latent energy change	(-)
F_A	Air drag	(N)
F_G	Gravity force	(N)
Fo	Fourier number	(-)
$Fo_{\surd A}$	Dimensionless time	(-)
$Fo_{\surd A,c}$	Fourier number based on the thermal diffusivity of coating	(-)
$Fo_{\surd A,d,f}$	Fourier number based on the time to freeze	(-)
Fr	Froude number	(-)
$F\rightarrow$	Surface tension force	($N.m^{-1}$)
G	Acceleration due to gravity	(ms^{-2})
G_k	Generation of turbulence kinetic energy due to mean velocity gradients	(-)
G_ω	Generation of turbulence dissipation due to mean velocity gradients	(-)
H	Total enthalpy	(J)
HF	Heat flow rate	(W)

H_f	Latent heat of fusion	($J.kg^{-1}$)
h	Heat transfer coefficient	($W.m^{-2}.K^{-1}$)
h_{conv}	Convective heat transfer coefficient	($W.m^{-2}.K^{-1}$)
h_{en}	Enthalpy	(J)
h_{ref}	Reference enthalpy	(J)
k	Kinetic energy	(-)
k_a	Thermal conductivity of air	($W.m^{-1}.K^{-1}$)
k_c	Thermal conductivity	($W.m^{-1}.K^{-1}$)
k_{coat}	Thermal conductivity of the coating	($W.m^{-1}.K^{-1}$)
$k_{eff,c}$	Effective thermal conductivity of the combined layer	($W.m^{-1}.K^{-1}$)
k_s	Thermal conductivity of solid	($W.m^{-1}.K^{-1}$)
k_l	Thermal conductivity of liquid	($W.m^{-1}.K^{-1}$)
L	Rate of energy transfer	(W)
L_c	Characteristic length scale	(m)
M	Mass of the object	(kg)
m	Mass of the droplet	(kg)
N	Total number of test	(-)
Nu	Nusselt number	(-)
n	Unit norm at the interface	(-)
n_w	Unit vectors normal to the wall.	(-)
Oh	Ohnesorge number	(-)
P	Pressure	(Pa)
Pr	Prandtl number	(-)
Q	Constant	(0.01)
Q_{conv}	Energy transfer due to convection from the ambient air	(J)
Q_l	Heat rate out of the droplet	(J)
R	Droplet radius	(mm)
$R_{c,long}$	Steady-state resistance expression	(-)
$\bar{R}$	Total average thermal resistance	(-)
$\bar{R}_d$	Average resistance in the droplet	(-)
$\bar{R}_{exp}$	Experimental value for the average resistance	(-)
$\bar{R}_s$	Average resistance in the surface	(-)
$\bar{R}_{total}$	Total average thermal resistance	(-)

R_{1D}	1-D resistance through the coating	(-)
R_{2s}	Steady-state constriction resistance through the substrate	(-)
R_{cond}	Thermal resistance by conduction	(-)
R_{conv}	Thermal resistance by convection	(-)
R_{coat}	Coating resistance	(-)
R_{sub}	Substrate resistance	(-)
Re	Reynolds number	(-)
Re_d	Reynolds number of the falling droplet	(-)
Re_{mix}	Internal mixing Reynolds number	(-)
Re_r	Reynolds number of the radial flow	(-)
R_t	Thermal resistance	(-)
R	Initial droplet radius	(m)
r_s	Droplet average radius	(m)
$r_{s,m}$	Maximum spread radius	(m)
S	Source	(-)
$S^*_{\sqrt{A}}$	Dimensionless shape factor	(-)
St	Stefan number	(-)
S_k	Source term for k	(-)
S_ω	Source term for ω	(-)
T	Temperature	(K)
ΔT	Temperature difference between phases	(K)
ΔT	Temperature difference between the average temperature of the droplet which is its fusion temperature, and the substrate temperature at some semi-infinite distribution below the surface	(K)
T_a	Air/ambient air temperature	(K)
T_d	Droplet temperature	(K)
T_f	Freezing temperature	(K)
T_l	Liquid temperature	(K)
T_m	Melting temperature	(K)
T_{ref}	Reference temperature	(K)
T_s	Solid temperature	(K)
T_{sub}	Substrate temperature	(K)
T	Time	(s)
$t_{freezing\ time}$	Freezing time	(s)

t_i	Time to impact	(s)
t_w	Unit vectors tangential to the wall.	(-)
t^*	Dimensionless time	(-)
t_{avg}^*	Average dimensionless time	(-)
t_{spread}	Total spreading time of the impinging droplet	(s)
t_{equ}	Total equilibrium time of the impinging droplet	(s)
u_t	Terminal velocity	($m.s^{-1}$)
V	Control volume	(-)
V	Droplet volume	(m^3)
v	Velocity of fluid	($m.s^{-1}$)
$\bar{v}$	Mean velocity	($m.s^{-1}$)
v_a	Air velocity	($m.s^{-1}$)
v_p	Solid velocity due to the pulling of solidified material out of the domain	($m.s^{-1}$)
v_r	Velocity in r-direction	(-)
v_x	Velocity in x-direction	(-)
We	Weber number	(-)
X	Position of the moving boundary interface	(m)
Y_k	Dissipation of k	(-)
Y_ω	Dissipation of ω	(-)
α	Average thermal diffusivity of the liquid and solid at the fusion temperature	($m^2.s^{-1}$)
α_{diff}	Thermal diffusivity of the droplet	($m^2.s^{-1}$)
α_{eff}	Effective thermal diffusivity	($m^2.s^{-1}$)
α_l	Thermal diffusivity of liquid	($m^2.s^{-1}$)
α_q	Volume fraction of phase	(%)
α_s	Thermal diffusivity of solid	($m^2.s^{-1}$)
α_{vf}	Volume fraction of phase	(%)
α_{vf2}	Volume fraction of secondary phase	(%)
β	Liquid fraction	(%)
γ	Constant	(-)
η	Heating rate	(°/min)
Γ_k	Effective diffusivity of k	(-)
Γ_ω	Effective diffusivity of ω	(-)

Δ	Thickness of the coating	(mm)
δ^*	Dimensionless penetration depth	(-)
E	Constant value	0.001
K	Local interface curvature	(-)
μ	Viscosity	($kg.m^{-1}.s^{-1}$)
μ_a	Dynamic viscosity of the ambient air	($kg.m^{-1}.s^{-1}$)
μ_d	Droplet viscosity	($kg.m^{-1}.s^{-1}$)
μ_g	Gas viscosity	($kg.m^{-1}.s^{-1}$)
μ_t	Turbulent viscosity	($kg.m^{-1}.s^{-1}$)
Ξ	Spread factor	(-)
ξ_{avg}	Average spread factor	(-)
P	Density	($kg.m^{-3}$)
ρ_a	Density of the ambient air	($kg.m^{-3}$)
ρ_g	Gas density	($kg.m^{-3}$)
ρ_l	Liquid density	($kg.m^{-3}$)
ρ_w	Average density of water	($kg.m^{-3}$)
σ	Surface tension	($N.m^{-1}$)
σ_k	Turbulent Prandtl numbers for k	(-)
σ_ω	Turbulent Prandtl numbers for ω	(-)
v_d	Kinematic viscosity of droplet	($m^2.s^{-1}$)
Ω	Specific dissipation rate	(-)

CHAPTER 1[1]

LITERATURE REVIEW

1.1 Introduction

Icing poses serious hazards to Arctic offshore applications. While operating in Arctic waters, marine vessels and offshore structures often experience operational and safety problems (Makkonen, 1984a; Ryerson, 2009, 2011). Numerous ship losses due to icing have been reported by Aksyutin (1979), DeAngelis (1974) and Shellard (1974). An overview of available literature indicates that the first systematic research on vessel icing was conducted in the United Kingdom in 1957, after losing two British steam trawlers, the Lorella and Roderigo, during an icing storm (Trawler Ic. Res., 1957; Zakrzewski and Lozowski, 1991). Later, Japan, the Soviet Union and Canada lost several vessels in the cold waters of the Sea of Japan and Bering Sea, North Pacific Ocean and Alaskan waters (Zakrzewski and Lozowski, 1991). These losses caused the launching of several organizations, such as the British Shipbuilding Research Association, Japanese Research Program, Soviet Program, US Army Cold Regions Research and Canada's National Research Council. These organizations investigate ice accretion mechanisms on vessels, develop vessel icing forecasting techniques, collect field data, and examine the effect of ice loads on vessel safety and stability (Sawada, 1968; Zakrzewski and Lozowski, 1991). Their research revealed that icing due to the freezing of wave-generated sea spray is the

[1] This chapter is written based on: Sultana, K.R., Dehghani, S.R., Pope, K., Muzychka, Y.S., 2017a. A Review of Numerical Modelling Techniques for Marine Icing Applications, In Cold Regions Science and Technology, Volume 145, 2017, Pages 40-51.

main source of vessel icing (Borisenkov and Panov, 1972; Panov, 1976; Shekhtman, 1967, 1968). Recently, Bodaghkhani et al. (2016) reviewed sea spray dynamics that can cause marine icing. Additionally, Saha et al. (2016a) conducted experiments to show the behaviour of water jets after their impact on a vertical surface. Furthermore, Dehghani et al. (2016a, 2016b, 2017a) modeled the movement of sea spray clouds using trajectory analysis, breakup phenomena and size-velocity dependence characteristics.

During cold climate conditions, vessels and offshore structures can experience atmospheric icing and sea spray icing (Makkonen, 1984a). Borisenkov and Panov (1972) analyzed data from over 2000 icing events on Soviet fishing vessels and reported that 89.8% of those icing events occurred due to sea spray alone. Additionally, 6.4% occurred due to sea spray combined with fog, rain or drizzle, 1.1% occurred due to sea spray with snow, and 2.7% occurred due to atmospheric icing. Brown and Roebber (1985) analyzed some data from Canadian ship meteorological reports and found that a frequency range of 81% to 97% is provided for icing due to sea spray for some regions of the Canadian East Coast. Additionally, a range of 1% to 17% is given for icing from atmospheric sources. Although the effect of atmospheric icing is minor, it still needs to be considered (Makkonen, 1984a). Makkonen (1984a) explained that the accretion of atmospheric icing does not decrease with elevation, whereas sea spray is affected by height.

Sea spray icing is restricted to lower heights and surfaces such as decks, derricks and handrails. Sea spray does not usually reach higher than approximately 16 m above the sea surface (World Meteorological Organization, 1962). Dehghani et al. (2016b, 2017a) showed that the maximum height of spray clouds for a medium-sized fishing vessel in the

Sea of Japan is about 8.5 m. Therefore, the importance of atmospheric icing is that it typically occurs on the upper parts of the vessels, includes masts and antennas, among others (Makkonen, 1984a).

This chapter is focused on a review of state-of-the-art of existing literature related to ice accumulation on marine vessels and offshore structures. Various meteorological and oceanographic factors that influence vessel icing are described. Further, a comprehensive study of current marine icing models is presented.

1.2 Fundamentals of Icing

Over the past 40 years, researchers have published several studies to address the complexity of vessel icing (Lozowski et al., 2000; Lozowski and Gates, 1991; Lozowski and Makkonen, 2005; Zakrzewski and Lozowski, 1991). In offshore areas, vessel icing can occur from two specific sources: fresh water or atmospheric icing and saltwater or sea spray icing (Makkonen, 1984a). Atmospheric icing is mainly dangerous for aerospace and power transmission industries (Makkonen, 1984b; Sundin and Makkonen, 1998). Sea spray icing is hazardous for offshore vessels and structures (Makkonen, 1984a, 1987). Atmospheric icing normally occurs due to meteorological aspects, such as air temperature, wind speed, and liquid water content (Kraj, 2007; Minsk, 1980). Sea spray icing occurs due to wave generated spray and wind generated spray (Zakrzewski, 1986b). Figure 1.1 illustrates both atmospheric and sea spray icing.

Atmospheric icing can be divided into three categories: precipitation icing, in-cloud icing and hoar frost icing (Boluk, 1996; Fikke et al., 2006; ISO-12494; Richert, 1996). The

cause of precipitation icing is rain or drizzle, which may result in dry or wet snow and glaze formation (Farzaneh, 2008; Feit, 1987b; Parent and Ilinca, 2011).

Fig. 1.1 Ice accretion (a) atmospheric (Hållén, 2015) and (b) sea spray (Ice Sight).

In-cloud icing occurs due to extremely low temperature conditions, when small super-cooled liquid droplets in clouds immediately freeze after impact on the surface (Blackmore, 1996; Parent and Ilinca, 2011). This type of icing can be categorized into two forms: rime ice and glaze ice (Ilinca, 2011; Makkonen, 1984a; Minsk, 1980; Parent and Ilinca, 2011; Wang, 2008). Rime icing is further divided into hard rime and soft rime. Hard rime is caused by slower heat loss and soft rime is caused by quicker heat loss (Makkonen, 1984a; Minsk, 1980). Glaze ice is a kind of smooth, homogeneous and transparent ice (Makkonen, 1984a; Wang, 2008). This type of ice forms when droplets stay in a continuous film on the surface before freezing (Minsk, 1980). Lastly, hoar frost icing is mainly formed due to water vapor sublimation to ice (Makkonen, 1984a, 2000; Minsk, 1980).

Sea spray or marine icing is caused by two sources: wind spray and wave spray. DeAngelis (1974) reported that moderate icing mainly occurs with high wind speeds such as 6.5 ms^{-1} or more. Generally, wind spray is caused by droplets blowing off whitecaps on the ocean surface and remaining in the air for all wind conditions with constant water flux (Hansen, 2012; Jones and Andreas, 2012). Wave spray is caused by the collision of a vessel or offshore structures with waves (Hansen, 2012). Medium-size droplets can reach higher areas on vessels compared to small and large droplets (Dehghani et al., 2016a, 2016b). A collision can send a brief and periodic freezing spray flux onto the surface of the vessel, which creates icing (Hansen, 2012; Ryerson, 1995). In earlier publications, researchers reported that wave-generated sea spray is the most dangerous icing source for offshore vessels (Aksyutin, 1979; Brown and Roebber, 1985; Cammaert, 2013; Chung et al., 1995b; Kato, 2012; Makkonen, 1984a, 1984b; Ryerson, 2011; Shekhtman, 1968; Shellard, 1974; Tabata et al., 1963; Zakrzewski, 1986a, 1986b, 1987). Table 1.1 displays important information about marine icing sources in different regions.

During a sea spray event, weather and oceanographic conditions have a remarkable influence on vessel icing. Shekhtman (1967) demonstrated that most icing events happen with stormy conditions, high wind speeds and snowfall. Research sources reported that icing can start at air temperatures below -2 °C, and wind speeds above 6 to 8 ms^{-1} (Tabata, 1969). Sawada (1962) demonstrated that in very strong winds, icing can start at air temperatures higher than -3 °C. DeAngelis (1974) reported that moderate icing mainly occurs at an air temperature of -2 °C. Based on meteorological complex numbers, Kolosova et al. (1971) prepared a table which is further documented by Efimov (2012). The table

illustrates the probability of vessel icing given different meteorological conditions. Table 1.2 displays this information. Unfortunately, the original source is not available for further explanation.

Table 1.1 Causes of vessel icing (Kato, 2012; Zakrzewski, 1987).

Region	**Cause of icing (%)**			**References**
	Sea spray	**Spray and fog or rain or snow**	**Other sources**	
All seas	89.0 (82)[1]	7.0 (16) [1]	4.0 (2) [1]	Shekhtman (1968)
Nort-h Pacific	89.8	7.5	2.7	Aksyutin (1979)
North Atlantic Arctic	50.0	41.0	9.0	Aksyutin (1979)
Gulf of St. Lawrence	81.0	2.0	17.0	Brown and Roebber (1985)
Scotian Shelf	94.2	3.0	2.8	Brown and Roebber (1985)
Grand Banks	97.0	2.0	1.0	Brown and Roebber (1985)
NE Newfoundland Shelf	95.9	1.4	2.8	Brown and Roebber (1985)
Labrador Sea and Davis Strait	86.9	11.1	1.7	Brown and Roebber (1985)

[1]Reported cases of fast growth of ice are given in parenthesis, if known.

Table 1.2 Meteorological conditions causing vessel ice accretion (Efimov, 2012).

Complex number	Air temperature (°C)	Wind speed (ms^{-1})
1	≤ 0 (precipitations, mist)*	≤ 7.0
2	From 0 to -3.0	7.1 to 15.0
3	From 0 to -3.0	> 15.0
4	From -3.1 to -8.0	7.1 to 15.0
5	From -3.1 to -8.0	> 15.0
6	> -8.1	7.1 to15.0
7	> -8.1	> 15.0

*atmospheric icing and all others represent spray icing.

Borisenkov and Panov (1972) demonstrated that icing on a medium-size fishing vessel can occur at air temperatures from 0 °C to -26 °C, and wind speeds from 0 to 30 ms^{-1}. However, Panov (1976) extended the range of wind speeds up to 55 ms^{-1}. Shellard (1974) stated that the air temperature must be lower than the equilibrium freezing temperature of brine for ice accretion to occur in saltwater. Lundqvist and Udin (1977) mentioned that the ambient temperature must be below -2 °C for ice accretion in ocean water to occur. Various Russian sources documented that for ambient temperature below -18 °C, marine icing is not possible (Minsk, 1977). In those circumstance, the water droplets will freeze in the atmosphere and strike the vessel surface as small, dry, ice crystals. However, actual shipboard observations reported that ice accretion can happen at a temperature as low as -29 °C (Minsk, 1977). Furthermore, ship icing may be possible at sea surface temperatures

from 6 to 8 °C (Shekhtman, 1967). This investigation was further supported by Mertins' (1968) work.

Vessel icing mainly occurs with relatively warm spray and larger water droplets, high liquid water contents and high wind speeds (Blackmore, 1996; Ryerson, 1995). For fixed offshore structures, Andreas (2002) reported that wind generated sea spray is produced by three mechanisms, which in turn produce different types of droplets. The droplet type includes small film droplets ranging from 0.5 to 50 µm in radius, jet droplets ranging from 1 to 100 µm in radius and spume or spindrift droplets ranging from 20 to 500 µm in radius (Jones and Andreas, 2009). Makkonen (1984a) and Minsk (1977, 1980) reviewed several papers and explained the characteristics of icing sources in the atmospheric surface layer. Table 1.3 presents important highlights from their papers.

Table 1.3 Characteristics of icing sources in an atmospheric surface layer.

Source from sea spray	**Droplet diameter (µm)**		**LWC (gm^{-3})**	**Reference**
	Range	**Mean**		
On a moving ship	1000-3500	2400	0 - 219	Borisenkov and Panov (1974)
For braking waves	1000-3500	2400	4600	Borisenkov and Panov (1972)
For wave crests	60-1000	150-200	-	Borisenkov and Panov (1972), Wu (1973)
In first 10 cm	10-1000	200	-	Wu (1979)

1.3 Bulk Water Flux Modelling of Ice Accretion for Marine Aspects

This section discusses the applications of the numerical modelling of ice accretion in the marine icing sector. Various empirical and analytical models are also investigated.

1.3.1 Empirical modelling

Empirical models are generally based on the input parameters of atmospheric conditions such as wind speed, air temperature and sea surface temperature; which determine the severity of icing (Feit, 1987a; Obreiter, 1987; Rashid et al., 2016). Sawada (1966) demonstrated an ice accretion nomogram for use in the Sea of Japan. The result was derived from Japanese patrol and fishing vessels. The nomogram illustrates the relationship between vessel icing, air temperature and wind velocity; however, it does not consider sea temperature. Mertins (1968) developed a series of nomograms that focused on ice accretion rates on North Atlantic ships. The author also prepared comparisons of environmental factors and illustrated that the air temperature, wind speed and sea temperature are the most important parameters for vessel icing. Although the nomogram guided forecasting the severity of icing, it under-predicted the quantity of ice accretion (George, 1975; Stallabrass, 1980). Additionally, it assumed that when the air temperature was lower than -18 °C, there was no icing (Berenbeim, 1969).

From an actual shipboard icing observation, Minsk (1977) documented that icing can occur at a temperature as low as -29 °C. Additionally, Ono (1974) performed statistical analysis and categorized icing class through field observation data. Itagaki (1984) proposed a model based on a vessel's data from Ono (1974), which predicts the ice accretion rate on a static structure as a factor of air temperature and wind speed. Over the same period,

Makkonen (1984a) provided a nomogram based on offshore field observation data. Nomograms were further developed by Comiskey et al. (1984) and Wise and Comiskey (1980) for superstructure icing on the Alaskan waters. In addition to the work of Comiskey et al. (1984) and Wise and Comiskey (1980), other nomograms were proposed by Overland et al. (1986) to forecast dangerous locations. Feit (1987b) reported that the forecasting technique of Overland et al. (1986) gave a better prediction than Comisky's (1980). Although Overland et al.'s (1986) method predicts better icing statistics for fishing vessels, the model cannot be used for larger vessels or offshore structures (Kulyakhtin, 2014). Additionally, Makkonen (1989) criticized this methodology due to conceptual assumptions and physical analysis. Later, these criticisms were solved by Overland (1990). Makonnen et al. (1991) reported that the conceptual errors still exist in Overland's approach. The errors involve input sensitivity and forecasting ability. Overland (1990) illustrated that icing is highly sensitive to sea surface temperature, whereas Shellard (1974) demonstrated a contradictory argument. Shellard (1974) explained that the rapid supercooling of droplets causes the icing rate to be less sensitive to sea surface temperature. Makkonen et al. (1991) support Shellard's argument with convincing observational evidence. Furthermore, Makkonen et al. (1991) show their concern about the quality of Overland's data. Makkonen et al. (1991) noticed that the data was highly inconsistent when it was used by Overland to validate his work. However, Overland (1991) highly supports his algorithm and demonstrates that the NOAA algorithm is simple, reliable and consistent in comparison to existing icing data and weather forecast input. Kachurin et al. (1974) introduced a unique nomogram for predicting vessel icing phenomena. Based on theoretical considerations, the

authors forecasted the ice accumulation rate using a cylindrical object. In the icing algorithm methodology, the model considered thermodynamic equilibrium, surface film temperature, sea surface temperature, spray flux and wave height as direct parameters. According to Funk (2012) due to its thermodynamic equilibrium assumptions, the model is considered to be valuable and unique to understanding the icing process. Stallabrass (1980) argued that some assumptions, such as surface film temperature and freezing point, make the nomogram more complex. Later, Stallbrass (1980) proposed a less complicated model and calibrated it with Canadian icing observations. Makkonen (1987) also pointed out an error regarding the effect of spray salinity and provided some recommendations for Kachurin et al.'s (1974) model.

Although existing models are highly standardized for icing prediction, their applications are limited to particular regions. Further, the majority of observations correspond to smaller and medium sized vessels.

1.3.2 Analytical modelling

The Canadian Hydraulics Centre of the National Research Council of Canada developed a marine icing database in early 2000 (Kubat and Timco, 2005). This database was summarized for different environmental conditions. In a comprehensive review by Stallabrass, the physical icing data was collected from fishing trawlers sailing on the East coast of Canada (Funk, 2012; Kubat and Timco, 2005; Stallabrass, 1980). This data was used to calibrate the spray flux and droplet flight time equations. The droplets were assumed to be thermally homogeneous (Funk, 2012; Stallabrass, 1980). The work had established a relationship between the surface film temperature with both a freezing

fraction and a saltwater freezing point (Funk, 2012). After Stallabrass's retirement from National Research Council (NRC), the Canadian Hydraulics Center of NRC took initiatives to update this information into a modern database system. This database tool is used for predicting and simulating marine icing on offshore vessels operating in cold environments. Additionally, it allows the offshore petroleum industries to deal with the marine icing hazard in a timely and cost-effective manner. Using the regular ship icing monitoring results and icing reports, Brown and Agnew (1985) and Brown and Robber (1985) characterized and summarized the ice accretion in the Canadian coastal region. More recently, Blackmore and Lozowski (1994), Horjen and Vefsnmo (1985a), Ryerson and Gow (2000) and Zakrzewski (1986a) developed their individual analytical models using different algorithms and parameters. All of these models were very effective in the early stages of icing research.

By considering fresh water spongy spray on a vertical cylinder model, a theoretical spongy icing model was developed by Blackmore and Lozowski (1998). In the model, the authors considered the surficial morphology beneath a falling supercooled liquid film. The work reveals that spray supercooling enhances both the accretion rate and sponginess. Fukusako et al. (1989), Lock and Foster (1990) and Makkonen (1987) conducted several studies on cylindrical objects, where they considered the airstream and saltwater spray. Their main targets were to observe the growth rate of spongy ice, and to calculate the ice fraction and salt entrapment capacity. Various experimental and numerical studies were conducted on rime ice accretion. Auldl (1980) conducted some experiments on icing, with the main interest of investigating the thermodynamic properties of individual water

droplets in icing environments. Saha et al. (2016b) experimentally investigated the freezing characteristics of salt and fresh water droplets on supercooled surfaces.

Sultana et al. (2016) conducted numerical tests for predicting rime ice accretion phenomena. Lozowski et al. (1983) conducted numerical studies on an unheated, non-rotating cylinder to investigate ice accretion as a factor of angle around the cylinder. Both rime and glaze icing phenomena are tested in this study. To investigate icicle growth physics, theoretical models were presented by Chung and Lozowski (1990), Johnson and Lozowski (1988), Makkonen (1988), Makkonen and Fujii (1993) and Szilder and Lozowski (1993a, 1993b, 1995a, 1995b). In another study, Szilder and Lozowski (1995b) explained icicle growth physics through a three-dimensional random walk model. The authors considered motion, freezing probability and shedding as the model parameters. Additionally, the authors examined the effect of various model parameters on icicle growth geometry and freezing efficiency. To observe the icicle growth phenomenon on horizontal elongated structures like overhead lines, Makkonen and Fujii (1993) conducted wind tunnel experiments at moderate wind speeds, and demonstrated that an icicle spacing of 2 cm is insensitive to atmospheric conditions and structure dimensions.

Though the earlier research is important, most studies considered constant thermophysical properties, as well as constant time duration, and are not physical in a real-time situation. Therefore, investigating the transient phase change phenomena by means of temperature dependent properties is one of the main aims of this research.

1.3.3 Computer modelling

In addition to the empirical models stated by these marine researchers, many other computational models, such as RIGICE, RIGICE04, ICEMOD, and MARICE were developed to estimate the periodic sea spray icing phenomena. Table 1.4 shows a fundamental comparison of these models.

ICEMOD, ICEMOD2 and ICEMOD2.1

The first ICEMOD model was developed in Norwegian Hydrodynamic Laboratories, by Horjen and Vefsnmo of the research organization SINTEF (Horjen and Vefsnmo, 1985b, 1987; Vefsnmo et al., 1987). ICEMOD was the first time-dependent numerical model that was used for wave spray icing predictions (Horjen, 2013). The initial ICEMOD model was based on the equations for conservation of mass, heat, and salt within the brine film on the ice accreted surface (Lozowski et al., 2000).

The first ICEMOD model was limited to one-dimensional space in the way that it considered that the brine film covering the accreted ice only moved in one-direction. To overcome this limitation, an updated version of ICEMOD, renamed to ICEMOD2, was introduced by Horjen (2013).

Table 1.4 Analysis of existing marine icing models.

Model	Application	Time dependency	Numerical technique	Factors used		
				Spray flux	Water film dynamic	Thermodynamic equilibrium
ICEMOD	ODR, SIM	FTD (us)	-	✓	✓	✓
ICEMOD2	ODR, SIM	FTD (us)	FDM	✓	✓	✓
ICEMOD2.1	ODR, SIM	FTD (us)	FDM	✓	✓	✓
RIGICE	ODR	MT	FORTRAN-77	✓	✓	
RIGICE04	ODR	MT	ESS	✓	✓	
MARICE	SIM	FTD (us)	FVM	✓	✓	✓
Blackmore and Lozowski (1994)	SIM	-	-	✓		✓
Chung et al. (1995a)	SSIM	(s)	FORTRAN	✓	✓	✓
Lozowski et al. (2000)	SSIM	FTD (us)	-	✓		
Kato (2012)	SSIM	-	C++ 2010	✓		
Efimov (2012)	SIM	-	-	✓		
Hansen (2012)	SIM	-	BSDLWM			✓
Bjerkås (2006)	OS	-	CCT	-	-	-

The different notations are defined as follows:
BSDLWM= Backward Spatial Difference Lax-Wendroff Method; CCT= Cross Correlation Techniques; ESS= Excel Spread Sheet; FDM= Finite Difference Method; FORTRAN= FORmula TRANslation; FTD= Fully Time Dependent; FVM= Finite Volume Method; MT= Mean Time; OS= Offshore Structure; ODR= Offshore Drilling Rigs; s= steady; SIM= Ship Ice Modelling; SSIM= Super Structure Ice Modelling; us= unsteady.

A two-dimensional, time-dependent mathematical model was developed by using a boundary layer approximation along with continuity, energy and salt diffusion equations. These equations were applied on a cylinder, placed at an angle to the horizontal surface. The model assumes a uniform temperature profile and potential flow around the cylinder, and also assumes that icing will only occur on the upwind side of the cylinder. A finite-difference numerical method based on an extension of the two-step Lax–Wendroff scheme is used to solve the non-linear hyperbolic partial differential icing equations. The ice profile changes with time; hence, this model considered a constant wind field around the cylinder. A small time step of 0.016 s was applied in the numerical calculation to reduce the numerical noise. Additionally, mid-point evaluations were excluded in the ICEMOD2 scheme, which was used in the original Lax-Wendroff method. To solve the non-linear and ordinary differential droplet's equation, a fourth-order Runge–Kutta scheme along with the Adams–Moulton method was applied in this model. Finally, the model data was tested against real icing observation data, and satisfactory agreement was found between them. Furthermore, during the sensitivity test, it was found that variations of the relative wind direction had the most influential effect upon vessel icing (Horjen, 2013). Additionally, it was reported that when the wind speed was below 15 ms^{-1}, the wind-generated sea spray was negligible. However, the limitation of this model is that it divides the complete structures into a few parts, which creates inconsistencies in the final ice accretion results. Due to limitations of the input parameters, such as air velocity above the boundary layer, it also calculates less ice accretion beyond the boundary layer separation point. In addition,

due to the sponginess of accreted saline ice, it neglects heat transfer which is developed at the interface of brine film or ice surface.

ICEMOD2 was further developed by Horjen and renamed as ICEMOD2.1 (Horjen, 2015). This two-dimensional icing model is based on four differential equations: brine mass conservation equation, salt mass conservation equation, and linear momentum conservation equation in the x-axis, and y-axis. The brine film is assumed to be laminar in this model. The model represents a complete hydrodynamic model of momentum conservation, which includes molecular heat and salt transport in a laminar brine film layer which is supposed to be adjacent to the icing surface. It has been illustrated that the salinity of the brine film plays a major role in this model. The finite difference method in this model is also an extension of the two-step Lax-Wendroff scheme, like ICEMOD2. Moreover, appropriate time and space steps are chosen for solving the model's equations. A 4th order R-K method along with the Adam-Moulton method has also been applied in this model to solve the non-linear, ordinary differential droplet motion.

RIGICE and RIGICE04

RIGICE is another widely used numerical model of marine icing. RIGICE was developed in 1987 to determine the icing norms and extremes for an offshore structure located in Canadian waters (Brown et al., 1988; Roebber and Mitten, 1987). The main objective of the RIGICE model was to develop a simple and generalized algorithm. A FORTRAN code was initially used to develop the algorithm. The assumptions included in the initial RIGICE model were independent cylindrical geometry, fixed droplet diameter of 2 mm, negligible droplet cooling, and fixed liquid fraction at 0.26, among others. In the

RIGICE structure, the spray flux distribution was calculated by using the droplet trajectories, and a boundary layer model was applied to calculate the heat transfer coefficient for the upwind half of a cylindrical member. However, the spray droplet size is required to be assigned as an input, instead of an output of the model (Lozowski et al., 2000).

RIGICE04 is the modified version of N_RIGICE (Forest et al., 2005). Instead of using the old FORTRAN code, RIGICE04 used a new algorithm which was coded as an Excel spreadsheet with Visual Basic 6 subroutines (Forest et al., 2005). The upgraded algorithm includes more precise expressions for the equilibrium freezing point of brine, an empirical illustration for sponginess of accreted ice as a factor of ambient temperature, a spray liquid water content versus height model that corresponds to field data, and a new algorithm for calculating the frequency of significant spray events that produce spray clouds above 10 m. However, in a comparison of both models, it was found that the RIGICE04 model predicts lower values of total mass than the N_RIGICE model, due to the implementation of a new spray generation algorithm. Furthermore, the RIGICE04 predictions of ice accretion duration are compared with the ice accretion period on an offshore rig operation on the East coast of Canada. The comparison illustrated that the N_RIGICE model had overly predicted the duration, while the RIGICE04 model results were much closer to the measured duration. Though the RIGICE04 model is more accurate than the N_RIGICE model, it still requires quantitative verification by field measurements of icing data on structures.

The main differences between RIGICE and ICEMOD are as follows. The RIGICE uses time-averaged spray flux expressions obtained from Japanese fishing vessels, while the ICEMOD uses empirical data collected from drilling platforms. RIGICE uses time mean environmental inputs, whereas ICEMOD is a fully time dependent model. Unlike the ICEMOD model, the RIGICE model assumes uniform ice accretion over all structural members. RIGICE treats inclined and vertical members the same, whereas in the ICEMOD model, the inclination is an important factor to compute the brine film velocity. Additionally, the RIGICE model assumes a constant droplet and neglects the droplet cooling factor, while the ICEMOD model uses the median droplet diameter which is obtained from an empirical droplet size distribution, and droplet cooling is considered from the top of a droplet's orbit until it hits the structure. Both models consider simplified geometry and subdivide it into cylindrical and flat components. In the models, air flow around a component is assumed to be unaffected by other components of the structure, and the heat flux is approximated using empirical equations (Horjen, 2013; Kulyakhtin, 2014; Lozowski et al., 2000, 2002). Additionally, both models underestimate the heat transfer from the surface of large structures (Kulyakhtin and Tsaru, 2014).

MARICE

MARICE is a sea spray icing model that was developed in Norway. This is a three-dimensional, time-dependent model that uses the continuity, momentum and turbulence equations to calculate the airflow around a structure (Kulyakhtin and Tsarau, 2014). As part of the MARICE project, Kulyakhtin and Løset (2011) demonstrated a correlation between humidity level and in-flight spray temperature. Furthermore, to predict the precise

icing rate via accurate spray flow over the hull and superstructure of a ship, Kulyakhtin and others presented a 3D air-dispersed water flow model. Their proposed model was able to handle different turbulence models for predicting the collision efficiency and droplet flow pattern in the wake region which was developed behind the cylinder (Kulyakhtin et al., 2012a, 2012b, 2014). To activate their model, they applied several wind speeds, different droplet distributions, and various turbulence methods in the system, and illustrated that their model showed a promising improvement for calculating the ice accretion via different CFD methods.

The main advantage of MARICE is the application of CFD that can successfully calculate the turbulent airflow, heat transfer and trajectories of the droplets around a complete structure (Kulyakhtin et al., 2012a; Nakakita et al., 2010). Furthermore, it can calculate the icing rate by considering the heat conduction inside the accreted ice on the substrate's surface area (Kulyakhtin et al., 2016). Additionally, the icing data from the MARICE model can be stored in a database system that can be further used along with a weather forecast system to identify icing hazards of each particular marine vessel, depending on their characteristics (Kulyakhtin, 2014). Compared to ICEMOD and RIGICE04 model, MARICE can predict a more accurate heat transfer rate for large structures, and calculate ice growth and melting faster than the ICEMOD model (Kulyakhtin and Tsarau, 2014).

Some limitations still exist in the final model. For example, it neglected the droplet's surface tension effect, the impact force, the heat capacity effect of saline ice and

the surface roughness effect for ice accretion. Therefore, all these phenomena need to be considered for future models.

Other models

Blackmore and Lozowski (1994) introduced a different approach to the modelling of vessel spray icing. Instead of considering the heat balance between the icing surface and the airstream, their model considers the heat balance between the spray and airstream. In the model, the authors introduced a new concept called nucleated sea spray. For simplicity, the model considers several assumptions, such as continuous spray distribution and solid spray ice. However, the model includes all the significant atmospheric and oceanographic parameters as inputs. The parameters include wind speed, ship speed, wave impact angle, air temperature, sea surface temperature, salinity, vessel length, vessel beam, and freeboard. In terms of validations, the model considered a sea salinity of 32.5 ppt and a seastates of a 200 nm fetch, whereas for the Baltic Sea, it considered 5 ppt sea salinity and 100 nm seastate features. The model's sensitivity test demonstrated that air temperature, wind speed, wave height, ship speed, wave impact angle and vessel size are the influential factors for vessel icing. However, spray icing is less sensitive to sea-surface temperatures. The advantages of this model include simplicity and universality. It has been reported that if the length, beam, and freeboard are known, the model can predict the icing rate for various sizes of ships. Although the model shows promising performance against data and the Kachurin model, it requires further investigation regarding the nucleated spraying model. This is especially important for determining the environmental circumstances that influence ice accretion.

Chung (1995) and Chung et al. (1995a) developed a model in which they analyzed the distribution of ice accretion on a ship structure (Blackmore, 1996). Their intention was to examine the influence of ice distribution on the performance of ship dynamics. The model was divided into two parts: a sea spray icing model produced for the top side and a dynamic model used to predict the vessel's motion in a wave field while it is loaded with spray icing. The model used several input parameters, including air temperature, relative humidity, air pressure, sea surface temperature, wind speed and direction, fetch, ship speed and direction, and duration of the simulation (Chung, 1995). The output calculated the spongy ice thickness, spongy ice mass and spongy ice accretion rate for every grid cell. Additionally, the total accretion mass for the entire vessel and the overall icing rate can also be calculated from this model. Even though the work is a blueprint of numerical ice modelling, it still has a few limitations which make the model insufficient for real life situations. The limitations of Chung's model include constant time spray duration (around 3.5 seconds), negligible conductive heat loss from the substrate surface, conductive heat loss through the surface brine film is not explicitly included, the ice thickness is limited to a maximum height of 1 mm, and the object's surface is assumed to be planer and no curvature effects are considered for the mast. In contrast to Chung's model, several researchers from the University of Alberta have developed a three-dimensional model which forecasts superstructure icing (Lozowski et al., 2000). In their model, they divided the superstructure into four subdivisions: ahead of the main superstructure, the superstructure, the masts and antennae, and the decks. As input parameters, the model used air temperature, dew point temperature, air pressure, true or apparent wind speed and

direction, sea surface temperature, sea surface salinity, fetch, ship speed and course. For each forecasting time step the model computed ice accretion from a single spraying event, and the total accumulated ice accretion was determined by multiplying the number of spraying events during the time-step. Although the model can approximately predict the spray event, a few limitations still exist in this model. These limitations include that the model considered the ship movement as having only one degree of freedom, it neglects the ship dynamics, and neglects the effects on splashing of the pitch, roll, yaw, heave, surge and sway.

Ice loads on vessels cause many hazardous situations. Some methods for ice load measurements are described by Fazelpour et al. (2016a, 2016b). Infrared cameras are newly available equipment for ice load measurements (Fazelpour et al., 2016a, 2016b). As a consequence of calculating the superstructure ice load and changing stability, Kato (2012) proposed an algorithm which is very new and effective in the ship navigation field. For calculating ice accretion, it includes air temperature, relative wind speed and wave height. A free surface effect, which occurred due to the trapped water on the deck, was also added into the model. Lastly, the author integrated the model with ice bridge simulators and calculated computational data. Regardless of the effectiveness of this model, the work still needs a few modifications. For example, the model is not tested experimentally, and needs validation. The algorithm considers the static analysis of external conditions e.g. wind speed, air temperature etc; hence, a dynamic model needs to be proposed. Regarding the calculation of liquid water content (LWC), the model analyzed several methods; however, none of these calculations considered the object height and therefore, future models need

to include this factor. Efimov (2012) also proposed a model to study ice properties, the nature of icing, and different mechanisms of its accretion on the ship, which focused on the icing on a fixed plate, and plate wiggling harmonically in the vertical plane. To simplify this model, the author considered several assumptions, which are the shortcomings of this work. The limitations of Efimov's mathematical model are that all the droplets are assumed to be the same size, and there is no air drag effect, no reference to time, no acceleration or movement of the droplets, no slip between air and water droplets, the air and water droplets have the same velocity, the wind profile is described with a power equation, and the pack of droplets is cubic hexagonal.

Based on mass, heat, and salt conservation, a new numerical model was proposed by Hansen (2012) where the author calculated the icing rate for an entire vessel. Hansen used a polygon-based complex geometry and backward spatial difference Lax-Wendroff numerical method. To validate the work, the author used some offshore data from the Norwegian Sea and the Barents Sea. However, when the spray flux is low and the weather conditions are too mild, this method shows instability for dry ice accretion. Bjerkås (2006) studied the ice pressure on full-scale structures by means of field test observations. For analyzing the phenomenon, a cross-correlation technique based on the Continuous Wavelet Transform (CWT) system, is applied. Zarling (1980) conducted a numerical study and calculated the heat and mass transfer phenomena of a free-falling droplet in very cold atmospheric conditions, and demonstrated that nucleation of a water droplet can easily occur when the atmospheric temperature is around -18 °C or less.

1.4 Thesis Objectives

The literature review discussed only the marine icing works that have been conducted in past studies. All the empirical models discussed in the previous studies are highly standard and unique; however, more correct physical and realistic data are required, one of the aims of this thesis. Current work contributes a better understanding of the fundamentals of the ice accretion process on various substrates due to marine icing resulting from the sea spray or atmospheric moisture in cold region environments.

Figure 1.2 illustrates a typical spray generation situation, where numerous droplets are generated, carried by airflow, and then impact on an object's surface. The process before impact is known as pre-impact and the process after impact is called post-impact.

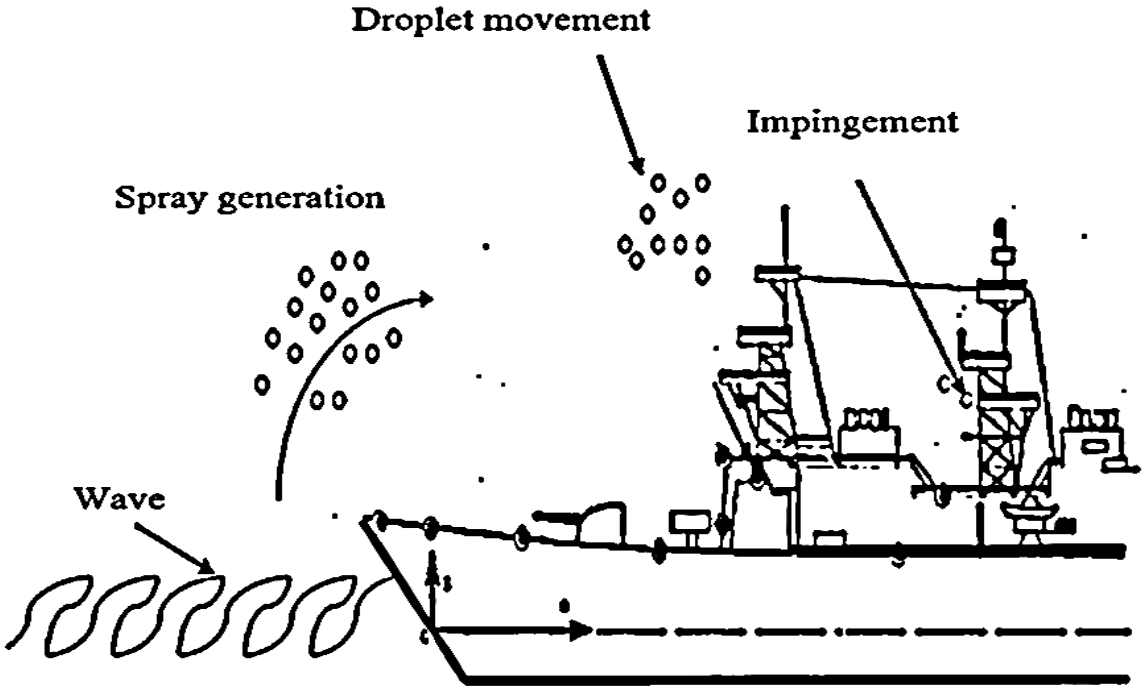

Fig. 1.2 Typical water spray generation process (Ryerson, 1992).

The pre-impact process involves droplet movement and cooling, whereas the post-impact process involves spreading, freezing and run-off. During the pre-impact process, droplets need to travel in the atmosphere, and a complex heat transfer process occurs between the droplets and environment, which affects the droplets' conditions. After impact, droplets might freeze on the surface or be deflected from the surface. Therefore, the post-impact process considers spreading, freezing and run-off. Table 1.5 presents the overall situation of pre-impact and post-impact processes.

Table 1.5 Classification of ice modelling.

Process	**Modelling category**
Spray or droplet generation	Pre-impact i
Droplet movement in the air	Pre-impact ii
Droplet impingement and freezing	Post-impact i
Water run-off	Post-impact ii

Based on field observations, various analytical and empirical models have been developed to predict spray generation, however, limited research has been conducted on spray or droplet movement, impingement, and the resulting heat transfer physics. This thesis aims to contribute to these particular areas by achieving the following objectives:

- Explore the main variables of icing in the context of marine vessels and offshore structures.

- Investigate the temperature dependent thermo-fluid beheviours inside a free-falling droplet and propose a scaling analysis to predict the internal circulation effect on the nucleation process.
- Demonstrate the post-impingement characteristics of water droplets onto an isothermal substrate and propose an analytical tool to verify the available results.
- Use a numerical tool to examine the interfacial heat transfer phenomena inside a solid substrate during the post-impingement process, an important aspect of the heat transfer process.
- Investigate the effect of surface properties (by applying coated/non-coated substrates) on droplet dynamics or the icing process by experimental methods.

1.5 Thesis Outline

The thesis begins with a brief overview of marine icing in the context of vessels and offshore structures, as well as the atmospheric icing process. Both fresh and salt water icing phenomena were considered. A summary of the objectives and a brief outline of the thesis are provided. A summary of the research methodology, along with an emphasis on phase change modelling using computational fluid dynamics and heat transfer methods, as well as experimental approaches are presented in Chapter 2. Results have been analyzed and presented in terms of processes that occur prior to and after droplet impact.

Ice accretion in cold regions is complicated and requires a better heat balance model. Additionally, more research and precise measurements are required for calculating the thermo-physical properties and heat transfer phenomena. Although previous research does provide valuable information, most of it is focused on fresh water droplets. Heat and

mass distribution inside a traveling saline water droplet, the hydrodynamic effect on droplet movement, and droplet deformation and break-up in the atmosphere are necessary. Chapter 3 investigates these phenomena. A numerical model is developed that simulates the Arctic environment, where a free-falling water (fresh/salt) droplet stays in the air for long residence times. Temperature dependent thermophysical properties are used to investigate the thermofluid beheviour. This work includes treatment of nucleation, internal circulation processes and the effects of drag. An analysis of the scaling of these results was also conducted.

Boundary conditions and environmental heat transfer to or from the substrate surface needs better approximation in future numerical modelling. Phenomena such as velocity distribution, air entrapment and temperature distribution inside the accreted ice also require more explanation for better understanding and for future modelling purposes. Chapter 4 presents an analysis of droplet impingement onto an isothermal substrate. The effect of droplet size and substrate temperature of solidification was investigated. This included numerical analysis and a comparison with experimental results. Chapter 5 presents the results of a new numerical model developed to investigate the interfacial heat transfer phenomenon as well as the splat dynamics.

Chapter 6 illustrates the experimental results of droplet impacts on various coated/non-coated substrates. The chapter is divided into three sections. In the first section, droplet-substrate wetting behaviour is investigated via the contact angle measurements. The next two sections investigate the post-impact spreading dynamics and freezing times as a function of droplet size, droplet materials, air temperature, substrate temperature,

substrate properties and coating/paint properties. Chapter 7 concludes with a brief discussion of this research followed by some recommendations for future work.

CHAPTER 2[2]

RESEARCH METHODOLOGY

2.1 Introduction

Phase change problems arise in many areas of research, including solidification of casting, icing, material processing and molecular diffusion flow applications (Ayasoufi, 2004; Basu and Date, 1988; Crank, 1984; Hu and Argyropoulos, 1996). The problem of phase changing from a liquid to a solid or vice versa is known as the Stefan problem, for the researcher who conducted the phase changing study on the melting of polar ice (Ayasoufi, 2004; Basu and Date, 1988; Crank, 1984; Hu and Argyropoulos, 1996). The Stefan problem is also referred to as a moving boundary problem (MBP), in which the interface or position of the moving boundary is determined as a function of time and space (Crank, 1984; Hu and Argyropoulos, 1996; Pardeshi et al., 2008; Voller, 1996).

A general solidification process involves a solid region, a liquid region and a solid-liquid interface region, which is also known as the mushy region (Pardeshi et al., 2008). The mushy region occurs at equilibrium temperature in the solid-liquid interface, which is the main feature of a phase change problem (Belhamadia et al., 2012; Hayashi, 1991; Woodruff, 1973). Special consideration is required for modelling the thermodynamic relation at the solid-liquid interface region (Ayasoufi, 2004; Lacorix and Voller, 1990). During solidification, latent heat is released at the interface region, which is transferred by

[2] This chapter is written based on: Sultana, K.R., Dehghani, S.R., Pope, K. and Muzychka, Y.S., 2018. Numerical Techniques for Solving Solidification and Melting Phase Change Problems, in Numerical Heat Transfer, Part B: Fundamentals, pp.1-17.

conduction in the solid phase, as well as by the combined effects of conduction and advection in the liquid phase (Basu and Date, 1988).

In earlier studies, researchers have applied many theoretical or experimental techniques to calculate the transient phase change. However, due to the presence of the mushy region in multi-dimensional problems, recent studies have found that numerical techniques are more efficient (Basu and Date, 1988). Based on this, the current thesis considers the numerical approach to investigate phase change. A comprehensive review of existing numerical techniques is presented. Generalized mathematical formulations, along with boundary conditions are covered in the first subsection. Based on conduction and convection phase change applications, the variable grid method is discussed in the following subsection, proceeded by the solution techniques for the fixed grid enthalpy method. Several co-authors have contributed to this analysis. Dr. Dehghani makes substantial contributions to conception and design, Drs. Pope and Muzychka participate in the article, revising it critically for important intellectual content and giving final approval of the version to be submitted as well as any revised version.

2.2 General Phase Change Formulation

A schematic diagram of a heat conduction controlled two-phase Stefan problem is presented in Figure 2.1. The domain of interest consists of a liquid region and a solid region, separated by a sharp, moving interface. The basic assumptions of this problem are that the density, specific heat and thermal conductivity of the solid are maintained constant. However, if the solid and liquid phases have different densities, then the liquid may acquire a convective motion (Gupta, 2003).

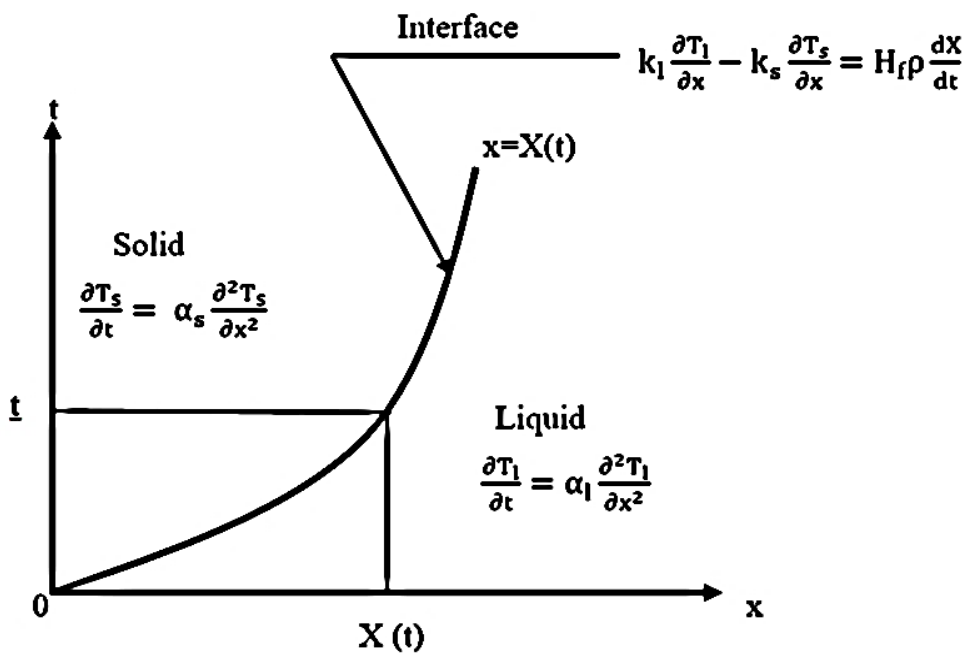

Fig. 2.1 Schematic diagram of a two-phase Stefan problem (Hu and Argyropoulos, 1996).

Heat conduction in the solid region is represented by the following equation (Ayasoufi, 2004; Furenes and Lie, 2006; Hu and Argyropoulos, 1996; Poirier and Salcudean, 1988; Voller and Cross, 1981a):

$$\frac{\partial T_s}{\partial t} = \alpha_s \frac{\partial^2 T_s}{\partial x^2} \quad for\ 0 < x < X(t), t > 0 \tag{2.1}$$

Heat conduction in the liquid region is represented by:

$$\frac{\partial T_l}{\partial x} = \alpha_l \frac{\partial^2 T_l}{\partial x^2} \quad for\ X(t) < x < \infty, t > 0 \tag{2.2}$$

Temperature at the solid-liquid interface region can be expressed as:

$$T\ (X\ (t), t) = T_m \quad t > 0 \tag{2.3}$$

Stefan condition at the solid-liquid interface region can be defined as:

$$k_l \frac{\partial T_l}{\partial x} - k_s \frac{\partial T_s}{\partial x} = H_f \rho \frac{dX}{dt} \qquad for\ x = X(t), t > 0 \tag{2.4}$$

where H_f is the latent heat that is released during solidification. Equation (2.4) represents the heat balance across the phase change boundary, $x = X(t)$. The initial and boundary conditions are:

$$T(x, 0) = T_s < T_m \quad for\ x > 0, X(0) = 0 \tag{2.5}$$

$$T(0, t) = T_l > T_m \quad for\ t > 0 \tag{2.6}$$

$$T(x, t) = T_s \quad for\ x \rightarrow \infty, t > 0 \tag{2.7}$$

The analytical solution of this one-dimensional Stefan freezing problem is (Voller and Cross, 1981a):

$$X(t) = 2\gamma(\alpha_s t)^{1/2} \tag{2.8}$$

$$\alpha_s = \frac{k_s}{\rho_s C_s}$$

2.3 Numerical Techniques for Solving Phase Change Problem

For solving a phase change problem, fixed and variable grid methods are available. Both methods utilize three kinds of discretization techniques, including finite-element, finite-difference and boundary element methods (Hu and Argyropoulos, 1996; Idelsohn et al., 1994). Based on the numerical applications, finite-difference methods (FDMs) may be classified into two main categories: fixed grid methods (FGMs) and variable grid methods (VGMs) (Furenes and Lie, 2006). A detailed discussion of these techniques is presented in the following subsections.

2.3.1 Variable grid methods

In a variable grid method, the total domain consists of two individual phases and an interface region (Basu and Date, 1988). This method helps to track the exact location of the moving boundary region on a grid point at each time step (Hu and Argyropoulos, 1996). VGM can be classified into two groups: front-tracking and front-fixing methods.

Front-tracking methods

This section reviews the front-tracking method, which calculates the location of the moving boundary at each time step. The front-tracking method is categorized by variable time steps (VTS) or an interface fitting method, and variable space grids (VSG) or dynamic methods (Hu and Argyropoulos, 1996).

Rather than using a fixed time step and searching for the new boundary, a variable time step was introduced by Douglas and Gallie (1955). In this method, they established a convergence and stability criteria for the implicit scheme solutions. The main facility of this technique is that it can dictate a grid line in space at each time level (Basu and Date, 1988; Gupta and Kumar, 1981; Samarkii et al., 1993; Shastri and Allen, 1998). However, the limitation of this method is that it can only consider a constant heat flux at a fixed object surface. To overcome this shortcoming, a modification was proposed by Gupta and Kumar (1981). By applying the same set of finite-difference equations, they extended the method for more general convective type boundary conditions, and revealed that their method represented a much stronger result than Douglas and Gallie's (1955) approach.

Over the same time period, Goodling and Khader (1974) proposed another variable time step method that incorporated a finite-difference form of the Stefan condition with a

new system of equations; which needs to solve for an arbitrary value of temperature near the moving boundary node, and then update it from the Stefan condition. However, Gupta and Kumar (1981) reported that Goodling and Khader's method does not converge as the computation progresses in time, and the error which is incorporated in the boundary condition behaves in an irregular fashion. Later, the authors proposed a new technique and showed that their method had better performance than Goodling and Kader's method. Recently, Feurenses and Lie (2006) have suggested a technique that can track the movement of interface location in a moving boundary value problem. They adopted a method that was initially proposed by Chun and Park (2000), and applied the event location technique for solving a phase change problem. Chun and Park (2000) used a fixed time step for their work, whereas, Feurenses and Lie (2006) used a variable time grid method. Additionally, instead of using enthalpy as a stable variable, Feurenses and Lie (2006) used temperature as a factor and applied it to each grid cell. A comparison was prepared with the analytical solution of the one-dimensional half space solidification problem, and it was found that for a one-dimensional phase change problem, the technique gives an accurate and fast solution. For equal thermal properties in solid and liquid regions, the proposed event location method showed good agreement with the exact solution of Chun and Park (2000).

In contrast to the interface fitting method, the dynamic grid method is such that the number of spatial intervals is kept constant and adjusted to ensure the moving boundary is on a particular grid point. By using the dynamic grid formulation, Murray and Landis (1959) initially solved the freezing problem, where they applied an explicit technique.

Heithz and Westwater (1970) solved a one-dimensional solidification problem, where they integrated the variable volume along with a high conductive liquid and applied it to a saturated fluid. Tien and Churchill (1965) extended this model to a cylindrical geometry problem. Instead of focusing on phase change, Crank and Gupta (1972) applied a non-uniform grid size around the moving boundary region and solved it by moving the entire uniform grid system with the velocity of the moving boundary. Based on cubic, spline, or polynomials, Crank and Gupta (1972) demonstrated two new schemes that were used to obtain the interpolated values of temperatures at the new grid points. By a Taylor series expansion of space and time variables, Gupta (1974) provided a new interpolation scheme and presented a new equation that was essentially a particular form of the Murray and Landis equation.

To eliminate the complexities generated during the coordinate transformation process for multi-dimensional problems, Kim and Kaviany (1990) proposed a newly transformed equation that preserves and utilizes the conservative forms, so the conservation principles are followed exactly in each phase. An implicit finite-difference method was required to solve the technique. The main advantage of this approach is that without doing iteration at each time step, it can update the interface location and is capable of handling many phase change problems where the phase change occurs at a distinct temperature. The limitation is that it cannot handle a problem where latent heat is released over a range of temperatures. For the application of a general finite-difference technique along with the front-tracking method, Parissenti and Niro (2015) proposed an approach where they considered a one-dimensional, three-phase Stefan problem along with a second-

order Lagrangian interpolation technique. They applied their technique to a low Stefan number complex multi-phase problem and validated their numerical model by considering a two-phase analytical solution. Moreover, they calculated the time-dependent temperature profile, as well as the movement of the boundary for that particular model and compared the numerical result with the previous work of Bonnerot and Jamet (1981), which produced similar results. The main difference is that the approach used a finite-difference technique and an adiabatic condition at the end of the slab, whereas, the earlier method used a finite-element technique. In addition, another comparison was carried out with Belkin's model and similarities were found for a non-dimensional ejected mass flow rates problem.

To solve two-dimensional Stefan problems, a finite-difference marching method was presented by Asaithambi (1990). The major feature of this method is that to solve numerical calculations, it can be employed on the boundary-fitted coordinates and the backward difference schemes. This method replicated the set of the problems found in Gupta and Kumar's (1986) work, and showed that for various grid spacing applications, this approach is very consistent and second-order accurate in space. Based on the finite-difference technique for a one-dimensional Stefan problem, Bonnerot and Jamet (1979) presented a third-order accurate discontinuous finite-element approach, as the initial singularities generate no irregularity in the computed results. For a two-dimensional phase change problem, a numerical method was developed by Yoo and Rubinsky (1983), in which they applied a finite-element method to yield the transient interface position. To obtain the solution, their method independently solved the energy equation on the moving interface region. The authors noticed that the result was inherently stable and capable of

handling multi-dimensional problems with complex boundary conditions. However, to obtain a direct calculation of thermo-physical properties and the heat transfer coefficient at the intermediate time level, Comini et al. (1974) applied a three-level time difference scheme to a transient phase change problem, where non-linear physical properties were involved. Further, Fabbri and Voller (1995) proposed a general grid scheme method that can be applied to problems that incorporate a phase change over a temperature range or involve kinetic undercooling. To get a numerical solution, they have applied the enthalpy method on a continuously deforming finite element grid.

A technique called the method of lines was proposed by Meyer (1977) that converts the partial differential equation into a set of simultaneous ordinary differential equations (1998), and the stiffness that arises in the governing equations makes the method less popular to apply in phase change problems (Polis and Goodson, 1976). To tackle these difficulties, Shastri and Allen (1998) applied a stiff solver CVODE in their model, and reported that the combination of the enthalpy method and the method of lines is very favorable when small time steps are coupled with stringent accuracy. However, a limitation is that this method is not suitable for handling mushy region problems.

Front-fixing methods

An alternative way to track the moving front is to fix it by introducing a new space variable. The transformation was introduced by Landau (1950) and first applied to a finite-difference scheme by Crank (1957). Citron (1962) and Mastanaiah (1976) included temperature-dependent thermal properties such as thermal conductivity and specific heat in their method, and solved it by a Taylor series formulation technique. For a one-

dimensional freezing problem, the method was further implemented by Beaubouff and Chapman (1967). Additionally, Furzeland (1980) provided detailed comparisons of the boundary-fixing method for one-dimensional problems. A two-dimensional freezing problem was implemented by Duda et al. (1975), Saitoh (1978) and Hsu et al. (1981). Duda et al. (1975) proposed a technique for solving the moving irregular boundaries problem. In this technique, the authors include an immobilization transformation and a numerical scheme for solving the transformed equations.

To obtain a refined method, Hsu et al. (1981) formulated a coordinate transformation for their control volume formulation. Over the same period, Saitoh (1978) applied a transformation in the radial coordinates, which can provide a useful way to operate a phase-change boundary problem within an arbitrarily shaped region. Following the earlier work of Duda et al. (1975), Saitoh (1978) compared his numerical result for liquid solidification in a square region with experimental values and found a promising outcome. Moreover, the author performed a similar experiment for some triangular regions.

Winslow (1967) and Chu (1971) discussed curvilinear coordinates, where Chu demonstrated that his advised technique eliminates the programming difficulties of a finite-difference method near the curved boundaries. Furzeland (1977) summarized some of the transformations, orthogonal, and non-orthogonal functions. Additionally, Furzeland (1977) introduced a new parameter for smoothing the latent heat jump of the enthalpy function, and claimed that it is unconditionally stable and easy to apply to a moving boundary problem. To validate this theory Furzeland highly recommended an experimental study.

Instead of considering the Eulerian viewpoint, in an iso-therm migration method the Lagrangian method is used to track the medium of individual points which are associated with the iso-therms (Basu and Date, 1988). The iso-therm migration method was presented by Chernousko (1970) and individually by Dix and Cizek (1970). The authors explored their idea for a one-dimensional problem. By using an explicit finite-difference approximation to a non-uniform fixed grid mesh, Lazaridis (1970) solved a two-phase solidification problem in both two and three dimensions. By considering a quadratic temperature profile in the vicinity of the phase front, the author illustrated the heat-balance condition on the solidification boundary in Patel's form, and developed a numerical scheme based on the auxiliary set of differential equations, which indicates that the moving boundary is an iso-therm.

Turland (1979) and Turland and Wilson (1977) extended this method for a two-dimensional problem. Crank and Gupta (1975) mentioned that some discrepancies might appear due to the initial set of iso-therms when the calculation started. Further, Crank and Crowley (1978) discussed the accuracy and stability criteria for a multi-dimensional problem, which was introduced in Crowley (1978) and Elliott's (1976) work. Additionally, Crank and Crowley (1979) recommended an implicit formulation based on the Crank-Nicholson scheme. In their study, they showed that when the number of grids on a particular iso-therm is more than ten, the computational time for the implicit method is higher than the explicit scheme (Basu and Date, 1988). This type of method is easy to apply in variable thermal properties and moving phase boundary problems.

The earlier studies revealed that the variable time steps method can accurately calculate the interface region of one-dimensional, single-phase, and multi-phase problems, it requires more focus on accuracy, convergence, ease of programming, and experimental validation. Additionally, work is needed for convection type phase change applications.

2.3.2 Fixed grid method

The fixed grid scheme uses a fixed coordinate system to compute the velocity component and solves the transport equation for a phase change problem (1987). In this method, the heat flow equation is approximated by the finite-difference replacements used to calculate the values of temperature and time for the interface region (Hu and Argyropoulos, 1996). Based on earlier studies, the most prominent technique for illustrating the fixed grid method is the enthalpy method (1990). Due to its vast application, work on the enthalpy method can be categorized into two sub-sections: pure conduction with phase change problem and convection related problems (1987).

Enthalpy method: pure conduction with phase change

In a phase change problem, the thermal energy is absorbed or released at the interface region and drawn from one phase to another primarily by means of conduction (Basu and Date, 1988; Lacroix and Voller, 1990; Poirier and Salcudean, 1988; Shamsundar and Sparrow, 1975). The enthalpy method is one of the commonly used approaches for heat conduction controlled phase change problems.

For one-dimensional, no energy generation and constant thermo-physical properties within each phase, the conduction related enthalpy equation can be demonstrated

as (Ayasoufi, 2004; Hu and Argyropoulos, 1996; Voller, 1996; Voller and Cross, 1981a; 1983):

$$\rho \frac{\partial h_{en}}{\partial t} = \frac{\partial}{\partial x}(k_c \frac{\partial T}{\partial x}) \tag{2.9}$$

where the left-hand side represents the enthalpy and the right-hand side represents conduction heat transfer. The enthalpy is a function of temperature, and the relationship is generally considered to be a step function for isothermal phase change problems, and a linear function for non-isothermal phase change applications. Both isothermal and non-isothermal phase change cases can be illustrated by the following equations (Hu and Argyropoulos, 1996):

$$h_{en} = \begin{Bmatrix} C_s T & T \leq T_m & solid\ phase \\ C_l T + H_f & T > T_m & liquid\ phase \end{Bmatrix} \text{ for isothermal phase change.} \tag{2.10}$$

$$h_{en} = \begin{Bmatrix} & solid\ phase & \\ C_s T & T \leq T_m & \\ & solid/liquid\ phase & \\ C_{in} T + \dfrac{H_f (T - T_s)}{(T_l - T_s)} & T_s \leq T \leq T_l & \\ & liquid\ phase & \\ C_l T + H_f + C_{in}(T_l - T_s) & T \geq T_l & \end{Bmatrix} \text{ for non} \tag{2.11}$$

$$- \text{ isothermal phase change.}$$

Eyres et al. (1946) were the first to use the enthalpy method in a heat conduction problem (Hu and Argyropoulos, 1996). Additionally, Dusinberre used this approach for solving a phase change problem (Basu and Data, 1988; Dusinberre, 1945). Thereafter,

Albasiny (1956), Baxter (1962), and Price and Slack (1954) each applied this technique to solve freezing problems in a semi-infinite plane, finite slab and cylinder surface (Basu and Date, 1988). The main feature of the enthalpy method is that it provides the solid-liquid interface as a part of the solution without explicit tracking (Ayasoufi, 2004; Beckett et al., 2001).

Rose (1960) introduces a weak solution for Stefan problems in a finite-difference scheme. Friedman (1968) and Lions (1969) analyze and extend the solution. Several authors propose different theories to apply the enthalpy method directly to the problem. Bonacina et al. (1973) use a three–level implicit scheme to find a stable and convergent numerical solution for a one-dimensional, two-phase Stefan problem. They substitute the enthalpy jump at the interface region with an equivalent heat capacity, which is equal to the multiplication of density and specific heat.

Atthey (1974) used the discontinuous form of the enthalpy function in a one-dimensional explicit form. The one-dimensional, two-phase Stefan problem is specifically dependent on temperature zone width (Bonacina et al., 1973; Furzeland, 1980). Crowley (1978) extended the scheme for a two-dimensional form for two models with two different surface conditions for inward solidification of a square cylinder of liquid, which is initially at its freezing temperature. The surface temperature was lowered at a constant rate, which agrees with Saitoh's (1976) experimental results. An explicit finite-difference scheme was used to solve the enthalpy calculations in a twenty-by-twenty spatial mesh domain. In the second problem, where the surface temperature was dropped discontinuously and then maintained constant, the same enthalpy method was re-applied to a forty-by-forty mesh

domain. This result is graphically compared with Allen and Severn (1962), Lazaridis (1970) and Crank and Gupta's (1975) work. In contrast to Crowley's work (1978), Rao and Sastri (1984) proposed a method where they neglected the necessity of iterations at ordinary nodes which are away from the interface, and showed that for the calculation of interface movement along the diagonal of a prism, their proposed method is more accurate than Crowley (1978) and Lazaridis's (1970) work. Furzeland (1977) introduced a new parameter to smoothing the latent heat jump of the enthalpy function, and claimed that it is unconditionally stable and easy to apply to the moving boundary problem. Furzeland (1977) highly recommended an experimental study to validate this theory.

For multi-dimensional Stefan problems, Budak et al. (1965) and Samarskii and Moiseynko (1965) were the first to use smoothed enthalpy functions in multi-dimensional problems with locally one-dimensional finite-difference methods. Couch et al. (197) and Meyer (Meyer, 1973, 1975) suggested two-dimensional implicit finite-difference and finite-element schemes for moving boundary problems. In the former paper, Meyer (1973) expressed interest in the efficient numerical solution of the non-linear equations where the implicit formulation is required. Instead of using the discontinuous enthalpy equation, the author applied the continuous piecewise linear enthalpy on a general domain subjected to prescribed temperatures on the boundary region for an approximate Stefan problem, and demonstrated that the resulting non-linear algebraic equations are solvable with a Gauss-Seidel method. In contrast to Meyer's work, for a multi-dimensional problem, Bonacina et al. (1973) and Comini et al. (1974) used a three-level scheme, where the authors investigated the influence of temperature, dependent properties such as thermal

conductivity, heat capacity, rate of internal heat generation and the effect of phase change dynamics on surface heat transfer coefficients. Their investigations give a new insight that the assumption of pure conduction in the liquid phase is not always correct, whereas an equivalent thermal conductivity dependent on the Rayleigh number can be used when convection is important. Besides the analysis of thermo-physical properties, Elliot (1987) concentrated on the error analysis of the enthalpy method for the multi-dimensional Stefan problem, by means of an implicit time-discretization technique.

In a phase change problem, an important and difficult task is to accurately determine the moving boundary region (Basu and Date, 1988; Pardeshi et al., 2008). This is because during phase change, a transient phenomenon is developed in the interface area that creates a waviness characteristic in the solution. Shamsundar (1978) observed this phenomenon while solving a one-dimensional problem with Meyer's (1971) model. Shamsundar (1978), while calculating heat flux predictions, reported that this behaviour was one of the inherent characteristics of the enthalpy model, and speculated that it might occur if the temperature is kept constant for a two-phase node or control volume area. Voller and Cross (1981a) had a stepwise temperature increment while solving the Goodrich's (1978) problem, incorporated with the Meyer's (1971) model. The authors proposed a modified scheme of the enthalpy equation to remove the waviness in the solution. They described an implicit scheme, which integrated with an appropriate time step so that the boundary can accurately move from one node point to another for each chosen time step. They named it "node-jumping scheme" and the way of solving the enthalpy equations was named "variable time-step enthalpy formulation". The advantage

of this approach is that the location of the new phase-change boundary will be known at each time step, which means the nodal enthalpy and the temperature distributions can easily be calculated, whether or not the heat parameters in both phases are different. Consequently, Voller and Cross (1981b) have extended their one-dimensional method to a two-dimensional freezing problem for a cylindrical coordinate system and confirmed that their explicit numerical scheme can be satisfactorily applied to the phase change problem of a circular cylinder. Bell (1982) began work on the enthalpy solution for a two-phase Stefan freezing problem, which was initially posed by Goodrich (1978). As mentioned earlier, Goodrich described the one-dimensional Stefan problem by developing a new method, which was based on the central-difference formulation with the Gaussian elimination technique. However, this technique is used at ordinary nodes to track the interface boundary location. The author claimed that this technique is much superior to the apparent heat capacity formulation and less expensive to solve nodal iteration calculations. The limitation of this study is that it is unable to solve the temperature distribution problem which arises in two-phase regions. To overcome this shortcoming, Bell (1982) calculated the local solidification time of a control volume by an analytical method and reported that the time over which temperature, obtained by enthalpy formulation, remains constant is equal to the solidification time of that control volume. Additionally, the author demonstrated that the temperature within the solid region phase is quasi-steady, which makes the temperature distribution linear. A numerical solution is the most appropriate way to calculate this phenomenon accurately. In this study, Bell justified Voller and

Cross's (1981a) suggestion of the stepwise increment of temperature, and applied a finite-difference technique to represent this phenomenon.

By applying a linear enthalpy distribution between nodes, Tacke (1985) proposed an explicit finite-difference formula to get an inherent oscillation-free solution in the enthalpy method. This method suggests that the enthalpy of the control volume where the phase front locates is equal to the total enthalpy given by the usual enthalpy method. Therefore, the phase front obtained by this technique becomes a new grid point where the solution becomes oscillation-free, in both temperature and moving boundary positions. Although the solution is very accurate in the case where there is a high ratio of latent heat to sensible heat, it is limited to a one-dimensional problem and uses the same material properties for both phases. Pham (1985) proposed a new three-level enthalpy scheme that is capable of resisting the jumping of the latent heat peak, and works well for pure cooling phase change as well as abrupt enthalpy change problems. This technique uses the finite-difference approach to solve problems. The following year, Pham (1986) again offered a technique where the finite-element scheme is used by lumping the thermal capacitance at the node. The proposed method is similar to Zienkiewicz et al.'s (1973) work, however, Zienkiewicz et al. considered the latent heat at the nodes, rather than lumping the sensible heat. Compared to previous approaches, the method is computationally simple and effective, visually consistent, and easier to apply in the explicit enthalpy method.

For constant specific heat, Voller et al. (1990) developed a new algorithm that can accurately track the solid-liquid interface, and has the ability to predict the temperature profile at each time step. They summarized several enthalpy-based algorithms and

compared their performance. By separating the sensible and latent heat terms, Voller (1985) developed an alternative formulation of an enthalpy form and introduced a latent heat source in a new equation, which acts like a linearization term in the subsequent iterative solution. The main advantage of this equation is that it only considers one variable, temperature, which is explicitly solved at each time step and the iterative scheme does not depend on the iterated value. For the calculation of one-dimensional and two-dimensional problems, this method is 20-25% faster than earlier methods. It is compatible with the control volume conservation technique for numerical predictions with complex geometries or variable properties. To make the enthalpy method more physically accurate, Voller (1990) introduced a new variable called "local liquid fraction" which is normally located in the control volume of fusion. This method is implicitly solved by considering the heat conduction equation along with a source term consisting of a liquid fraction. Although the method is faster in computation, it creates transient oscillations in the phase boundary calculation. One reason is that the phase front, which is considered in this problem, is accounted for as a control volume, rather than a surface.

Enthalpy method: convection with phase change

When the liquid phase does not remain stationary, conduction heat transfer may be superimposed by convection heat transfer (1992). By considering the energy balance of a control volume, $\boldsymbol{V}$**,** with surface area, $\boldsymbol{A}$, Shamsundar and Sparrow (1975) added the fluid motion or convection term to the regular enthalpy equation, making it valid throughout the entire domain (Crank, 1984; Shamsundar and Sparrow, 1975):

$$\frac{d}{dt}\int_{\boldsymbol{V}} h_{en} d\boldsymbol{V} + \int_{\boldsymbol{A}} h_{en}\boldsymbol{V}.d\boldsymbol{A} = \int_{\boldsymbol{A}} k_c \nabla T.d\boldsymbol{A} \tag{2.12}$$

where the second term on the left-hand side accounts for any fluid motion due to density changes or convection.

Basu and Date (1988) discussed various formulations and classifications of melting and solidification problems, with and without the convection term (Samarskii et al., 1993). Bonacina et al. (1973) emphasized the effect of the Rayleigh number when convection became important in a phase change problem. To allocate the movements of boundaries in both coordinates and directions, an extended finite-difference technique, including the convection and volume change formulation was presented by Kim and Kaviany (1992). In this technique, they discretized the pseudo-velocities that arose from immobilization which corresponded to the geometrical relation, and associated them with the moving control volumes. The pseudo-velocity field is capable of solving the continuity equation independently and makes the method suitable for diffusion-controlled, moving boundary problems. Feulvarch and Bergheau (2007) modeled the latent heat effects that can appear during industrial phase change processes such as quenching, by means of the finite-element discretization technique. Assuming the enthalpy is a function of temperature, their method was developed for both transient heat conduction and diffusion-convection type problems. They presented an implicit time discretization technique for an isothermal phase change problem, and illustrated how it is more efficient due to its large time step application. They used welding and heat treatment software named SYSWELD to run their finite-element

steps. Rabin and Korin (1993) worked on a model where they addressed the radiation heat transfer process in the enthalpy model.

Based on the enthalpy method, Cao et al. (1989) and Voller and Prakash (1987) discussed various numerical models, where their main focus was on the convection term in a multi-dimensional phase change problem. Cao et al. (1989) discussed problems with explicit attention to the nature of the phase change front, while Voller and Prakash (1987) focused on introducing a new area called a "mushy region". Voller and Prakash (1987) proposed a new method that is able to solve the convection-diffusion mushy region problem, including pure materials and alloy solidification. A finite-difference technique, a linear relationship between enthalpy and temperature and a Darcy source approach for both linear and non-linear problems, are applied in their work. A forty-by-forty uniform square grid is chosen for solving the problem. From preliminary results, the authors suggested that the Darcy source is efficient to model the effect of the mushy region's porosity on the flow field. Additionally, the result indicated that the nature of the porosity has a significant effect. For validation, Voller and Prakash (1987) compared their porous media model with other recognized models, and emphasized the need for further research to be consistent with Darcy's law, which is dependent on the geometric motion of the mush. Darcy's law is applicable when the flow appears in a porous medium, and the law states that velocity of flow in a porous medium is proportional to the pressure gradient (Basu and Date, 1988).

To account for the nature of the mushy region, Voller and Brent (1990) investigated several alternative approaches: the mushy fluid, columnar zone and mixed zone. They focused on creating a coupling between the assumed nature of the mushy region and the

enthalpy equation. The authors reported that the mushy fluid approach would be appropriate for modelling the solidification of waxy materials. Additionally, the columnar zone approach is suitable for the problems with columnar crystal structures. Furthermore, the mixed approach indicates a convenient means by which the mushy fluid approach can be easily applied in a control volume code. Swaminathan and Voller (Swaminathan and Voller, 1992) extended the earlier one-dimensional "source based" enthalpy scheme to two-dimensional problems, and addressed the fluid flow term in the equation. The main difference between this method and earlier source-based methods is the consistent linearization of the discretized source term, which assures its optimal convergence on all problems. This method can deal with the temperature-enthalpy relationship in a very efficient way, and can be used in both control volume and finite-element approaches. Table 2.1 summarizes important factors that are involved in the enthalpy method.

In conclusion, the fixed grid method is easier to program, and less computational cost is required to solve phase change. Additionally, the fixed grid method along with an enthalpy technique can successively handle multi-dimensional problems for both pure and binary materials without having any major difficulties. Thus, the current study will consider the fixed grid and enthalpy method for further investigations.

Table 2.1 Evolution of enthalpy formulation categorized by applied factors for both conduction and convection problems.

Author	Numerical technique		Factors		Remarks
	Method	Time dependency	Latent heat	Specific heat	
Bonacina et al. (1973)	FDM	I		✓	Applied equivalent heat capacity term at the interface region
Comini et al. (1974)	FDM	I		✓	Observe the thermal properties
Furzland (1977)	FDM	I	✓		Smoothing the latent heat of enthalpy
Feulvarch and Bergheau (2007)	FEM	I	✓		New technique for isothermal phase change problem
Pham (1985)	FDM	-	✓		Capable to resist the jumping of the latent heat peak
Voller (1985)	FDM	E	✓		Introduce a latent heat source in a new equation
Voller and Cross (1983)	FDM	-		✓	Tracking the interface region accurately

FDM = Finite Difference Method; FEM = Finite Element Method; I = Implicit; E = Explicit.

2.4 Computational Methodology

This section demonstrates the numerical methodologies that calculate the phase change, turbulence and free surface modelling. Based on earlier studies, current research uses the fixed grid enthalpy method for investigating the water droplet solidification process. Furthermore, the Volume of Fluid (VOF) method is used to track the interface and free boundaries, and turbulence modelling is applied for solving the flow equations. Linking these methods and investigating the gaps are crucial for progress in this field.

According to Crank (1984) the classical enthalpy method helps to reduce the discontinuities that arise during phase change predictions. Additionally, this method allows the discontinuity to be implicitly included in the heat conduction equation and the domain to be represented as a single phase with variable physical properties. The heat exchange between droplet, air and substrate are modelled using the following energy equation (Ansys Fluent theory guide, 2013; Voller and Prakash, 1987):

$$\frac{\partial}{\partial t}(\rho H) + \nabla.(\rho v H) = \nabla.(k_c \nabla T) + S \tag{2.13}$$

The initial term on the left-hand side represents enthalpy, and the next term represents a convective energy transfer due to rotational or translational motion of the solid. The two terms on the right-hand side of the equation demonstrate the heat flux due to conduction and the energy source, respectively. Now, the total enthalpy is represented by (Ansys Fluent theory guide, 2013; Karlsson, 2013):

$$H = h + \Delta H \tag{2.14}$$

$$h = h_{ref} + \int_{T_{ref}}^{T} c_p \, dT \tag{2.15}$$

$$\Delta H = \beta H_f \tag{2.16}$$

Here, h_{ref} and T_{ref} are the reference sensible heat and temperature, C_p is the specific heat at constant pressure, and H_f is the latent heat of material, respectively. In the "enthalpy-porosity technique" a quantity called liquid fraction *(β)* is used, which indicates the fraction of the cell volume that is in liquid form, and is associated with each cell in the domain. The liquid fraction *(β)* is based on the enthalpy balance. A mushy zone (partially solidified region) is shown as $0 < \beta < 1$. When β decreases during solidification in a cell, velocity drops to zero. This process is accomplished using source term *(S)* to modify the momentum equation. From the momentum equation, the source term can be represented as (Zheng et al., 2014):

$$S = \frac{(1-\beta)^2}{(\beta^3 + \varepsilon)} A_{mush}\left(v - v_p\right) \tag{2.17}$$

where ε is a small number to prevent zero and v_p is the pull velocity. In the current study, the pull velocity term is considered to be zero.

2.4.1 Fluid flow conservation equation

Fluid flow and transport phenomena are governed by conservation of mass, momentum and energy. The mass or continuity equation for a compressible fluid under laminar flow conditions can be presented as (Siddhartha et al., 2007):

$$\frac{\partial}{\partial t}(\rho) + \nabla.(\rho v) = 0 \tag{2.18}$$

where ρ represents the density, $\nabla.()$ is the divergence operator, and v represents the velocity of fluid. The initial term of the equation is the rate of change of density with respect to time, and the last term is the net flow of mass out of element boundaries. For a 2D axisymmetric geometry, the continuity equation is (Ansys Fluent theory guide, 2015):

$$\frac{\partial \rho}{\partial t} + \frac{\partial}{\partial x}(\rho v_x) + \frac{\partial}{\partial r}(\rho v_r) + \frac{\rho v_r}{r} = 0 \tag{2.19}$$

When the air is incompressible and its density and viscosity are assumed constant, the momentum equation yields the following form of the Navier-Stokes equations (Kulyakhtin, 2014; Pope, 2000; Siddhartha et al., 2007):

$$\frac{\partial}{\partial t}(v) + (v.\nabla)v = -\frac{1}{\rho}\nabla P + \vartheta \nabla^2 v \tag{2.20}$$

where P is the pressure, and ϑ is the kinematic viscosity. For a 2D axisymmetric geometry, the axial and momentum conservation equations can be represented by (Ansys Fluent theory guide, 2015):

$$\begin{aligned} \frac{\partial}{\partial t}(\rho v_x) + \frac{1}{r}\frac{\partial}{\partial x}(r\rho v_x v_x) + \frac{1}{r}\frac{\partial}{\partial r}(r\rho v_r v_x) \\ = -\frac{\partial P}{\partial x} + \frac{1}{r}\frac{\partial}{\partial x}\left[r\mu\left(2\frac{\partial v_x}{\partial x} - \frac{2}{3}(\nabla.v)\right)\right] \\ + \frac{1}{r}\frac{\partial}{\partial r}\left[r\mu\left(\frac{\partial v_x}{\partial r} + \frac{\partial v_r}{\partial x}\right)\right] + F_x \end{aligned} \tag{2.21}$$

$$\frac{\partial}{\partial t}(\rho v_r) + \frac{1}{r}\frac{\partial}{\partial x}(r\rho v_x v_r) + \frac{1}{r}\frac{\partial}{\partial r}(r\rho v_r v_r) \tag{2.22}$$

$$= -\frac{\partial P}{\partial r} + \frac{1}{x}\frac{\partial}{\partial x}\left[r\mu\left(\frac{\partial v_r}{\partial x} + \frac{\partial v_x}{\partial r}\right)\right]$$

$$+ \frac{1}{r}\frac{\partial}{\partial r}\left[r\mu\left(2\frac{\partial v_r}{\partial r} - \frac{2}{3}(\nabla . v)\right)\right] - 2\mu\frac{v_r}{r^2} + \frac{2}{3}\frac{\mu}{r}(\nabla . v) + F_r$$

To model turbulence, Eq. (2.20) can be solved in combination with additional algebraic or partial differential equations. The key word "to model" signifies that certain processes are modelled based on empirical knowledge to obtain; for example, the correct values of the mean airflow (Kulyakhtin, 2014). The Reynolds-averaged Navier-Stokes (RANS) is one of the main approaches (Ansys Fluent theory guide, 2015). RANS determines the mean velocity field $\bar{v}$. RANS models decompose the velocity component into the mean, $\bar{v}_i$, and fluctuating components. For the velocity components:

$$v_i = \overline{v_i} + v_{ii} \tag{2.23}$$

The same is done for pressure and energy. Therefore, Eq. (2.20) is rewritten in the form:

$$\frac{\partial \overline{v_i}}{\partial t} + \bar{\upsilon}.\nabla\overline{v_i} = -\frac{1}{\rho}\frac{\partial \bar{P}}{\partial x_i} + \vartheta\nabla^2\overline{v_i} - \frac{\partial}{\partial x_i}\left(\overline{v_j v_{ii}}\right) \tag{2.24}$$

The last term in Eq. (2.24) is the Reynolds stresses, which represent the energy dissipation in the turbulent eddies and are obtained from a turbulent or turbulent-viscosity model. The turbulent viscosity can be obtained from an algebraic relation, such as in the mixing-length model, or from turbulence quantities, such as the turbulent kinetic energy, k, and the turbulent dissipation, ω, for which the transport equations are solved (Pope, 2000). An

example of such equations is the widely used standard *k-ω* model (Ansys Fluent theory guide, 2015):

$$\frac{\partial}{\partial t}(\rho k) + \frac{\partial}{\partial x_i}(\rho k v_i) = \frac{\partial}{\partial x_j}\left(\Gamma_k \frac{\partial k}{\partial x_j}\right) + G_k - Y_k + S_k \tag{2.25}$$

$$\frac{\partial}{\partial t}(\rho \omega) + \frac{\partial}{\partial x_i}(\rho \omega v_i) = \frac{\partial}{\partial x_j}\left(\Gamma_\omega \frac{\partial \omega}{\partial x_j}\right) + G_\omega - Y_\omega + S_\omega \tag{2.26}$$

where k is the kinetic energy, ω is the specific dissipation rate, G_k is the generation of turbulence kinetic energy due to mean velocity gradients, G_ω is the generation of ω, Γ_k and Γ_ω are the effective diffusivity of k and ω, Y_k and Y_ω are the dissipation of k and ω due to turbulence, and S_k and S_ω are the source terms, respectively.

The effective diffusivities for the *k-ω* model are given by (Ansys Fluent theory guide, 2012):

$$\Gamma_k = \mu + \frac{\mu_t}{\sigma_k} \tag{2.27}$$

$$\Gamma_\omega = \mu + \frac{\mu_t}{\sigma_\omega} \tag{2.28}$$

where σ_k and σ_ω are the turbulent Prandtl numbers for k and ω, respectively. The turbulent viscosity, μ_t, is computed by combining k and ω as follows:

$$\mu_t = \alpha^* \frac{\rho k}{\omega} \tag{2.29}$$

The coefficient α^* damps the turbulent viscosity, and is given by

$$\alpha^* = \alpha_\infty^* \left(\frac{\alpha_0^* + {Re_t}/{R_k}}{1 + {Re_t}/{R_k}}\right) \tag{2.30}$$

where

$$Re_t = \frac{\rho k}{\mu_\omega} \tag{2.31}$$

$$R_k = 6 \tag{2.32}$$

$$\alpha_0^* = \frac{\beta_i}{3} \tag{2.33}$$

$$\beta_i = 0.072 \tag{2.34}$$

The generation of turbulence kinetic energy and specific dissipation rate are defined as (Ansys Fluent theory guide, 2012:

$$G_k = -\rho \overline{v_i' v_j'} \frac{\partial v_j}{\partial x_i} \tag{2.35}$$

$$G_\omega = \alpha \frac{\omega}{k} G_k \tag{2.36}$$

The coefficient α is given by

$$\alpha = \frac{\alpha_\infty}{\alpha^*} \left(\frac{\alpha_0 + {Re_t}/{R_\omega}}{1 + {Re_t}/{R_\omega}} \right) \tag{2.37}$$

where R_ω=2.95. The dissipation of k is given by (Ansys Fluent theory guide, 2012):

$$Y_k = \rho \beta^* f_{\beta^*} k \omega \tag{2.38}$$

$$f_\beta^* = \begin{cases} 1 & x_k \leq 0 \\ \dfrac{1 + 680 x_k^2}{1 + 400 x_k^2} & x_k > 0 \end{cases} \tag{2.39}$$

$$x_k \equiv \frac{1}{\omega^3} \frac{\partial k}{\partial x_j} \frac{\partial \omega}{\partial x_j} \tag{2.40}$$

$$\beta^* = \beta_i^* [1 + \zeta^* F(M_t)] \tag{2.41}$$

$$\beta_i^* = \beta_\infty^* \left(\frac{4/15 + \left(Re_t / R_\beta \right)^4}{1 + \left(Re_t / R_\beta \right)^4} \right) \tag{2.42}$$

$$\varsigma^* = 1.5 \tag{2.43}$$

$$\beta_{\infty=}^* 0.09 \tag{2.45}$$

The dissipation of ω is given by

$$Y_\omega = \rho \beta f_\beta \omega^2 \tag{2.46}$$

$$f_\beta = \frac{1 + 70 x_\omega}{1 + 80 x_\omega} \tag{2.47}$$

$$x_\omega = \left| \frac{\Omega_{ij} \Omega_{jk} S_{ki}}{(\beta_\infty^* \omega)^3} \right| \tag{2.48}$$

$$\Omega_{ij} = \frac{1}{2} \left(\frac{\partial v_i}{\partial x_j} - \frac{\partial v_j}{\partial x_i} \right) \tag{2.49}$$

$$\beta = \beta_i \left[1 - \zeta^* F(M_t) \frac{\beta_i^*}{\beta_i} \right] \tag{2.50}$$

$$F(M_t) = \begin{cases} 0 & M_t \leq M_{to} \\ M_t^2 - M_{to}^2 & M_t > M_{to} \end{cases} \tag{2.51}$$

$$M_t^2 \equiv \frac{2k}{a^2} \tag{2.52}$$

$$M_{to} = 0.25 \tag{2.53}$$

$$a = \sqrt{\gamma R T} \tag{2.54}$$

$$S_{ij} = \frac{1}{2} \left(\frac{\partial v_j}{\partial x_i} + \frac{\partial v_i}{\partial x_j} \right) \tag{2.55}$$

An example of the *k*-ω model shows the basic principle behind RANS models, which try to mimic experimental results without capturing details of the physical processes.

2.4.2 Volume of Fluid (VOF)

Various numerical studies have been conducted to investigate hydrodynamic processes. Several different methods, including Front Tracking (Griebel and Klitz, 2014; Manservisi and Scardovelli, 2009; Tryggvason et al., 2001; Unverdi and Tryggvason, 1992), Level Set (Carviezel et al., 2008; Griebel and Klitz, 2014; Osher and Sethian, 1988; Oukach et al., 2012; Suli et al., 2017), lattice-Boltzmann (Gunstensen et al., 1991; Grunau et al., 1993; Mukherjee and Abraham, 2007; Nourgaliev et al., 2003; Shan and Chen, 1993; Shan and Doolen, 1995; Tanaka et al., 2011), Volume of Fluid (Hirt and Nicolas, 1981; Lunkad et al., 2007; Nikolopoulos et al., 2007; Šikalo et al., 2005(a-c); Strotos et al., 2011) and Coupled Level Set VOF (Bourlioux, 1995, Keshavarzi et al., 2012; Menard et al., 2007, Sussman and Puckett, 2000; Son, 2003, Son and Hur, 2002, Wang et al., 2009; Yang et al., 2007) have been employed for interface capturing in ship hydrodynamics community. The CLSVOF method takes advantage of both the Level Set (LS) and Volume of Fluid (VOF) methods where mass conservation is well preserved and the geometric properties, such as normal and curvature, can be easily estimated from the LS function. Another benefit of the combined method is that no major modifications are needed to the original LS based code. However, the CLSVOF method is not easy to implement. This is because the VOF method alone is already difficult; the additional complexity of the CLSVOF method is the LS re-distance (Wang et al., 2008).

The first numerical simulation of fluid dynamics of droplet splashing has been conducted by Harlow and Shannon (Diaz and Ortega, 2010; Fukai et al., 1995; Harlow and Shannon, 1967); by applying the Marker and Cell technique, they calculated the spreading

of a liquid droplet onto a flat plate. However, the authors neglected factors such as viscosity, surface tension, and wetting effects in their model, which caused disadvantages on the liquid-gas interface calculation at the solid surface (Diaz and Ortega, 2010; Fukai et al., 1995). Few commercial codes such as MAC, FLOW-3D, SOLA-VOF, RIPPLE-VOF, etc. are used by Liu et al. (1993), Pasandideh-Fard et al. (2002) and Trapaga and Szekely (1991). These codes are based on the fixed grid technique; hence, they pose problems when a large deformation of the computational domain occurs.

Based on the previous studies, the VOF method has been proven popular, as well as the most reliable method in recent years for tracking, modelling and simulating the motion of moving interfaces or boundaries (Lopes, 2013). Thus, to track and follow the evolution of the interface between the two fluids (water droplet and air), the study considered the VOF method. The VOF method belongs to the Euler-Euler framework where all phases are considered as continuous. The VOF method uses a phase indicator function, also known as color function or volume fraction (α), to track the interface region between more than one phase (Malgarinos et al., 2014). Hence, a volume fraction, α_{vf}, is illustrated as the percentage of volume covered by the liquid phase within a computational cell with respect to the total volume of the computational cell (Hirt and Nichols, 1981, Strotos et al., 2008):

$$\alpha_{vf} = \frac{\text{Volume of liquid phase}}{\text{Total volume of the control volume}} \tag{2.56}$$

The volume fraction (α_{vf}) takes the value of zero if the computational cell is covered only by gas, and the value of one of the cells is completely covered by liquid. Additionally, for in-between values, the cell lies in an interface region between the two fluids.

The volume fraction for the primary-phase is obtained by (Siddhartha et al., 2007):

$$\sum_{q=1}^{n} \alpha_q = 1 \tag{2.57}$$

In the VOF model, the movement of a moving interface is computed by solving an advection equation for the volume fraction of the secondary phase:

$$\frac{\partial \propto_q}{\partial t} + v.\nabla\alpha_q = 0 \tag{2.58}$$

The surface tension force is used as a source term in the momentum equation and the CSF surface tension model is defined as (Lopes, 2013; Zheng et al., 2014):

$$F^{\rightarrow} = \sigma \frac{\rho\kappa\nabla\alpha_{vf_2}}{\frac{1}{2}(\rho_1 + \rho_2)} \tag{2.59}$$

where the local interface curvature κ and the unit norm at the interface n is:

$$\kappa = -(\nabla.n) = \frac{1}{|n|}\left[\left(\frac{n}{|n|}.\nabla\right)|n| - (\nabla.n)\right] \tag{2.60}$$

where $= \nabla\alpha_q$. The wall adhesion angle is defined as unit normal n, and is evaluated using the contact angle, $\Theta_{w.}$ The surface normal as the cell next to the wall is:

$$n = n_w\, cos(\theta_w) + t_w\, sin(\theta_w) \tag{2.61}$$

where n_w and t_w are the unit vectors normal and tangential to the wall. The main objective of Equation (2.61) is to apply a prescribed value of the contact angle, at the wall, as a boundary condition. Depending on this value, the normal to the interface unit vector at the wall boundary condition cell n is rotated, and the interface forms the defined angle, when in contact with the wall surface (Malgarinoe et al., 2014).

2.5 Experimental Design and Methodology

Experimental techniques are employed to examine the spreading and freezing of water droplets on cold, dry substrates. In this section, details of the experimental design and methodology are presented.

2.5.1 Test substrate

To ensure a variation in the droplet dynamics and heat transfer of a droplet impinging on a cold, dry, solid substrate, various impact surfaces were selected. These substrates included bare aluminum and bare steel with different coating properties. These coatings were considered for the very specific marine icing need, and commercially applied on decks, and hulls and railings in offshore vessels. Intershield 300 aluminum and bronze color epoxy, interbond 201 green epoxy, and interthane 990 part A polyurethane were purchased directly from the Akzo Nobel International marine paints supplier, and the amerlock epoxy coating was collected from the stock of mechanical engineering machine shop of Memorial University of Newfoundland. It was recorded that amerlock epoxy coating was purchased directly from PPG Protective Marine Coatings. All the coatings are classified based on their applications and presented in Tables 2.2 and 2.3.

Table 2.2 Details of substrate dimensions.

Substrate dimensions	15 cm × 15 cm × 0.95 cm

Table 2.3 Test surfaces.

Serial	Descriptions of substrate material
1.	Bare aluminum 6061 with typical surface finish.
2.	Bare steel with typical surface finish.
3.	SBS
4.	SBS with intershield 300 AE. The DFT of the paint is at 5 mils. Applied as a primer.
5.	SBS with AE and intershield 300 BE. The DFT of the intershield 300 BE is at 5 mils. Applied as a primer.
6.	SBS with AE, BE and interbond 201 GE. The DFT of the interbond 201 GE is at 6 mils. Applied as a deck paint.
7.	SBS with AE, BE and interthane 990 part A polyurethane. The DFTof interthane 990 part A polyurethane is at 2-3 mils. Applied as a railing paint.
8.	SBS with amerlock epoxy coating. The DFT of amerlock epoxy coating is 6-8 mils. Applied as a hull paint.

SBS = Sand blasted steel, AE = Aluminum epoxy, BE = Bronze epoxy, GE = Green epoxy, DFT = Dry film thickness

2.5.2 Determination of surface roughness and coating thickness

The influence of surface roughness and coating thickness on heat transfer and spreading processes of a droplet on dry surfaces were investigated. A Mitutoyo Surftest 301 was used to examine the surface roughness of each substrate. Furthermore, a Mitutoyo Micrometer (Model no: H-2780) was used to measure the thickness of the coating on each substrate. Roughness and thickness were measured at different locations on the substrate surface. Atleast five measurements were performed for each sample. The details are presented in Tables 2.4 and 2.5.

Table 2.4 Details of surface roughness.

Substrate details	Surface roughness (µm)
Bare aluminum 6061 with typical surface finish	0.62
Bare steel with typical surface finish	1.66
SBS	3.38
SBS with intershield 300 AE	2.19
SBSwith AE and intershield 300 BE	1.66
SBS with AE, BE and interbond 201 GE	2.55
SBS with AE, BE and interthane 990 part A polyurethane	0.43
SBS with amerlock epoxy coating	2.28

SBS = Sand blasted steel, AE = Aluminum epoxy, BE = Bronze epoxy, GE = Green epoxy.

Table 2.5 Details of coating thickness.

Substrate details	Coating thickness (mm)
SBS with intershield 300 AE	0.0254
SBS with AE and intershield 300 BE	0.2794
SBS with AE, BE and interbond 201 GE	0.5842
SBS with AE, BE and interthane 990 part A polyurethane	0.3302
SBS with amerlock epoxy coating	0.1524

SBS = Sand blasted steel, AE = Aluminum epoxy, BE = Bronze epoxy, GE = Green epoxy.

2.5.3 Experimental set-up

The main procedure was to allow a single droplet to impact, spread and freeze on the impact substrate. The major components of the set-up were: a droplet generator, thermal

camera, high speed camera, test substrates and a cold environment. The purpose was to replicate typical artic conditions in a lab setting. The droplet generator was mounted on a height-adjustable frame. The droplet falling height was set at 90 cm. A 60 ml syringe along with three needle sizes were used to produce droplets with diameters of 3, 4 and 5 mm. Standard deviation is related to at least ten cases for small sized droplets (i.e. 3 and 4 mm) and five different tests for the largest one (i.e. 5 mm). For each trial, a droplet was released onto a clean surface that had been precooled to the desired temperature. Before each test, various droplets were cleared away to confirm the liquid was free of air bubbles. Figure 2.2 illustrates the schematic of the equipment and experimental set-up.

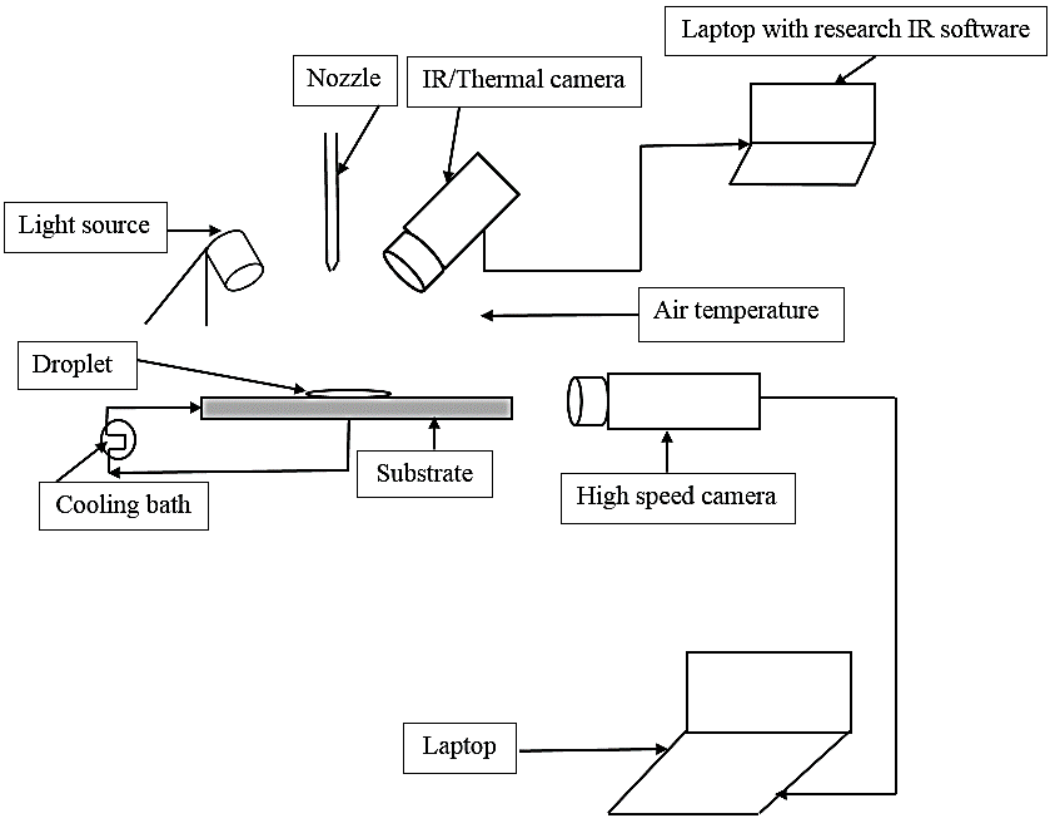

Fig. 2.2 Schematic of experimental set-up.

The cold room is one of three cold rooms located in the Mechanical Engineering Building at the Memorial University of Newfoundland. The forced air cooling unit and associated temperature controls are capable of maintaining the temperature in the cold room between 0 °C and -25 °C.

Square plates measuring 15 cm × 15 cm, with a thickness of ⅜ inch were fabricated to emulate typical surfaces; i.e., hulls, decks, and railings on marine and offshore vessels. Figure 2.3 shows a sample of the substrates.

A thermal bath (AX 150-A25, Thermo Scientific) was used and connected to a cooling plate underneath the substrate to ensure the lower side of the plate was at a constant temperature within ± 0.1%. A 1:1 ratio of water and ethylene glycol mixture was used as the circulating coolant in the thermal bath. The temperature of the bath the and the room were set to be equal for two trial temperatures -15 °C and -18°C. A temperature and humidity sensor (Rotronic HF 532, Switzerland, ± 0.1 ºC accuracy for temperature and ± 0.8% accuracy for humidity) were used in the experiment. Relative humidity measurements ranged between 65 to 72% during the tests. A thin layer of frost onto the cold surfaces was observed in some cases; however, its effect on droplet dynamics or freezing was beyond the scope of the present work. In a work, Jadidi et al. (2018) mentioned that if the ratio of air temperature and relative humidity is less than one, the droplet spreading factor for hydrophilic surfaces increase significantly, whereas this decreasing ratio does not put any influence on the maximum spreading for the superhydrophobic surface.

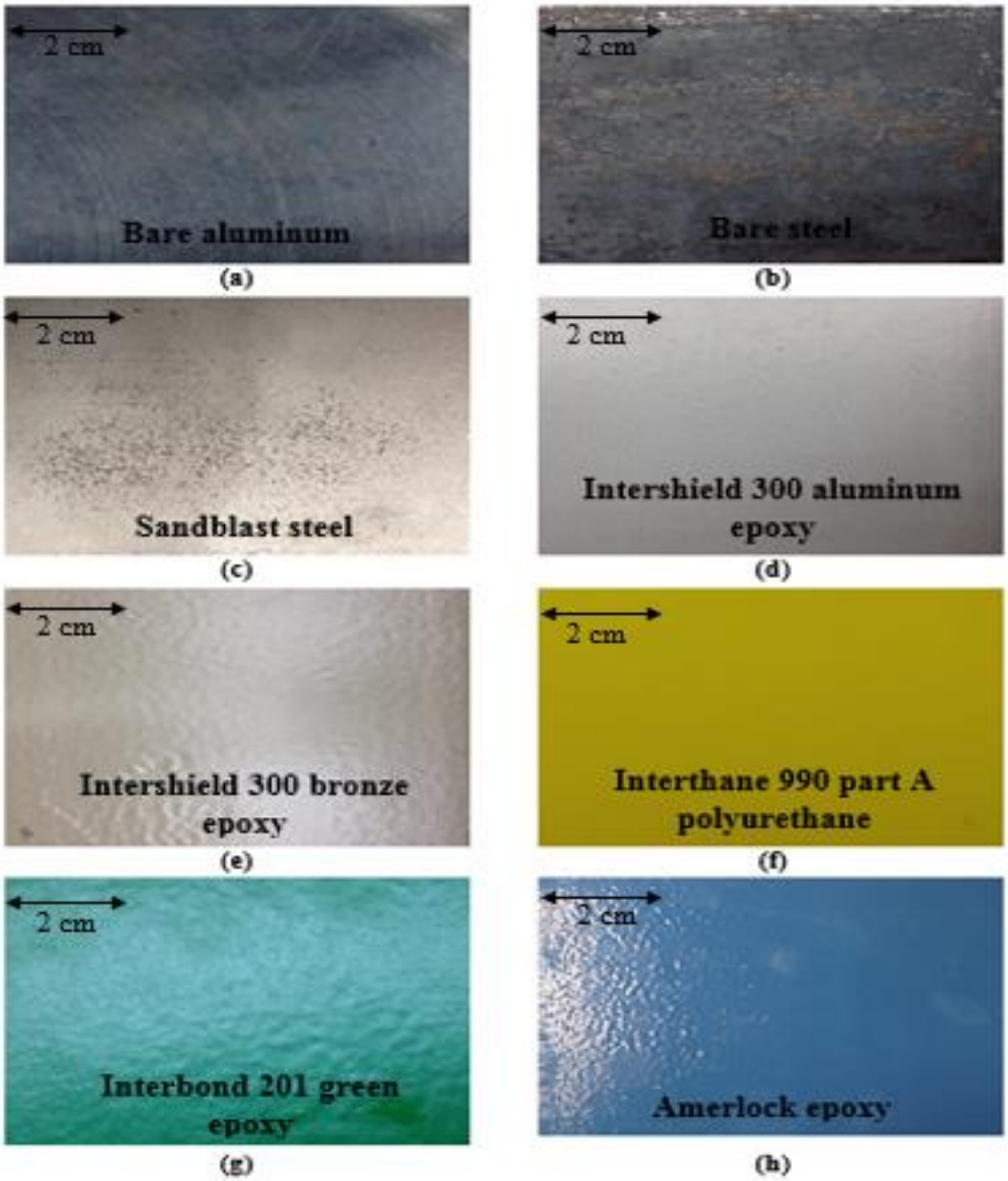

Fig. 2.3 Photographs of top surfaces.

A Phantom V611 high-speed camera operating at 10,000 fps was positioned to record the vertical trajectory of the droplet just prior to impact and the spreading dynamics, and then stored in computer 2 for further analysis. The full resolution of 1280 × 800 was

used for the recordings to optimize the view area. A high magnification zoom macro lens (Sigma 105mm f/2.8 EX DG macro lens) was used. Exposure time varied from 200 to 1000 μs. A long wave infrared camera (FLIR E60 with a spatial resolution of 320 x 240) with a frame rate of 60 frames per second was used to calculate the transient temperature profile. The measurement was conducted immediately after droplet impact onto the substrate. It is assumed that the heat transfer at the liquid-air interface is small compared to the heat transfer between the droplet and the surface, thus, the IR camera measures the droplet-substrate interface temperature.

The IR camera was calibrated prior to the experiment with a thermocouple for known temperature points. Additionally, to avoid the angular variation of infrared emissivity, the IR camera was kept normal to the droplet top to measure the droplet top temperature. However, due to coatings or shininess of the substrates, emissivity factors of 0.8 to 0.9 were chosen to avoid misleading temperatures. The overall uncertainty for temperature measurement associated with the emissivity value and the IR camera is around ±5 °C. To compensate this resolution error, as suggested by the camera manual (for low temperatures), this experiment used black masking tape (S-2491BL) around the substrate, to adjust the emissivity value, and force the indicator to display the correct temperature of the material, however, some errors (for example, ±25%) still exist. An LED light source was used to provide illumination for photography. A salinity meter was used to measure the salinity of the salt water, and calibrated against a standard solution. The accuracy of the measurement is about ± 0.5%. Tables 2.6 and 2.7 present the experimental test conditions. At least ten measurements were performed to measure the droplet size.

Table 2.6 Details of test fluid.

Fluid type	Fresh water, salt water
Droplet size (mm)	3 (±0.05), 4 (±0.03), 5 (±0.01)

Table 2.7 Details of test conditions.

Water temperature (°C)	2
Ambient temperature (°C)	-15, -18
Substrate temperature (°C)	-15, -18

2.6 Summary

The chapter addresses the advantages and disadvantages of methods (variable grid and fixed domain) used for phase changes. In the variable grid method, interface profile can be accurately predicted, whereas, in fixed domain method, interpolation is required to find the interface. Using the fixed domain method is easier and more efficient while handling multidimensional, and pure to alloy solidification as four different zones – solid, eutectic, mush and liquid, can be easily incorporated through proper enthalpy-temperature relationships. Though it is easier to implement a fixed domain method, it has some drawbacks – stepwise increment of temperature, enthalpy, etc. with time when pure metal is being used for analysis. In brief, using one over other technique depends not only on the problem type but also on setting up priorities set by a user for accuracy, computational efficiency and ease of programming. The chapter also addresses the experimental techniques along with their boundary conditions and limitations.

CHAPTER 3[3,4]

PRE-IMPACT PROCESS-ii: SPRAY OR DROPLET MOVEMENT IN AIR

3.1 Introduction

Marine icing, which is typically caused by wind and wave spray, is a major concern for marine industries in Arctic and Sub-Arctic regions. Compared to wind spray, wave spray is the most significant source of vessel icing and can pose hazards to vessels and rigs operating in cold climates.

During a typical spray generation situation, numerous droplets are produced. Various numerical and experimental models have been developed to predict icing from spray (Berriman and Unwin, 1994). Gao et al. (2000) examined the phase change characteristics of industrial waste water droplets under various ambient air conditions and reported that for a freely falling droplet, ice nucleation began at the edge of the bottom of the droplet and propagated over the entire surface area. Furthermore, the authors explained that the chemical components in the waste water significantly affected the freezing dynamics. Zarling (1980) used saltwater spray to study the nucleation phenomenon below -18 ºC of different sized droplets at variable heights and concluded that the height and droplet diameter play major roles in the phase change process. The study did not consider the temperature dependence of the thermophysical properties of water. Dye and Hobbs

[3] This chapter is written based on: Sultana, K.R., Pope, K. Lam, L. and Muzychka, Y.S., 2017b. Phase Change and Droplet Dynamics for a Free Falling Water Droplet. International Journal of Heat and Mass Transfer, 115, pp.461-470.

[4] Sultana, K.R., Pope, K., Muzychka, Y.S., 2017c. Numerical Prediction of Transient Cooling and Phase Change of a Falling Water Droplet in Sub-Zero Air Temperatures. 2nd Thermal and Fluid Engineering Conference, TFEC2017. Las Vegas, NV, USA.

(1968) conducted another experimental study where they found that when a water droplet nucleated at warmer temperatures, then froze at a lower temperature, disruptive behavior was observed. The authors also demonstrated the shattering phenomena, and described that the shattering phenomena are observed under non-equilibrium conditions. The authors speculated that a droplet that is nucleated under thermal equilibrium conditions will probably be less prone to fragmentation than a droplet which is nucleated under non-equilibrium conditions. This is because in an equilibrium condition, there is less water trapped in the ice shell that remains to be frozen. The unfrozen water will expand during freezing.

Individual droplets in an airflow can experience oscillations in shape, and may break-up via different modes, depending on various dimensionless numbers such as the Weber number and the Laplace number, induction time, and characteristic break-up time, among others (Dubrovskii et al., 1990; Shreiber et al. 1996; Volkov et al., 2015, 2016; Wierzba, 1990).

Figure 3.1 illustrates the forces that affect the trajectory of a free falling droplet. The boundary layers and circulations are developed due to the relative motion between the droplet center and ambient air. Previous studies found that gravity, buoyancy, air drag and accelerating body force influence the water droplet motion during its flight time (Fu et al., 2006; Kulyakhtin and Tsarau, 2014; Kulyakhtin et al., 2014; Lozowski et al., 2000; Lorenzini and Saro, 2013; Macdonald and McCartney, 1987; Makkonen, 2000).

McDonald (1954) studied the shape and internal motion of a free falling droplet and reported that surface tension, hydrostatic pressure, external aerodynamic pressure,

electrostatic charge, and internal circulation influence the shape of a large droplet. Bond (1927) identified that in a dissimilar liquid, internal motions of a droplet are characterized by the external Reynolds number, as well as the relative viscosity of the interior and exterior fluids. Yao and Schrock (1976) experimentally studied droplet transient deformation and found that for a droplet diameter of more than 4 mm, a non-spherical shape is formed during free fall. Horton et al. (1965) demonstrated that when a droplet does not circulate during its free fall, it behaves like a rigid sphere. When circulation is present, the solute is transferred from the interior of the droplet to the phase boundary via convection.

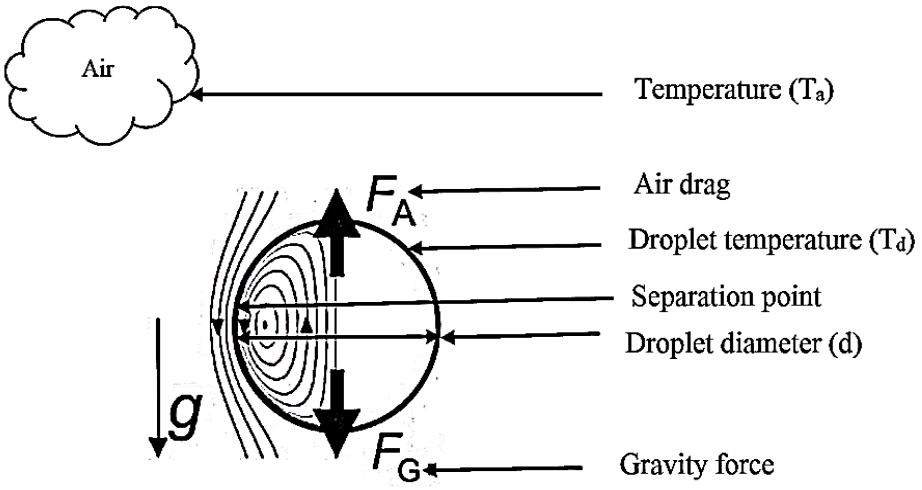

Fig. 3.1 Effect of internal circulation and air drag on a free-falling droplet.

Despite the enormous technical importance, knowledge about how variable thermophysical properties, accelerating body force, droplet size and imbalanced thermal distribution affect the phase change phenomena is still missing in the literature. The aim of

this chapter is to investigate the phase change of free falling droplets in a sub-zero environment. The modelling methodology and the results of this paper provide new insights on phase change and droplet dynamics and contribute to the understanding of mechanisms involved with spray freezing applications.

3.2 Scaling Analysis of Freezing Process of a Free Falling Droplet

The scaling analysis accounts for the internal circulation to calculate the freezing time. In this case, the evaporation and the radiation heat transfer are neglected. Therefore, considering an energy balance on a free falling droplet:

$$E_{phase\ change} + E_{sensible\ temperature\ change} = E_{convected\ from\ air\ into\ droplet} \tag{3.1}$$

Temperatures of the pre-impact droplets are close to the fusion temperatures; therefore, energy release due to sensible temperature change is small. Table 3.5 lists the sensible and latent energy associated with solidification by drop size.

$$E_{phase\ change} \approx E_{convected\ from\ air\ into\ droplet} \tag{3.2}$$

Equation (3.2) can be re-written as:

$$\frac{H_f \rho V}{t} \approx h_{conv} A_s (T_d - T_a) \tag{3.3}$$

where H_f is the latent heat of fusion for water, ρ is density of water, V is the droplet volume, h_{conv} is the convective heat transfer coefficient on the outside of the droplet, A_s is surface area of the droplet, T_a is the ambient air temperature, and T_d is the average droplet temperature. The approximate time to freezing can then be expressed as:

$$t \approx \frac{H_f \rho V}{h_{conv} A_s \Delta T} \tag{3.4}$$

Using substitution, and assuming that the temperature of the droplet is at the freezing temperature $T_d = T_f$, the Equation (3.4) can be re-written as:

$$t \approx \frac{R^2}{\alpha_{diff} StNu} \tag{3.5}$$

where R is the droplet radius, α_{diff} is the thermal diffusivity of the droplet, St is the Stefan number for the droplet $\left(St = \frac{C_p \Delta T}{H_f}\right)$, and Nu is the Nusselt number which can be determined by the Ranz and Marshall correlation for external convection of air around a droplet (Ranz and Marshall, 1952):

$$Nu = 2 + 0.6 Pr^{0.33} Re^{0.5} \tag{3.6}$$

Heat transfer inside a droplet is enhanced by circulation and mixing. Yao and Schrock (1976), citing Lamb (1932), Hadamard (1911) and Rybczynski (1911), recommended considering the circulation and mixing as an effective thermal diffusivity by modifying it with a Reynolds number for the internal mixing, Re_{mix}. The variable Re_{mix} is much larger than the Reynolds number associated with the external flow around a droplet.

The internal mixing Reynolds number is defined as (Yao and Schrock, 1976):

$$Re_{mix} = \frac{v_a d}{2\left(1 + \frac{\mu_d}{\mu_g}\right)\upsilon_d} \tag{3.7}$$

In this thesis, the author adapts Yao and Schrock's expression to account for the effects of heat transport due to internal circulation and mixing.

Yao and Schrock (1976) proposed the following expression for effective thermal diffusivity:

$$\alpha_{eff} = \alpha_{diff}(1 + QRe_{mix}) \tag{3.8}$$

where Q is a constant. By using the Yao and Schrock's value, which is $Q = 0.01$, the scaled time to freezing becomes:

$$t \approx \frac{R^2}{\alpha_{eff} StNu} \tag{3.9}$$

Non-dimensionalizing time to freeze, Equation (3.9) can be re-written as:

$$Fo \sim \frac{1}{StNu} \tag{3.10}$$

where Fo is the Fourier number $\left(Fo = \frac{t\alpha_{eff}}{R^2}\right)$. Equations (3.7) and (3.8) provide an effective thermal conductivity, which, in this thesis, is on the order of 10 to 100 times that of a non-circulating liquid. In Equation (3.8), several effects are not captured, however, those are accounted for in the numerical model. As the ice shell develops, the heat is transferred from the liquid, through the shell, to the atmospheric air. Since the thermal conductivity of the shell is larger, resistance to heat transfer is lowered. Furthermore, the liquid would encounter a drag force from the stationary shell that would counteract the mixing effect. Equation (3.10) provides a method for scaling the numerical time to freeze and understanding the relationship to the parameters: α_{eff}, R, Nu and Ste which is discussed in the results section.

3.3 Numerical Model and Methodology

In the numerical analysis, a computational domain of a structural quadrilateral mesh with 4,525,180 cells is considered. Initially, a spherical water droplet with 300 cells is patched at the inlet section. The patching option is required to designate the specified values for a certain region, which is advantageous for computing a problem step-by-step

when more than one phase is simulated. After patching, the droplet freely falls from a vertical height of 10 m. Table 3.1 and Fig. 3.2 represent all the necessary information regarding the numerical grid and the applied boundary conditions.

Table 3.1 Details of the numerical grid.

Dimensions of the computational domain	10 m × 3.3 m
Total number of cells	4,525,180
Smallest cell size near the air-water interface region	0.00002 m

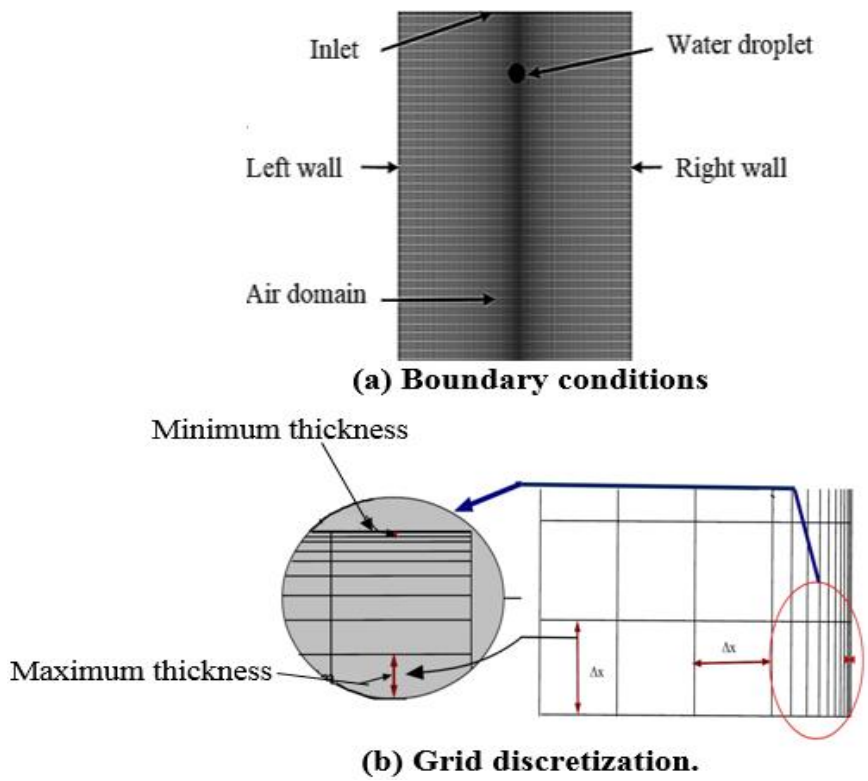

Fig. 3.2 Computational domain for numerical predictions of gas-liquid phase change.

Figure 3.2 demonstrates the initial boundary conditions and the position of the water droplet that was set between the wall and center axis. The top wall is defined with an inlet boundary condition, and the left and right boundaries are defined as symmetrical. Air is considered as the primary phase and water is considered as the secondary phase in the domain. Various grid thicknesses are applied inside the domain. The smallest grid thickness is applied in the air-water interface region so that the interface phenomenon can be captured accurately.

Due to the phase change process, a non-linear behavior appeared during the solution. Therefore, to minimize this non-linearity, a lower Courant number using a very small time step (1×10^{-6}) is selected for the interface tracking and computational domain. The Courant Number describes the portion of a cell that a solute will traverse by advection in a given time step (Giraldo, 2018; Inside mines). Tables 3.2 and 3.3 provide the reference values for the different simulations.

Table 3.2 Parameters to study droplet freezing in air.

Properties	**Droplet diameter (mm)**	**Air temperature (°C)**
Fresh and salt water (34 ppt)	2, 4, 6	-10 and -18

Table 3.3 Physical properties of air and water.

Surface tension ($N.m^{-1}$)	0.07617
Dynamic viscosity of water ($kg.m^{-1}.s^{-1}$)	0.00178
Kinematic viscosity of water ($m^2.s^{-1}$)	1.939×10^{-6}
Dynamic viscosity of air ($kg.m^{-1}.s^{-1}$)	1.7196×10^{-5}
Kinematic viscosity of air ($m^2.s^{-1}$)	1.33×10^{-5}
Latent heat of fusion ($J.kg^{-1}$)	334,000

An initial water temperature of 2 °C and physical properties such as density, viscosity, specific heat, and the surface tension are computed based on each temperature and salinity (Sébastien, 2008; Sharqawy et al., 2010; water density calculator, 2017). A piecewise-linear relationship is applied to compute the thermophysical properties with respect to corresponding temperatures. The thermophysical properties are presented in Table 3.4. Table 3.5 demonstrates the sensible and latent energy for fresh water droplets.

Table 3.4 Thermophysical properties of water at several temperatures.

Water type	Temperature (°C)	Density ($kg.m^{-3}$)	Specific heat ($J.kg^{-1}.K^{-1}$)	Thermal conductivity ($W.m^{-1}.K^{-1}$)	Phase
Fresh	2	1004.0	4204	0.56	Liquid
Fresh	0	916.00	2050	2.22	Solid
Fresh	-1	917.00	2059	2.23	
Fresh	-10	918.00	2000	2.30	
Fresh	-18	918.00	1954	2.28	
Salt	2	999.96	3998	0.57	Liquid
Salt	0	999.86	3997	0.56	
Salt	-1	999.69	2719	0.55	Solid
Salt	-10	998.15	2159	1.99	
Salt	-18	994.86	2079	2.08	

Table 3.5 Sensible and latent energy for fresh water droplets.

Droplet diameter (mm)	Sensible energy change (J)	Latent energy change (J)
2	0.315	1.341
4	2.516	10.725
6	4.915	36.26

3.4 Results and Discussion

In this section, numerical predictions of droplet freezing during free fall in air are presented. Figure 3.3 illustrates contours of average liquid fraction and average static

temperature of a 6 mm fresh water droplet, falling from the height of 10 m, at an ambient temperature of -18 °C. Various residence times are represented.

During the free fall, the droplet is not in thermal equilibrium with ambient air, and the droplet's internal temperature is higher than the outer surface temperature. This distinguishing characteristic is more visible in the current work because we consider the temperature dependent properties such as density, heat capacity, and thermal conductivity during the simulations. From those properties, specific heat is significantly changed during phase change.

The temperature gradient causes the droplet to lose thermal energy and cool as it falls. This thermal imbalance affects nucleation, the initial stage of a phase change process. During the initial nucleation stage, it is observed that the volume fraction of the solid particle is very small and has a distinct temperature. Song et al. (2010) demonstrated that the distinguishing features of a phase transition are an abrupt change in thermophysical

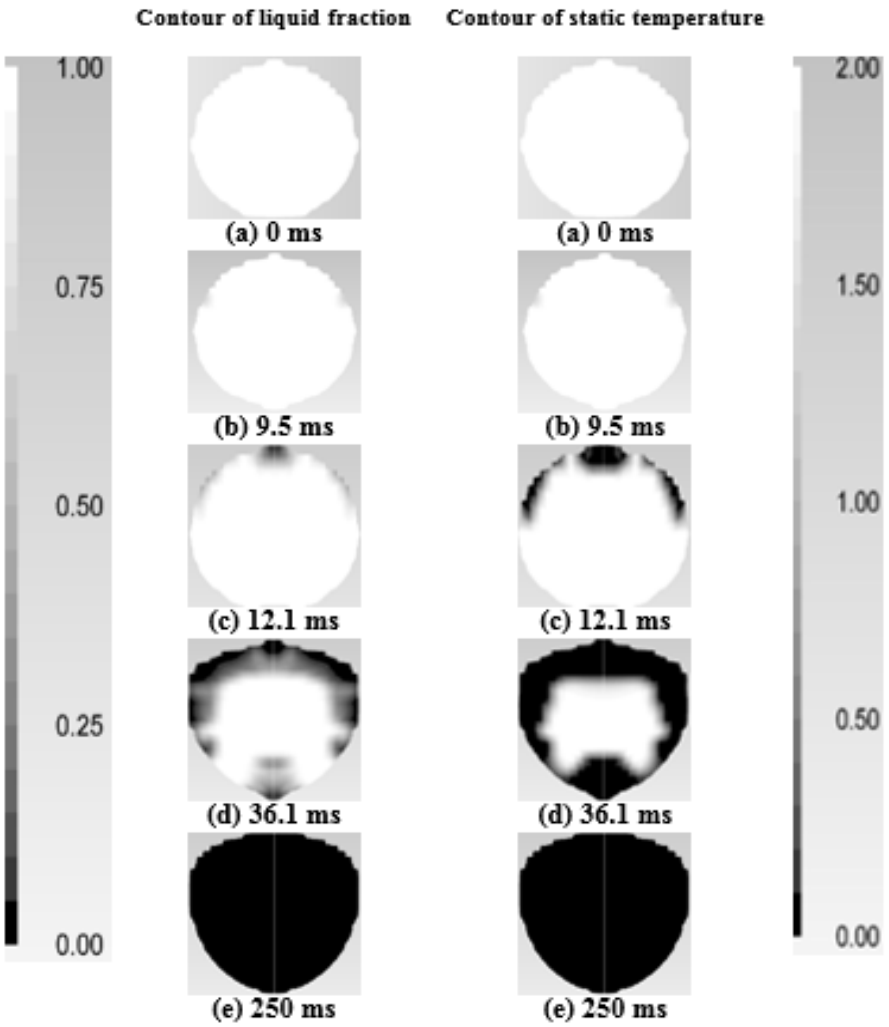

Fig. 3.3 Phase change and transient temperature of a free falling droplet.

properties, specifically the density, heat capacity, and thermal conductivity, which correspond to a thermodynamic variable such as temperature. Furthermore, this phenomenon holds when the droplet is at a higher temperature than the equilibrium freezing or melting temperature (Gupta, 2003); i.e. for fresh water, it is 0 ºC, and for salt water it is approximately -2 ºC (IMO, 2011). A similar phenomenon was also observed by Langham and Mason (1958), in which the authors performed a laboratory experiment

inside a cold chamber and found that the droplets were thermally imbalanced with the environment when nucleation commenced.

In the liquid fraction contour, tiny clusters of ice nuclei appear on the droplet surface, as shown in Fig. 3.3 (b). The ice cluster is the result of thermal fluctuations inside the liquid molecules (Gupta, 2003; Sastry, 2005). Following the initial nucleation phenomenon, a solid shell grows rapidly inwards from the surface of the droplet, as shown in Fig. 3.3 (c). In an experimental study, Gao et al. (2000) also observed the phenomenon for the suspended industrial waste water droplets that started to freeze from the outside inwards. They demonstrated that the droplet surface freezing is a function of ambient air temperature and the nature of the water.

For an isolated droplet in air, the fragmentation process is very common (Majithia et al., 2008). During freezing, water density decreases, and liquid volume expands; therefore, some of the liquid water is squeezed out onto the ice surface, which creates fragmentation or cracks on the outer solid shell of the frozen or partly frozen droplet (Tabakova and Feuillebois, 2004). Due to the fragmentation process, water droplets take the shape of a small ice splinter (Choularton et al., 1978; Dye and Hobbs, 1968). Dye and Hobbs (1968) demonstrated that these ice splinters are represented as particles of ice, rather than by ice nuclei. Gao et al. (2000) illustrated that when a droplet freezes faster due to oscillation, it may seem more oblate than prolate ellipsoids at cold air temperatures. This thesis shows these fragmentation phenomena in Figs. 3.3 (d-e). However, due to the short air residence time the author is unable to determine the exact quantity.

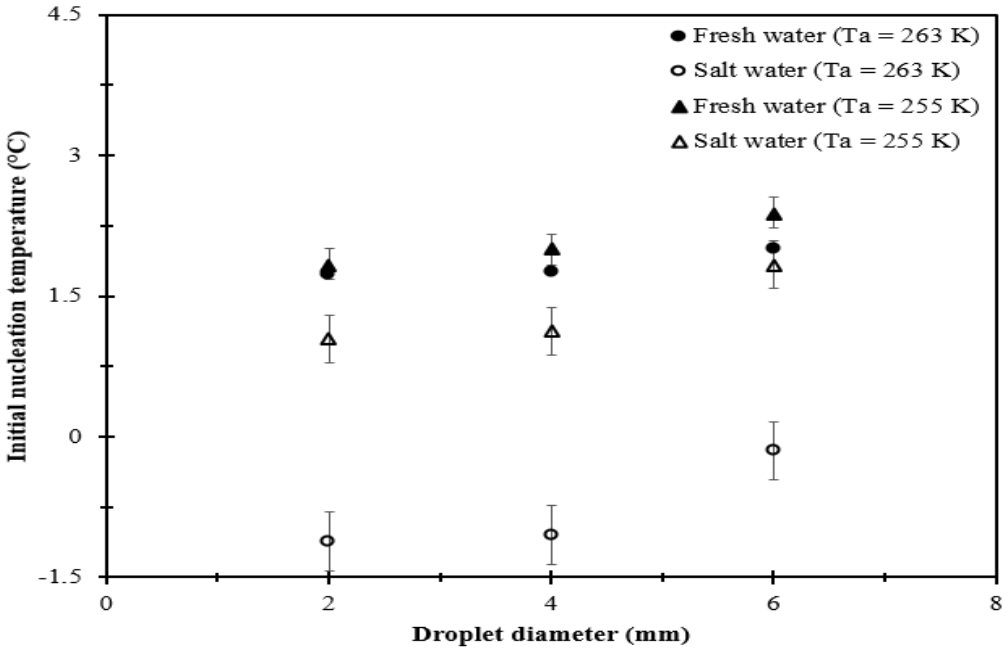

Fig. 3.4 Comparison of nucleation temperature for different sized droplets.

The current study also investigates the initial nucleation temperatures for different water types in various environmental conditions. Figure 3.4 illustrates that the initial nucleation temperature is higher for an ambient temperature of -18 °C than of -10 °C. At least five measurements were conducted for each sample. The current investigations predict that the initial nucleation temperature is different for fresh and salt water droplets. For these experiments, the fresh water droplet's nucleation remains in the positive temperature range. For a salt water droplet, the nucleation temperature remains lower than fresh water. A possible cause is the depression of freezing point, which assumes thermophysical properties such as thermal conductivity, specific heat and the density might influence the nucleation phenomenon. Macklin (1962) speculated that the time taken for a droplet to freeze depends on its heat capacity and the rate at which the heat of fusion may be dissipated to the atmosphere. Zarling (1980) explained that at an ambient temperature

of -18 °C, a salt water droplet has a chance to nucleate when it falls from a very long distance.

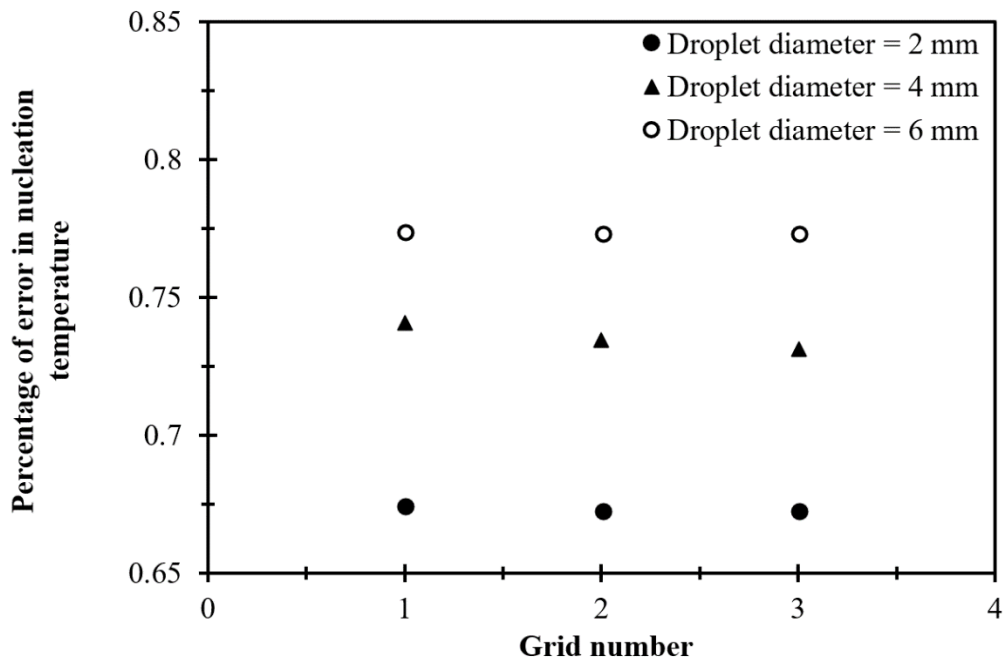

Fig. 3.5 Grid independency test for fresh water droplets at an ambient temperature of -18 °C.

Figure 3.5 shows a grid independent solution where the theoretical nucleation temperature is compared with the numerically obtained nucleation temperature. The error is defined as:

$$\text{Percentage of error} = \frac{\text{Numerical result} - \text{Theoretical result}}{\text{Numerical result}} \times 100 \tag{3.11}$$

The grids are: grid 1 = 100 × 100, grid 2 = 200 × 200, and grid 3 = 300 × 300, where the meshes are selected to increase the level of refinement near the solid-liquid interface, and steep temperature gradients are represented during phase change. The calculation shows that for three different grid systems, the maximum simulation error for determining the nucleation temperature is approximately 0.77%. However, the simulated results are

almost the same for the three different grid systems, illustrating that the results are not mesh-affected. In order to obtain a better image resolution, denser mesh (grid 3) is chosen for simulations.

For a free falling droplet, the heat transfer is enhanced by forced convection (Dye and Hobbs, 1968), which can also accelerate the phase change process. The present investigations found that the larger sized droplets have a higher nucleation temperature than smaller droplets. One of the possible reasons is the size of the contact surface area, as a larger exposed surface area can quicken the nucleation process. This result is in agreement with the experimental studies of Carte (1956) and Kuhns and Mason (1968), who reported that the freezing temperature of small droplets is lower than for large droplets. Additionally, Dye and Hobbs (1968) reported that when a droplet falls through the atmosphere, its temperature is controlled by its size. Oscillation, internal temperature and terminal velocity can also accelerate nucleation. Gunn and Kinzer (1949) demonstrated that a larger droplet has higher oscillations than a smaller droplet, which can increase the nucleation process.

For nearly all numerical predictions, the nucleation temperature is 0.3% to 0.4% higher than the equilibrium freezing temperature, which indicates the presence of heterogeneous nucleation. Heterogeneous nucleation usually appeared due to films at the air-water interface (Davey et al., 1994; Gavish et al., 1990; Wood et al., 2002). When the droplet travels through air, some air bubbles can be entrapped inside the droplet which may cause early nucleation. In the current simulation, Fig. 3.6 shows an air entrapment condition.

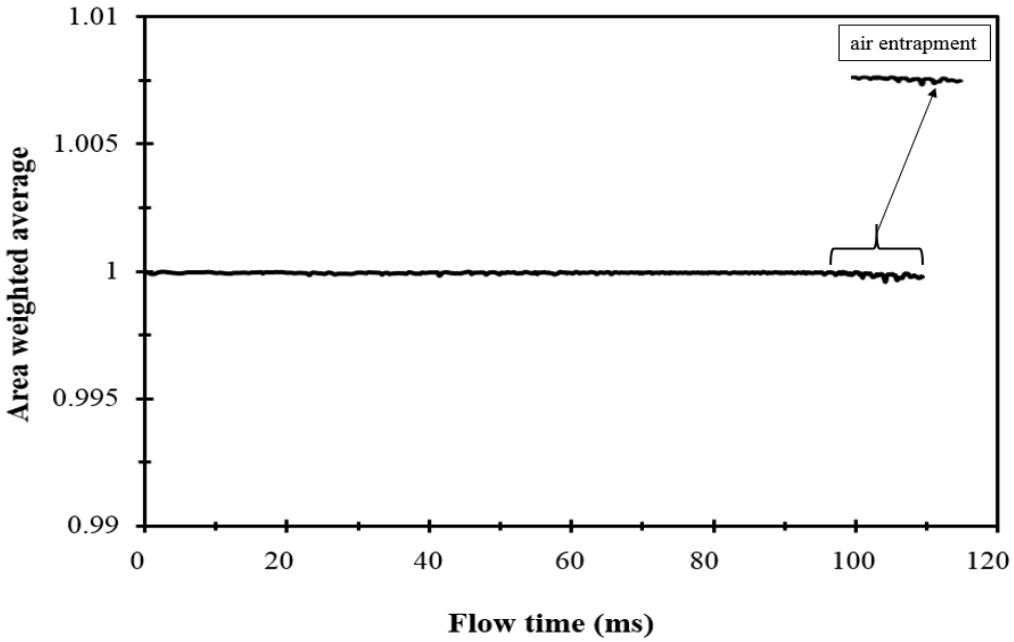

Fig. 3.6 Average volume fraction and air entrapment of a free falling water droplet.

This figure illustrates that at the initial stage, the droplet is completely filled with water, indicated by the area weighted average volume fraction of 1. As time progresses, the droplet starts to fall. During the traveling time, the droplet comes into contact with the ambient air, where some air bubbles are entrapped inside the droplet. Thus, some inconsistencies appeared in the volume fraction line. The top right corner of Fig. 3.6 represents the inconsistent phenomenon. These inconsistencies indicate that the droplet does not contain only water, however, some small amount of air is also present inside the droplet.

Due to interfacial temperature gradients, a free falling droplet may also experience internal circulation when it moves in a non-isothermal flow field (Lozinski and Matalon, 1993). These internal circulations temporarily increase the surface area by oscillating the droplet. Furthermore, the transport process was accelerated by extending the surface area facing the air stream (Gao et al., 2000; Yao and Schrock, 1976).

Figure 3.7 displays the non-dimensional time to freeze, Fo, against the inverse product of the Nusselt and Stefan numbers, for both fresh and salt water droplets. As illustrated in Fig. 3.7, the fresh water and salt water droplets followed a linear trend line, which suggests that it is a reasonable approximation for the timing of droplet phase change incorporating the effects of circulation and mixing. Taking a least square's fit, the approximation for time to freeze becomes:

$$t \approx \frac{R^2}{\alpha_{eff}}\left(1.3 + \frac{4.68}{StNu}\right) \tag{3.12}$$

Equation (3.12) provides an analytical expression that can be used to estimate the time to freeze for a free falling fresh or salt water droplet at a sub-zero ambient temperature.

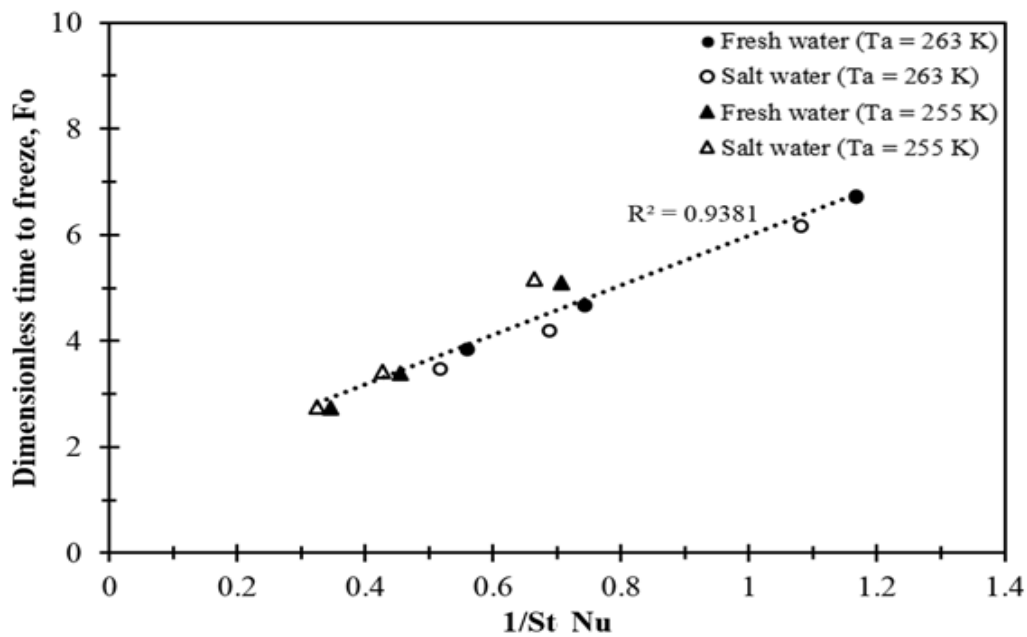

Fig. 3.7 Dimensionless analysis incorporating the effects of internal circulation and mixing.

When droplets nucleate before they reach thermal equilibrium with the environment, or begin nucleation at a higher temperature and then freeze quickly at a lower temperature, they demonstrate more disruptive behavior, such as shattering during freezing, than droplets that are frozen at thermal equilibrium (Dye and Hobbs, 1968). Figure 3.8 details the droplet deformation and fragmentation phenomena. As the droplet accelerates, the aerodynamic forces tend to distort the original shape of the droplet. Due to the shear interaction of the two phases across the liquid-gas interface, the droplet has rotational and internal circulation during its travel time.

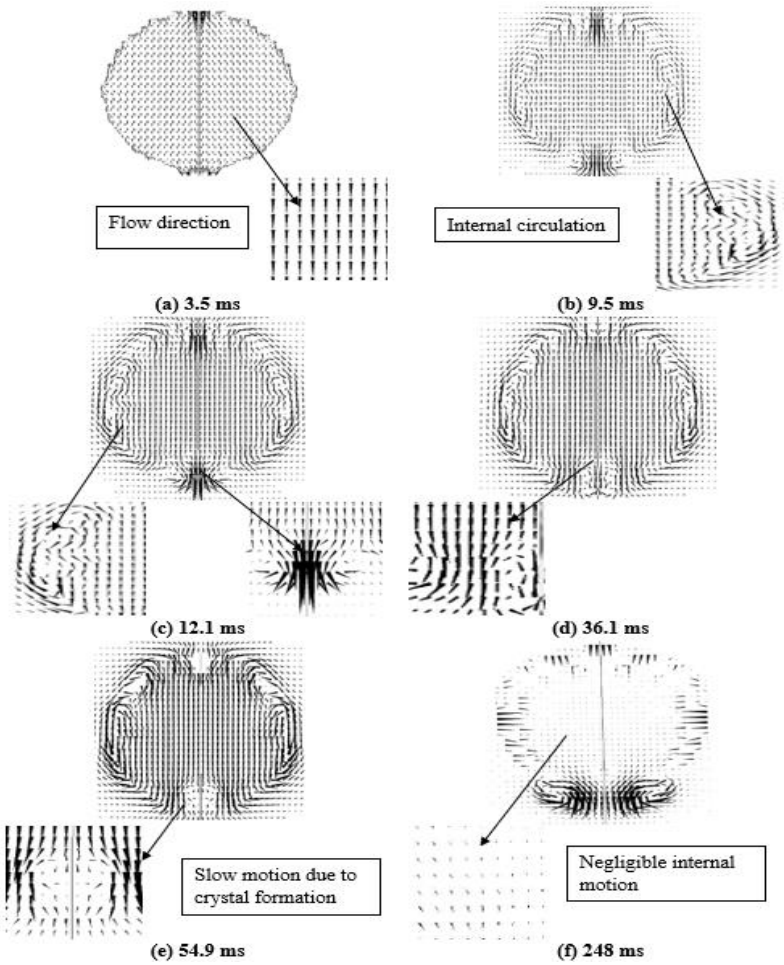

Fig. 3.8 Internal motion of a free falling droplet for different residence times.

In Fig. 3.8, the initial spherical shape of the droplet is visible. However, as time progresses, the fluid in the separation point starts to circulate. Mcdonald (1954) illustrated that rather than skin-friction drag at the surface of a liquid droplet, surface airflow at the separation point generates strong vertical circulation. Figure 3.8 (b) to (e) represent this situation. The shaking produces contributes to a warmer nucleation (Alexiades and Solomon, 1993; Dorsey, 1948). Later, a solid crystalline structure forms on the droplet circumference during freezing as a non-isothermal flow field is applied, which changes the droplet shape and slows down the motion, as shown in Fig. 3.8 (f). Yao and Schrock (1976) found that for a droplet diameter of more than 4 mm, a non-spherical shape is developed during its free fall, which agrees well with the new numerical predictions presented in this thesis.

The Reynolds (Re) and Weber (We) numbers are used to investigate the unsteady droplet behaviour in a hot or cold air medium. The Weber number is very important in defining the characteristics of droplet deformation (Shreiber et al., 1996; Wierzba, 1990) and the Reynolds number determines the regimes of various flow patterns. To determine the Reynolds and Weber numbers, Volkov et al. (2015) presented some dimensionless formulations, which are applied in the current study:

$$We = \frac{v^2 d \rho_l}{\sigma} \tag{3.13}$$

$$Re = \frac{vd}{2\upsilon_d} \tag{3.14}$$

In Fig. 3.9, various dimensionless numbers are presented in terms of different droplet sizes and velocities. Fresh water droplets are considered, and the numerical results

for both -10 ºC and -18 ºC ambient air are compared with the available experimental data of Volkov et al. (2015) for an ambient air of 27 ºC.

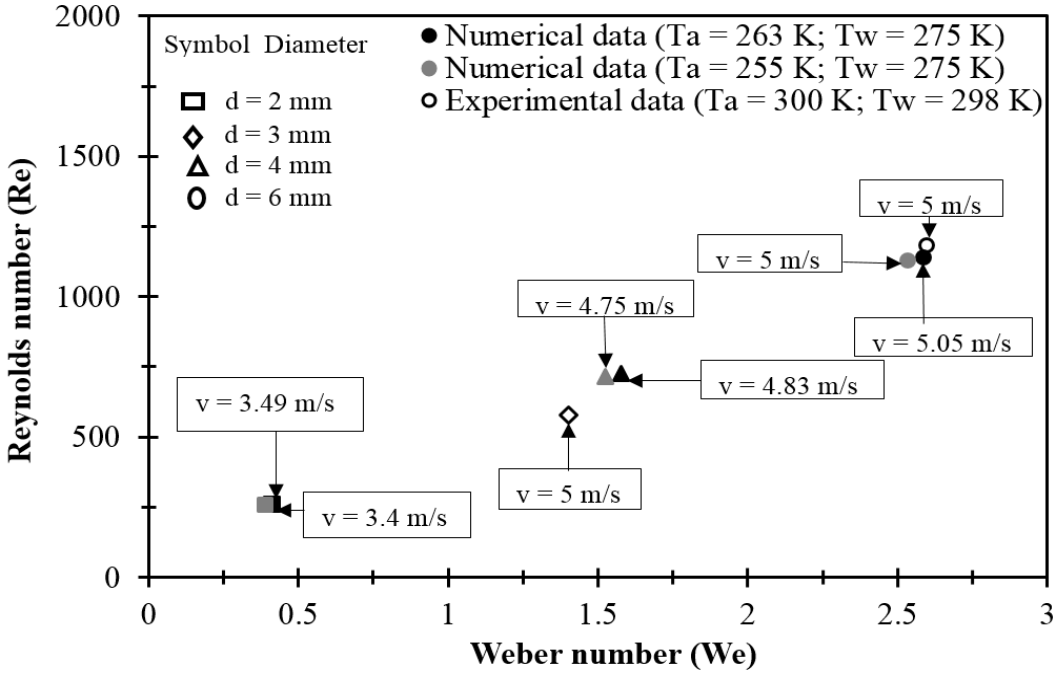

Fig. 3.9 Comparison of numerical predictions with the available experimental data.

For both experimental and numerical cases, the Weber number increases with an increment of droplet size; however, the values are very low. As suggested by Sirignano (2000) and Wierzba (1990), for small Weber numbers, some vibrations might develop; however, no significant break-up will occur. Therefore, for a long residence time, the larger sized droplets might experience a flattening deformation without break-up. Furthermore, as the droplet size increases, the value of Reynolds number increases.

The medium to high Reynolds number indicates that the larger sized droplets might experience a strong aerodynamic interaction with the surrounding gas and the oscillations might affect the overall droplet shape. However, Volkov et al. (2015) speculated that the

Reynolds and Weber criterions are not enough to describe the deformation, especially when the durations of droplet travel are much higher than their characteristic sizes.

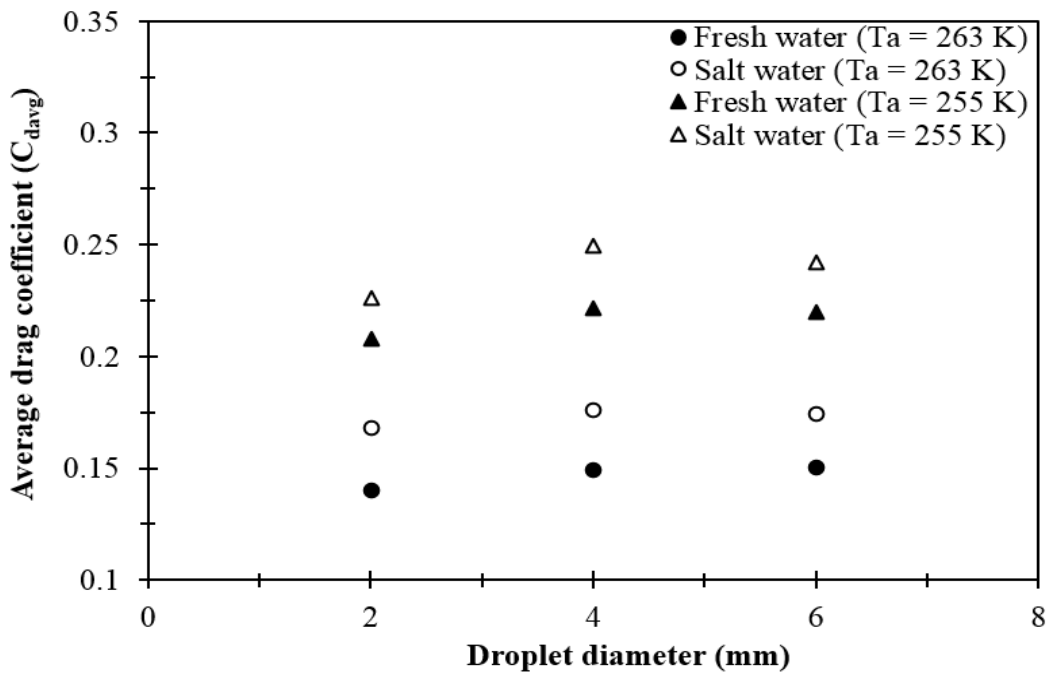

Fig. 3.10 Average drag coefficient at different atmospheric temperatures.

To investigate the effect of body force on a free falling droplet, a drag force calculation is performed. The calculation used an improved correlation, which was initially presented by Fakhari and Rahimian (2011):

$$C_D = \frac{4}{3}\frac{(\rho_l - \rho_g)}{\rho_g\, g}\frac{1}{Fr^2} \tag{3.15}$$

where $(\rho_l - \rho_g)$ is the density variation, g is the gravitational acceleration, d is the droplet diameter, and Fr denotes the Froude number which is defined as (Fakhari and Rahimian, 2011):

$$Fr = \frac{u_t}{\sqrt{gd}} \tag{3.16}$$

where u_t is the terminal velocity. The results of this calculation are presented in Fig. 3.10.

Figure 3.10 illustrates that the drag coefficient is insensitive to droplet radius and, in some cases, slightly decreased with an increment of droplet size. This prediction agrees well with the experimental investigation of Gunn and Kinzer's (1949), in which the authors tested the drag coefficient of various sized free falling droplets in stagnant air. Furthermore, the plot demonstrates that the average drag coefficient at -18 ºC is higher than at -10 ºC, which is primarily attributed to the influence of terminal velocity (Beard and Pruppacher, 1969). The presence of a multiphase mixture in the droplets at a lower temperature reduces the terminal velocity by reducing internal motion. Pitter and Pruppacher (1973) illustrated that the terminal velocity of a droplet could be decreased by 6% to 7% during a few seconds of freezing. Additionally, the existence of internal circulations can also influence the overall drag force (Megaridis et al., 1994).

3.5 Conclusions

This chapter investigated the temperature distribution and phase change process of a free falling droplet according to the temperature dependent thermophysical properties. The results characterized freezing behaviour in free falling fresh and salt water droplets which were not in thermal equilibrium with the ambient air. The simulation results also showed that the nucleation process could occur at higher temperatures than the equilibrium freezing point. Additionally, it predicted that the nucleation temperature was controlled by the droplet's volume and atmospheric temperature.

Internal circulation, drag effects, and the deformation process were also investigated in the present work. The circulation enhances heat transfer from the droplet to the surrounding air and can accelerate the nucleation phenomena in cold environmental conditions, as well as influence the fragmentation process. Results found that the nucleation temperature of fresh water droplets was higher than for salt water droplets. Furthermore, the drag force was not only a function of droplet size, but also of ambient temperature and internal circulation.

The proposed numerical model captures effects such as the changing thermal resistance of the droplet. The results of this chapter provide valuable new insights into spray dynamics and phase change.

CHAPTER 4[5]

POST IMPACT PROCESS-i: NUMERICAL MODELLING OF DROPLET IMPACT AND FREEZING ONTO AN ISOTHERMAL SUBSTRATE

4.1 Introduction

Icing poses a serious hazard to the safe operation of equipment in cold regions. This phenomenon is prevalent in marine, power, automobile and aerospace industries, as well as meteorology to refrigeration sectors (Dalili et al., 2009; Hermes et al., 2009; Laforte et al., 1998; Liu et al., 2007; Myers and Charpin, 2004; Punge and Kunz, 2016; Wu and Webb, 2001; Wu et al., 2007, 2016; Zhang et al., 2016a, 2017a). Therefore, to predict ice accretion rate, it is necessary to investigate the droplet impingement phenomena.

Figure 4.1 describes a typical diagram of droplet impingement. Prior to impact, the droplet travels at an unsteady velocity and undergoes shape change (Sultana et al., 2017). As a water droplet impacts on the solid substrate, a thin liquid film develops at the contact point and spreads uniformly in the radial direction, which is referred to as “wetting” the surface (Bernardin et al., 1997). The hydrodynamic phenomena involve spreading and oscillation in which transient velocity fields are established on the substrate surface. Heat transfer starts after impingement, where the spreading loses energy to the substrate. Past studies reveal that the freezing time of water droplets is affected by many factors, such as droplet size and substrate temperature. The primary goal of this study is to identify these

[5] This chapter is written based on: Sultana, K.R., Pope, K., Muzychka, Y.S., 2016. Numerical Predictions of Solidification and Water Droplet Impingement. In Arctic Technology Conference. Offshore Technology Conference.

factors that influence the freezing process, and to elucidate the complex mechanisms involved with spreading and solidification of high impact droplets.

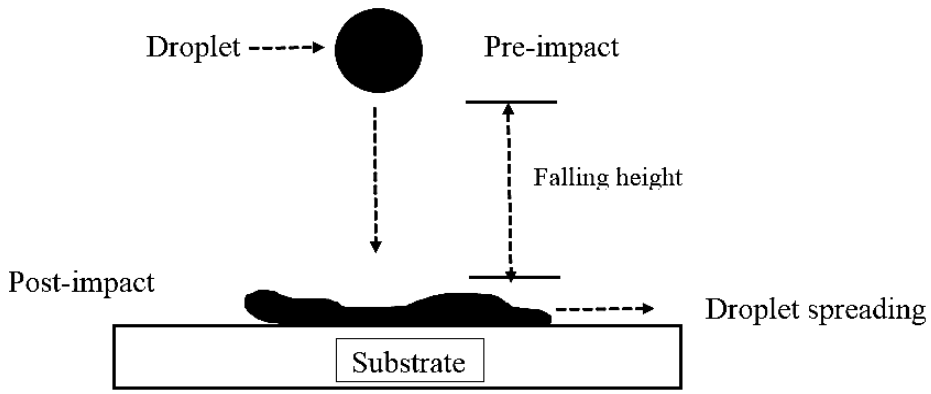

Fig. 4.1 Schematic of droplet impact and spreading on a solid substrate.

Droplet impact and solidification is a complex process involving phase change heat transfer and moving boundaries (Zhang et al., 2017b). Bonomo (2013) and Enriquez et al. (2012) demonstrated that when a droplet freezes on a very cold surface, freezing starts from the plate surface and moves upward as it solidifies. Tabakova and Feuillebois (2004) demonstrated that the freezing process of a supercooled sessile liquid water droplet lying on a cold substrate is primarily dominated by conduction. For low Prandtl numbers, Inada (1988) concluded that the convection intensity near a solid substrate is so low, that the conduction equation is sufficient for estimating the temperature distribution in a thin layer of liquid near the solid substrate. The author conducted the test for a liquid metal droplet. Strub et al. (2003) studied sessile freezing water droplets in a humid airflow and demonstrated that the phase transition from a supercooled liquid droplet to solid is influenced by conduction and convection heat transfer mechanisms, as well as evaporation

and sublimation mass transfer. Bhardwaj et al. (2007) studied a variety of liquids impinging on isothermal and non-isothermal surfaces. They reported that the Weber number affects spreading, in that large Weber numbers produce higher spread factors. When a warm droplet impacts a surface at a colder temperature, heat is transferred from the droplet through convection and conduction. Convection occurs in the droplet and the conduction is in the substrate. However, they did not address the dominating heat transfer mode. Fukusako et al. (1989) reported that air temperature, droplet size, droplet temperature and droplet mass flow rate are significant factors for icing. Additionally, the substrate temperature and the chemical components in water influence freezing. Fumoto and Kawanami (2012) explained that the freezing behaviour of a fresh water droplet is strongly influenced by the substrate temperature and thermophysical properties. Jin et al. (2016) studied the impact and freezing process of a water droplet on different inclined cold substrates, such as red copper, quartz glass, carbon fiber reinforced composite (CFRC) and glass fiber reinforced composite. The authors showed that cold surfaces affected not only the freezing time of water droplets, but also the shape of ice beads that result in the final shape of the freezing droplet. Li et al. (2011) conducted an experimental study to investigate the influence of freezing on the impingement process of a single water droplet on aluminum substrates. The author used the water droplets ranging from 0.5 mm to 2.5 mm in diameter, the impact velocities were from 0.8 ms^{-1} to 20 ms^{-1} and substrate temperatures included 20 °C and –13 °C. The results revealed that solidification did not influence the first spreading phase, and its effect on the receding phase was only visible for longer receding phases.

Spreading is an important factor in droplet freezing, which is affected by several parameters, such as droplet temperature, substrate temperature, impact velocity and material characteristics. Previous studies have identified several dimensionless numbers, such as the Reynolds, Froude, Weber, Stefan and Ohnesorge numbers to be important for characterizing the process. Schiaffion and Sonin (1997) explained that for small sized droplets, the effect of gravity is negligible and the dynamics of spreading can be characterized by three main dimensionless parameters (the Weber, Reynolds and Ohnesorge numbers). Madejski (1976) found that the degree of droplet flattening depends upon the Weber, Reynolds and Peclet numbers. The author assumed that the substrate is isothermal and thermal properties of the cold substrate surface have no influence on the magnitude of droplet flattening. Pasandideh-Fard et al. (1996) developed an analytical equation to predict the relation between the maximum spread factor and the Reynolds number for low impact droplets in the absence of heat transfer. Li et al. (2011) concluded that the higher the impact velocity, the less prominent the receding phase. Xu et al. (2012) demonstrated that a higher impact velocity expanded the flattening diameter and promoted retraction. Increased droplet size increases the spreading time, spreading diameter, gliding maximum diameter and maximum displacement (Mohammadi, 2016).

For numerical studies, Fukai et al. (1995) were the first to implement the contact angle as a boundary condition in cases of water droplet impact onto a cold, flat surface. They followed a 2D axisymmetric Lagrangian approach, which was deformed according to the shape of the droplet free surface. The authors reported that the droplet's impact velocity significantly influenced the spreading behavior. In the context of tin droplet

deformation, Pasandideh et al. (1998) considered a complete numerical solution of the Navier-Stokes and energy equations, based on a modified SOLA-VOF method, to model solidification and heat transfer. Sultana et al. (2016) conducted a numerical study to model the freezing evolution of a micro sized free falling droplet, and showed that salt water droplets have a longer freezing time than fresh water droplets. Karlsson (2013) conducted numerical studies on a fresh water sessile droplet's solidification process; however, in the model, the author neglected the gravitational effect, phase interaction and water droplet movement. The author showed that the solidification process was enhanced by lowering the substrate temperature. Liu et al. (1993) conducted a numerical study on molten droplets in plasma spray processes and reported that increasing initial droplet velocity can significantly enhance the flattening extent of a droplet. Total freezing time and the final diameter of the spread is dependant on the initial droplet velocity, droplet temperature and substrate temperature (Liu et al., 1993).

The literature is, however, limited to using small, such as micrometric, sized droplets with very low to high impingement velocities. Furthermore, metallic droplets or immobile droplets have been considered during freezing. Hence, it is necessary to develop new models for simulations of droplet impact, spreading and solidification for high impact water droplets. The purpose of this study is to simulate the fluid flow, heat transfer and solidification phenomena during the impact of a water droplet onto an isothermal substrate using a finite volume methodology. Numerical simulations are conducted to investigate the effect of droplet size and substrate temperature on droplet spreading and solidification. Results are compared with published experimental data. A scaling analysis is also

performed to investigate the thermal resistance of various sized droplets.

4.2 Numerical Model and Methodology

Figure 4.2 illustrates the schematic diagram of the computational domain. A 130 cm × 12.7 cm × 12.7 cm rectangular domain is represented. A total of 1,157,625 cells are produced during meshing.

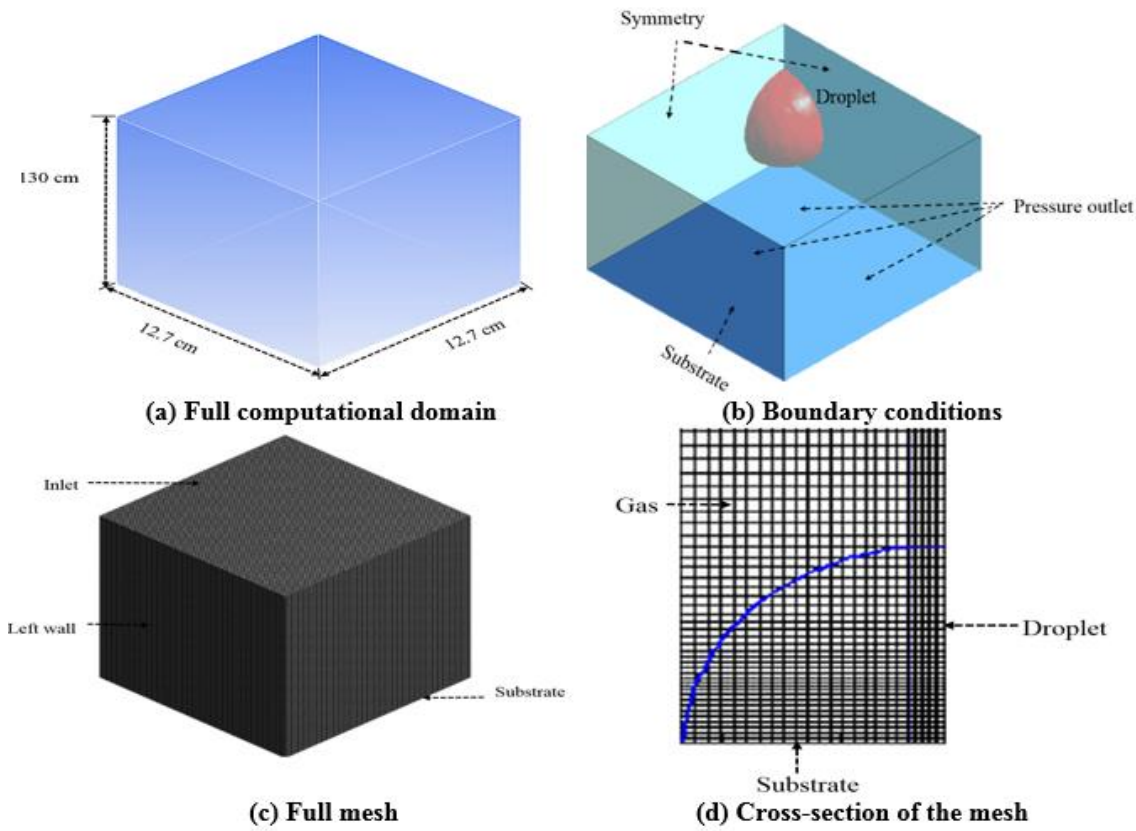

Fig. 4.2 Schematic of computational domain.

Due to this long computational domain and the high number of nodes, the simulation has a long computational time. Boundary conditions are as follows: pressure outlet is considered at the inlet and symmetry at the vertical boundary walls. An isothermal boundary condition is imposed onto the substrate surface. Initially, a spherical droplet is

patched at the center of the domain and allowed to free fall. When the droplet impinges onto the substrates, it deforms, and then spreads into a thin layer. Therefore, to capture the hydrodynamic behaviour, the smallest cell is applied in the droplet-surface interface region.

During the calculations, the properties of the solid material (aluminum) were assumed constant. However, the properties of the liquid are assumed to be a function of temperature (csgnetwork, Fukusako and Yamada, 1993; uwaterloo). Details of the numerical grid, computational conditions and material properties are presented in Tables 4.1 - 4.4.

A pressure implicit scheme with the splitting of operator (PISO) scheme is applied to the pressure-velocity coupling in the momentum equation (Issa, 1985). To reduce the high Courant number effect, a small time step (1×10^{-6}) with 20 internal iterations per time step is used in the simulation. From a computational standpoint, a large number of numerical iterations are required to obtain the thermal and flow field results during any phase change process. The time step is continuously monitored and the convergence for each time step is considered at the residual values of 1×10^{-5}.

Table 4.1 Details of the numerical grid for zero substrate thickness.

Dimensions of the computational domain	1.3 m × 0.127 m × 0.127 m
Total number of cells	1,157,625
Smallest cell size near the air-water interface	0.000025 m
Smallest cell size near the water-substrate interface	0.00002 m

Table 4.2 Initial boundary conditions.

Droplet diameter (mm)	2, 3, 4, 5
Droplet temperature (°C)	18
Air temperature (°C)	18
Substrate temperature (°C)	-20 and -25

Table 4.3 Thermophysical properties of water (constant).

Parameter	**Value**
Fluid type	Fresh water
Surface tension ($N.m^{-1}$)	0.07617
Viscosity ($kg.m^{-1}.s^{-1}$)	0.001003
Latent heat of fusion ($J.kg^{-1}$)	336,000

Table 4.4 Temperature dependent thermophysical properties for fresh water.

Temperature (°C)	**Density ($kg.m^{-3}$)**	**Specific heat ($J.kg^{-1}.K^{-1}$)**	**Thermal conductivity ($W.m^{-1}.K^{-1}$)**	**Phase**
18	998.00	4077.40	0.60	Liquid
12	999.28	4086.30	0.59	
2	1000.40	4109.60	0.57	
0.1	1000.50	4116.10	0.57	
0	999.87	2067.00	2.21	Solid
-2	999.69	2053.22	2.23	
-10	998.16	1998.10	2.32	
-20	993.68	1998.10	2.43	
-25	989.89	1894.75	2.48	

The conditions are similar to the study of Saha et al. (2016b), where the authors studied the freezing process of various sized, fresh water droplets at a room temperature of 18 °C. The water droplets fall from a height of 130 cm onto a cold aluminum surface. The plate dimensions were 12.7 cm × 12.7 cm, and it was cooled from below by a constant cooling bath. The tests were conducted at a room temperature of 18 °C and constant atmospheric pressure. The initial droplet temperature was 18 °C. The droplet temperature and the spreading were investigated by means of a thermal camera and a high-speed camera.

4.3 Scaling Analysis of Sensible and Latent Energy Change During Solidification of Post-Impact Droplet

This section provides an estimation of the thermal resistance between the temperature of the substrate, T_{sub} and the average temperature of the droplet, T_d. The nature of the thermal boundary condition at the interface between the droplet and the substrate plays an important role in the solidification process. The thermal resistance network is useful in scalling up the spreading dynamics. Further, it calculates the energy transfer between the droplet and the substrate at some depth.

The shape of the post impact droplet is approximated by a disk with average radius, r_s. Evaporation between the droplet and the air is considered negligible, as is radiation heat transfer to the surroundings. Contact resistance between the surface and the droplet is neglected. The boundary condition at the surface is considered isothermal.

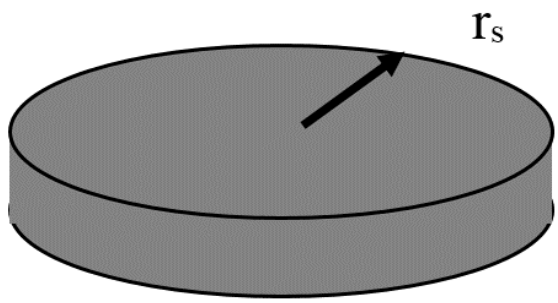

Fig. 4.3 Schematic of disk-shaped droplet.

The primary mechanisms of energy transfer within the droplet are conduction and convection. Convection to the air is very small and is considered negligible in the study. Convection is initially due to spreading, then as the droplet freezes, it becomes solely internal circulation.

The total resistance between the temperature of the surface and the average temperature of the droplet is modeled as:

$$R_t = \left(\frac{1}{R_{conv}} + \frac{1}{R_{cond}}\right)^{-1} \tag{4.1}$$

where R_{cond} is the thermal resistance due to conduction and R_{conv} is the thermal resistance due to convection.

The length scale for transient conduction into the drop is $L_c \sim \sqrt{\pi\, \alpha_{diff} t}$ (Nellis and Klein, 2008), such that resistance to transient conduction may be represented as:

$$R_{cond} \sim \frac{\sqrt{\pi \alpha_{diff} t}}{k_c A_s} \tag{4.2}$$

where $A_s = \pi r_s^2$ is the spread area.

Convection within the droplet enhances energy transfer. Schiaffino and Sonin (1997) categorized droplet deposition based on Weber number, $We = \frac{\rho L_c\, v^2}{\sigma}$ and

Ohnesorge number, $\boldsymbol{Oh} = \frac{\mu}{\sqrt{\rho\sigma L_c}}$. For a high Weber number and low Ohnesorge number, the spreading process is categorized as "inviscid and impact driven". Most of the spreading occurs in a short period and is driven by the dynamic pressure of impact. The impact velocity and droplet size characterize the velocity of spread and over a short time, viscous effects can be neglected (Schiaffino and Sonin, 1997). For external laminar flow and Prandtl number, $Pr >> 1$, the Nusselt number may be scaled by $Nu \sim Pr^{1/3}\sqrt{Re}$ (Jiji, 2009). The convection heat transfer coefficient then takes the form:

$$h_{conv} \sim \frac{k_c Nu}{L_c} \sim \frac{C_l k_c Pr^{1/3}\sqrt{Re_r}}{r_s} \tag{4.3}$$

where the characteristic length scale for convection is the spread radius, C_1 is a scaling coefficient, $Re_r = \frac{\rho v r_s}{\mu}$ is the Reynolds number of radial flow, and v is the velocity just prior to impact. The thermal resistance due to convection scales as:

$$R_{conv} \sim \frac{1}{h_{conv} A} \sim \frac{r_s}{C_l k_c Pr^{1/3}\sqrt{Re_r} A_s} \tag{4.4}$$

Equation (4.1) becomes (Madejski, J., 1975):

$$R_{droplet} = \frac{\sqrt{\pi \alpha_{diff} t}}{k_c A_s \left(1 + \frac{C_l Pr^{1/3}\sqrt{Re_r \alpha_{diff} t}}{r_s}\right)} \tag{4.5}$$

The second term in the parenthesis can be considered the relative contribution of convection to energy transfer within the droplet. This treatment of enhancement due to circulation is similar to that used by Yao and Schrock (1976) and Sultana et al. (2017) in the context of circulation within free falling droplets. Equation (4.5) represents resistance as a function of time, the time-averaged resistance from $t = 0$ to t_f is approximated by:

$$R_{avgdroplet} \sim \frac{2\sqrt{\pi \alpha_{diff} t_f}}{3k_c A_s \left(1 + \frac{C_l Pr^{1/3} \sqrt{Re_r \alpha_{diff} t_f}}{r_s}\right)} \tag{4.6}$$

To capture the influence of the Weber number, the resistance is scaled by the Weber number and the expression becomes:

$$R_{avgdroplet} = \frac{C_2 \sqrt{\pi \alpha_{diff} t_f}}{We\ k_c\ A_s \left(1 + \frac{C_l Pr^{1/3} \sqrt{Re_r \alpha_{diff} t_f}}{r_s}\right)} \tag{4.7}$$

where C_2 is a scaling factor.

When the substrate is considered isothermal, e.g., a liquid-cooled cold plate is used as the substrate, the thermal resistance in the substrate is minimal. Moreover, the energy transfer from the droplet to the substrate is governed primarily by the thermophysical properties of the droplet, pre-impact Reynolds and Weber numbers, and the topological surface properties e.g roughness or contact angle.

4.4 Results and Discussion

Figure 4.4 represents a time series of the temporal evolution of the temperature of various sized fresh water droplets. Images are taken at the solid-liquid interface region.

The time variations of the droplet temperature start from the moment when it impinged on the cold substrate. Initially, the temperature of the liquid water droplet is high (red in color) which is a homogeneous temperature of 18 ºC, and the substrate is considered as an isothermal temperature of -25 °C. This is because the substrate has an infinite thermal capacity; therefore, heat imparted to the substrate would be conducted away immediately from the interface, such that a fixed substrate temperature is always upheld.

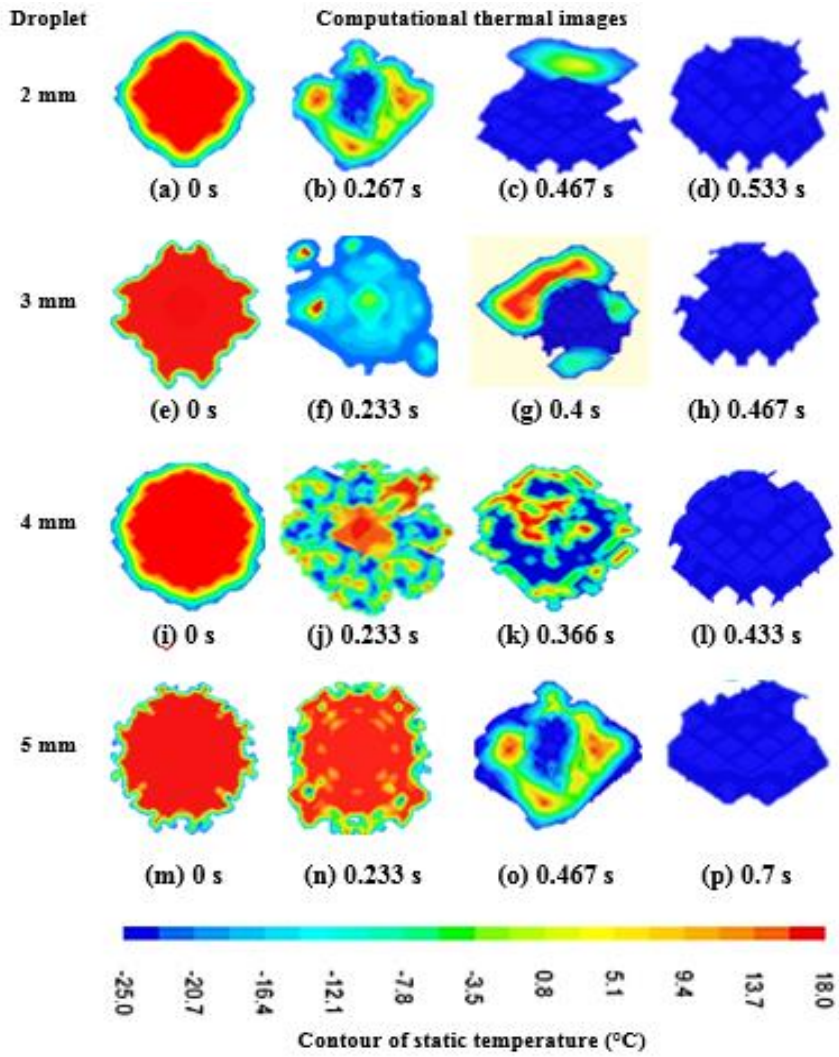

Fig. 4.4 Internal temperature distribution of various sized droplets on an isothermal surface.

During droplet impact, the fluid exhibits different forms of spreading behavior. In the absence of solidification, the droplet would expand, retract, and oscillate, and obtain a final equilibrium shape. In the presence of solidification, the final shape depends on the relationship between spread time and solidification time. In this study, the final shape ranges from splat to a disk in shape. For smaller droplets (i.e., 2 mm), solidification starts from the center of the droplet, and then the solid-liquid interface moves towards the outer

surface of the droplet (as a function of time) until solidification is complete. This is because the smaller sized droplet has low kinetic energy that eventually limits the spreading area, and restricts finger formation. Thus, the peripheral area gets thicker than the midpoint region, and cools slower than the center. However, it is different for the larger sized droplet. A larger droplet has high kinetic energy that helps to create a greater impact force upon impact (Fukusako et al., 1989), increasing the spreading area. As the area increases, the fluid layer gets thinner in the peripheral regions of the splat and causes faster solidification due to lower thermal resistance.

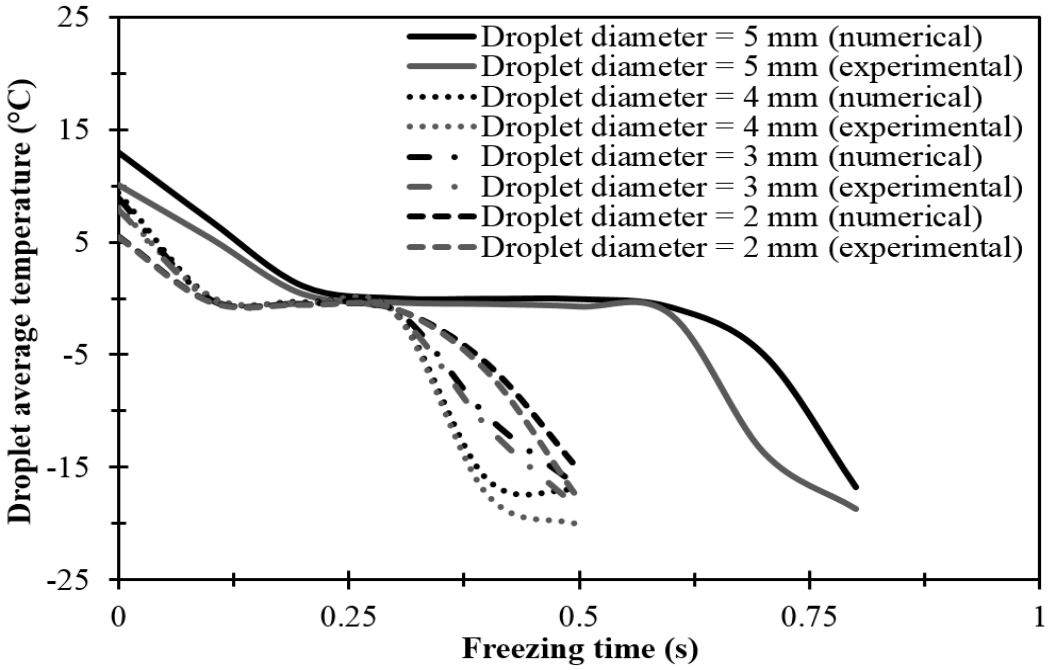

Fig. 4.5 Temperature variation of a water droplet during the impact on an isothermal substrate.

The time history of temperature illustrates the process of liquid-to-solid transformation during phase change as shown in Fig. 4.5. At impact, thermal energy leaves

the droplet. Once the temperature reaches the fusion temperature, the liquid droplet begins solidifying, forming a liquid-solid stage. Depending on droplet size, this liquid-solid stage varies between 0.15 s and 0.45 s. Later, the droplet is almost solidified and undergoes additional sensible energy changes, and reaches the substrate temperature. Excellent agreement is obtained between the numerical and the experimental results from Saha et al. (2016b).

The current study considers a grid independent test where three different mesh sizes are used, presented in Table 4.5. Special consideration is focused on the impact zone area. The impact zone is identified as the region near the droplet-substrate area where the maximum effect of the flow field and solidification is observed.

Table 4.5 Mesh analysis test.

Mesh statics	**Smallest cell size near the water-substrate region** ***(*$\Delta x \times \Delta y \times \Delta z$***)**
Mesh 1	0.025 mm × 0.04 mm × 0.04 mm
Mesh 2	0.025 mm × 0.03 mm × 0.03 mm
Mesh 3	0.025 mm × 0.02 mm × 0.02 mm

For the grid test, the error is defined as:

$$\text{Percentage of error} = \frac{\text{Experimental result} - \text{numerical result}}{\text{Experimerntal result}} \times 100 \tag{4.8}$$

Three different sized mesh, minimum errors are obtained for mesh 3. The error is reduced by reducing the grid spacing near the droplet-substrate area. For mesh 3, the maximum error is almost 11% and the minimum error is about 0.05%. For the three

different grid sizes, the errors are very close to each other, which indicates grid independence. However, for minimal errors, mesh 3 is chosen for all the simulations.

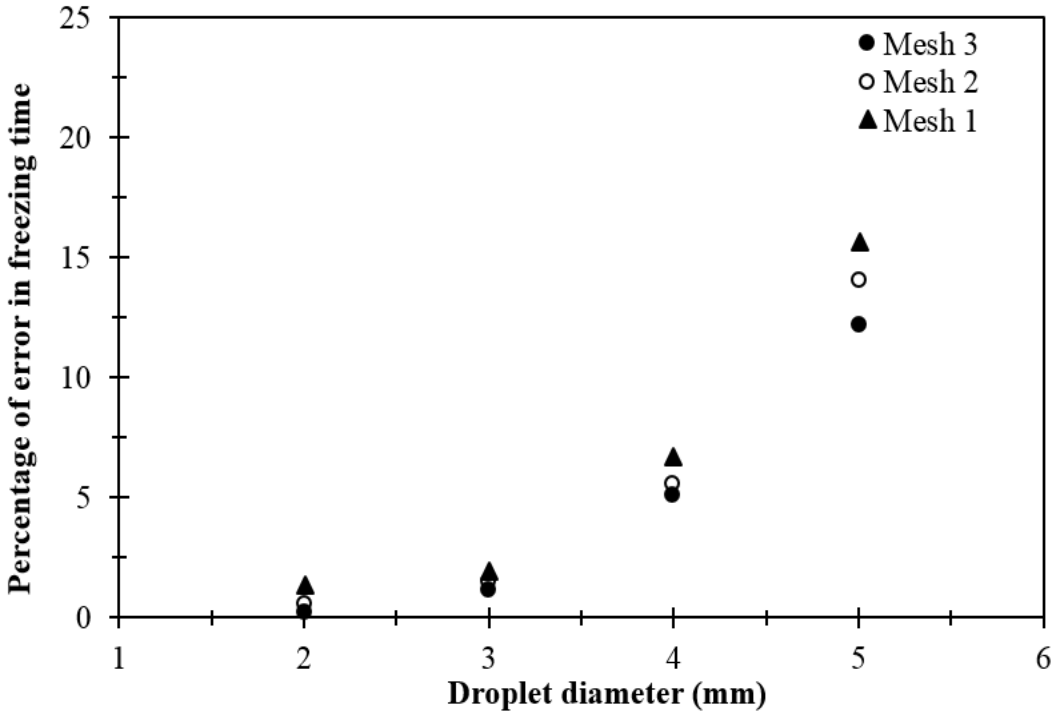

Fig. 4.6 Mesh independency study.

Figure 4.7 demonstrates a graphical comparison of droplet freezing time at two different substrate temperatures. No growing ice layer was observed on the substrate, which could be due to the constant boundary temperature condition (relatively dry environment) assumed in the numerical analysis. The freezing time is calculated by means of non-dimensional Fourier number and defined as:

$$Fourier\ number\ (Fo) = \frac{\alpha_{diff} t_{freezing\ time}}{d^2} \tag{4.9}$$

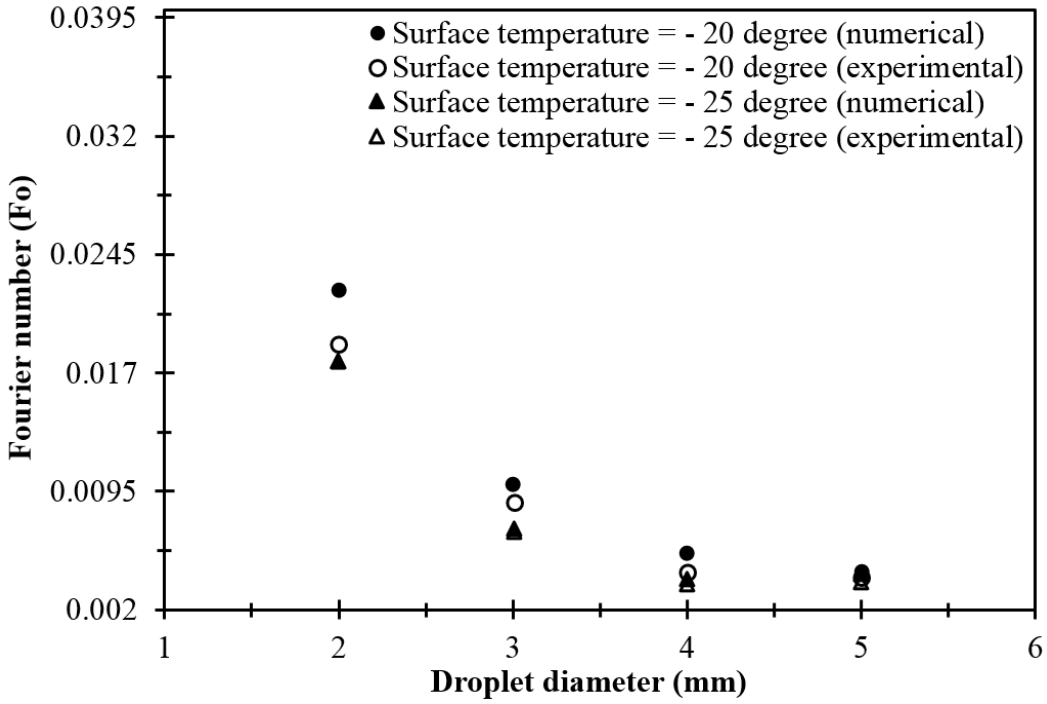

Fig. 4.7 Comparison of dimensionless freezing times for different sized droplets.

It is observed that the smaller sized droplet has a higher Fourier number than the larger sized droplets. Furthermore, the lower substrate temperature yields a shorter freezing time than the higher substrate temperature. This is because the lower substrate temperature produces a larger temperature variation that drives heat transfer, allowing the droplet to dissipate the thermal energy at a faster rate. Similar phenomena have also observed by Zhang et al (2017b) in the study of sessile droplets, where the authors explained that the droplet freezing time is highly influenced by substrate's temperature. Mishchenko et al. (2010) explained that after impingement, the interface temperature is strongly dominated by the substrate temperature, and not the initial droplet temperature. The current investigation found that for the same substrate temperature, the thermal exchange of smaller droplets represented by the dimensionless freezing time, is slightly faster than the

bigger sized droplets. These kinds of results or phenomena could be used in low relative humidity conditions, where the evaporation or the condensation of the droplet could be controlled, and also to ensure that all the droplets land on the dry surface rather than condensate/evaporate.

Figure 4.8 demonstrates the spread factor as a function of droplet radius. The flattening, or the spreading ratio is defined as the ratio of final droplet radius (r_s) to the initial droplet radius (r) along the substrate after impingement. It is expressed as (Aziz and Chandra, 2000; Li et al., 2011; Oukach et al., 2012; Tabbara and Gu, 2012):

$$Spread\ factor\ (\xi) = \frac{Final\ droplet\ radius\ along\ the\ substrate\ after\ impact}{Initial\ droplet\ radius} = \frac{r_s}{r} \tag{4.10}$$

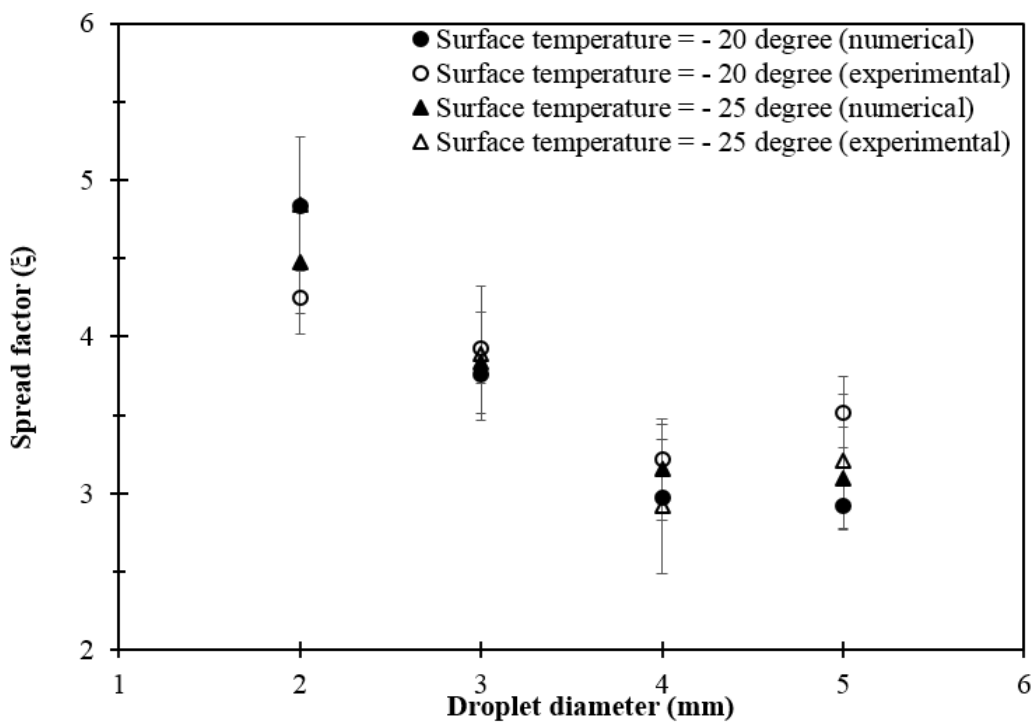

Fig. 4.8 Spread factor as a function of droplet diameter.

The ratio of spread area to initial radius is higher for smaller droplets. One possible cause is the absence of retraction. As the spreading area increases, the surface tension effect decreases, exerting less resistance against droplet spreading, which increases the amount of spreading. The spread factor upholds a downward linear relation with the droplet diameter. Furthermore, it is observed that the spreading area increases with increasing the substrate temperature. This is because the lower substrate temperature influences the faster freezing rate. Therefore, the velocity vectors are held earlier in the lower substrate temperature than the higher temperature substrate. The phenomenon suggested that the spread factor is a function of the impingement conditions as well. Both results are validated against the experimental results of Saha et al. (2016b), and found a very good agreement. The maximum relative error between the spreading factor from the numerical and experimental calculations is found 12% and 16%, respectively for the surface temperature of -20 °C and -25 °C.

Figures 4.9 and 4.10 demonstrate a time series of velocity vectors where the various sized droplets impact on a very cold substrate at a temperature of -25 °C. When a water droplet impacts a surface, it appears as a truncated sphere with a high velocity jet shooting out as a thin liquid film (Figs. 4.9(a)-4.10(a)). The bulk volume of liquid then spreads in the radial direction, from the impact point, as a thin liquid lamella (Figs. 4.9(b)-4.10(b)).

Since the 5 mm droplet has high kinetic energy, more instabilities develop on the periphery of the droplet, which causes the formation of tiny fingers. These fingers trap air bubbles and promote heterogeneous freezing at the liquid-substrate interface (Jung et al., 2012; Sultana et al., 2017). Therefore, some void regions are observed on the advancing

edges of the 5 mm droplet (Fig. 4.10(b)). Due to less inertia, the spreading area of a 2 mm droplet is much more limited. Therefore, no fingers or void regions are observed.

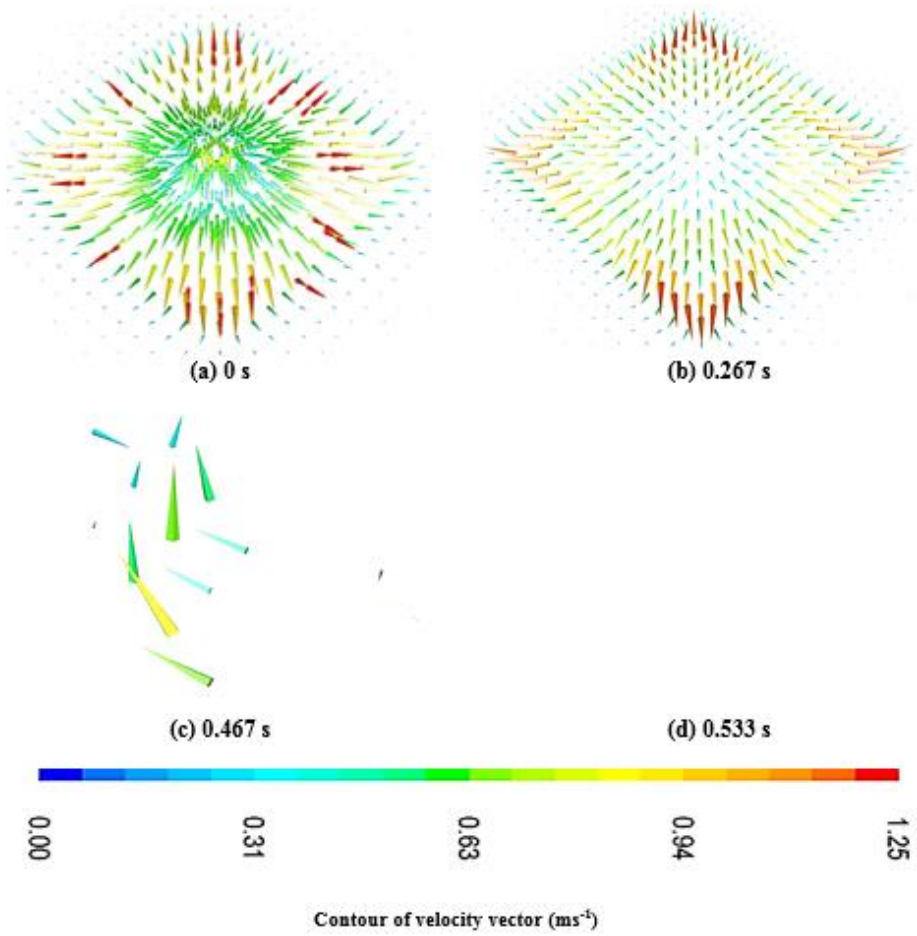

Fig. 4.9 Impact and spreading characteristics of a 2 mm diameter water droplet.

As time progresses, the water droplet recoils. It is found that while recoiling, for a 2 mm droplet, most of the velocities are stopped by freezing (Fig. 4.9(c)). Whereas for a 5 mm droplet, the phenomenon is a little slower (Fig. 4.10(c)). One of the possible reasons is the mass of the droplet. As mass increases, the droplet freezing time while recoiling is

much slower. Afterward, as time progresses, at 0.533 and 0.7 s, both the droplets are completely frozen, therefore, no vector images appear in Figures 4.9(d) and 4.10(d).

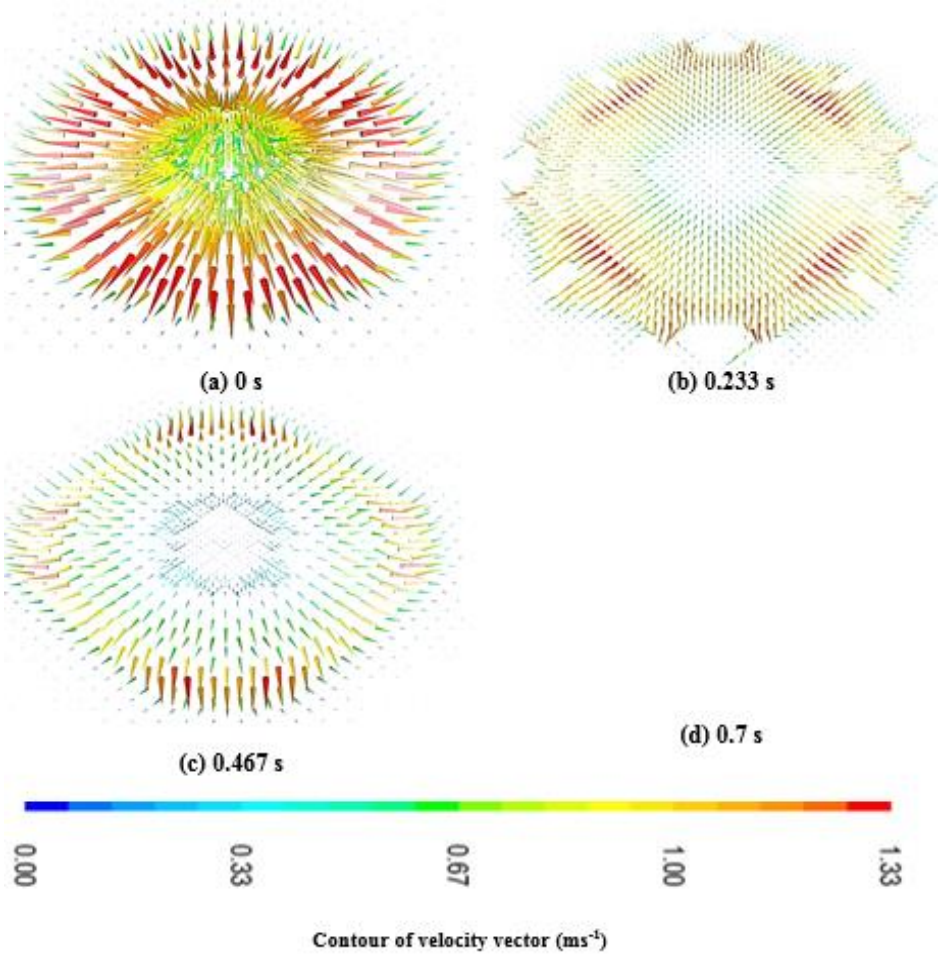

Fig. 4.10 Impact and spreading velocities of a 5 mm diameter water droplet.

Thermal resistance values for the numerical and experimental data are obtained from $R_t = \frac{\Delta T}{L}$, where ΔT is the difference between the ambient and fusion temperatures, $T_a - T_f$, and L is the sum of sensible and latent energy transfer out of the drop, divided by time to freeze, t_f. The sensible energy change is scaled by:

$$E_s \sim \rho_w C_{pw} \forall \left(T_a - T_f\right) \tag{4.11}$$

where ρ_w and C_{pw} are averages of properties at T_a and T_f. The latent energy is scaled by $E_l \sim \rho \forall H_f$ where ρ is calculated using average properties at T_f and the surface temperature, T_{sub}. Table 4.6 shows latent and sensible energy values corresponding to droplet diameter.

Table 4.6 Sensible and latent energy.

Droplet diameter (mm)	Sensible energy change (J)	Latent energy change (J)
2	0.315	1.341
3	1.062	4.525
4	2.516	10.725
5	4.915	20.948

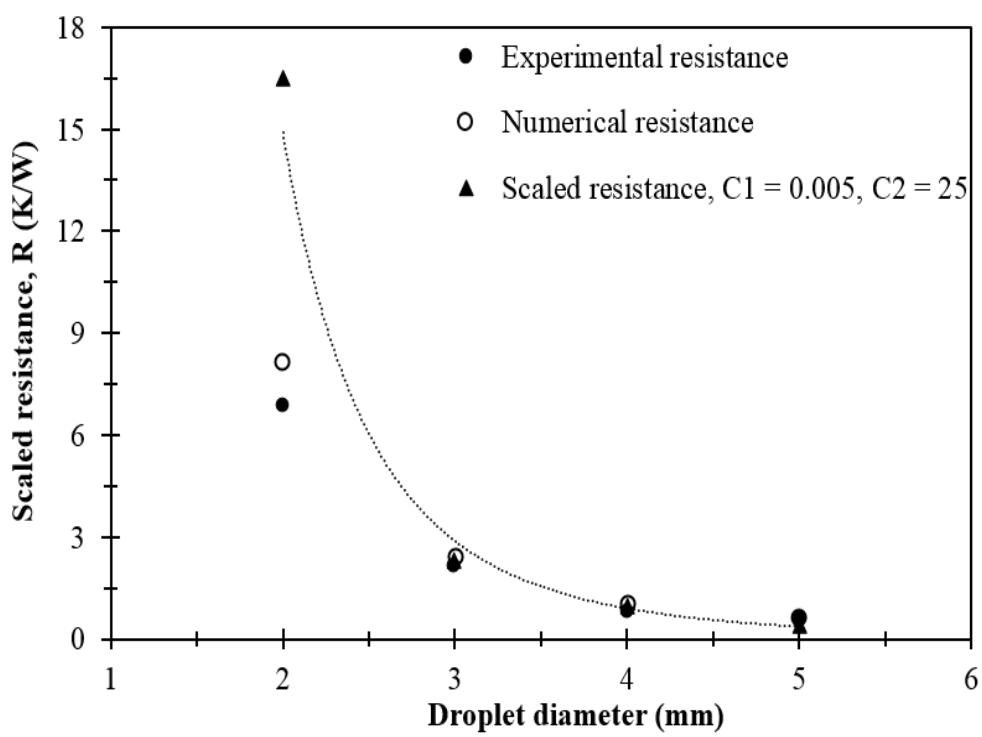

Fig. 4.11 Scaled thermal, experimental and numerical resistance for substrate of -20 °C.

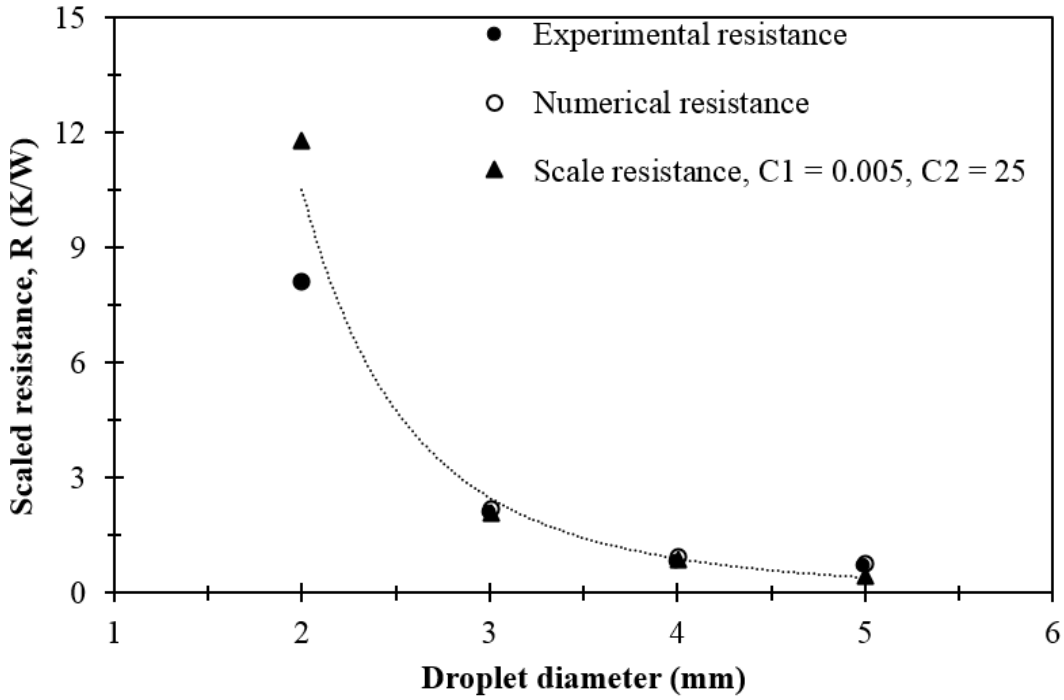

Fig. 4.12 Scaled thermal, experimental and numerical resistance for substrate of -25 ^{o}C.

Figures 4.11 and 4.12 demonstrate the scaled resistance where the thermal resistance of the substrate at -20 °C is greater than that at -25 °C. One of the possible reasons is the freezing time. High substrate temperature leads to a longer cooling period that supports droplet retraction. Droplet retraction increases the droplet height and influences the thermal resistance.

Thermal resistance is non-dimensionalized by thermal conductivity and the spread radius, $R^* = k_c r_s R$. In order to account for spread factor and surface temperature, experimental and numerical values can be related to $\frac{\Delta T}{L}$, non-dimensionalized by k and r_s in the following relation:

$$R^* \sim \frac{4Fo\xi}{3St} \tag{4.12}$$

$St = C_p \left(\frac{T_{sub}-T_f}{H_f}\right)$ where St is the Stefan number.

The dimensionless relation is shown in Fig. 4.13. The scaled expression better represents the high impact physics of the larger droplets that correspond to lower values of $Fo\xi/St$.

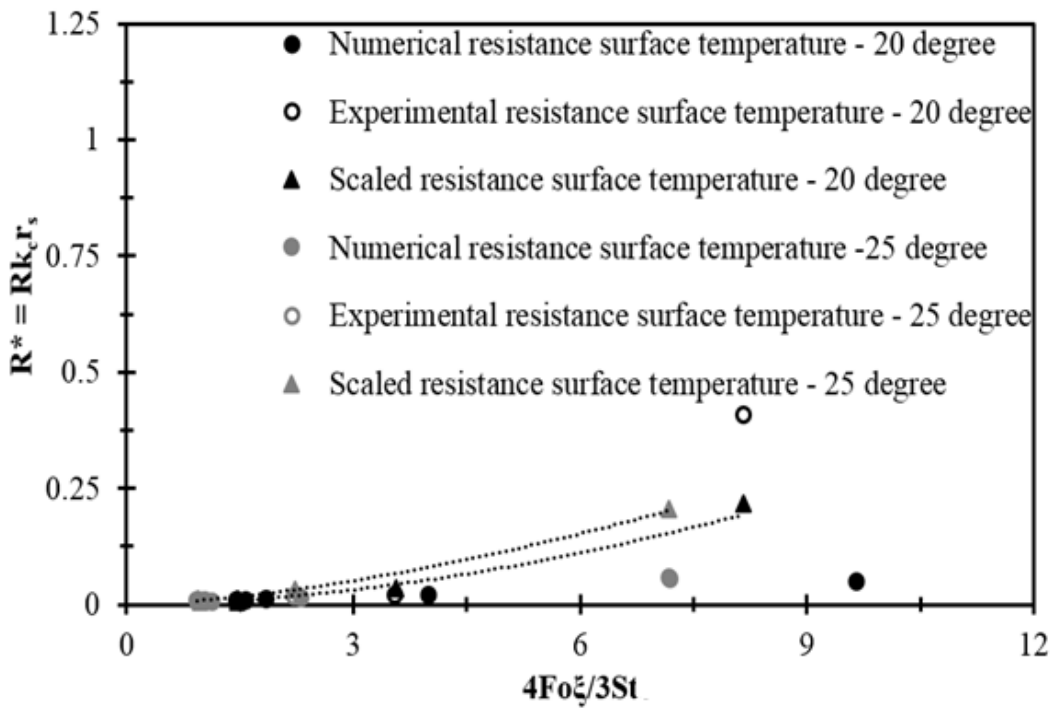

Fig. 4.13 Dimensionless resistance plotted against dimensionless $\Delta T/L$.

4.5 Conclusions

The normal impact with the solidification of a liquid water droplet onto a rigid isothermal substrate was studied. The effects of several key factors on the spreading and solidification of the droplet on the substrate were examined.

The results show that droplet solidification is a transient process that is significantly influenced by the substrate temperature and the spreading area. Lower substrate temperature promotes a faster freezing rate. In addition, for the same substrate temperature, the thermal exchange capacity of smaller droplets was higher than that for the larger sized droplets. The droplet mass and the spreading area were the most significant variables for freezing. Additionally, the flow time had an important effect on freezing.

The scaling found that a small droplet with a diameter of 2 mm and a low Weber number was not well represented by a high impact model. For larger droplets, scaling of thermal resistance corresponded well with numerical and experimental values and demonstrated the dependence on spread factor, Fourier and Stefan numbers.

CHAPTER 5

POST-IMPACT PROCESS-i: NUMERICAL INVESTIGATION OF DROPLET SPREADING AND HEAT TRANSFER ON COLD SUBSTRATE

5.1 Introduction

Interfacial heat transfer is an important study in cooling and freezing applications to provide a better understanding of the fundamentals of thermal contact and develop more accurate engineering modelling. Numerous studies have been conducted on modelling droplet impact on substrates. Bennett and Poulikakos (1994) demonstrated that the thermal conductivity of a surface highly influences the cooling rate of the splat. Aziz and Chandra (2000) conducted a study to investigate the effect of varying impinging velocity and substrate temperature using the impact of molten tin droplets on a stainless steel substrate. The authors photographed and measured the variation of droplet deformation and temperature difference during impact. Fukumoto et al. (2011) studied the effect of substrate temperature on the spreading and solidification behaviour of a free falling molten droplet. The authors concluded that the substrate temperature and the ambient pressure have an equivalent effect on heat transfer at the droplet-substrate's interface contact condition. Thermal resistance models have been used, e.g., in the context of electronics cooling to identify the relative contribution of multiple thermal mechanisms to transport (Hodes et al., 2014; Lam et al., 2015; Phillips, 1988). Furthermore, the solidification of droplets is significantly influenced by thermal contact resistance or surface resistance (Kamnis and Gu, 2005). Although the thermal contact resistance between the droplet and the substrate has a substantial effect in the solidification process (Trapaga et al., 1992; Pasandideh-Fard

and Mostaghimi, 1996), it has been ignored in most studies (Bertagnolli et al., 1995; Liu et al., 1993).

The literature is, however, limited to using metallic droplets, no phase transition or using an isothermal, dry substrate (Marengo et al., 2011). The spreading, freezing and the interfacial heat transfer behaviour of a water droplet can differ fundamentally from a metal droplet or on an isothermal substrate. In this connection, the investigation of the impact of a water droplet on a non-isothermal solid surface is of scientific and applied importance.

5.2 Numerical Model and Methodology

Figure 5.1 shows the typical definition of the flow domain, as well as the typical grid and boundary conditions for simulating droplet impingement onto a solid substrate. The geometry contains two domains: (i) droplet and the surrounding air and (ii) substrate. The droplet impingement height is maintained at 130 cm. The thickness and the width of the substrate are 1.09 d and 5.09 d, respectively, where d is the initial diameter of the droplet. The benchmark for substrate width and thickness is followed from the work of Shukla et al. (2015) and Tabbara and Gu (2012). The magnitude of contact resistance was obtained from Ansys Fluent software, and the contact angle measurement was performed in the MUN engineering laboratory.

A total of 2,159,688 cells are produced during the meshing. Boundary conditions are as follows: pressure outlet is considered at the inlet and symmetry at the boundary walls. An interface condition is imposed onto the substrate surface.

Initially, a spherical droplet is patched at the center of the domain and applied to free fall. When the droplet impinges on the substrate, it deforms, spreads and stabilizes as

a thin layer. Since the overall dynamics occurred on the substrate surface, it is necessary to consider the smallest cells in the droplet-surface interface region. Tables 5.1 to 5.2 represent the details of the numerical grid and computational conditions, while the input parameters used in the computations are summarized in Tables 5.3 to 5.4.

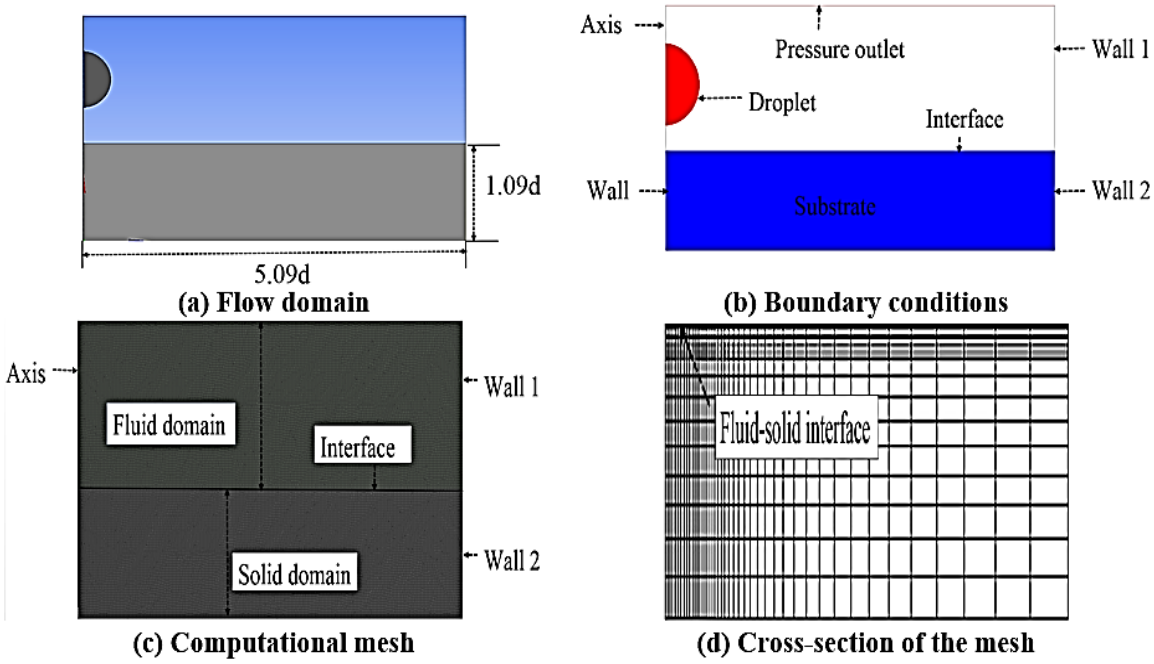

Fig. 5.1 Schematic of computational domain.

Table 5.1 Details of the numerical grid for a thicker substrate.

Height of the computational domain	1300 mm
Total number of cells	2,159,688
Smallest cell size near the air-water interface	1.6661×10^{-3} mm
Smallest cell size near the water-substrate interface	1.6661×10^{-3} mm

Table 5.2 Input parameters used in the computed predictions.

Droplet diameter (mm)	2, 3, 4, 5
Droplet temperature (°C)	18, -15, -18
Air temperature (°C)	18
Substrate temperature (°C)	-15, -18, -20, -25
Contact angle between the liquid and solid surface (°)	72
Thermal contact resistance ($m^2.K.W^{-1}$)	10^{-6}

Table 5.3 Thermophysical properties of material used in this study (Oukach et al., 2012).

Substrate material	Aluminum
Thermal conductivity ($W.m^{-1}.K^{-1}$)	237
Density ($kg.m^{-3}$)	2700
Specific heat ($J.kg^{-1}.K^{-1}$)	900

Table 5.4 Temperature dependent thermophysical properties for fresh water.

Temperature (°C)	**Density ($kg.m^{-3}$)**	**Specific heat ($J.kg^{-1}.K^{-1}$)**	**Thermal conductivity ($W.m^{-1}.K^{-1}$)**	**Phase**
18	998.00	4077.40	0.60	Liquid
17	998.41	4079.50	0.60	
12	999.28	4086.30	0.59	
7	999.94	4096.00	0.58	
5	1000.10	4100.90	0.58	
2	1000.40	4109.60	0.57	
0.1	1000.50	4116.10	0.57	
0	999.87	2067.00	2.21	Solid
-2	999.69	2053.22	2.23	
-10	998.16	1998.10	2.32	
-20	993.68	1998.10	2.43	
-25	989.89	1894.75	2.48	

5.3 Results and Discussion

Figures 5.2 details the thermal evolution inside a thick substrate, where the ambient temperature is 18 °C and the substrate is maintained at a temperature of -25 °C. A 5 mm droplet is considered for the current case and shows the evolution of the "heat affected zone" in the substrate at different flattening times of the droplet.

From the contour, it is observed that when the droplet lands, the substrate temperature begins to rise due to heat exchange between the droplet and substrate. It is found that at the impact position, the contact temperature is higher, and it is lower in the vicinity of the spreading front in the entire spreading process. Le Bot et al. (2005) explained that the thermal exchanges at the first contact are more important than the others. Since the heat is continuously distributed to the plate, the substrate is maintaining a non-uniform temperature condition.

The figure illustrates that as soon as the flattening is completed and the splat is cooled, the heat flow through the substrate surface is reduced. Le Bot et al. (2005) demonstrated that when the entire splat solidified, the interface temperature reduced more rapidly as the latent heat was totally released. Although the current investigations found a non-uniform temperature on the substrate surface during droplet impact, the change is minimal. Bhola and Chandra (1999) and Ruiz and Black (2002) speculated that a substrate can be considered as an isothermal substrate when droplets are placed on a high thermal conductivity substance. This is because the high thermal conductivity immediately takes away the heat. Since the current study considers a high thermal conductivity aluminum

substrate, and the thermal increment is minimal, droplet impingement in a semi-infinite domain can be treated as an isothermal substrate.

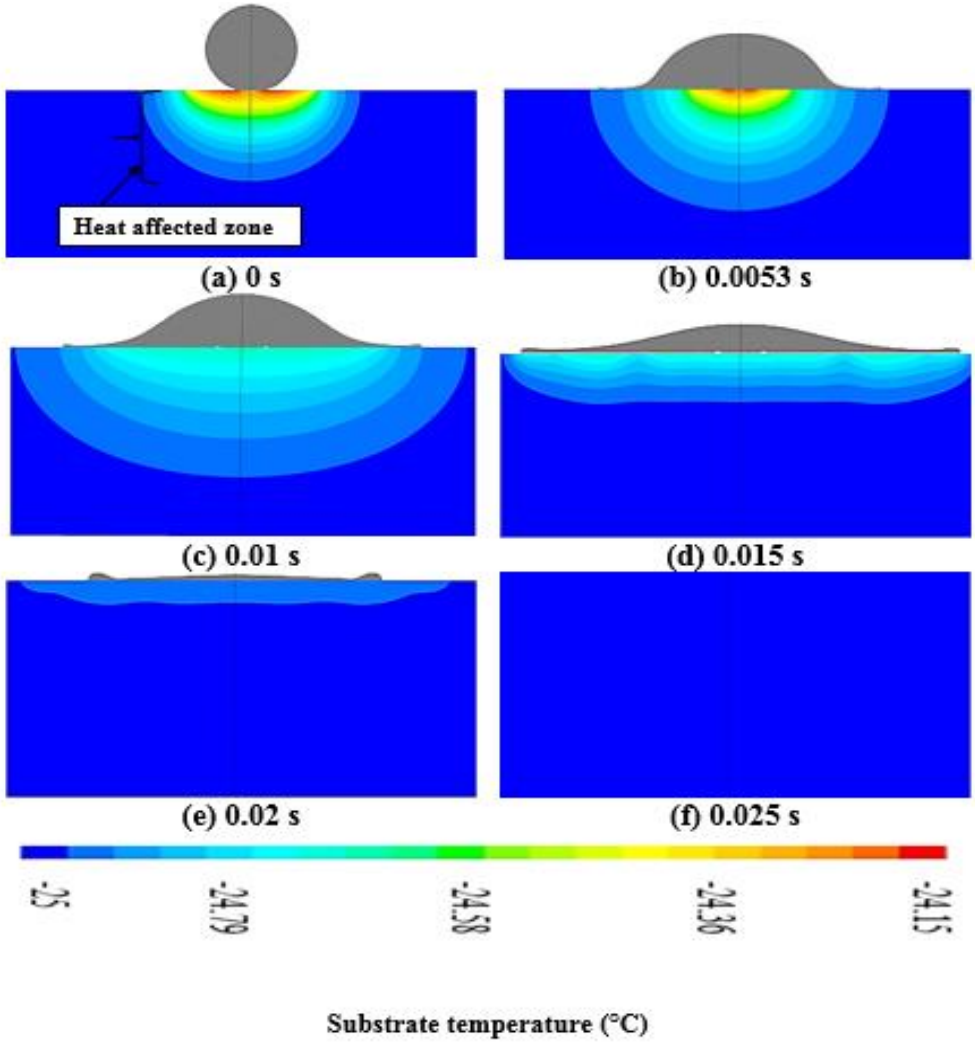

Fig. 5.2 Temperature contour inside the substrate at different spreading times of droplet.

Figure 5.3 represents the temperature increment history in the droplet-substrate interface region where the various sized droplets have impinged on a substrate with a temperature of -25 °C. From the figure, it is found that for large sized droplets, the temperature increment is maximum; whereas, it is minimum for the small sized droplets.

One possible reason is the droplet volume and the spreading area. The larger the volume is, the longer time it takes to solidify, eventually increasing the substrate temperature.

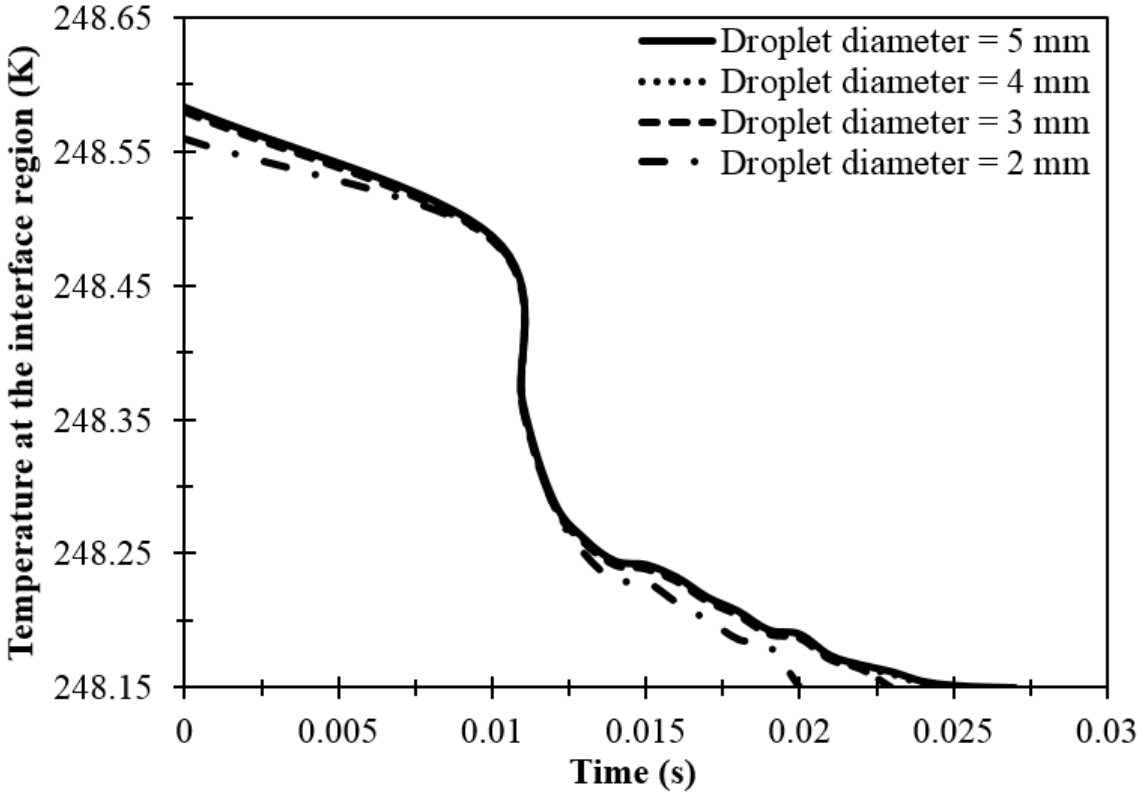

Fig. 5.3 Transient temperature history in the droplet-substrate interface region.

Figure 5.4 demonstrates a mesh convergence study with various mesh thicknesses. The grids are considered as: mesh 1 ($1.6661 \times 10^{-3} \times 1.6661 \times 10^{-3}$), mesh 2 ($1.5681 \times 10^{-3} \times 1.5681 \times 10^{-3}$) and mesh 3 ($1.4437 \times 10^{-3} \times 1.4437 \times 10^{-3}$), where the meshes are selected to increase the level of refinement near the solid-liquid interface, and where the steep temperature gradients are performed. Based on a comparison of the temperature increments at the interface region, mesh 1 was selected as an acceptable resolution level to perform all the numerical simulations. Furthermore, the calculation shows that for three

different grid systems, the maximum simulation error for determining the temperature increment is approximately 1.6 %. However, the illustrated results are almost the same for the three different grid systems, demonstrating that the results are not mesh affected.

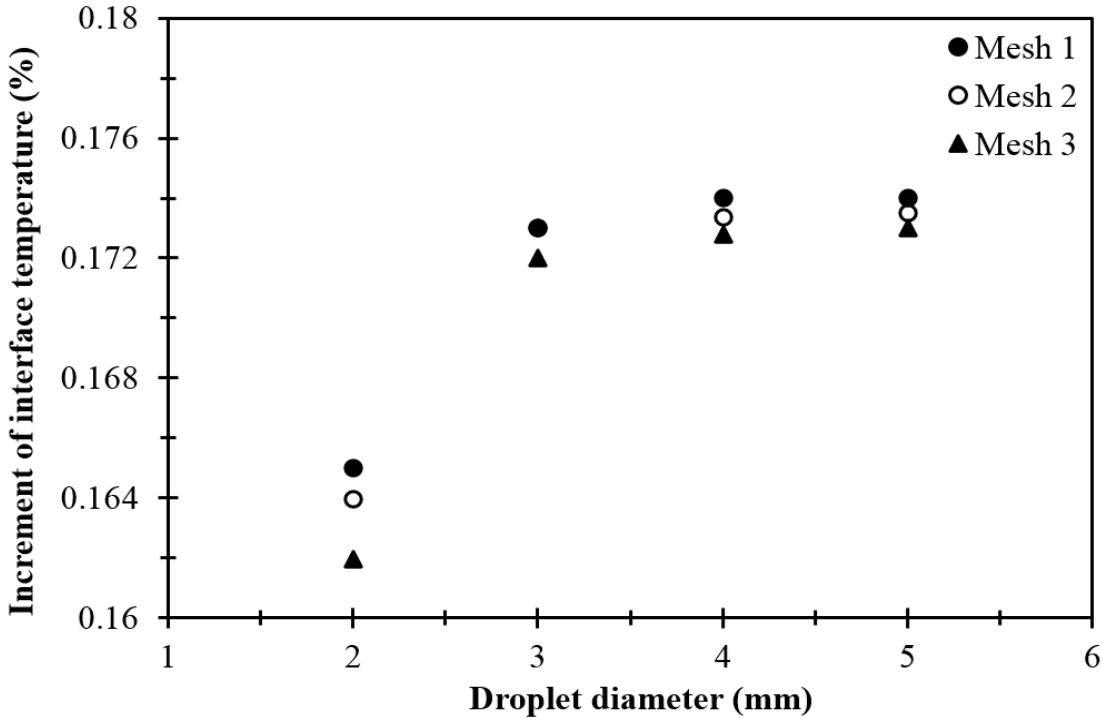

Fig. 5.4 Mesh independent study on a substrate temperature of -25 °C.

Figure 5.5 illustrates the effect of ambient temperature on the increment of droplet-substrate interface temperature and thermal penetration depth. The study is considered for a fresh water droplet diameter of 5 mm.

The dimensionless penetration depth and the increment of interface temperature is defined as:

$$\text{Dimensionless penetration depth } (\delta^*) \tag{5.1}$$

$$= \frac{\text{Maximum thermal penetration depth in the substrate}}{\text{Total substrate width}}$$

$$\text{Increment of interface temperature} \tag{5.2}$$

$$= \frac{\text{Temperature diffrence of the substrate} \times 100\%}{\text{Original temperature of the substrate}}$$

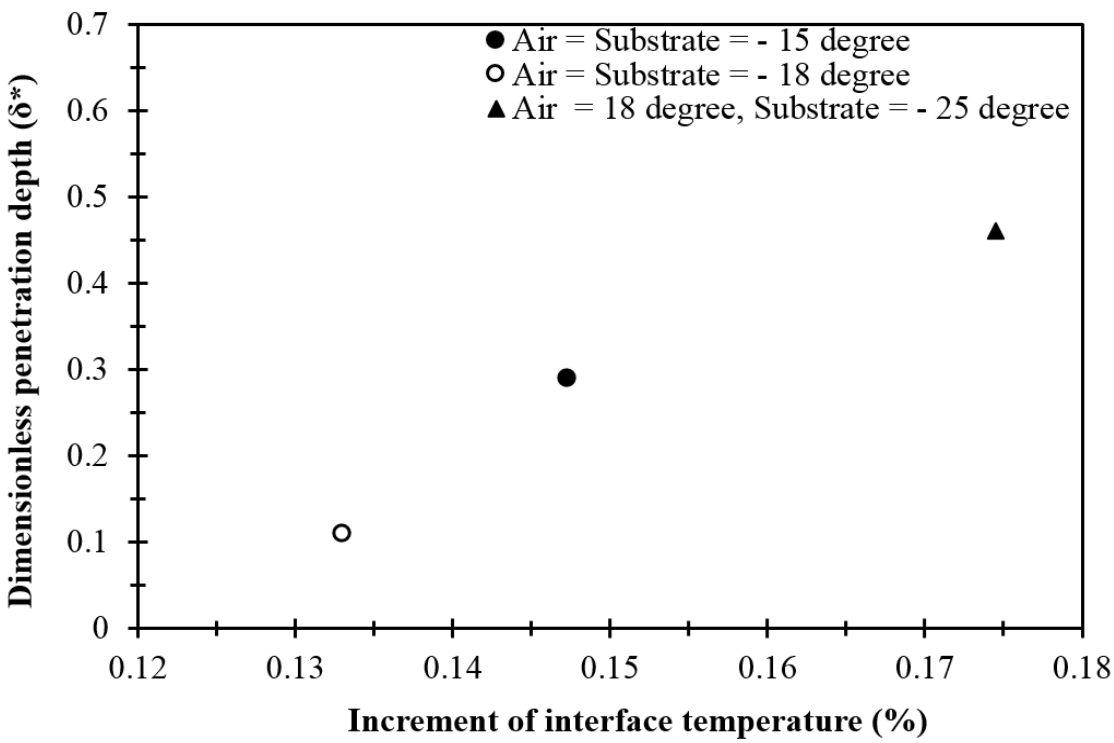

Fig. 5.5 Effect of ambient temperature on droplet-substrate interface region.

The figure shows that the maximum value of penetration depth and interface temperature is found for positive air temperature. One possible cause is the cooling time. For positive air temperatures, the substrate gets a longer time to cool, therefore, the heat

can penetrate the maximum distance. However, for colder temperatures, the droplet or the interface cooling time is lower, and eventually, the penetration depth is shorter.

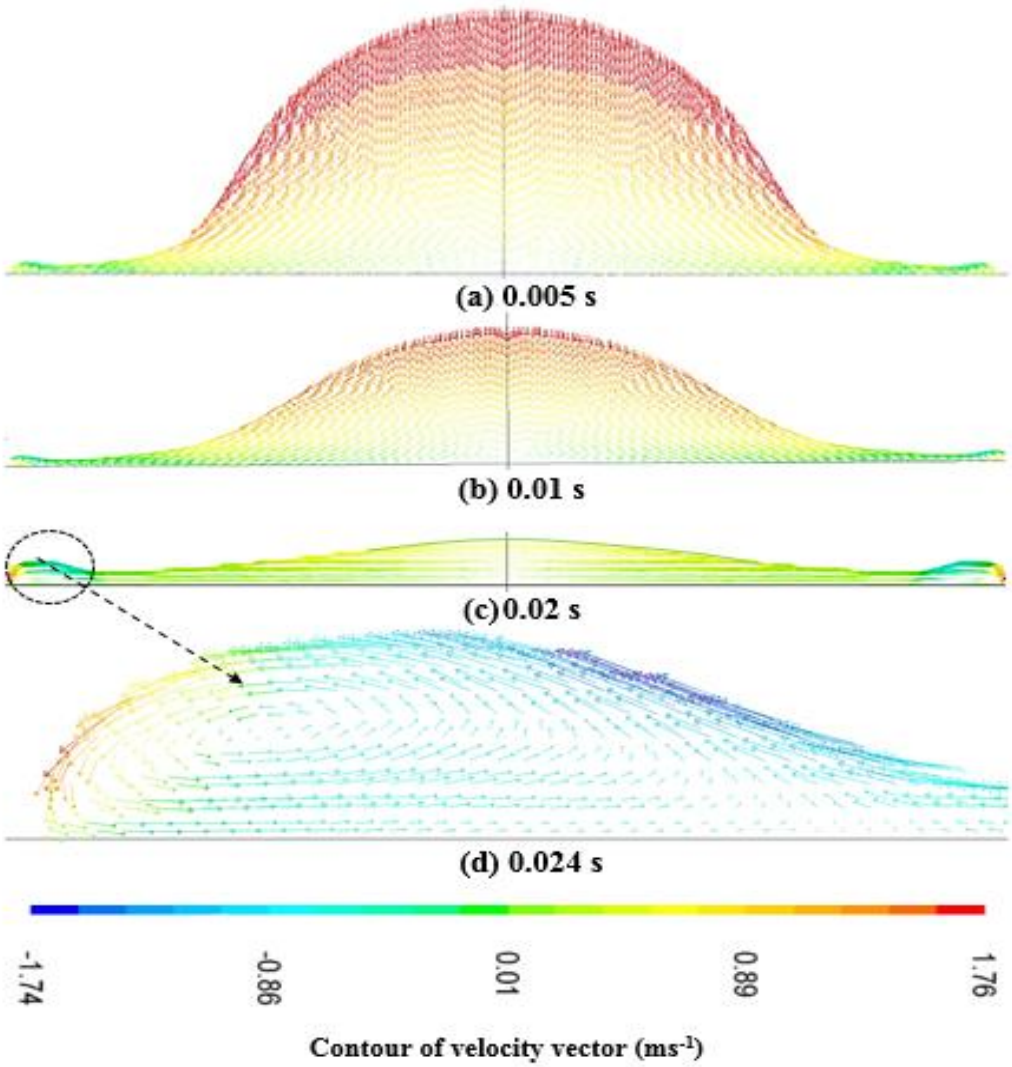

Fig. 5.6 Time evolution of the shape of the impinging droplet and the velocity field.

Figure 5.6 represents the evolution of the spreading process for a 5 mm fresh water droplet that impacts onto a solid substrate at a temperature of –25 °C. Initially, the droplet velocity is higher, however, as time progresses the velocity gets slower, and the splat becomes thinner and wider onto the substrate. Furthermore, during the spreading process,

small circulation zones have appeared on the droplet's periphery. For better clarity of the recirculation, a zoomed image is provided in Fig. 5.6(d). Strotos et al. (2008) explained that the lower substrate temperature and the buoyancy effects within the droplet might generate this kind of internal circulation. This circulation creates a mixing effect of internal convection that promotes the heat transfer process of the droplet-substrate interface region, as well as the droplet freezing process (Dai et al., 2002).

5.4 Conclusions

To evaluate the effects of interfacial heat transfer beheviour between a water droplet and substrate surface, millimeter sized free falling droplets were impacted. The variations of the substrate temperature were calculated numerically. The results indicate that for high thermal conductivity, the substrate acts like a semi-infinite, iso-thermal substrate. Furthermore, the temperature variation increased as the droplet volume increased.

The results demonstrate that for positive air temperatures, the heat can penetrate a longer distance compared to negative air temperatures. Transition timing is one of the reasons for this circumstance. Internal circulation was also observed in the current study. The circulation was developed at the peripheral edge of the droplet and increased the heat transfer rate, which promoted solidification within the droplet. Due to the combined effect of the fluid motion and solidification, the droplet experienced a bumped shape on the top layer.

From a researcher's viewpoint, analysis of droplet impingement, spreading and solidification offer very interesting challenges. Some of these interactions, although

known, are very difficult to quantify, to such extent that they can be incorporated into a computer program. The author believes this numerical modelling helps to visualize the inherent fluid characteristics while spreading and the coupling between flow and interface mechanisms on a more fundamental level in simple flow geometry. For future study, more work is needed in the form of a semi-analytical modelling to be able to characterize the beheviour more generally.

CHAPTER 6[6]

POST-IMPACT PROCESS- i: EXPERIMENTAL RESULTS OF DROPLETS DYNAMICS AND FREEZING PROCESS

6.1 Introduction

Ice accretion on exposed surfaces may cause serious hazards on offshore structures and vessels. Practically, there is no material that can completely reduce ice accretion on its surface (Arianpour et al., 2013; Kulinich and Farzaneh, 2009a, 2009b; Landy and Freiberger, 1967), however, found that some coatings provide slow ice accretion on surfaces.

Numerous theoretical, experimental and numerical studies have been conducted on liquid-solid interaction dynamics, including spreading patterns, material properties and freezing times (Fukai et al., 1995, 2000; Kang and Lee, 2000; Mao et al., 1997; Mundo et al., 1995; Pasandideh-Fard et al., 1996; Reznik and Yarin, 2002; Sedev et al., 1993; Siddhartha et al., 2007; Šikalo et al., 2002, 2005a-c). In their studies, they discussed various important factors that are essential to calculate droplet dynamics; including density, surface tension, viscosity, static and dynamic contact angle, roughness, droplet impact velocity and surface inclination. Gupta and Kumar (2010) demonstrated that the resulting phenomena and the final shape of the droplet on a substrate depend on various factors; including the properties of the droplet and impinged surface, the droplet impingement velocity, droplet

[6] This chapter is written based on: K.R. Sultana, L. Lam, K.Pope, Y.S. Muzychka,
Effect of Substrate Constriction Resistance on Phase Change in Fresh and Sea Water Droplets. Journal of Ocean Engineering (manuscript).

size, angle of attack to the substrate, droplet physical properties, surface wettability and surrounding pressure. Furthermore, Fauchais et al. (2004) and Mostaghimi et al. (2002) demonstrated that the final morphology of the splat depends on droplet size, temperature and velocity. Gajewski (2008) concluded that for small droplet volumes (40μm or less) the properties and roughness of the solid substrate are negligible. Fukumoto et al. (2011) explained that a free falling droplet has enough kinetic energy for splashing after impacting onto the solid surface. Prajitno et al. (2016) illustrated that the wettability of stainless steel with different surface roughnesses strongly depends on the surface finish of stainless steel and relation to heat transfer phenomena. Based on various experimental parameters such as droplet temperature, substrate temperature, impact velocity and material characteristics, previous studies have identified several dimensionless numbers, such as the Reynolds, Froude, Weber, Stefan and Ohnesorge numbers. These numbers are important to characterize the transport. Schiaffion and Sonin (1997) explained that for small-sized droplets, the gravity effect is negligible, and the dynamics of spreading can be characterized by three main dimensionless parameters such as the Weber, Reynolds and the Ohnesorge number.

To predict the ice accretion rate, it is necessary to investigate the after impingement resulting effect. Researchers have published several theoretical, experimental and numerical studies to address the complex ice accretion phenomenon (Lozowski and Gates, 1991; Lozowski and Makkonen, 2005; Lozowski et al., 2000; Zakrzewski and Lozowski, 1991). Researchers have investigated the most influential heat fluxes for icing (Blackmore, 1996; Blackmore et al., 2002; Blackmore and Lozowski, 1994; Chung and Lozowski,

1990; Dehghani et al., 2017b; Dehghani-Sanij et al., 2017; Horjen, 1983, 1990, 2013; Horjen and Vefsnmo, 1985a; Jones, 1996; Kato, 2012; Kulyakhtin et al., 2013, 2016; Kulyakhtin and Løset, 2011; Kulyakhtin and Tsarau, 2014; Lozowski et al., 1983, 2000; Makkonen, 1986, 2000; Myers and Charpin, 2004; Myers and Hammond, 1999; Naterer, 2011; Overland et al., 1986; Szilder et al., 1988). The main heat transfer mechanisms are conduction, convection, evaporation, radiation, heat capacity of the impinging spray, kinetic energy, aerodynamic heating and release of latent heat. The effects of kinetic energy and aerodynamic heating are negligible from all of the fluxes (Lozowski et al., 2000). Strub et al. (2003) demonstrated that the phase transition from a supercooled liquid droplet to solid is influenced by the conduction and convection heat transfer processes as well as the evaporation and sublimation mass transfer phenomena. Naterer (2003) explained the processes of rime/dry ice, transition and combined rime/glaze ice condition and demonstrated the heat conduction equation simultaneously with the mass balance in the ice and unfrozen water layers, including incoming water droplets. Madejski (1976) hypothesized that solidification occurs after the completion of spreading. Furthermore, the author assumed that the splat looks like a disc and it has a constant thickness and a time dependent diameter. Bennett and Poulikakos (1994) and Kang et al. (1994) also explained the prediction. The researchers illustrated that freezing starts only after the completion of droplet spreading, and the splat has the form of a disc. Yang et al. (2011) described the instantaneous and non-instantaneous freezing. The instantaneous freezing appeared when the temperature of the impinging droplet is below –4 °C and the metal surface temperature

is below –20 °C. The non-instantaneous freezing occurred when the droplet temperature is above –4 °C and the metal surface temperature is above -20 °C.

Ryerson (2011) discussed ice protecting chemicals and coating facilities for the safety functions of offshore platform operations. The chemicals include sodium chloride, calcium chloride, magnesium chloride, calcium magnesium acetate, potassium acetate, sodium acetate, and so on. These chemicals are compared to each other based on their performance and low corrosion potentials. Furthermore, the author suggested that coatings should be applied to wet areas and must be investigated before applying to decks, stairs and work areas. Dryden et al. (1985) claimed that in steady state case, the effect of the coating is primarily dependent on the relative thermal properties of the coating and the substrate. To investigate the delayed freezing process, Boinovich et al., (2014) conducted some experiments on various (hydrophilic, hydrophobic and superhydrophobic) coated surfaces. The authors showed that the longest freezing delay was observed in the superhydrophobic coating on the aluminum substrate. However, during the test, the authors considered a supercooled sessile water droplet under isothermal conditions. Huang et al. (2012) discussed the effect of contact angle on water droplet freezing for a series of hydrophobic substrates. Their experimental investigations suggested that a longer contact angle causes a longer freezing time. Ou et al. (2015) conducted some experimental studies on the sessile droplet freezing and ice adhesion on different wettable aluminum surfaces, and concluded that superhydrophobic surface could retract sessile droplet freezing and lower the ice adhesion strength. Zhang et al. (2017c) conducted some experimental studies on 10, 20 and 30 μL sessile water droplets with consideration of the supercooling effect.

The authors suggested that the final droplet profile is less dependent on the amount of supercooling because it is less influenced by the freezing rate.

This chapter provides experimental results that have been analyzed to determine the droplet dynamics and freezing time of fresh and salt water droplets on various cold, dry surfaces. Droplet dynamics are determined by examining the contact angle, spreading patterns and spreading radius on various substrates. Different droplet diameters and fluid properties have been analyzed during the test. Furthermore, the effect of atmospheric temperatures has also been examined in this study. The timescales to initiate and complete freezing are examined. Lastly, the current research studies the impact of various factors, such as the effects of fluid properties, substrate materials, droplet diameter and atmospheric temperature on the freezing process.

6.2 Contact Angle Measurements

The contact angle is an important parameter that describes the wettability of a solid surface (Gajewski, 2008; Yuan and Lee, 2013; Yue et al., 2016). Additionally, it plays an important role in heat and mass (Prajitno et al., 2016). Small contact angles (0 - 90°) characterize hydrophilic or wetting surfaces, where the liquid spreads across the surface (Bernardin et al., 1996; Gajewski, 2008; Prajitno et al., 2016; Sommers et al., 2017). High contact angles (90 - 140°) characterize hydrophobic or non-wetting surfaces, where the droplet substrate interactions are weak and the liquid beads up on the solid surface (Bernardin et al., 1996; Gajewski, 2008; Prajitno et al., 2016; Sommers et al., 2017). The static contact angle is an important parameter for modelling the droplet dynamics. The value of the static angle changes during droplet spreading and becomes the dynamic contact

angle. The magnitude of the apparent dynamic contact angle changes during its advancing (larger values) or receding periods (smaller values). Further, the liquid lamella rim develops as either thick, when the center begins to rise, or thin, when the central liquid column decreases. The difference between advancing and receding contact angles defines the contact angle hysteresis (Gajewski, 2008; Hu et al., 2015; Lafuma and Quéré, 2003; Milne and Amirfazil, 2009; Mohammadi, 2016). Larger contact angle hysteresis values are associated with lower droplet mobility and therefore higher water retention (Sommers et al., 2017).

The wetting properties such as water contact angle (CA) and contact angle hysteresis (CAH) were examined by an OCA 15EC video-based optical contact angle measuring instrument. Contact angles were measured by the sessile-droplet method where the water droplet delivered was gently placed onto the respective substrate, and its shape was analyzed by using the goniometer optics and SCA 20 software. The droplet shapes were recorded every two seconds. A Hamilton 500 µl syringe was used to supply the droplet. A minimum of five measurements at different locations was recorded for static contact angle measurement for each substrate. All the measurements were taken at room temperature. Figure 6.1 describes the contact angle measurement set-up.

Table 6.1 describes the details of the measured wettability of all test samples. The results demonstrate that the contact angle varies with substrate properties. One of the possible reasons is the surface energy. Prajitno et al. (2016) concluded that the contact angle value depends on surface roughness.

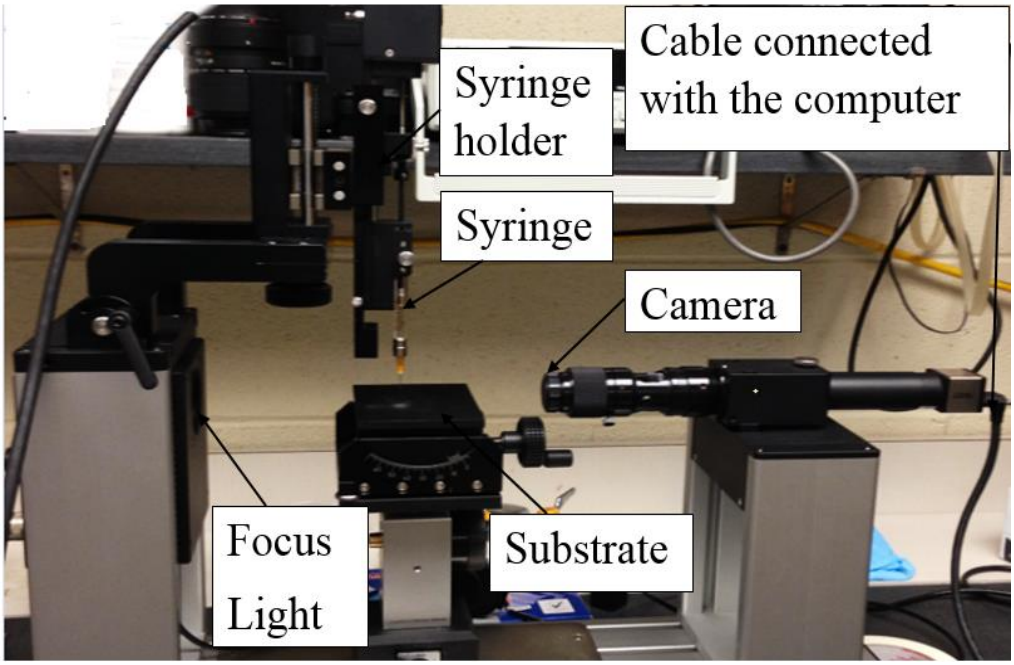

Fig. 6.1 Experimental set-up of contact angle measurement.

The magnitudes of the static contact angles are different for fresh and salt water droplets. Salt concentration in a water droplet changes the contact angle on hydrophilic substrates (Sghaier et al., 2006). Figure 6.2 shows the experimental data for the static contact angle, tested on a 990 polyurethane epoxy substrate at a room temperature of 18 °C. The measurement was conducted immediately after the droplet impact spreading on the substrate. The magnitude of the static contact angle was calculated by means of a video-based computational software called SCA 20. This software analyzed the droplet shape (measuring range 1- 180°) by means of a sessile drop method. In the current study, a total of five numbers of repetitive measurements were conducted to minimize the error of attaining the static contact angle. The graphical plot of Fig. 6.3 reported that the measured data were mostly uniform, and the average value was considered.

Table 6.1 Details of static contact angles on test substrates.

Substrate details	Static angle (°)	
	Fresh water	Salt water
Bare aluminum 6061 with typical surface finish	71.34	71.85
Bare steel with typical surface finish	44.3	70.0
Sand blasted steel	83.61	82.71
Sand blasted steel with intershield 300 aluminum epoxy	74.97	73.9
Sand blasted steel with aluminum epoxy and intershield 300 bronze epoxy	69.24	69.23
Sand blasted steel with aluminum epoxy, bronze epoxy and interbond 201 green epoxy	79.5	76.85
Sand blasted steel with aluminum epoxy, bronze epoxy and interthane 990 part A polyurethane	74.08	78.86
Sand blasted with amerlock epoxy coating	69.8	77.37

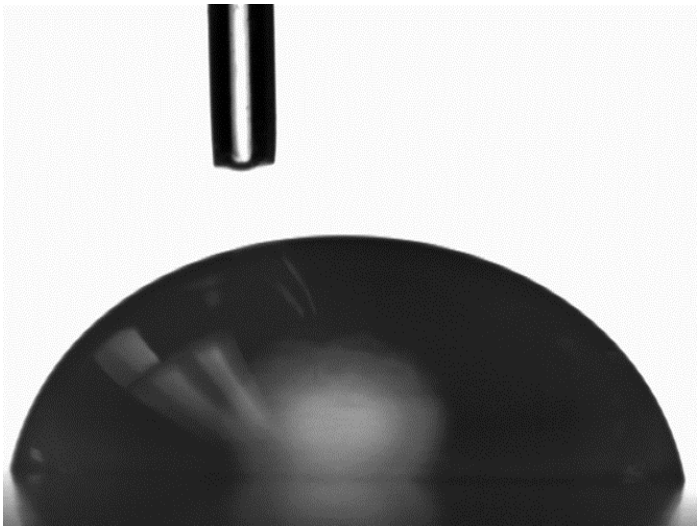

Fig. 6.2 Sample of static contact angle test of a salt water droplet.

Figure 6.4 shows the experimental data for the dynamic contact angle test of salt water on an interbond 201 green epoxy substrate at a room temperature of 18 °C. The test was conducted immediately after the droplet impact. The needle was used to pin the droplet for obtaining the advancing and the receding contact angle data. The graphical data is presented in Fig. 6.5. It is observed that the data are initially non-uniform, however, after a certain period, they become uniform and smooth. Current work considered the uniform result.

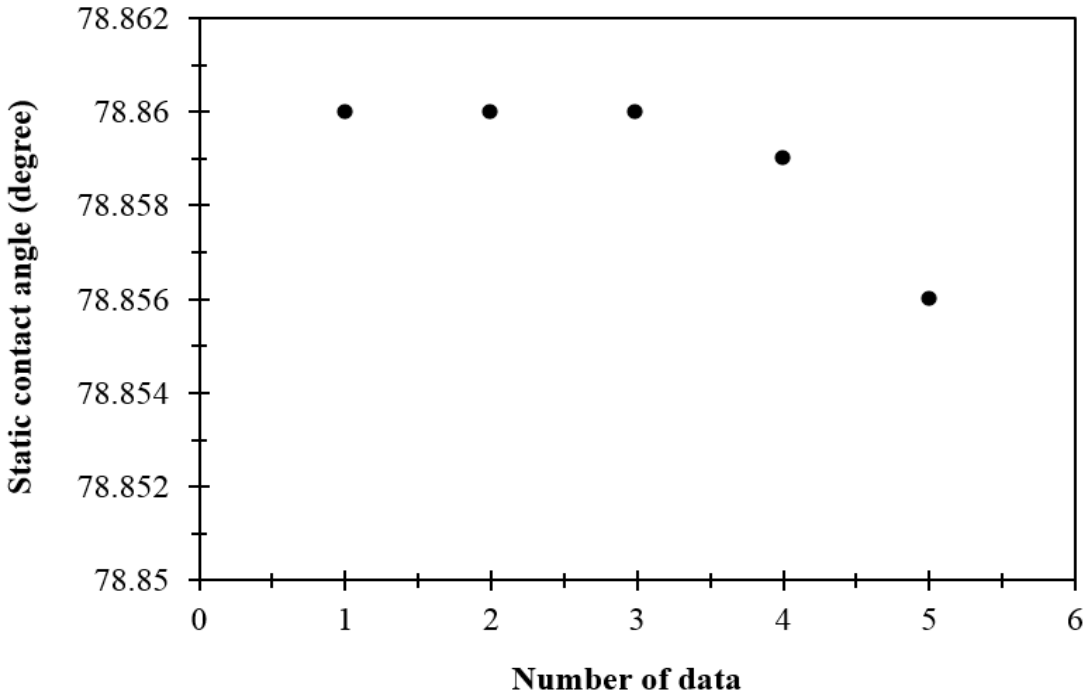

Fig. 6.3 History of static contact angle measurements.

Table 6.2 illustrates the magnitude of advancing and receding contact angle on various substrates. It is observed that the advancing and receding contact angles are different for different substrates. Furthermore, the magnitudes are different for both fresh

and salt water droplets. Possible causes are surface energy, spreading behavior and the chemical impurities of the liquid.

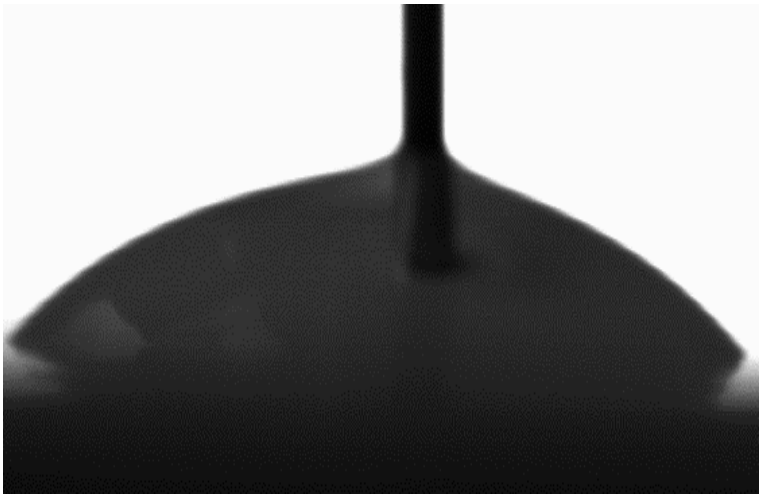

Fig. 6.4 Sample of dynamic contact angle test of a salt water droplet.

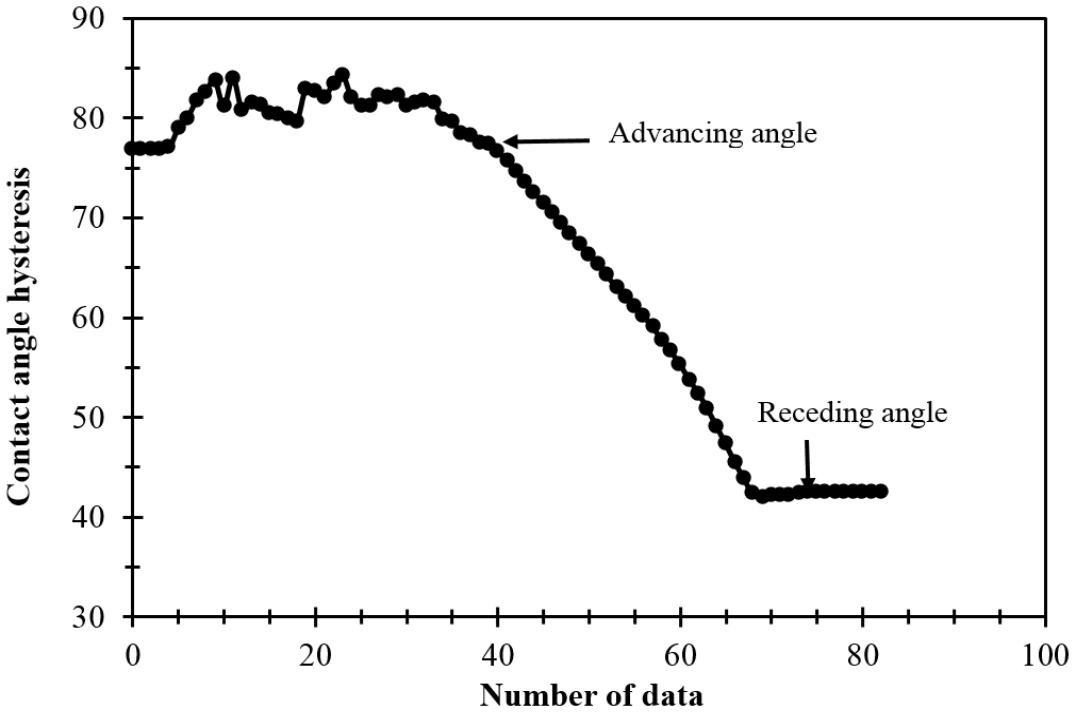

Fig. 6.5 Contact angle hysteresis of a salt water droplet.

De Gennes (1985) concluded that the advancing and receding contact angle hysteresis is attributed to the substrate's morphology; such as surface roughness and chemical heterogeneity. Furthermore, Bernardin et al. (1997) explained that the contact angle is highly influenced by the surface finish and the presence of impurities on the surface of both fluid and solid.

Table 6.2 Details of advancing and receding contact angles on test substrates.

Substrate details	**Fresh water**		**Salt water**	
	Advancing angle (°)	**Receding angle (°)**	**Advancing angle (°)**	**Receding angle (°)**
Bare aluminum 6061 with typical surface finish	74.26	30.16	74.82	32.22
Bare steel with typical surface finish	58.75	25.29	58.16	24.02
Sand blasted steel	85.24	32.47	85.39	36.64
Sand blasted steel with intershield 300 aluminum epoxy	77.85	41.09	74.85	40.59
Sand blasted steel with aluminum epoxy and intershield 300 bronze epoxy	72.02	38.45	86.99	35.75
Sand blasted steel with aluminum epoxy, bronze epoxy and interbond 201 green epoxy	80.41	35.92	76.92	42.54
Sand blasted steel with aluminum epoxy, bronze epoxy and interthane 990 part A polyurethane	77.13	35.37	78.90	41.11
Sand blasted steel with amerlock epoxy coating	71.21	36.09	78.21	48.91

Since the dynamic contact angle variations for both fresh and salt water droplets are minimal, the current investigation predicted that the substrate morphology is the main factor that controls the dynamic contact angle hysteresis.

6.3 Droplet Dynamics

When a droplet impacts, it deforms, spreads and recoils. Later, after a certain period, the droplet obtains its final shape. These phenomena are commonly known as droplet dynamics. Table 6.3 illustrates the pre-impact velocities of various droplets.

Table 6.3 Details of pre-impact velocities. Reynolds and Weber numbers.

Droplet diameter (mm)	**Fresh water**			**Salt water**		
	Velocity (ms^{-1})	**Weber number (*We*)**	**Reynolds number (*Re*)**	**Velocity (ms^{-1})**	**Weber number (*We*)**	**Reynolds number (*Re*)**
3	3.91	6548	607	3.92	6044	618
4	3.99	8910	842	4.00	8223	858
5	4.04	11277	1079	4.04	10381	1094

Figure 6.6 illustrates the sequential images of a 5 mm salt water droplet impinged onto sand blasted steel with aluminum epoxy, bronze epoxy and interthane 990 part A polyurethane substrate at an ambient temperature of -15 °C.

The first image in the sequence represents the initial spherical droplet before it impacts. Just after the impact, the droplet has begun to spread, flatten and deform (2nd photograph). As the spreading continues, it is observed in the 3rd photograph that the periphery of the droplet looks slightly thicker than the center of the droplet. At this point,

the initially spherical droplet appears to be a “disk” of water with a somewhat thicker and bumpier circumferential “ring”. The disk continues to spread until it reaches its maximum spread outsize. However, this shape in the third photograph of the sequence does not represent the final shape of the droplet. Due to the effect of surface tension force and the receding contact angle, the spreading disk starts to recoil on the surface. The fourth photograph of the sequence represents the final shape of the droplet onto a coated cold surface.

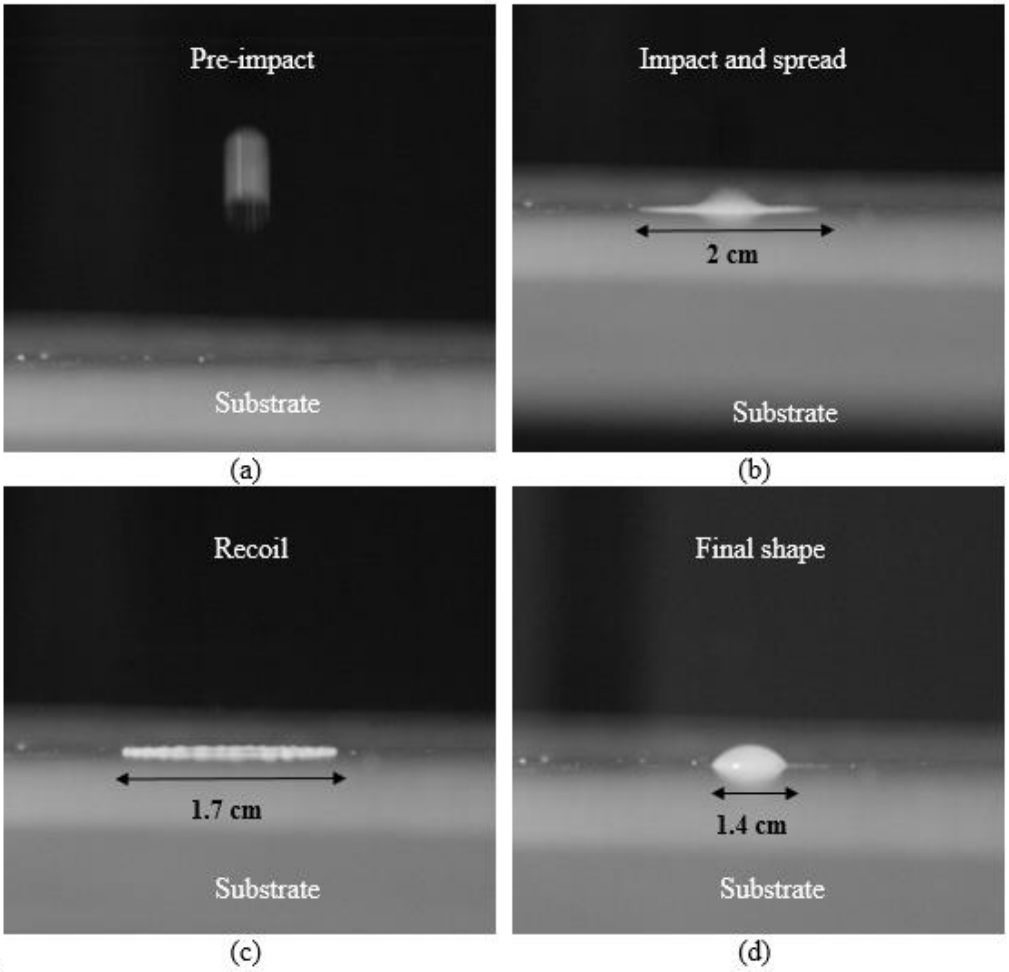

Fig. 6.6 Sequential images of droplet dynamics onto an epoxy coated substrate.

For comparison with the spreading of a droplet on a bare surface, Fig. 6.7 shows the sequential images of a 5 mm salt water droplet impinged onto a bare aluminum substrate at an ambient temperature of -15 °C.

The first photograph in the sequence represents the pre-impact movement of a free falling droplet. In this case, when the droplet impacts, a splashing is observed (2nd photograph), whereas, it is not observed in the coated surface. Substrate roughness has a significant effect on droplet dynamics (Mundo et al., 1995). Surface roughness promotes droplet breakup (Bernardin et al., 1997; Engle, 1955). Rough surfaces cause prompt splashing on droplet impact (Hao, 2017). In the current case, the surface roughness of bare aluminum and 990 Polyurethane substrates are 0.62 µm and 0.43 µm, respectively. Liu et al. (2010) reported that splashing is a function of surface roughness and droplet liquid properties.

Mohammadi (2016) speculated that every aspect of droplet's dynamics is strongly related to parameters such as droplet liquid properties and surface morphology. Furthermore, on the aluminum surface, the peripheral ring appears less thick than the coated surface, and due to high thermal conductivity, the peripheral motion of the droplet arrests during the recoiling stage (3rd photograph). Hence, the last photograph in this sequence represents a thin and flat layer of ice, whereas, on the coated surface the equilibrium or the final shape of the droplet appears somewhat as a "hemispherical" profile. Fukumoto et al. (2011) reported that disk-shaped splat can be attributed essentially to good contact at splat-surface interface, in other words, good wetting condition. However, these differences illustrate that the coating properties have a substantial effect on spreading

diameter and final droplet shape, which is of particular importance.

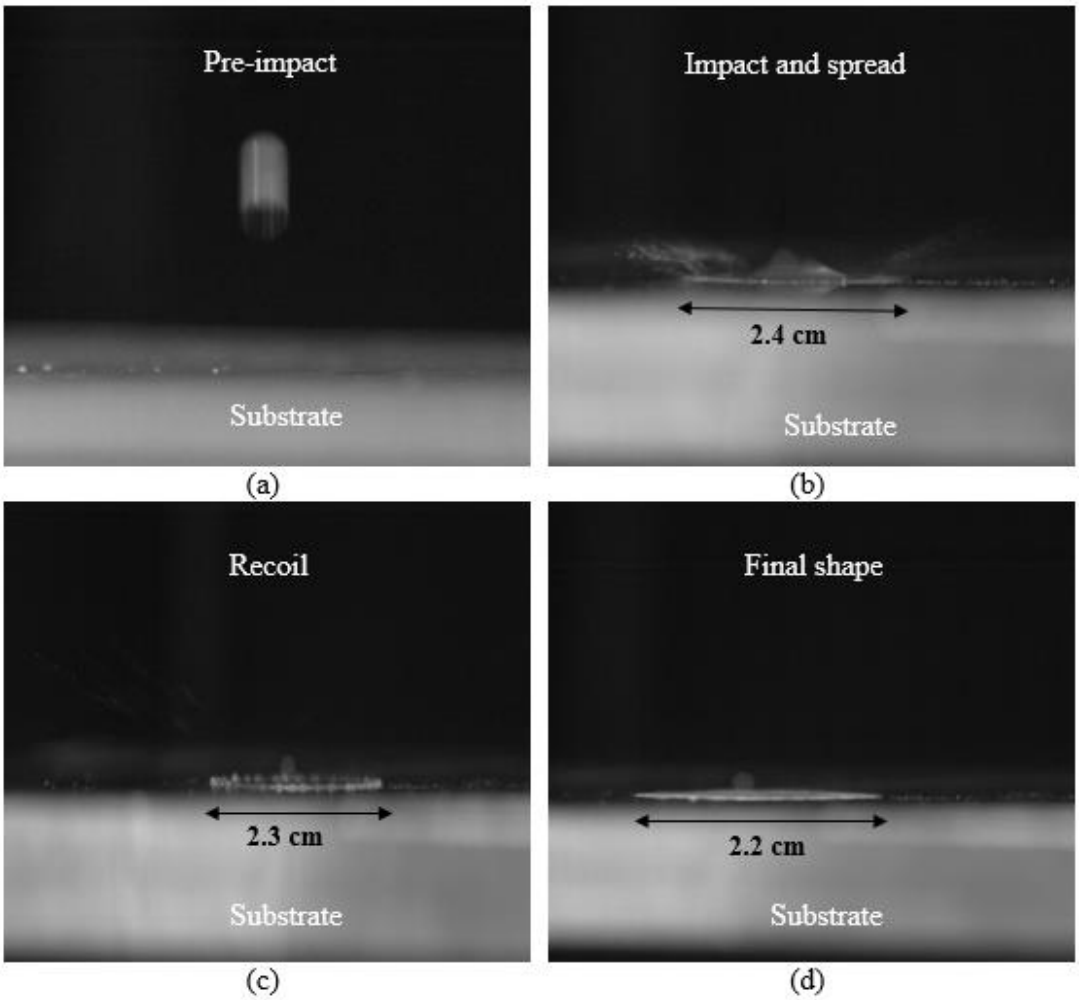

Fig. 6.7 Sequential images of droplet dynamics onto a bare aluminum substrate.

Figure 6.8 represents the experimental result of the final shape and size of 5 mm salt water droplets impacting on various substrates at an air temperature of -18 °C. Depending on the substrates, the frozen droplets look flat and smooth, with a high bead and donut (depression in the center) like shape. For instance, in the 201 green epoxy coated substrate, the final shape of the impinged droplet looks like the donut shape, which is

depressed in the middle. In the 990 polyurethane and the amerlock coated substrates, the final droplet has a high bead in the center, and in the bare aluminum substrate, the final droplet looks very flat and smooth. Possible causes are substrate materials and thermophysical properties, and droplet spreading time. Yang et al. (2011) suggested that the freezing patterns of water droplets are dependent on the properties of substrate materials.

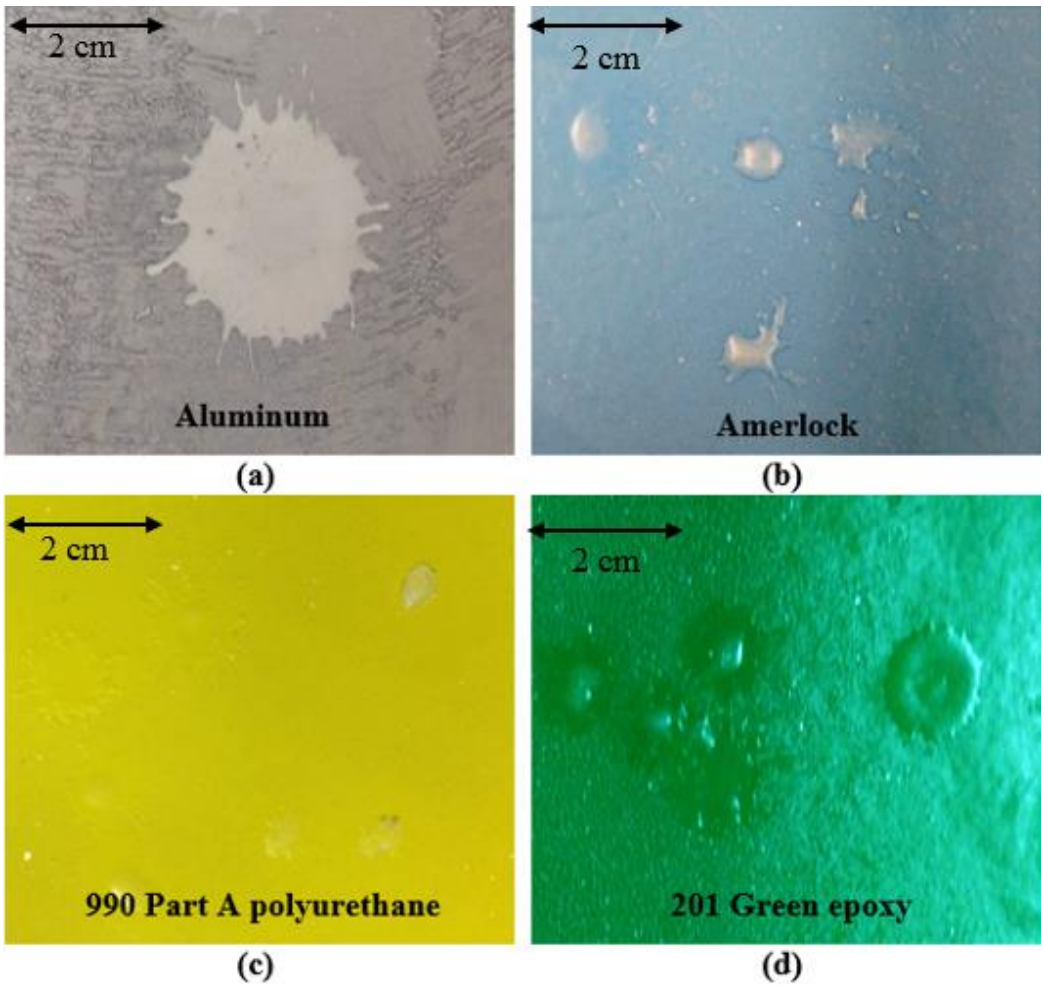

Fig. 6.8 Experimental results of final droplet shape on various cold substrates.

6.4 Dimensionless Analysis on Droplet Dynamics[7]

Spray arising from an ocean or lake surface travels a relatively short distance compared to, e.g., rainfall. As a droplet falls, it accelerates but does not attain a terminal velocity. The unsteady motion of the drop can be characterized by considering the balance between gravitational and drag forces.

$$ma = mg - \frac{1}{2} C_D \rho_a A_p V^2 \tag{6.1}$$

where m is the mass of the droplet, a is the acceleration of the droplet, g is acceleration due to gravity, C_D is the drag coefficient, ρ_a is the density of the ambient air, and A_p is the projected area. It can be arranged as a differential equation

$$m\frac{dV}{dt} + \frac{C_D \rho_a A_p}{2} V^2 = \mathrm{mg} \tag{6.2}$$

Notably, since the drag term is small for very low velocities, the velocity can be scaled by

$$V_0 \sim gt \tag{6.3}$$

For long times, the droplet reaches a terminal velocity

$$V_{term} = \sqrt{\frac{2mg}{C_D \rho_a A_p}} \quad t \to \infty \tag{6.4}$$

Between the two limits, Eq. 6.2 has an exact solution (Ritger and Rose, 2000)

$$V(t) = \sqrt{\frac{2gm}{C_D \rho_a A_p}}\ tanh\left(t\sqrt{\frac{C_D \rho_a A_p g}{2m}}\right) \tag{6.5}$$

with Eqs. 6.3 and 6.4 as asymptotes. The ratio of V_0 *to* V_{term} provides dimensionless time

[7] This section is produced by Dr. Lisa Lam, Postdoctoral Fellow.

$$\frac{V_0}{V_{term}} \sim t\sqrt{\frac{C_D \rho_a A_p g}{2m}} \sim \tilde{t} \tag{6.6}$$

and dimensionless velocity is

$$\tilde{V} = \sqrt{\frac{C_D \rho_a A_p}{2mg}} V \tag{6.7}$$

The dimensionless form of Eq. 6.5, $\tilde{V} = tanh(\tilde{t})$, and asymptotes are shown in Fig. 6.9.

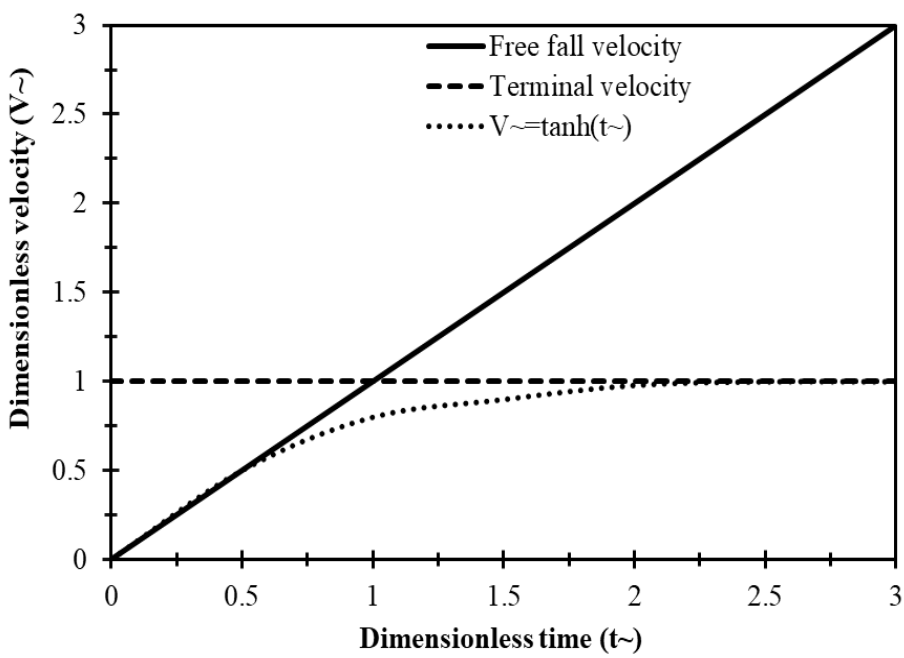

Fig. 6.9 Plot of exact solution and asymptotes for free falling body.

The dimensionless time is an indicator of whether the pre-impact drop velocity falls within the realm of "short" time when $\tilde{t} << 1$ or "long" time when $\tilde{t} >> 1$. For $\tilde{t} \sim O(1)$, as is the case here, Eq. 6.5 applies.

The shapes of the droplets were experimentally observed in frames just prior to impact, and the widths were measured. The pre-impact drop appeared to be round, with the

width unchanged from that of the initial release. Therefore, the projected area for scaling is considered circular with a diameter of $d_e = (6\mho/\pi)^{1/3}$. Clift et al. (2005) provide a discussion of drag on spheres and correlations for C_D based on experimental data. For $260 \leq Re_d \leq 1500$

$$log_{10}\, C_D = 1.6435 - 1.1242 log_{10}(Re_d) + 0.1558[log_{10}(Re_d)]^2 \tag{6.8}$$

where $Re_d = (\rho_a V d_e)/\mu_a$ is the Reynolds number of the falling drop, and μ_a is the dynamic viscosity of the ambient air. For $1500 \leq Re_d \leq 1200$

$$log_{10}\, C_D = -2.4571 + 2.5558\, log_{10}(Re_d) - 0.9295[log_{10}(Re_d)]^2 + 0.1049[log_{10}(Re_d)^3 \tag{6.9}$$

The velocity is found by first finding the time to impact, t_i, which is taken from

$$s(t) = \frac{2m}{C_D \rho_a A_p}\, ln\left[Cosh\left(t\sqrt{\frac{C_D \rho_a A_p g}{2m}}\right)\right] \tag{6.10}$$

where $s(t) = 0.9$ m is the distance traveled for the cases considered here. Using the distance to impact, the Equation (6.10) is solved for t. The pre-impact velocity is calculated by iterative calculations of velocity, Re_d, C_D, and t_i. After two iterations, the value of velocity did not change within three decimal places. Air viscosity and density values vary with temperature but do not vary with relative humidity when the air temperature is below 0 °C (Tsilingiris, 2008). Tables 6.4 and 6.5 list the dimensionless impact times, Reynolds numbers, drag coefficients and pre-impact velocities for freshwater and saltwater droplets in the air at T_{air} = -15 °C and T_{air} = -18 °C.

The pre-impact velocity of the water droplet was estimated experimentally by observing two consecutive frames just prior to impact, and found to be in good agreement with scaled results.

Table 6.4 Dimensionless time, pre-impact Reynolds number, drag coefficient and velocity for fresh water droplets in air at -15 and -18°C.

Droplet diameter (mm)	**Dimensionless time ($\tilde{t}$)**	**Pre-impact**			
		Reynolds number		**Drag coefficient, C_D**	**Velocity, V (ms^{-1})**
		$Re_{d,-15}$	**$Re_{d,-18}$**		
3	0.57	975	986	0.47	3.89
4	0.48	1328	1344	0.45	3.97
5	0.42	1686	1700	0.43	4.02

Table 6.5 Dimensionless time, pre-impact Reynolds number, drag coefficient and velocity for salt water droplets in air at -15 and -18°C.

Droplet diameter (mm)	**Dimensionless time, ($\tilde{t}$)**	**Pre-impact**			
		Reynolds number		**Drag coefficient, C_D**	**Velocity, V (ms^{-1})**
		$Re_{d,-15}$	**$Re_{d,-18}$**		
3	0.59	983	994	0.47	3.92
4	0.45	1335	1352	0.44	3.99
5	0.39	1688	1708	0.43	4.04

Post-impact spread radius

The post-impact droplets spread quickly to a maximum radius, then the amount of retraction on each surface is influenced by the thermal resistance for each case. For shorter

times, the final shape resembles that of a splat with a radius close to that of the maximum. As resistance increases, time to freeze increases, allowing more retraction and resulting in smaller final radii.

The maximum spread radius is approximated using the relation from Pasandideh-Fard et al. (1996) for We » 12

$$\xi_m \sim 0.5 Re_{d,l}^{1/4} \tag{6.11}$$

where $\xi_m = r_{s;m}/r_d$ is the spread factor based on the maximum spread radius, $r_{s,m}$, and $Re_{d,l} = \rho_l r_{s,m} V/\mu_l$ is the Reynolds number of the pre-impact drop based on the liquid properties. Maximum spread radii were observed in the camera footage and match closely with Eq. 6.11. For the uncoated metal, the time to freeze was much smaller than the time to spread, and the droplet's final radius was close to that of Eq. 6.11. For scaling purposes, the radius on coated metals is approximated by

$$r_s \sim C_2 r_{s,m} \tag{6.12}$$

where C_2 is a scale factor.

6.5 Determination of Thermophysical Properties

The density of the epoxy materials was measured in the Memorial University of Newfoundland (MUN) engineering laboratory. The thermal conductivity test was performed at Dalhousie University. To minimize the error, a repeatability study was conducted. At least three measurements were performed for each sample and the average value was considered. The authors wish to thank Michel Johnson (Department of Chemistry and Clean Technologies Research Institute at Dalhousie University) for conducting the test, as well as acquisition and interpretation of the PPMS data. The specific

heat was determined in the chemistry laboratory of Memorial University of Newfoundland (MUN). A Toledo DSC1 Differential Scanning Calorimeter was used to measure the specific heat. STARe Excellence software version 9.20 was used to analyze the measured data.

Table 6.6 Details of thermophysical properties of test substrates.

Substrates	**Density ($kg.m^{-3}$)**	**Specific heat ($J.kg^{-1}.K^{-1}$)**	**Thermal conductivity ($W.m^{-1}.K^{-1}$)**
Bare aluminum 6061	2712	870	204
Bare steel	8000	490	45
Intershield 300 aluminum epoxy	1170	0.4094	0.6586
Intershield 300 bronze epoxy	1115	0.17643	0.7265
Interbond 201 green epoxy	1075	0.3664	0.5676
990 part A polyurethane	1080	0.5388	0.3858
Amerlock epoxy	1420	0.118	0.4685

Using the method proposed by Kline and McClintock (1953), the measurement uncertainties are determined. A sample calculation is presented. An expression for experimental specific heat is:

$$C_p = \frac{HF}{M\eta} \tag{6.13}$$

where C_p is the specific heat, HF is the heat flow rate, M is the mass of the measuring object, and η is the heating rate. Now, the quantities of interest are (Mettler Toledo DSC1 manual):

$$\partial C_{p_{error_experiment}} = \sqrt{\left(\frac{\partial C_p}{\partial HF}\partial HF\right)^2 + \left(\frac{\partial C_p}{\partial M}\partial M\right)^2 + \left(\frac{\partial C_p}{\partial \eta}\partial \eta\right)^2} \quad (6.14)$$

where ∂HF= ∂M=∂η= are assumed as 0.1% and by calculation $\frac{\partial C_p}{C_p} = 0.17$ which is very small uncertainty and can be neglected. Similarly, the uncertainties obtained from density and thermal conductivity is less than unity and can be neglected. Table 6.7 represents the thermophysical properties of fresh and saltwater ice. It is observed that the fresh water ice properties are very different from the saltwater ice properties. Furthermore, the authors (Dehghani et al., 2018) assumed that the fresh saltwater is also different than "old" saltwater. The brine content is one of the main properties to influence this phenomenon.

Table 6.7 Thermophysical properties of ice and salt water ice (Cox and Weeks, 1975; Dehghani et al., 2018; Weeks, 2010).

Properties	Salt water ice	Fresh water ice
Cp ($J.kg^{-1}.K^{-1}$)	6319	2102
K ($W.m^{-1}.K^{-1}$)	2.10	2.26
ρ ($kg.m^{-3}$)	928	917

6.6 Normal Freezing Process

Normal freezing occurs when the tested material changes its phase at its specific value (Alexiades and Solomon, 1993), for instance, 0 °C for pure water and -2 °C for saltwater (Alexiades and Solomon, 1993; IMO, 2011; Mintu et al., 2016).

Figure 6.10 illustrates the phase change process of a 3 mm fresh water droplet impacted on an interthane 990 part A polyurethane epoxy coated substrate at an ambient temperature of -18 °C.

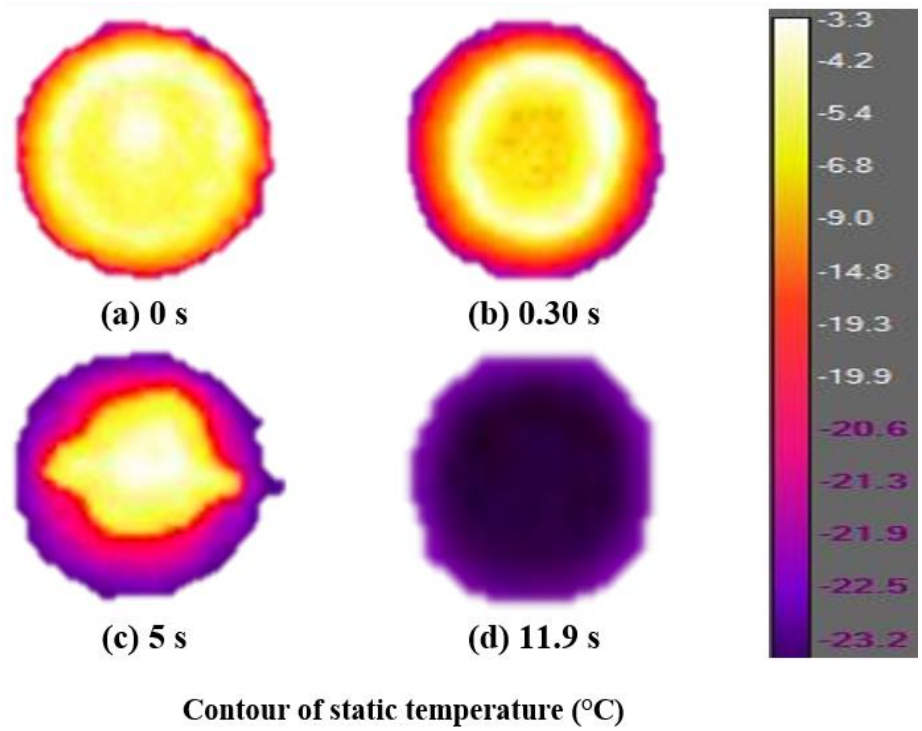

Fig. 6.10 Thermal images of a 3 mm fresh water droplet.

The measurement is conducted immediately after the droplet's impact on the substrate. Due to the smooth and polished surface, the reflectiveness is so high that accurate temperature measurements are not always detected by the infrared camera (Omega). For instance, in Fig. 6.13, the minimum temperature of the legend is displayed -23.2 °C where the actual value is -18 °C. To compensate the resolution error, as suggested by the camera manual (for low temperatures), this experiment used black masking tape (S-2491BL) around the substrate, to adjust the emissivity value, and force the indicator to display the

correct temperature of the material, however, some errors (for example, ±25%) still exist. In the first photograph, the outer edge of the droplet is much colder than the center. As time progresses, the droplet starts to cool and change its phase. The phase change happens from the outer surface to the inner. Finally, the droplet reaches the substrate temperature and appears as a disk-like shape.

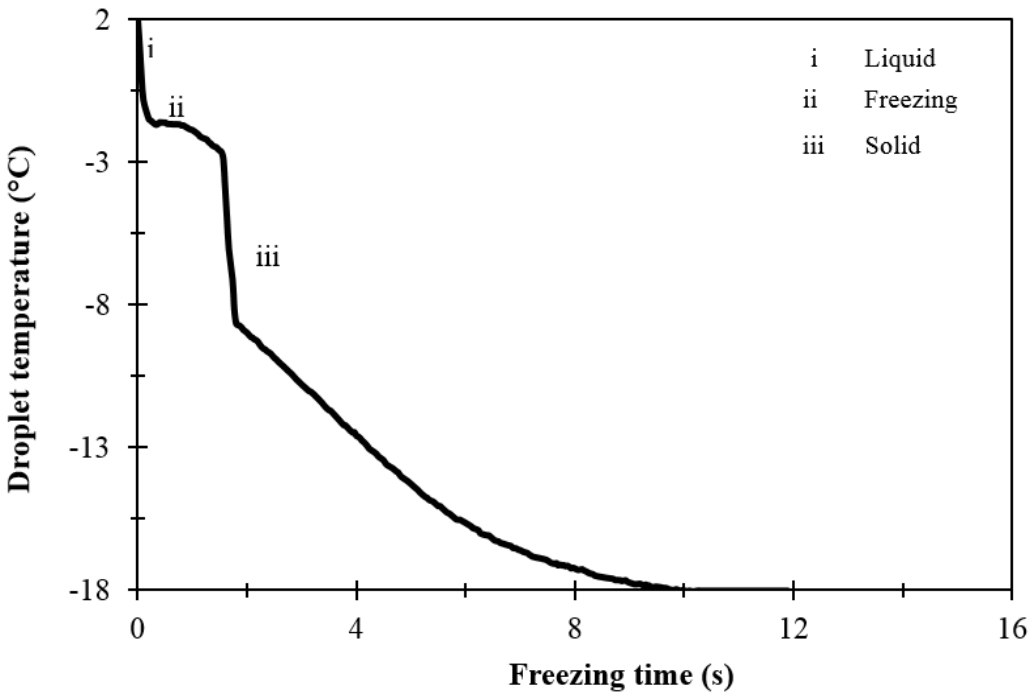

Fig. 6.11 Normal freezing curve of a 3 mm fresh water droplet.

Figure 6.11 illustrates the graphical representation of a normal freezing process of a 3 mm fresh water droplet impacted on an interthane 990 part A polyurethane epoxy coated substrate at an ambient temperature of -18 °C. In this freezing process, there is no recalescence stage (Tanner, 2011). Therefore, the normal freezing process is divided into three stages: the liquid stage (the initial cooling stage of the liquid), the crystallization or

freezing stage and the cooling stage of the solid particle (Alexiades and Solomon, 1993; Tanner, 2011).

In this figure, at the beginning of the liquid stage, the material is at its normal temperature. As soon as the droplet reaches the freezing temperature, the nucleation (and hence the crystallization) starts. In the phase change process, the release of latent energy does not lead to a temperature increment (Tanner, 2011), however; to a significant declination in the droplet's cooling rate. At the end of the freezing process, the ice thickness increases, the increasing ice thickness declines the temperature gradient further, and continues until the droplet freezes completely and reaches the surface temperature.

6.7 Supercooling Effect

Supercooled freezing occurs when the material changes its phase below the phase change temperature (Alexiades and Solomon, 1993). The phenomenon is very common for water (Tanner, 2011). In the current investigations, some supercooling effects were observed. An impinging supercooled droplet suggests an unfrozen metastable layer of liquid; however, in the current situation, the phenomena are not substantial. It is assumed that the high impact force and the circulation effect prevented a layer from forming. Furthermore, the heat transfer rate at the liquid-air interface including these incoming droplets is minimal.

Figure 6.12 illustrates the thermal images of a supercooled 5 mm salt water droplet impacted on an interbond 201 green epoxy coated substrate at an ambient temperature of -15 °C. The measurement was conducted immediately after the droplet impact on the substrate. Due to the emissivity effect of the thermal camera, the display temperature bar

represents a higher value than the actual temperature. For instance, in Fig. 6.12 the minimum temperature of the legend is displayed -21.4 °C, whereas the actual value is -15 °C. To minimize the resolution error, the same black masking tape technique was used during the experiment that is discussed in the previous section.

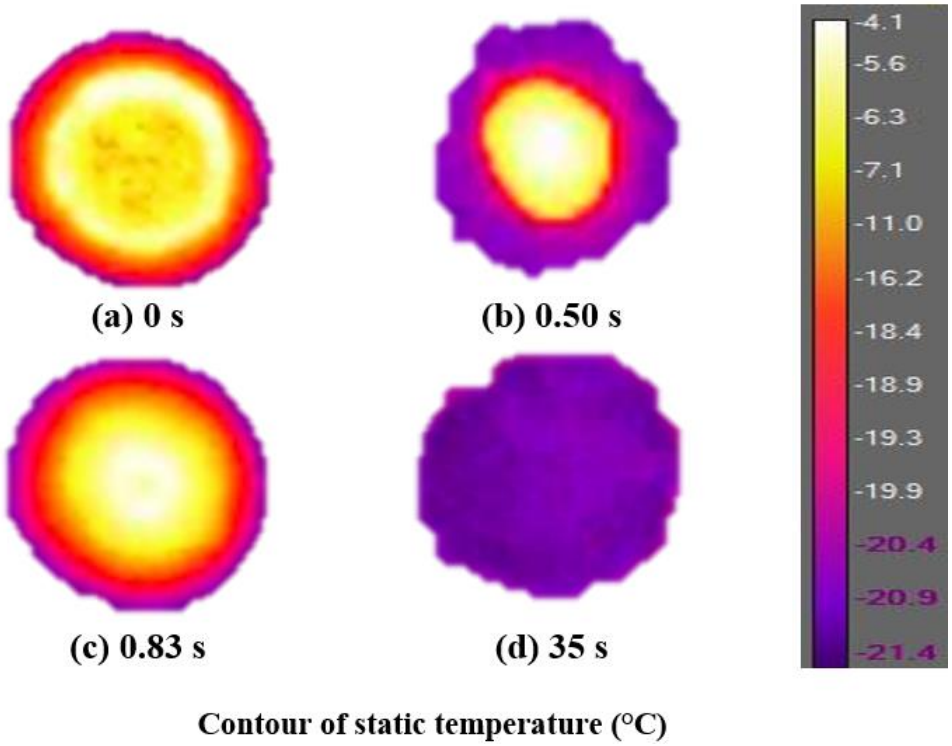

Fig. 6.12 Thermal images of a supercooled 5 mm salt water droplet.

In the first image, it is observed that the center temperature of the droplet is higher than the outer edge temperature. As time progresses, the droplet starts to cool. In the second image, it is found that the droplet is cooling from the outside to the inside. However, in the third photograph, the droplet shows a supercooling effect where the temperature rapidly increases back to the melt temperature when the crystallization does not occur. This can only occur if the latent heat released upon freezing is enough to increase the temperature

to an equilibrium freezing point temperature, i.e. the material was not cooled too much (Alexiades and Solomon, 1993). Furthermore, as time progresses, the water-ice mixture is completing a phase change toward ice. After completely frozen, the droplet's temperature continues to decrease due to the continuous cooling by the cold plate.

Figure 6.13 shows the graphical representation of a supercooling freezing curve for a 5 mm salt water droplet impacted on an interbond 201 green epoxy coated substrate at an ambient temperature of -15 °C.

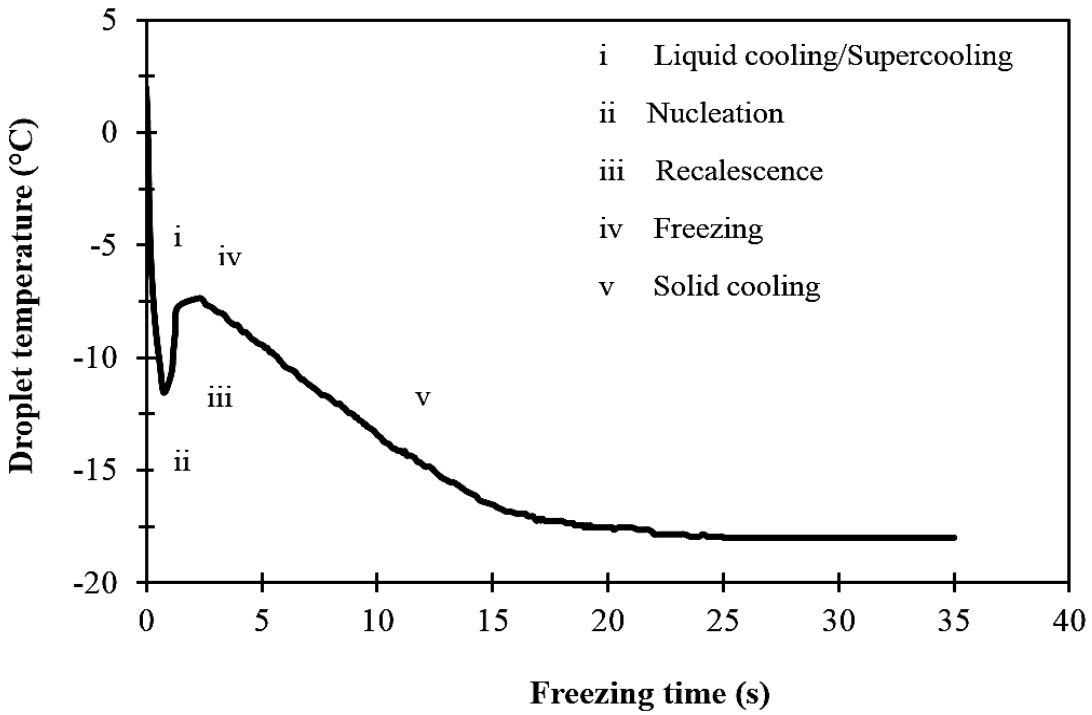

Fig. 6.13 Supercooling freezing curve of a 5 mm salt water droplet.

Supercooling, or undercooling, is the process in which the crystallization of the liquid substance can begin at a temperature that lies far below the material's fusion temperature (Hindmarsh et al., 2003; Tanner, 2011). The supercooling freezing process can be divided into five distinct stages such as: liquid cooling (supercooling), nucleation,

recalescence, freezing and solid cooling (Zhang et al., 2017a, 2017b). From these time stages, the nucleation, recalescence and freezing stages are directly related to droplet freezing (Zhang et al., 2017a, 2017b).

Nucleation is the process in which, at random sites throughout the liquid molecules start clustering in a well-defined way to develop tiny crystals (Herlach et al., 2016; Tanner, 2011). Once nucleation starts, in the recalescence stage, the crystal nuclei drive the rapid crystal growth from the crystal nuclei (Hindmarsh et al., 2003; Sultana et al., 2016; Tanner, 2011; Zhang et al., 2017a, 2017b-c). At the end of the recalescence stage, the material changes into a uniform mixed-phase state, which is comprised of a mixture of ice and water. In this stage, the temperature rises due to the release of energy called latent heat (Tanner, 2011). It was observed that the growth of recalescence temperature was very rapid and highly unrepeatable for other experiments. Chemical impurities of water droplets might induce this phenomenon. It is not observed for fresh water droplets. However, analysis of this unusual phenomenon requires further investigations. Later, the freezing stage occurs when the crystal growth takes place, and continues until the remaining water-ice mixture is completely solidified. At the cooling stage, the solidified droplet cools down to the surface temperature.

In addition to the interbond 201 green epoxy coated substrate, the supercooling effect of a water droplet was also observed for other substrates. Figure 6.14 illustrates the complete summary of the experimental results regarding the supercooling effect. It is observed that the droplets on the epoxy coated substrates exhibit the supercooling effect; however, no supercooling is observed on the bare substrates. One of the primary reasons

for this behavior is the thermal conductance. Thicker epoxy layers transport thermal energy slower. Yang et al. (2011) demonstrated that the influence of droplet freezing speed might be diminished by the reduction of metal conductivity.

The range of initial phase change temperature and time are also dependent on substrate materials. This kind of nucleation or phase change mechanism can be addressed as heterogeneous nucleation, where the nucleation agents are cold substrates (Feuillebois et al., 1995; Hoke, 2000; Jin and Hu, 2010; Jin et al., 2013; Jin et al., 2014; Marín, et al., 2014; Mohammadi, 2016; Sastry, 2005; Snoeijer and Brunet, 2012; Suzuki et al., 2007; Wang et al., 2006; Wu et al., 2007). Furthermore, a lower static contact angle influences the heterogeneous ice nucleation process (Varanasi et al., 2009).

Yang et al. (2011) illustrated that the instantaneous and non-instantaneous freezing of a supercooled water droplet depends on the surface of the metal substrate, ambient air temperature and droplet temperature. The study also demonstrated that there was a supercooling effect observed for salt water, but not fresh water droplets. This phenomenon suggested that chemical impurities such as salinity have a significant effect on the supercooling process.

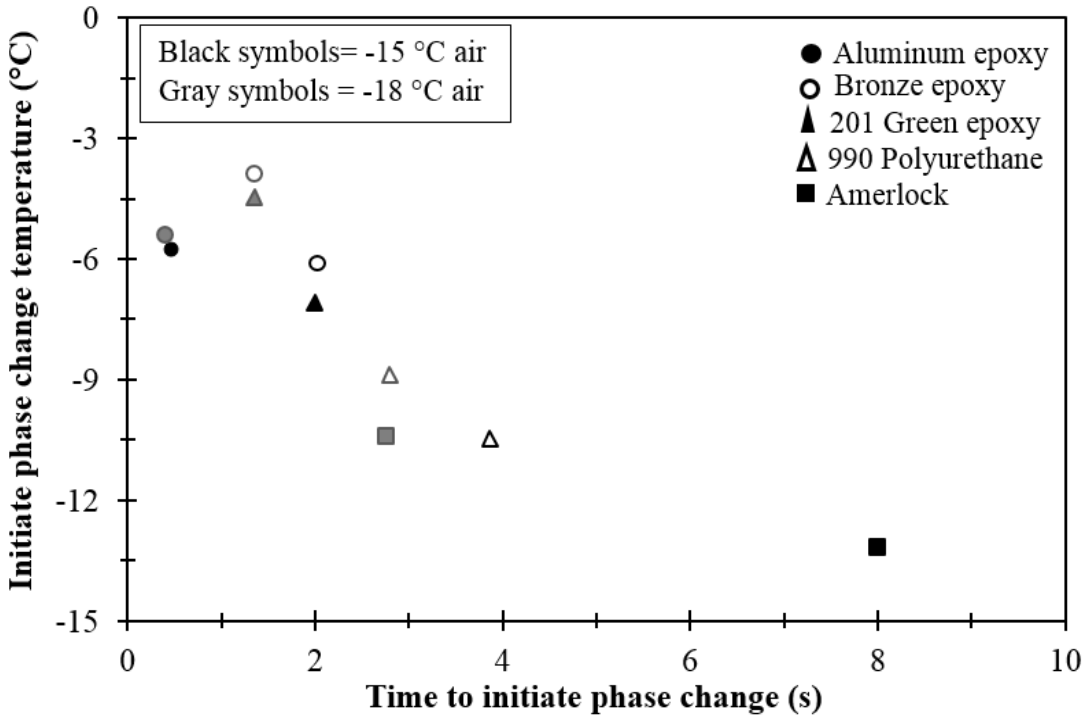

Fig. 6.14 Summary of the supercooling effect of salt water on various substrates.

6.8 Dimensionless Analysis on Droplet Freezing[8]

A water droplet impinging and solidifying on a marine substrate under typical arctic conditions transfers energy to the substrate and the atmosphere through a number of mechanisms. These mechanisms are characterized by using a thermal resistance network between the temperature of the substrate at some depth, the fusion temperature of the drop and the atmosphere.

The primary mechanisms of transferring energy from the atmosphere to the droplet are convection and radiation, and within the droplet are conduction and convection. Under marine conditions, the convection heat transfer coefficient, h_{conv}, is dependent on wind

[8] This section is produced by Dr. Lisa Lam.

velocity with a typical range of 10 to 30 ms^{-1} (Dehghani-Sanij et al., 2017). It is estimated using the local Nusselt number for turbulent flow over a flat plate, $Nu_x = 0.0296Re_a^{4/5}\ Pr_a^{1/3}$ from (Bergman et al., 2011) where *Re* is the Reynolds number of the airflow, and *Pr* is the Prandtl number of the air flow. The heat transfer coefficient is $h = Nu_x k_a/L_c \sim O(10)\ W/m^2K$ where k_a is the thermal conductivity of air, and L_c, is a length of 10 to 30 *m*. Taking the post-impact surface area of the drop as A_s, and using Newton's law of cooling, the energy transfer due to convection from the ambient air $q_{conv} = hA_s\ (T_a - T_d) \sim O(10^{-3})$ Watts, would be $q_{conv} \sim O(10^{-3})\ Watts$ where T_a is the air temperature and T_d is the temperature of the drop. An estimate of the maximum energy added to a droplet in the open air via solar radiation depends on the spread radius and droplet shape, as well as time exposed to sunlight and terrestrial location. Given a solar constant of 700 Wm^{-2}, it would be on the order of 10^{-2} Watts for drops between 3 and 5 mm in diameter.

Under the experimental conditions, the air velocity was small, thus the convection effect on the droplet was negligible. Radiation heat transfer to the droplet is also negligible, as is the temperature difference between the droplet and the walls of the cold room. Energy contributions from convection and radiation are small compared to the latent energy released during solidification and are neglected in the subsequent analysis. Additionally, the contact resistance between a drop and the surface has been studied in the context of molten metal droplet impingement and solidification with values ranging between 10^{-4} to 10^{-6} KW^{-1} (Aziz and Chandra, 2000; Liu et al., 1995). Hence, it is neglected here. Evaporation is often considered negligible under marine conditions due to the typically high ambient relative humidity (Kulyakhtin and Loset, 2011). Lorenzini and Onorio (2013)

observed that when relative humidity is greater than 60%, evaporation drops to zero. Under experimental conditions, the relative humidity was in the range of 65 to 75%; therefore, evaporation between the droplet and the air is not considered in the following analysis.

When the droplet impacts onto the substrate, the energy transfer from the droplet is considered to be the energy required for bulk solidification. The temperature difference between the droplet and the surface drives the energy transfer. Additionally, the kinetic energy that is coming from the impinging droplet is captured in the Reynolds number that is embedded in the thermal resistance due to circulation. In the current work, the temperatures of the pre-impact droplets are close to the fusion temperature, T_f; therefore, energy release due to sensible temperature change is small and less sensitive to the placement of the boundary conditions associated with the droplet's kinetic energy.

From the standpoint of the substrate, the droplet can be considered to be an isothermal source with an average temperature equal to its fusion temperature. Using the resistance network in Fig. 6.15, the solidification time can then be scaled by the thermal resistance.

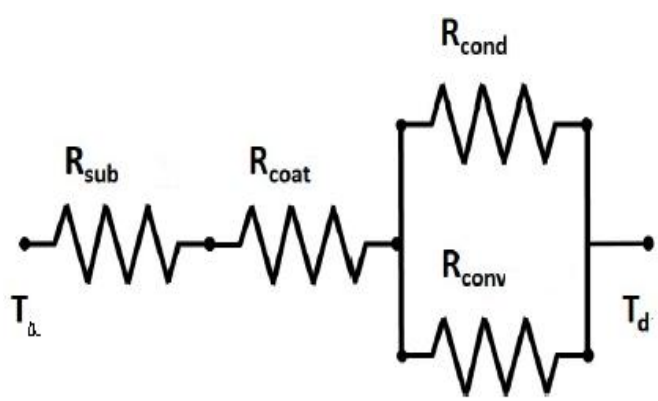

Fig. 6.15 Simplified schematic of thermal resistance network.

The time to freeze can be estimated by setting the rate of energy released from the drop equal to the rate of the energy transfer through the drop and substrate.

$$Q_l = Q_{d,s} \tag{6.15}$$

Considering the energy released during solidification to be the latent heat of fusion, the heat rate out of the drop is scaled by $Q_l \sim \rho \square H_f/t_f$ where ρ is the density based on average properties of the liquid and solid states at T_f , $\square = 4/3\pi r^3_d$ is the volume of the pre-impact drop, H_f is the latent heat of fusion, and t_f is the time to freeze. The rate of energy transfer through the drop to the substrate can be expressed in terms of thermal resistance as $Q_{d,s} = \Delta T/\bar{R}_{total}$ where ΔT is the temperature difference between the average temperature of the drop, which is it's the fusion temperature, and the substrate temperature, T_s, at some semi-infinite distance below the surface. The total average thermal resistance, $\bar{R}_{total}$ is the sum of the average resistance in the drop, $\bar{R}_d$ and the average resistance in the surface $\bar{R}_s$.

$$\overline{R_{total}} = \overline{R_d} + \overline{R_s} \tag{6.16}$$

Thermal resistance and time are rendered dimensionless using the square root of the contact area between the drop and the surface as the length scale, $L_c = \sqrt{A}$. Dimensionless time is $Fo_{\sqrt{A}} = \alpha t/\pi r^2_s$ where α is the average thermal diffusivity of the liquid and solid states at the fusion temperature and $R^*_{\sqrt{A}} = Rk\sqrt{\pi} r_s$

Rearranging Eq. 6.15, the dimensionless time to freeze, $Fo_{\sqrt{A},f}$, can be expressed as

$$Fo_{\sqrt{A},f} \sim C_1 \frac{\overline{R^*_{\sqrt{A},total}}}{\sqrt{\pi}\xi^3 St} \tag{6.17}$$

where St is the Stefan number and $\xi = r_s/r_d$ is the spread factor.

Thermal resistance within droplet

In order to find the thermal resistance to energy transfer within the drop, conduction and convection are considered to work in parallel,

$$R_d = \left(\frac{1}{R_{conv}} + \frac{1}{R_{cond}}\right)^{-1} \tag{6.18}$$

where R_d is the thermal resistance between the temperature of the surface and the average temperature of the drop, R_{cond} is the thermal resistance due to conduction and R_{conv} is the thermal resistance due to convection. The length scale for transient conduction into the drop is $L_c \sim \sqrt{\pi \alpha t}$ (Nellis and Klein, 2008). Resistance due to transient conduction can be represented by $R_{cond} \sim \sqrt{\pi \alpha t}/(kA)$ where $A = \pi r_s^2$ is the contact area between the drop and the surface. Convection within the droplet enhances energy transfer. Schiaffino and Sonin (1997) categorized droplet deposition based on Weber number, $We = \rho V L_c/\sigma$, and Ohnesorge number, $Oh = \mu/\sqrt{\rho \sigma L_c}$. For a high Weber number and low Ohnesorge number, which is the case here, the spreading process is categorized as "inviscid and impact driven". Most of the spreading occurs in a short period and is driven by the dynamic pressure of impact. The impact velocity and drop size characterize the velocity of spread, and over a short time, viscous effects can be neglected (Schiaffino and Sonin, 1997). For external laminar flow and Prandtl number » 1, the Nusselt number, may be scaled by $Nu \sim Pr^{1/3}\sqrt{Re}$ (Jiji, 2009) where $Pr = \upsilon/\alpha$. The convection heat transfer coefficient (considering the flow over a flat plate) then takes the form

$$h \sim \frac{kNu}{L_c} \sim \frac{kPr^{1/3}\sqrt{Re_r}}{r_s} \tag{6.19}$$

where the spread radius, r_s, is the characteristic length scale for convection, C_3 is a scaling coefficient for the circulation, $Re_r = \rho V r_{s,m}/\mu$ is the Reynolds number of the radial flow, and V is the velocity just prior to impact. The thermal resistance due to convection becomes

$$R_{conv} \sim \frac{1}{hA} \sim \frac{r_s}{C_l k Pr^{1/3} A \sqrt{Re_r}} \tag{6.20}$$

The transient resistance within the drop then takes the form

$$R_d = \frac{\sqrt{\pi \alpha t}}{kA\left(1 + \frac{C_3 Pr^{1/3}\sqrt{Re_r \alpha t}}{r_s}\right)} \tag{6.21}$$

The second term in the parenthesis can be considered the relative contribution of convection to energy transfer within the drop. This treatment of enhancement due to circulation is similar to that used by by Yao and Schrock (1976) and Sultana et al. (2017) in the context of circulation within free falling droplets. The resistance is rendered dimensionless by, $R^*_{\sqrt{A},d} = R_d k \sqrt{\pi} r_s$ and can be expressed as a function of the Fourier number, Reynolds number and Prandtl number:

$$R^*_{\sqrt{A},d} \sim \frac{\sqrt{Fo_{\sqrt{A}}}\sqrt{\pi}}{1 + C_3 \sqrt{\pi} Pr^{1/3} \sqrt{Re_r} \sqrt{Fo_{\sqrt{A}}}} \tag{6.22}$$

where $Fo_{\sqrt{A}}$ and Pr are based on the average thermal properties of the liquid and solid states at the fusion temperature. Notably the above expression is a function of dimensionless time. In order to acquire an average value over time, the mean value theorem is used and Eq. 6.18 is integrated for the time period $Fo_{\sqrt{A},d} = 0 \rightarrow Fo_{\sqrt{A},d,f}$

$$\bar{R}^* = \frac{1}{Fo_{\sqrt{A},d,f}} \int_0^{Fo_{\sqrt{A},d,f}} R^* dFo_{\sqrt{A},d} \tag{6.23}$$

where $Fo_{\sqrt{A},d,f}$ is the Fourier number based on the time to freeze. The time-averaged thermal resistance in the drop becomes

$$\bar{R}^*_{\sqrt{a},d} \sim \frac{2ln\left[1 + C_3\sqrt{\pi}Pr^{1/3}\sqrt{Re_r}\sqrt{Fo_{\sqrt{A},d,f}}\right]}{C_3^3\pi PrRe_r^{3/2}Fo_{\sqrt{A},d,f}} - \frac{2}{C_3^2\sqrt{\sqrt{\pi}Pr^{2/3}Re_r\sqrt{Fo_{\sqrt{A},d,f}}}} + \frac{1}{C_3Pr^{1/3}\sqrt{Re_r}} \tag{6.24}$$

The transient effects are time averaged to fit with the steady state nature of the model. This is a scaling exercise which provides an estimate, not an exact value.

Transient constriction resistance

Heat transfer to the surface from a small drop undergoing phase change is a transient process, characterized by a thermal wave spreading into the substrate. The presence of one or more freezing droplets produces a non-uniform heat flux distribution over the surface of the substrate that causes thermal spreading into the substrate. Thermal spreading (or constriction) resistance occurs when the heat flow in a medium encounters a change in aspect ratio that causes the heat flux lines to spread or constrict, resulting in additional thermal resistance to the transport path. Mikic (1969) showed that the effect of the thermal properties of the surface material, in particular the spreading or constriction resistance, was a significant effect in dropwise condensation. Yovanovich (1997) characterized transient constriction resistance in flux tubes for a variety of isoflux source shapes. He used the square root of the area to non-dimensionalize the characteristic length scale in the resistance expression, $R^*_0 = k\sqrt{A}R_0$. He also developed a universal time function for calculation of spreading resistance from polygonal and hyper-ellipse-shaped planar

sources as a function of $Fo_{\sqrt{A}}$ where A is the active contact area of various shape sources. For short time frames where $Fo_{\sqrt{A}}<0.004$, the dimensionless spreading resistance is a linear function of $Fo_{\sqrt{A}}$. For long times when $Fo_{\sqrt{A}} \geq 1000$, R^*_0 is close to its steady state value. The region $.004 < Fo_{\sqrt{A}} \leq 1000$ is considered a transition region. This thesis follows that approach here to approximate the spreading resistance in coated and non-coated substrates.

Moreover, Yovanovich et al. (1995) developed a general model for transient heat conduction from a variety of isothermal shapes into infinitely large, constant property surroundings. They used the Churchill-Usagi method to blend short term heat flux solutions with long term steady state solutions based on the dimensionless shape factor $S^*_{\sqrt{A}} = S/\sqrt{A}$. Using the characteristic length scale, $L_c = \sqrt{A}$, they showed that the short term solutions all collapse into a single linear asymptote, $1/(\sqrt{\pi Fo_{\sqrt{A}}})$ and the long term behavior approaches that of the dimensionless shape factor. The blending parameter, n, is unique to each source shape and was optimized using numerical data. For a circular source, as is the case here, $n = 1.10$, and the maximum difference between the blended model and numerical results was 1.83%. The dimensionless heat flux for a circular source as a function of $Fo_{\sqrt{A}}$ is

$$Q^*_{\sqrt{A}} = \left[\left(\frac{1}{\sqrt{\pi Fo_{\sqrt{A}}}}\right)^n + \left(S^*_{\sqrt{A}}\right)^n\right]^{1/n} \tag{6.25}$$

where $Q^*_{\sqrt{A}} = QL_c/(kA\Delta T)$ is shown in Fig. 6.16.

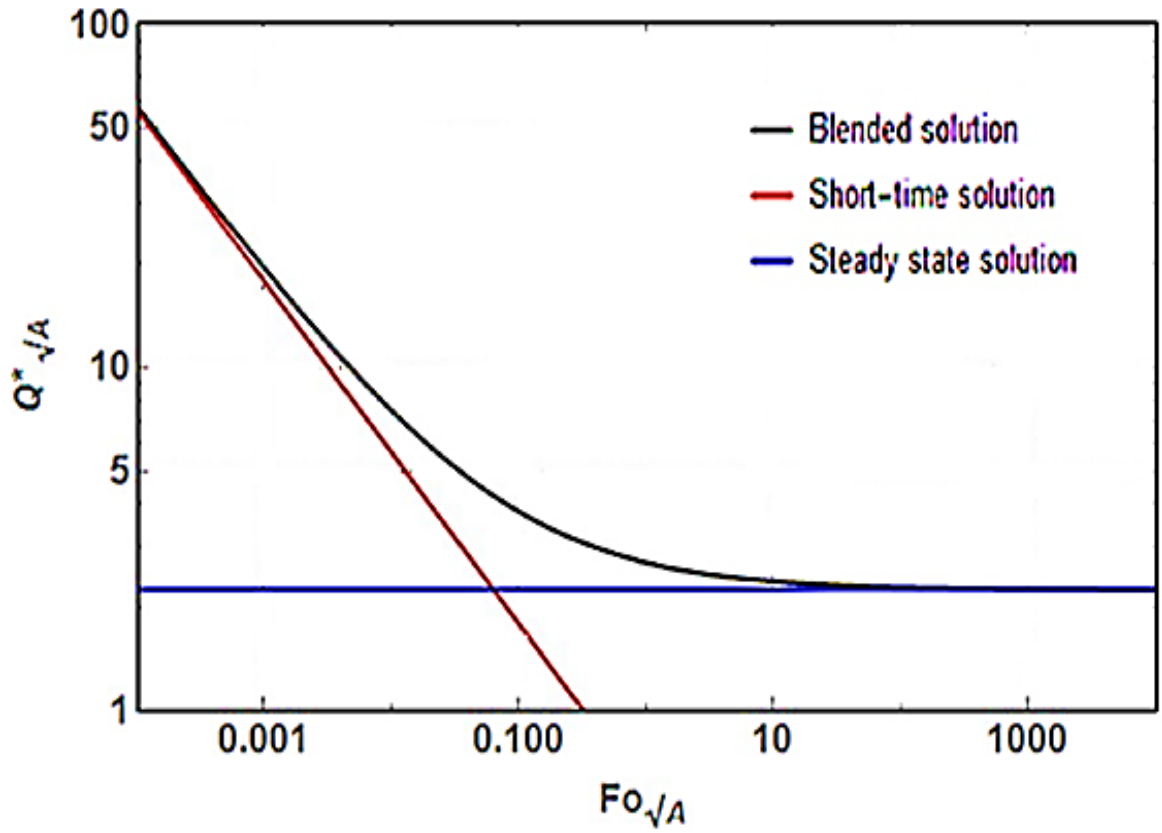

Fig. 6.16 Blended model of dimensionless heat flux from a circular source into a half space (Yovanovich et al., 1995).

The thermal resistance, $R^*_{\sqrt{A}}=1/Q^*_{\sqrt{A}}$, follows

$$R^*_{\sqrt{A}} = \left[\left(\sqrt{\pi Fo_{\sqrt{A}}}\right)^m + \left(\frac{1}{s^*_{\sqrt{A}}}\right)^m\right]^{1/m} \tag{6.26}$$

where $m = - n$ and is show in Fig. 6.17.

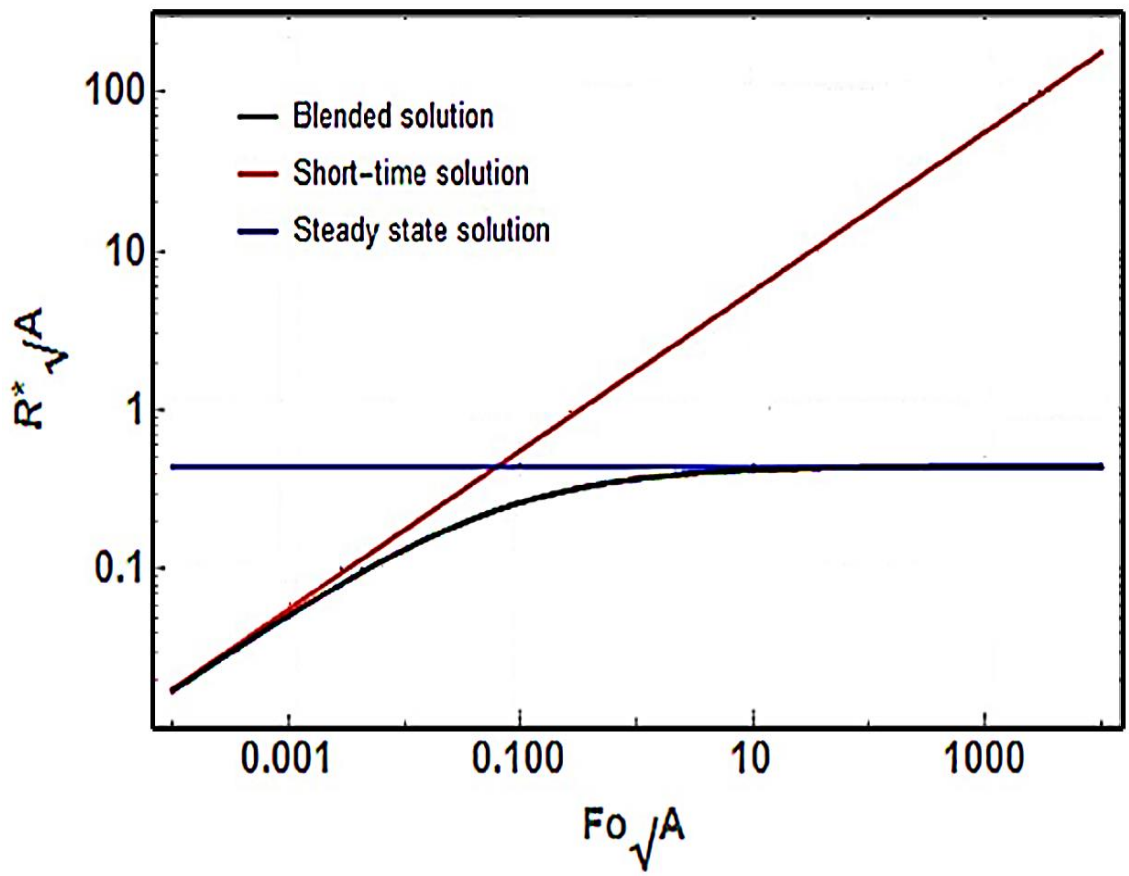

Fig. 6.17 Dimensionless transient constriction resistance in a half-space with a disk-shaped isothermal source (Yovanovich et al., 1995).

For a circular source, the shape factor is $S = 4r_s$ (Bergman et al., 2011), the dimensionless shape factor is $S^*_{\sqrt{A}} = 4/\sqrt{\pi}$. For a particular substrate, the dimensional resistance in KW^{-1} is

$$R_s = \frac{1}{kr_s\sqrt{\pi}}\left[\left(\frac{4}{\sqrt{\pi}}\right)^{1.1} + \left(\sqrt{\frac{r_s^2}{\alpha t}}\right)^{1.1}\right]^{-1/1.1} \tag{6.27}$$

Integrating Eq. 6.27 with respect to time results in a hyper-geometric function that can be solved to obtain an analytical expression.

Here values for the time-averaged resistance are calculated by numerically integrating the following

$$\overline{R_s} = \frac{1}{t_f}\int_0^{t_f} R_s dt \tag{6.28}$$

Effect of a coating on constriction resistance

The addition of a coating adds resistance to the heat transfer path. Dryden et al. (1985) studied the effect of coatings on constriction resistance. They developed steady-state resistance expressions for thin and thick coatings on a substrate which are applicable for $Fo_{\sqrt{A}} \rightarrow \infty$.

For steady-state and a thin coating which is a poor conductor, as is the case here, the extra resistance due to the coating will have a one-dimensional effect.

$$R_s = R_{2s} + R_{1D} \tag{6.29}$$

where R_{1D} is the one-dimensional resistance through the coating

$$R_{1D} = \frac{1}{\pi R}\frac{\delta}{r_s}\left[\frac{1}{k_{coat}} - \frac{1}{k_s}\right] \tag{6.30}$$

where δ is the thickness of the coating, R is the radius of the source, and k_{coat} and k_s are the thermal conductivities of the coating and the substrate, respectively. Eq. 6.29 is applicable when $\delta/r_s \ll 1$. When $k_{coat} \ll k_s$, it can be simplified to

$$R_{1D} = \frac{\delta}{\pi r_s^2 k_{coat}} \tag{6.31}$$

R_{2s} is the steady-state constriction resistance through the substrate.

$$R_{2s} = \frac{1}{4k_s r_s} \tag{6.32}$$

Equation 6.29 becomes

$$R_s = \frac{1}{4k_s r_s} + \frac{\delta}{\pi r_s^2 k_{coat}} \tag{6.33}$$

To find a general expression for the transient thermal resistance through the coating and the substrate, the composite solution technique of Churchill and Usagi (1972) is used

$$R_{cs} = \left[\left(R_{c,short}\right)^m + \left(R_{cs,long}\right)^m\right]^{1/m} \tag{6.34}$$

where $R_{c,short}$ and $R_{c,long}$ are the short-time and steady-state resistance expressions, respectively and n = 1.1. The short-time resistance is taken from Yovanovich (1997) as

$$R_{c,short} = \frac{\sqrt{\pi}\sqrt{Fo_{\sqrt{A},c}}}{\sqrt{\pi} k_{coat} r_s} \tag{6.35}$$

where $Fo_{\sqrt{A},c}$ is the Fourier number based on the thermal diffusivity of coating. The steady-state expression, $R_{c,long}$, is taken from Eq. 6.33. The transient thermal resistance through the coating and substrate becomes

$$R_{cs} = \left[\left(\frac{\sqrt{Fo}_{\sqrt{A},c}}{k_{coat} r_s}\right)^m + \left(\frac{1}{4k_s r_s} + \frac{\delta}{\pi r_s^2 k_{coat}}\right)^m\right]^{1/m} \tag{6.36}$$

$$R_{cs} = \left[\left(\frac{t\alpha_c}{k_{coat} r_s^2 \sqrt{\pi}}\right)^m + \left(\frac{1}{4k_s r_s} + \frac{\delta}{\pi r_s^2 k_{coat}}\right)^m\right]^{1/m} \tag{6.37}$$

The cases considered here involve coatings with 1 to 3 layers, the combination of which is very thin compared to the diameter of the post-impact drop. For very short times, the thermal wave exists only in the top layer. The transient resistance is a function of the properties of the top coat. For steady-state, the thermal conductivity of the coating is the effective thermal conductivity of the combined layers, $k_{eff,c}$. It is based on the thermal conductivity and thickness of each layer, e.g, for two layers,

$$k_{eff} = \frac{k_1 k_2 (l_1 + l_2)}{k_2 l_1 + k_1 l_2} \tag{6.38}$$

and for 3 layers

$$k_{eff,c} = \frac{k_1 k_2 k_3 (l_1 + l_2 + l_3)}{k_2 k_3 l_1 + k_1 k_3 l_2 + k_1 k_2 l_3} \tag{6.39}$$

Equation 6.36 becomes

$$R_{cs} = \left[\left(\frac{\sqrt{t\alpha_c}}{k_{coat}\sqrt{\pi r_s^2}} \right)^m + \left(\frac{1}{4k_s r_s} + \frac{\delta}{\pi r_s^2 k_{eff,c}} \right)^m \right]^{1/m} \tag{6.40}$$

The above is a transient expression. To obtain an average resistance expression, the mean value theorem is used, and Eq. 6.40 is integrated with respect to time for $t = 0 \rightarrow t_f$. Here, values for the time-averaged resistance are calculated by numerically integrating the following

$$\bar{R}_{cs} = \frac{1}{t_f} \int_0^{t_f} R_c s dt \tag{6.41}$$

Results:

There are a number of competing mechanisms influencing the spreading and solidification process of the droplets. No oscillation was observed in the experimental post-impact drops. Solidification occurred during retraction. The thermal resistance and time to freeze determined the degree of retraction. The experimental time to freeze for each drop on each substrate was extracted from the thermal images. The experimental value for the average resistance is calculated from $\bar{R}_{exp} = \Delta T = Q_l$. Table 6.8 lists the latent energy associated with solidification by drop size. The scaled value of $\bar{R}_{total}$ is calculated from Eq. 6.16, using Eq. 6.24 for resistance in the drop, and either Eq. 6.27 or Eq. 6.36 for resistance

through the uncoated or coated substrate, respectively; as well as using the experimental time to freeze. The scaling constants C_2 and C_3 are adjusted in $\bar{R}_{total}$ such that the values are close to those of $\bar{R}_{exp}$ for each substrate.

Droplet solidification on uncoated substrates

On the uncoated metals, the time to freeze is small such that drops spread quickly and freeze at the onset of retraction. The droplet's final radius after solidification is close to that of Eq. 6.13.

Equation 6.17 is plotted in Fig. 6.18. A value of C_2 = 1 is used in Eq. 6.14 corresponding to the maximum radius from Eq. 6.13. A value of C_3 = 0.005 is used in Eq. 6.24, which corresponds to a convection enhancement ranging from 3 to 12% for freshwater and 4 to 16% for saltwater.

Table 6.8 Latent energy released during solidification.

Droplet diameter (mm)	Latent energy (J)
3	4.77
4	11.30
5	22.08

Convection enhancement is somewhat larger in the saltwater drops due to the higher Reynolds and Prandlt numbers. Both the Reynolds and Prandlt numbers of saltwater are nearly twice those of freshwater due to its higher dynamic viscosity. A linear fit of the data in Fig. 6.18 provides the following relationship

$$Fo_{\sqrt{A},f} = 1.238 \frac{\bar{R}^*_{\sqrt{A},total}}{\sqrt{\pi}\xi_m^3 st} \tag{6.42}$$

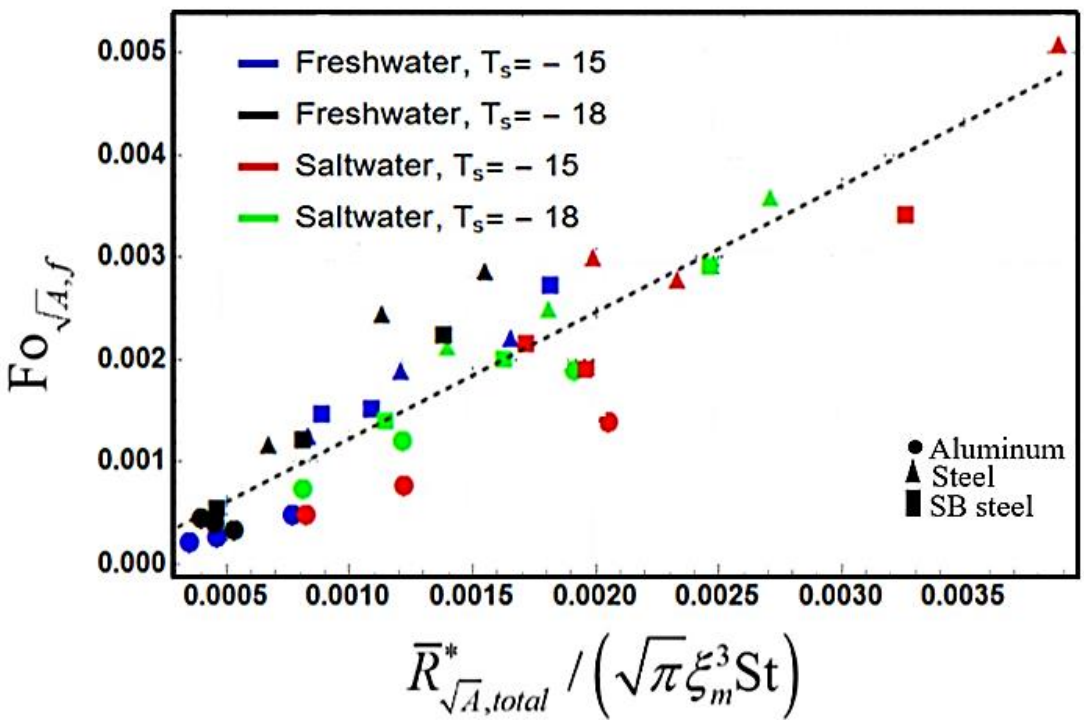

Fig. 6.18 Dimensionless time to freeze though the drop and uncoated substrates.

Droplet solidification on coated substrates

1) Primer coats: Figure 6.19 shows Eq. 6.17 plotted for the cases where primerA and primerB are the top coats. As successive layers are added atop the steel, the thermal resistance increases and the time to freeze increases. A value of C_2 = 0.8 is used in Eq. 6.14, reflecting some shrinkage of the area through which the energy transfer occurs. A value of C_3 = 0.001 is used in Eq. 6.24, corresponding to convection enhancement ranging from 3 to 6% for freshwater and 4 to 10% for saltwater. A linear fit of the data provides

$$Fo_{\sqrt{A},f} = 1.79\frac{\bar{R}^*_{\sqrt{A},total}}{\sqrt{\pi}\xi^3 St} + 0.003 \tag{6.43}$$

Notably the values of $Fo_{\sqrt{A},f}$ and $\bar{R}^*_{\sqrt{A},total}$ are an order of magnitude higher than those on the uncoated surfaces, highlighting the poor thermal conductance of the primer coats.

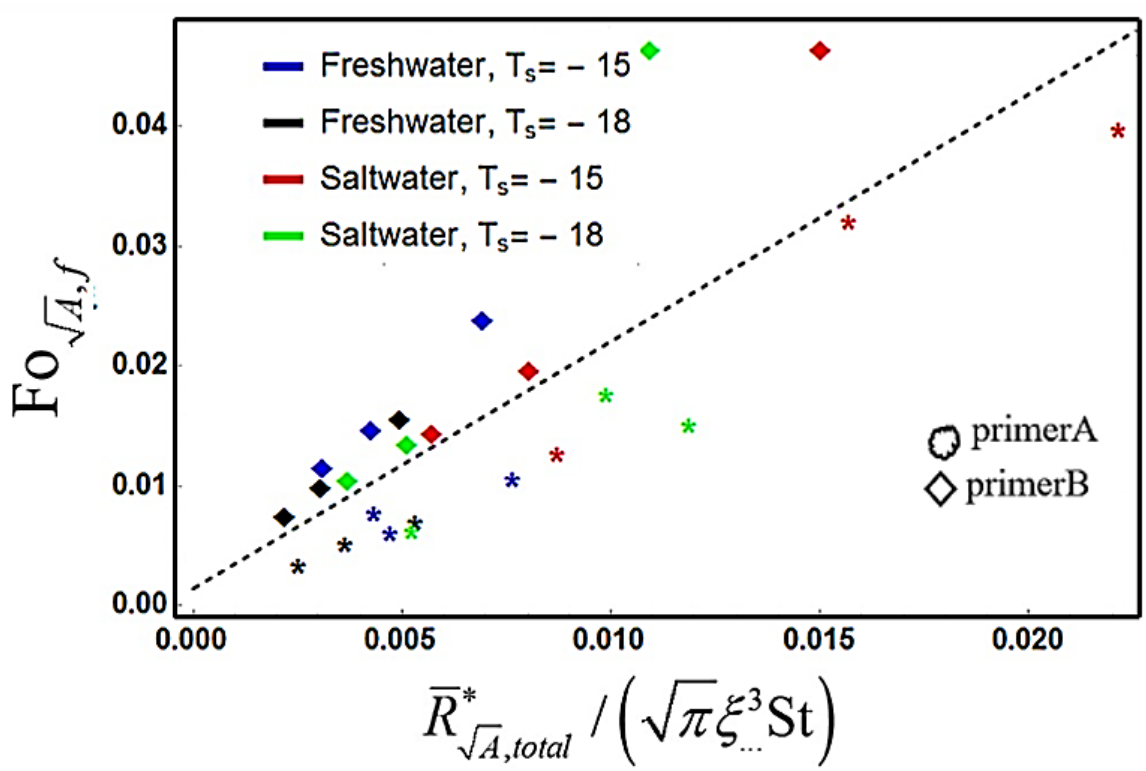

Fig. 6.19 Dimensionless time to freeze through the drop and primer coated substrates.

2) Marine coatings: Figure 6.20 shows Eq. 6.17 for the cases where marine coatings are the top coats: Amerlock 2, Interbond 201 and Interthane 990. Due to the high thermal resistance in these surfaces, the time to freeze is longer and the post-impact drops retracted significantly. On these surfaces, many of the post-impact drops exhibited fingering and a crown shape. Most often, all of the liquid then retracted. Many, but not all, of the post-impact drops retracted to a bead shape. Values of C_2 = 0.5, 0.45, and 0.4

are used in Eq. 6.14 to scale the radius for the Interbond 201, Interthane 990 and Amerlock 2, respectively. The significant retraction increases the height of the drop, thus the length scale for energy transfer through it. A value of C_3 = 0.005 is used in Eq. 6.24 for all three cases corresponding to convection enhancement ranging from 37 to 120% for freshwater and 60 to 140% for saltwater. There is more time for circulation within the drop, and convection plays a larger role in the transport.

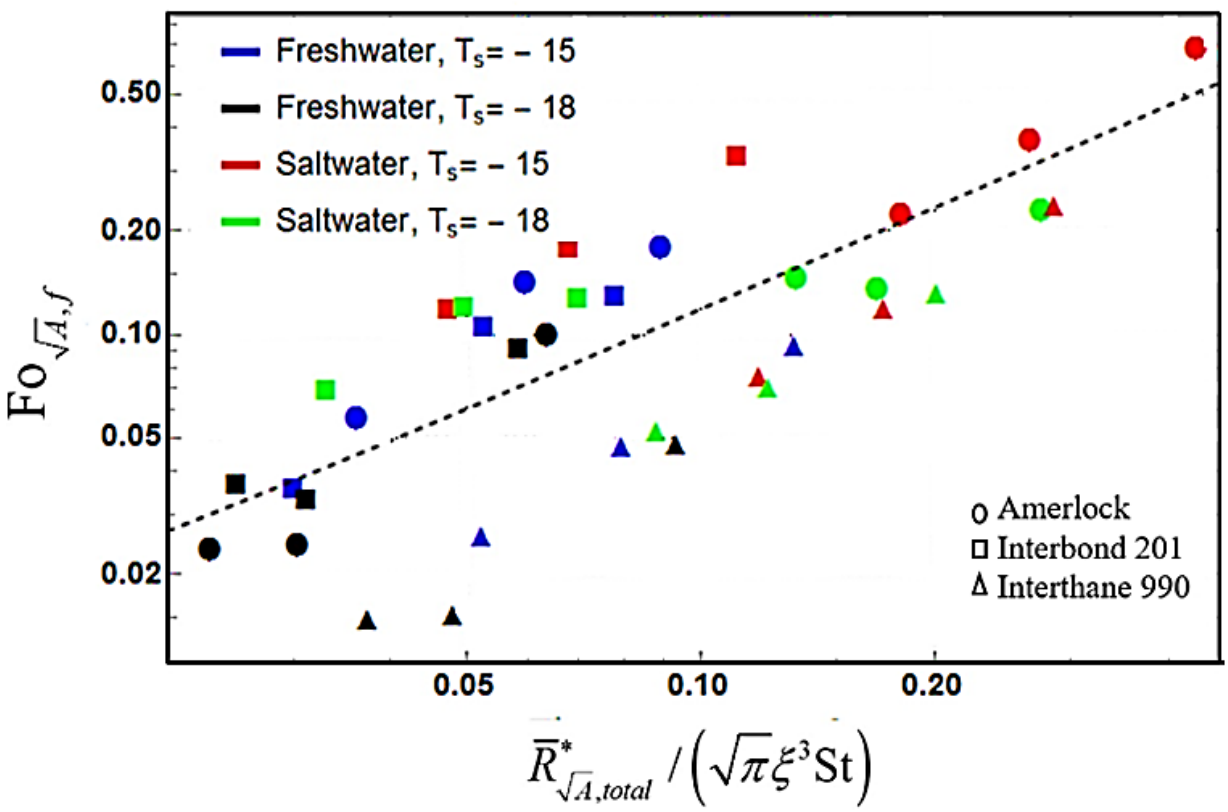

Fig. 6.20 Dimensionless time to freeze through the drop, primers, and coatings.

A linear fit of the data provides

$$Fo_{\sqrt{A},f} = 1.154\frac{\bar{R}^*_{\sqrt{A},total}}{\sqrt{\pi}\xi^3 St} + 0.003 \tag{6.44}$$

The values of $Fo_{\sqrt{A},f}$ and $\bar{R}^*_{\sqrt{A},total}$ are an order of magnitude higher than those on the surfaces coated with primer, and 2 orders of magnitude higher than the uncoated surfaces. This is due to the low thermal diffusivity and conductivity of the marine coatings and demonstrates that they are indeed good insulators.

3) Coated and Uncoated surfaces: Figure 6.21 plots Eq. 6.17 on a logarithmic scale due to the high range of $Fo_{\sqrt{A},f}$. As time to freeze grows, the average thermal resistance does not grow linearly. A nonlinear fit of the data for all samples provides

$$Fo_{\sqrt{A},f} = 1.364\left(\frac{\bar{R}^*_{\sqrt{A},total}}{\sqrt{\pi}\xi^3 St}\right)^{1.1} \tag{6.45}$$

The value of the constant in Eq. 6.44 is very close to the theoretical value of C_1 = 4/3.

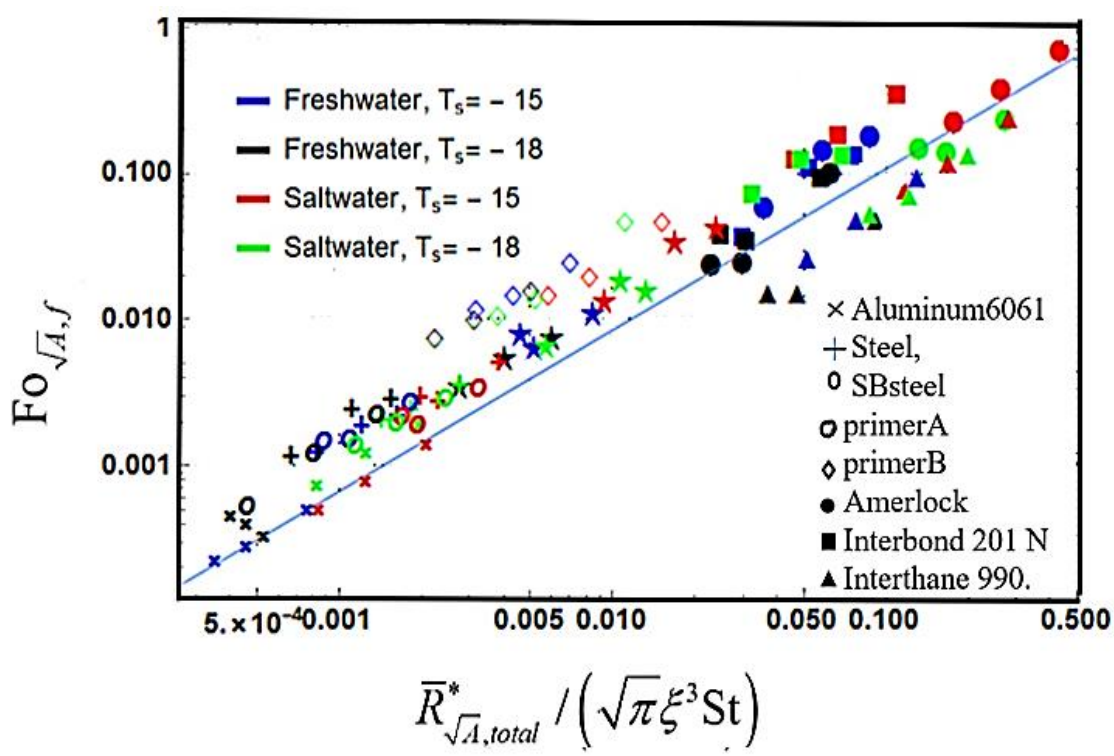

Fig. 6.21 Dimensionless time to freeze through the drop, primers, and coatings for both coated and uncoated surfaces.

6.9 Conclusions

This chapter investigated the fluid dynamics and phase change process of water droplets on various marine coated substrates. Fresh and salt water droplets of various sizes impinged on the cold substrates with different environmental conditions. Current results revealed that the contact angle varies with substrate properties. Additionally, the magnitudes of the static contact angle were different for fresh and salt water droplets. This may be a result of water salinity. Moreover, impurities in fluids change the contact angle characteristics. Further, the dynamic contact angle is a function of the substrate and liquid properties.

In both fresh and salt water, the high spread factor was observed for the bare substrate and the lowest spread factor was observed for the epoxy coated substrates. Additionally, the fresh water droplets had a higher spread factor than the salt water droplets. Furthermore, the colder the substrate, the larger the spreading it provided. Current results suggest that the air temperature, substrate temperature, coating thickness and the liquid surface tension are the most important parameters affecting the spreading patterns.

In both fresh and salt water, the droplet was easier to freeze on bare substrates than on the coated substrates. The supercooling degree significantly influenced the water droplet freezing rate and time. A supercooling effect was only found for salt water droplets and the epoxy coated substrates. One primary cause was the thermal conductance. The thicker the epoxy layer, the less heat it transported. Additionally, the fluid properties, surface roughness, contact angle hysteresis and the specific heat also promote the supercooling effect.

CHAPTER 7

DISCUSSION AND RECOMMENDATIONS

7.1 Discussion

Ice accretion poses serious hazards to Arctic offshore applications. To ensure a safe working environment in the Arctic, it is necessary to investigate this phenomenon. This thesis investigated these phenomena into two categories: pre-impact and post-impact. Both experimental and computational techniques were performed. Some valuable outcomes are discussed below:

The pre-impact result suggested that internal circulation enhances heat transfer to the surrounding air and increases the nucleation process. For a fixed falling distance, the larger sized droplets have a higher nucleation temperature than the smaller sized droplets, regardless of droplet properties.

The post-impact studies found that the droplet solidification process is primarily influenced by substrate temperature, droplet mass and spreading area. The analytical study found that a small droplet, such as 2 mm, is not sufficient to produce high impact velocity. Numerical modelling showed that any heat imparted to a semi-infinite substrate would be conducted away immediately from the interface, such that a fixed substrate temperature is always upheld.

Experimental studies on droplet dynamics highlighted that the droplet spread factor is larger for bare substrates and smaller in coated substrates. Surface roughness, fluid and substrate properties, and contact angle hysteresis are identified as the primary cause. In the droplet freezing study it is observed that the droplet freezes slowly on the coated substrate,

compared to the bare substrate. The primary cause is the thermal contact resistance between the droplet-substrate interface. Further, the supercooling effect is observed for salt water and coated substrates. Fluid properties and the coating thickness are a possible cause for this kind of phenomenon.

In conclusion, all the modelling assumptions used in this thesis were reasonable, with appropriate justification based on established research reports in the literature. Therefore, the results can be used in practical application/full-scale modelling.

7.2 Main Contributions

Contribution 1: Icing involves many physical parameters, and even though this study has been conducted over decades, many of these significant parameters are still not well described. Finding out these factors is one of the main challenges for the study of atmospheric and sea spray icing (RQ-1). A detailed investigation was provided (Sultana et al., 2017a)

Contribution 2: Understanding the physics and numerical modelling is needed to take precautions against icing. Several marine icing models have been developed over decades. To analyze their capabilities, a critical comparison is required (RQ-2). A comprehensive discussion was provided in Chapter 1 (Sultana et al., 2017a)

Contribution 3: Does a numerical model exist that is capable of capturing all the transient beheviours while phase change happens (RQ-3)? This question was answered in Chapter 2, where the existing numerical techniques were analyzed based on their basic mechanisms, such as changing fluid properties with temperature, the dynamic behaviours of spreading

and receding under the influence of solidification, as well as the thermal contact resistance (Sultana et al., 2018)

Contribution 4: A research question in this Ph.D. study was the thermo-fluid characteristics inside a traveling droplet (RQ-4). The investigations in the literature are limited and it is expensive to perform in full-scale measurement. Therefore, for a preliminary answer, RQ-4 was addressed using CFD, which was capable of predicting the phenomena. RANS turbulence models were used with extreme care. Further, the accuracy of CFD was compared with the analytical results (Sultana et al., 2017(b-c))

Contribution 5: This study builds upon previous work by Saha et al. (2016b) by closely examining the phase change process. The question was how precisely a CFD can handle the spreading or freezing process of water droplets when they impact on an isothermal substrate (RQ-5). The detailed development of the solidifying splat morphology presented in this study highlights the potentiality of the computational approach. Further, the computational results agree with the experimental data available in the present study, suggesting that the basic impacting, spreading and freezing mechanisms have been revealed in the numerical model.

Contribution 6: One of the research questions was; when a splat spreads or solidifies, then how far can the thermal wave penetrate (RQ-6)? Chapter 5 sheds light, in particular, on the heat transfer at the interface between the water droplet and a non-isothermal substrate surface. Some of these interactions, although known, are very difficult to quantify to such an extent that they can be incorporated into a computer program. The authors believe,

however, that even though the computer simulation presented here does not include all interactions, it does provide a good approximation.

Contribution 7: How do the coating layers affect the droplet dynamics/freezing process (RQ-7)? This answer was described in Chapter 6. This study develops a new experimental set-up that provides a suitable floor for the investigation of water break-up phenomena on impact and describes in detail how the solidification process varies with parameters (for instance, substrate properties, various droplet sizes, fluid properties and impact velocities). The study observed that the disk-shaped splat can be attributed essentially to good contact at splat/substrate interface, in other words, good wetting at the interface. On the contrary, splash splat formed. In the experiments, the difficulty freezing was commonly found in the coated surfaces. The experimental data also show that the supercooling effect is only observed for salt water droplets impacted on the coated substrates.

7.3 Recommendations

Numerical and experimental studies were conducted to understand the main features of the Arctic icing phenomena. The results have provided new information regarding the droplet dynamics and phase change physics. However, for further research, the following topics are recommended:

- For better understanding the complex phase change process, droplet impingement on a cylindrical, vertical or tilted surface should be taken into account. Varying object position might change the freezing time and profile of the droplet.
- Shattering or fragmentation was observed in the free falling study, however, the effect of pressure inside the ice shell deserves more attention in future research.

- For the pre-impact study, future modelling should look-upon the effect of surface tension or Weber number in detail.
- While the numerical model sheds insight into the thermal profile at the interface, more work is needed in the form of semi-analytical modeling to be able to characterize the behaviour more generally.
- Though the experiment provides valuable new insights about coated/un-coated substrates, powerful computer aided simulations are required.
- To understand the more realistic scenario, multiple droplet impingement on an advancing ice layer needs to be studied. The flow in the mushy zone, its shape, and relation with coated/un-coated substrates are important issues to look upon in future modelling.
- Droplet impacts on icing surfaces need to be recommended. Temperature distribution inside the accreted ice and air entrapment can be useful information for further research.
- Humidity plays a significant role in low temperature cases. The thin layer of frost formed on the substrate surface does affect the freezing rate, as well as droplet dynamics. Future research is recommended in this area.
- Salinity is an important issue in salt water freezing. Future modelling should include some important factors, such as: brine rejection from the saline ice, brine distribution and its impact on the properties and beheviour of the impinging droplet

References

Aksyutin, L. R., 1979. Icing of ships. Leningrad: Sudostroenye publishing house. (in Russian)

Albasiny, E.L., 1956. The solution of non-linear heat-conduction problems on the Pilot Ace, 1956: Proc. IEEE B: Radio and Electronic Engineering, 1(103), pp.158-162.

Alexiades, V., Solomon, A., 1993. Mathematical modeling of melting and freezing processes, CRC Press, Hemisphere publishing corporation, 1993.

Allen, D.N.de G., Severn, R.T., 1962. The application of relaxation methods to the solution of non-elliptic partial differential equations-III, Quat. J. Mech. Appl. Math. 15, pp.53-62.

Ansys Fluent Theory Guide, 2012.

In online: http://www.afs.enea.it/project/neptunius/docs/fluent/html/th/node66.htm)

Ansys Fluent Theory Guide, 2013.Solidification and Melting, Vesion-15.

Ansys Fluent Theory Guide, 2015.

Andreas, E.L., 2002. A review of the sea spray generation function for the open ocean. Adv. Fluid Mech. 33, pp.1-46.

Arianpour, F., Farzaneh, M., Kulinich, S.A., 2013. Hydrophobic and ice-retarding properties of doped silicone rubber coatings. Applied Surface Science, 265, pp.546-552.

Asaithambi, N.S., 1990. Numerical modeling of Stefan problems, Math. Computer Model. 14, pp.139-144.

Atthey, D., 1974. A finite difference schemes for melting problems, J. Int. Math. Appl. 13, pp.353-66.

Auldl, H.E., 1980. The thermodynamics of icing sprays (Master thesis). University of Alberta, Canada.

Ayasoufi, A., 2004. Numerical simulation of heat conduction with melting and/or freezing by space-time conservation element and solution element method. PhD Thesis, The University of Toledo, Ohio.

Aziz, S.D., Chandra, S., 2000. Impact, recoil and splashing of molten metal droplets. International journal of heat and mass transfer, 43(16), pp.2841-2857.

Basu, B., Date, A.W., 1988. Numerical modelling of melting and solidification problems—A review, Sadhana, 13(3), pp.169-213.

Baxter, D.C., 1962. The fusion times of slabs and cylinders, J. Heat Trans. 84(4), pp.317-325.

Bhardwaj, R., Longtin, J.P., Attinger, D., 2007. A numerical investigation on the influence of liquid properties and interfacial heat transfer during microdroplet deposition onto a glass substrate. International Journal of Heat and Mass Transfer, 50(15), pp.2912-2923.

Beard, K., Pruppacher H.R., 1969. A determination of the terminal velocity and drag of small water drops by means of a wind tunnel. Journal of the Atmospheric Sciences, 26(5), pp. 1066-1072.

Beaubouef, R.T., Chapman, A.J., 1967. Freezing of fluids in forced flow, Int. J. Heat Mass Transfer, vol. 10, pp.1581–1587.

Beckett, G., Mackenzie, J.A., Robertson, M.L., 2001. A moving mesh finite element method for the solution of two-dimensional Stefan problems, J. Comput. Physics, 168(2), pp.500-518.

Belhamadia, Y., Kane, A.S., Fortin, A., 2012. An enhanced mathematical model for phase change problems with natural convection, Int. J. Numer. Anal. Model, 3(2), pp. 192-206.

Bell, G.E., 1982. On the performance of the enthalpy method, Int. J. Heat and Mass Trans., 25(4), pp.587-589.

Bennett, T., Poulikakos, D., 1994. Heat transfer aspects of splat-quench solidification: modelling and experiment. Journal of Materials Science, 29(8), pp.2025-2039.

Bergman, T.L., Incropera, F.P., Lavine, A.S. and Dewitt, D.P., 2011. Introduction to heat transfer. John Wiley & Sons.

Berenbeim, D.Y., 1969. Hydrometeorological conditions of vessel icing. Meteorology and hydrology. No. 5.

Bernardin, J.D., Mudawar, I., Walsh, C.B., Franses, E.I., 1997. Contact angle temperature dependence for water droplets on practical aluminum surfaces. International journal of heat and mass transfer, 40(5), pp.1017-1033.

Bernardin, D., J.O.H.N., Stebbins, C.J., Mudawar, I., 1996. Effects of surface roughness on water droplet impact history and heat transfer regimes. International Journal of Heat and Mass Transfer, 40(1), pp.73-88.

Bertagnolli, M., Marchese, M., Jacucci, G., 1995. Modeling of particles impacting on a rigid substrate under plasma spraying conditions. Journal of Thermal Spray Technology, 4:41-9.

Berriman, J., Unwin, N., 1994. Analysis of transient structures by cryo-microscopy combined with rapid mixing of spray droplets. Ultramicroscopy, 56(4), pp. 241-252.

Bhola, R., Chandra, S., 1999. Parameters controlling solidification of molten wax droplets falling on a solid surface. Journal of materials science, 34(19), pp. 4883-4894.

Bjerkås, M., 2006. Ice actions on offshore structures with applications of continuous wavelet transforms on ice load signals (PhD thesis). Norwegian University of Science and Technology, Norway.

Blackmore, R.Z., 1996. Vessel icing and spongy accretion modelling. PhD Thesis. University of Alberta, Alberta, Canada.

Blackmore, R.Z., Lozowski, E.P., 1994. An heuristic freezing spray model of vessel icing. Int. J. Offshore and Polar Eng. 4(02).

Blackmore, R.Z., Lozowski, E.P., 1998. A theoretical spongy spray icing model with surficial structure. Atmos. Res. 49(4), 267-288.

Bodaghkhani, A., Dehghani, S.R., Muzychka, Y. S., Colbourne, B., 2016. Understanding spray cloud formation by wave impact on marine objects. Cold Reg. Sci. Technol., 129, 114-136.

Boinovich, L., Emelyanenko, A.M., Korolev, V.V., Pashinin, A.S., 2014. Effect of wettability on sessile drop freezing: when superhydrophobicity stimulates an extreme freezing delay. Langmuir, 30(6), pp.1659-1668.

Boluk, Y., 1996. Adhesion of freezing precipitates to aircraft surfaces. Transport Canada, pp. 44.

Bond, W.N., 1927. Bubbles and drops and Stokes' law, The London, Edinburgh, and Dublin Philosophical Magazine and Journal of Sci. 4(24), pp. 889-898.

Bonacina, C., Comini, G., Fasano, A., Primicerio, M.L., 1973. Numerical solution of phase-change problems, Int. J. Heat and Mass Trans. 16(10), pp.1825-1832.

Bonnerot, R., Jamet, P., 1979. A third order accurate discontinuous finite element method for the one-dimensional Stefan problem, J. Computational Physics, 32(2), pp.145-167.

Bonnerot, R., Jamet, P., 1981. A Conservative Finite Element Method for One Dimensional Stefan Problems With Appearing and Disappearing Phases, J. Computational Physics, 41, pp. 357–388.

Bonomo, M.E., 2013. Analyzing the singularities of freezing sessile water droplets. Honors Thesis.

Borisenkov, Ye.P., Panov, V.V., 1972. Primary results and prospects for investigating the hydrometerological conditions of ship icing. Arkticheskii I Antarkticheskii Nauchno-Issledovatiel'skii Institut, Trudy, No. 298, Leningrad, 5-33 (in Russian).

Bourlioux, A., 1995. A coupled level-set volume-of-fluid algorithm for tracking material interfaces. In proceedings of the 6th international symposium on computational fluid dynamics, Lake Tahoe, CA (Vol. 15).

Brown, R.D., Agnew, T.A., 1985. Characteristics of marine icing in Canadian waters. Proc. of the Intl. Workshop on Offshore Winds and Icing, 78- 94.

Brown, R.D., Roebber, P., 1985. The ice accretion problem in Canadian waters related to offshore energy and transportation. Canadian Climate Centre Rep. 85-13, 295.

Brown, R.D., Horjen, I., Jorgensen, T., Roebber, P., 1988. Evaluation of state-of-the-art drilling platform ice accretion models. Proc. 4th Intl. Workshop on Atmospheric Icing of Structures, pp. 208-213.

Budak, B., Sobol'eva, E., Uspenskii, A., 1965. A difference method with coefficient smoothing for the solution of Stefan problems. USSR Computational Math. Mathematical Physics 5, pp.59-76.

Cammaert, G., 2013. Impact of marine icing on Arctic offshore operations. Arctic Marine Operations Challenges & Recommendations, 5.

Cao, Y., Faghri, A., Chang, W.S., 1989. A numerical analysis of Stefan problems for generalized multi-dimensional phase-change structures using the enthalpy transforming model, Int. J. Heat Mass Trans. 32, pp.1289-1298.

Carte, A.E., 1956. The freezing of water droplets, in: Proceedings of the Physical Society. Section B, 69(10), pp.1028.

Caviezel, D., Narayanan, C., Lakehal, D., 2008. Adherence and bouncing of liquid droplets impacting on dry surfaces. Microfluid Nanofluid; 5(4):469–78.

Chernousko, F.L., 1970. Solution of non-linear heat conduction problems in media with phase changes, Int. Chem. Eng. 10, pp.42-8.

Chu, W.H., 1971. Development of a general finite difference approximation for a general domain part I: Machine transformation, J. Computational Physics 8, 392-408. Canadian Petroleum Technol. 9, pp.107-111.

Chun, C.K., Park, S.O., 2000. A fixed-grid finite-difference method for phase-change problems, Numer. Heat Trans. B, 38, pp.59–73.

Chung, V.K.K., 1995. Ship icing and stability (PhD thesis). University of Alberta, Canada.

Chung, K.K., Lozowski, E.P., 1990. On the growth of marine icicles. Atmosphere Ocean, 28(4), pp.393-408.

Chung, K.K., Lozowski, E.P., 1998. A three-dimensional time-dependent icing model for a stern trawler. Journal of Ship Research, vol. 42, pp. 266-273.

Chung, K.K., Lozowski, E.P., Pawlowski, J.S., Xu, Q., 1995a. Ship icing and stability. Proc. of the 1st Asian Computational Fluid Dynamics Conference, Vol.1, pp.275-280.

Chung, K.K., Lozowski, E.P., Zakrzewski, W.P., Gagnon, R., 1995b. A model for spraying and three-dimensional icing on a stern trawler. Proc. Of the Intl. Conf. Offshore Mech. and Arctic Engg, ASME, pp. 123-123.

Churchill, S., Usagi, R., 1972. A general expression for the correlation of rates of transfer and other phenomena. AIChE Journal, vol. 18, no. 6, pp. 1121–1128.

Choularton, T.W., Latham, J., Mason, B.J., 1978. A possible mechanism of ice splinter production during riming, Nature, 274(5673), pp. 791-792.

Citron, S.J., 1962. Proc. Fourth U.S. Nat. Congress of Appl. Mech. ASME, pp.1221-1227.

Clift, R., Grace, J.R., Weber, M.E., 2005. Bubbles, drops, and particles. Courier Corporation.Comini, G., Guidice, S.D., Lewis, R.W., Zienkiewicz, O.C., 1974. Finite element solution of non-linear heat conduction problems with special reference to phase change. Int. J. Numer. Methods 8, pp.613–24.

Comiskey, A.L., Leslie, L.D., Wise, J.L., 1984. Superstructure icing and forecasting in Alaskan waters. University of Alaska Arctic Environmental Information and Data Center. pp.30. (Unpublished).

Couch, E.J., Keller, H.H., Watts, J.W., 1970. Permafrost thawing around producing oil wells, J. Canadian Petroleum Technol. 9.

Cox, G.F., Weeks, W.F., 1975. Brine drainage and initial salt entrapment in sodium chloride ice (No. CRREL-RR-345). COLD REGIONS RESEARCH AND ENGINEERING LAB HANOVER NH.

Crank, J., 1984. Free and moving boundary problems (p. 425). Oxford: Clarendon press.

Crank, J., 1957. Two methods for the numerical solution of moving-boundary problems in diffusion and heat flow, Quart. J. Mechanics and Appl. Math. 10, pp.220-231.

Crank, J., Crowley, A.B., 1978. Isotherm migration along orthogonal flow lines in two dimensions, Int. J. Heat and Mass Trans. 21, pp.393-398.

Crank, J., Crowley, A.B., 1979. On an implicit scheme for the isotherm migration method along orthogonal flow lines in two dimensions, Int. J. Heat and Mass Trans. 22, pp.1331-1337.

Crank, J., Gupta, R.S., 1975. Isotherm migration method in two dimensions. Int. J. Heat and Mass Trans. 18, pp.1101-1107.

Crank, J., Gupta, R.S., 1972. A method for solving moving boundary problems in heat flow using cubic splines or polynomials, J. Inst. Math. Appl. 10, pp.296–304.

Crowley, A.B., 1978. Numeric al solution of Stefan problems, Int. J. Heat and Mass Trans. 21, pp.215-17.

Csgnetwork. Online link: http://www.csgnetwork.com/h2odenscalc.html

Dai, M., Perot, J.B., Schmidt, D.P., 2002. Heat transfer within deforming droplets. Proceedings of ASME, Internal Combustion Engine Division, September, New Orleans.

Dalili, N., Edrisy, A., Carriveau, R., 2009. A review of surface engineering issues critical to wind turbine performance. Renewable and Sustainable Energy Reviews, 13(2), pp.428-438.

Davey, R.J., Maginn, S.J., Steventon, R.B., Ellery, J.M., Murrell, A.V., Booth, J., Godwin, A.D., Rout, J.E., 1994. Nucleation of crystals under Langmuir monolayers-kinetic and morphological data for the nucleation of ice. Langmuir, 10(6), pp.1673-1675.

DeAngelis, R.M., 1974. Superstructure icing. Mar. Wea. Log 18, 1-7.

De Gennes, P.G., 1985. Wetting: statics and dynamics. Reviews of modern physics, 57(3), pp.827.

Dehghani, S. R., Muzychka, Y. S., Naterer, G. F., 2016a. Droplet trajectories of wave-impact sea spray on a marine vessel. Cold Reg. Sci. Technol., 127, pp. 1–9.

Dehghani, S. R., Naterer, G. F., Muzychka, Y. S., 2016b. Droplet size and velocity distributions of wave-impact sea spray over a marine vessel. Cold Reg. Sci. Technol., 132, pp. 60–67.

Dehghani, S. R., Muzychka, Y. S., Naterer, G. F., 2017a. Water breakup phenomena in wave-impact sea spray on a vessel. Ocean Eng., 134, pp. 50–61.

Dehghani, S. R., Naterer, G. F., Muzychka, Y. S., 2017b. Transient heat conduction through a substrate of brine‐spongy ice. Heat and Mass Transfer. DOI 10.1007/s00231-017-2016-5.

Dehghani-Sanij, A.R., Dehghani, S.R., Naterer, G.F., Muzychka, Y.S., 2017. Sea spray icing phenomena on marine vessels and offshore structures: review and formulation. Ocean Engineering, 132, pp.25-39.

Dehghani, S.R., Muzychka, Y.S., Naterer, G.F., 2018. A finite difference solution for freezing brine on cold substrates of spongy ice. International Journal of Heat and Fluid Flow, 69, pp.174-184.

Dhiman, R., Chandra, S., 2005. Freezing-induced splashing during impact of molten metal droplets with high Weber numbers. International journal of heat and mass transfer, 48(25), pp.5625-5638.

Diaz, A.J., Ortega, A., 2010. Numerical investigation of a liquid droplet transported by a gas stream impinging on a heated surface: single-phase regime. In Thermal and Thermomechanical Phenomena in Electronic Systems (ITherm), 12th IEEE Intersociety Conference on (pp. 1-9).

Dix, R.C., Cizek, J., 1970. The isotherm migration method for transient heat conduction analysis, 4th Int. Heat Trans. Conf. 1, pp.1-10.

Dorsey, N.E., 1948. The freezing of supercooled water, Transactions of the American Philosophical Soc. 38(3), pp.247-328.

Douglas, J., Gallie, T.M., 1955. On the numerical integration of a parabolic differential equation subject to a moving boundary condition, Duke Math. J., 22, pp.557-572.

Dryden, J.R., Yovanovich, M.M., Deakin, A.S., 1985. The effect of coatings on the steady-state and short time constriction resistance for an arbitrary axisymmetric flux. Journal of heat transfer, 107(1), pp.33-38.

Dubrovskii, V.V., Podvysotskii, A.M., Shraiber, A.A., 1990. Measuring natural oscillation periods for droplets and two-component particles. Journal of Engineering Physics and Thermophysics, 58(5), pp. 622-625.

Duda, J.L., Malone, M.F., Notter, R.H., 1975. Analysis of two-dimensional diffusion-controlled moving boundary problems. Int. J. Heat and Mass Trans. 18, pp.901-910.

Dusinberre, G.M., 1945. Numerical methods for transient heat flow, Trans ASME 67, pp.703–712.

Dye, J.E., Hobbs, P.V., 1968. The influence of environmental parameters on the freezing and fragmentation of suspended water drops. Journal of the Atmospheric Sciences, 25(1), pp.82-96.

Efimov, Y.O., 2012. Vessel icing on the Shtokman FPSO. Master thesis. University of Stavanger, Norway.

Elliott, C.M., 1976. PhD Thesis, Oxford University.

Elliott, C.M., 1987. Error analysis of the enthalpy method for the Stefan problem, IMA J. Numer. Analysis 7, pp.61-71.

Engel, O.G., 1955. Waterdrop collisions with solid surfaces. Journal of research of the national bureau of standards, 54(5), pp.281-298.

Enríquez, O.R., Marín, Á.G., Winkels, K.G., Snoeijer, J.H., 2012. Freezing singularities in water drops. Physics of Fluids (1994-present), 24(9), pp. 091102.

Eyres, N.R., Hartree, D.R., Ingham, J., Jackson, J., Sarjant, R.J., Wagstaff, J.B., 1946. The calculation of variable heat flow in solid, Phil. Trans. R. Soc. A 240, pp.1–57.

Fabbri, M., Voller, V.R., 1995. Numerical solution of plane front solidification with kinetic undercooling. Numer. Heat Trans. B, 27, pp.467-486.

Fakhari, A., Rahimian, M.H., 2011. Investigation of deformation and breakup of a falling droplet using a multiple-relaxation-time lattice Boltzmann method. Computers & Fluids, 40(1), pp. 156-171.

Farzaneh, M. ed., 2008. Atmospheric icing of power networks. Springer Science & Business Media.

Fauchais, P., Fukumoto, M., Vardelle, A., Vardelle, M., 2004. Knowledge concerning splat formation: an invited review. J. Therm. Spray Technol. 13 (3), pp.337–360.

Fazelpour, A., Dehghani, S. R., Masek, V., Muzychka, Y. S., 2016a. Infrared image analysis for estimation of ice load on structures. Arctic Technology Conference, Offshore Technology Conference.

Fazelpour, A., Dehghani, S. R., Masek, V., Muzychka, Y. S., 2016b. Effect of ambient conditions on infrared ice thickness measurement. IEEE Conf. Newfoundland and Labrador Section.

Feit, D.M., 1987a. An operational forecast system for superstructure icing, OPC Contribution No. 18. Online link: polar.ncep.noaa.gov/mmab/papers/tn18/OPC18.pdf

Feit, D.M., 1987b. Forecasting of superstructure icing for Alaskan waters. Vol.12 (2), pp. 5-10.

Feuillebois, F., Lasek, A., Creismeas, P., Pigeonneau, F., Szaniawski, A., 1995. Freezing of a subcooled liquid droplet. Journal of colloid and interface science, 169(1), pp.90-102.

Feulvarch, E., Bergheau, J.M., 2007. An implicit fixed-grid method for the finite-element analysis of heat transfer involving phase changes. Numer. Heat Trans., Part B: 51, pp.585–610.

Fillion, R.M., Riahi, A.R., Edrisy, A., 2017. Design factors for reducing ice adhesion. Journal of Adhesion Science and Technology, pp.1-14.

Fikke, S.M., Ronsten, G., Heimo, A., Kunz, S., Ostrozlik, M., Persson, P.E., Sabata, J., Wareing, B., Wichura, B., Chum, J., Laakso, T., 2006. COST 727: atmospheric icing on structures: measurements and data collection on icing: state of the art. Meteo Schweiz.

Forest, T.W., Lozowski, E.P., Gagnon, R.E., 2005. Estimating marine icing on offshore structures using RIGICE04. NRC publications archive (NPArC).

Friedman, A., 1968. The Stefan problem in several space variables. Trans. American Math. Soc. 133, pp.89-114.

Fukai, J., Shiiba, Y., Yamamoto, T., Miyatake, O., Poulikakos, D., Megaridis, C.M., Zhao, Z., 1995. Wetting effects on the spreading of a liquid droplet colliding with a flat surface: experiment and modeling. Physics of Fluids, 7(2), pp. 236-247.

Fukusako, S., Horibe, A., Tago, M., 1989. Ice accretion characteristics along a circular cylinder immersed in a cold air stream with seawater spray. Experimental Thermal and Fluid Science, 2(1), pp. 81-90.

Fukusako, S., Yamada, M., 1993. Recent advances in research on water-freezing and ice-melting problems. Experimental Thermal and Fluid Science, 6(1), pp.90-105.

Fukai, J., Etou, M., Asanoma, F., Miyatake, O., 2000. Dynamic contact angles of water droplets sliding on inclined hot surfaces. Journal of chemical engineering of Japan, 33(1), pp. 177-179.

Fukumoto, M., Yang, K., Tanaka, K., Usami, T., Yasui, T., Yamada, M., 2011. Effect of substrate temperature and ambient pressure on heat transfer at interface between molten droplet and substrate surface. Journal of thermal spray technology, 20(1-2), pp.48-58.

Fumoto, K., Kawanami, T., 2012. Study on freezing characteristics of supercooled water droplets impacting on solid surfaces. Journal of Adhesion Science and Technology, 26(4-5), pp. 463-472.

Hoke, J.L., 2000. The interaction between the test plate and frost layer through condensate distribution (Doctoral Dissertation). University of Illinois at Urbana Champaign, The Graduate College.

Funk, C., 2012. Freezing spray and ice accretion on vessels: a comprehensive summary. Proc. of the National Conference on Undergraduate Research (NCUR), Weber state university, Ogden UT.

Furenes, B., Lie, B., 2006. Using event location in finite-difference methods for phase-change problems. Numer. Heat Trans., Part B, 50, pp.143–155.

Furzeland, R.M., 1977. PhD thesis. Brunel University. Brunel University Math Report TR/77.

Furzeland, R.M., 1980. A comparative study of numerical methods for moving boundary problems. J. Inst. Math. Applics. 26, pp.411-429.

Gajewski, A., 2008. Contact angle and sessile drop diameter hysteresis on metal surfaces. Int. J. Heat and Mass Transfer, 51(19-20), pp.4628-4636.

Gao, W., Smith, D.W., Sego, D.C., 2000. Freezing behavior of freely suspended industrial wastewater droplets. Cold regions science and technology, 31(1), pp.13-26.

Gavish, M., Popovitz-Biro, R., Lahav, M., Leiserowitz, L., 1990. Ice nucleation by alcohols arranged in monolayers at the surface of water drops.

George, D.J., 1975. The frequency of weather conditions favourable for ship spray icing on the seas round Iceland during the 1972-73 winter. Mar. Obs, 45, pp.177-185.

Giraldo, F.X., 2018. Time-Integrator.

Online: http://faculty.nps.edu/fxgirald/projects/nseam/nps/new_section4.pdf

Goodrich, L.E., 1978. Efficient numerical technique for one-dimensional thermal problems with phase change, Int. J. Heat and Mass Trans. 21, pp.615-621.

Goodling, J.S., Khader, M.S., 1974. One dimensional inward solidification with a convective boundary condition, AFS Cast Metals Res. J. 10, pp.26-29.

Gupta, R.S., 1974. Moving grid method without interpolations, Comput. Meths. Appl. Mech. Eng. 4, pp.143–52.

Gupta, R.S., 2003. The Classical Stefan Problem: Basic concepts, modelling and analysis, Elsevier, (Vol. 45).

Gupta, R.S., Kumar, a., 1986. Approximate analytical solutions for multi-dimensional Stefan problems, Comput. Meths. Appl. Mech. Eng. 56, pp.127-138.

Gupta, A., Kumar, R., 2010. Droplet impingement and breakup on a dry surface. Computers & Fluids, 39(9), pp.1696-1703.

Gunn, R., Kinzer, G.D., 1949. The terminal velocity of fall for water droplets in stagnant air, Journal of Meteorology, 6(4), pp. 243-248.

Gunstensen, A.K., Rothman, D.H., Zaleski, S., Zanetti, G., 1991. Lattice Boltzmann model of immiscible fluids. Physical Review A, 43(8), pp. 4320.

Gupta, R.S., Kumar, D., 1981. Variable time step methods for one-dimensional Stefan problem with mixed boundary condition, Int. J. Heat and Mass Trans. 24, pp.251-259.

Griebel, M., Klitz, M., 2014. Simulation of droplet impact with dynamic contact angle boundary conditions. In Singular Phenomena and Scaling in Mathematical Models (pp. 297-325). Springer International Publishing.

Grunau, D., Chen, S., Eggert, K., 1993. A lattice Boltzmann model for multiphase fluid flows. Physics of Fluids A: Fluid Dynamics (1989-1993), 5(10), pp. 2557-2562.

Hadamard, J., 1911. Mouvement permanent lent d'une sphere liquide et visqueuse dans un liquide visqueux, Compt. Rend.,152, No. 25.

Hållén, J., 2015. Icing destroys transmission lines. Online: http://iwais.org/icing-destroys-transmission-lines/

Hansen, E.S., 2012. Numerical modelling of marine icing on offshore structures and vessels. Master thesis. Norwegian University of Science and Technology, Norway.

Hao, J., 2017. Effect of surface roughness on droplet splashing. Physics of Fluids, 29(12), p.122105.

Harlow, F.H., Shannon, J.P. 1967. The splash of a liquid droplet. Journal of Applied Physics 38 (10), pp. 3855-3866.

Hayashi, Y., 1991. Solidification and melting solutions, in Cheng, K.C., Seki, N. (Eds.), Freezing and melting heat transfer in engineering. New York: Hemisphere.

Heitz W. L., Westwater, J. W., 1970. Extension of the numerical method for melting and freezing problems. Int. J. Heat Mass Transfer 13, pp.1371–1375.

Herlach, D.M., Palberg, T., Klassen, I., Klein, S. and Kobold, R., 2016. Overview: Experimental studies of crystal nucleation: Metals and colloids. The Journal of Chemical Physics, 145(21), p.211703.

Hermes, C.J., Piucco, R.O., Barbosa Jr, J.R. and Melo, C., 2009. A study of frost growth and densification on flat surfaces. Experimental Thermal and Fluid Science, 33(2), pp.371-379.

Hindmarsh, J.P., A.B. Russell, X.D. Chen., 2003. Experimental and numerical analysis of the temperature transition of a suspended freezing water droplet. International Journal of Heat and Mass Transfer, 46:1199–1213, 2003.

Hirt, C. W., Nichols, B. D., 1981. Volume of Fluid (VOF) method for the dynamics of free boundaries. J. Computational Physics 39 (1), pp. 201-225.

Hodes, M., Zhang, R., Lam, L.S., Wilcoxon, R. and Lower, N., 2013. On the potential of galinstan-based minichannel and minigap cooling. IEEE Transactions on Components, Packaging and Manufacturing Technology, 4(1), pp.46-56.

Horjen, I., 1983. Icing on offshore structures. Atmospheric icing. Norwegian maritime research, 11(3), pp.9-22.

Horjen, I., 1990. Numerical modelling of time-dependent marine icing, anti-icing and de-icing (Ph.D. thesis). Norges Tekniske Hogskole (NTH), Trondheim, Norway.

Horjen, I., 2013. Numerical modeling of two-dimensional sea spray icing on vessel-mounted cylinders. Cold Reg. Sci. Technol. 93, 20–35.

Horjen, I., 2015. Offshore drilling rig ice accretion modeling including a surficial brine film. Cold Reg. Sci. Technol. 119, 84–110.

Horjen, I., Vefsnmo, S., 1985a. A numerical sea spray icing model including the effect of a moving water film. Proc. of Intl. Workshop on Offshore Winds and Icing, Halifax, NS, 152-164.

Horjen, I., Vefsnmo, S., 1985b. Computer modelling of sea spray icing on marine structures. Proc. of Symposium on Automation for Safety in Offshore Operations, pp. 315-323.

Horjen, I., Vefsnmo, S., 1987. Time-dependent sea spray icing on ships and drilling rigs — a theoretical analysis. Offshore Icing — Phase IV, NHL — Report STF60 F87130, pp. 87.

Horton, T.J., Fritsch, T.R., Kintner, R.C., 1965. Experimental determination of circulation velocities inside drops. The Canadian Journal of Chemical Eng. 43(3), pp. 143-146.

Hsu, C.F., Sparrow, E.M., Patankar, S.V., 1981. Numerical solution of moving boundary problems by boundary immobilization and a control volume based, finite difference scheme, Int. J. Heat and Mass Trans. 24, pp.1335-1343.

Hu, H., Argyropoulos, S.A., 1996. Mathematical modelling of solidification and melting: a review, Modelling Simul. Mater. Sci. Eng. 4, pp.371–396.

Hu, J., Xiong, X., Xiao, H., Wan, K.T., 2015. Effects of contact angle on the dynamics of water droplet impingement. Proceedings of the 2015 COMSOL Conference in Boston.

Hu, J., Xu, K., Wu, Y., Lan, B., Jiang, X., Shu, L., 2014. The freezing process of continuously sprayed water droplets on the superhydrophobic silicone acrylate resin coating surface. Applied Surface Science, 317, pp.534-544.

Huang, L., Liu, Z., Liu, Y., Gou, Y., Wang, L., 2012. Effect of contact angle on water droplet freezing process on a cold flat surface. Experimental thermal and fluid science, 40, pp.74-80.

Ice Sight. Ice protection system. Online: http://icesight.com/

Idelsohn, S.R., Storti, M.A., Crivelli, L.A., 1994. Numerical methods in phase change problems, Archives of Computational Methods in Eng. 1, pp.49-74.

Ilinca, A., 2011. Analysis and mitigation of icing effects on wind turbines. InTech Open Access Publisher.

IMO 2011, Sub-committee on stability and load lines and on fishing vessels safety, IMO.

Inada, S., 1988. Transient heat transfer from a free-falling molten drop of lead to a cold plate. Journal of chemical engineering of Japan, 21(6), pp.582-588.

Inside me. Online: http://inside.mines.edu/~epoeter/583/13/discussion/courant.htm

ISO-12494, 2001. Atmospheric icing of structures. ISO copyright office, Geneva, Switzerland, pp. 56.

Issa, R., 1985. Solution of the implicit discretized fluid flow equations by operator splitting. Journal of Computational Physics 62, pp.40–65.

Itagaki K., 1984. Icing rate on stationary structures under marine conditions. Cold Reg. Res. Eng. Laboratory: US Army Corps of Engineers.

Jadidi, M., Farzad, M.A., Trepanier, J.Y., Dolatabadi, A., 2018. Effects of Ambient Air Relative Humidity and Surface Temperature on Water Droplet Spreading Dynamics. In ASME 2018 5th Joint US-European Fluids Engineering Division Summer Meeting (pp. V001T15A006-V001T15A006). American Society of Mechanical Engineers.

Jiji, L. M., 2009. Heat Convection. Springer-Verlag, second ed.

Jin, Z., Hu, H., 2010. Quantification of unsteady heat transfer and phase changing process inside small icing water droplets. Rev. Sci. Instrum. 80, pp.054902.

Jin, Z., Jin, S., Yang, Z., 2013. Visualization of icing process of a water droplet impinging onto a frozen cold plate under free and forced convection, J. Visualiz. 16, pp.13–17.

Jin, Z., Wang, Y., Yang, Z., 2014. An experimental investigation into the effect of synthetic jet on the icing process of a water droplet on a cold surface. Int. J. Heat. Mass Transf. 72, pp. 553–558.

Jin, Z., Wang, Z., Sui, D., Yang, Z., 2016. The impact and freezing processes of a water droplet on different inclined cold surfaces. International Journal of Heat and Mass Transfer, 97, pp. 211-223.

Jin, Z., Cheng, X., Yang, Z., 2017. Experimental investigation of the successive freezing processes of water droplets on an ice surface. International Journal of Heat and Mass Transfer, 107, pp.906-915.

Johnson, K., Lozowski, E.P., 1988. The simulation of experimental freshwater icicle growth with a simple numerical model. Proc. IAHR Ice Syrup, 425-435.

Jones, K.F., 1996. Ice accretion in freezing rain. CRREL Rep. 96-2, Cold Reg. Res. Eng. Laboratory, Hanover.

Jones, K.F., Andreas, E.L., 2012. Sea spray concentrations and the icing of fixed offshore structure. Quart. J. Royal Meteorol. Soc. 138, pp. 131-144.

Jung, S., Tiwari, M.K., Doan, N.V. and Poulikakos, D., 2012. Mechanism of supercooled droplet freezing on surfaces. Nature communications, 3, p.615.

Kachurin, L.G., Gashin, L.I., Smirnov, I.A., 1974. Icing rate of small displacement fishing boats under various hydrometeorological conditions. Meteorlogiya I Gidrologiya 3, 50-60.

Kamnis S., Gu S., 2005. Numerical modelling of droplet impingement. Journal of Physics D: Applied Physics, 38(19), pp. 3664.

Kang, B., Zhao, Z., Poulikakos, D., 1994. Solidification of liquid metal droplets impacting sequentially on a solid surface. Transactions-American Society of Mechanical Engineers, Journal of Heat Transfer, 116, pp. 436-436.

Kang, B.S., Lee, D.H., 2000. On the dynamic behavior of a liquid droplet impacting upon an inclined heated surface. Experiments in fluids, 29(4), pp.380-387.

Karlsson, L., 2013. The dynamics of drops freezing on cold Surfaces. Master Thesis, Lulea University of Technology.

Kato, R., 2012. Modelling of ship superstructure icing (Master thesis). Norwegian University of Science and Technology, Trondheim, Norway.

Keshavarzi, G., Yeoh, G.H., Barber, T., 2013. Comparison of the VOF and CLSVOF Methods in Interface Capturing of a Rising Bubble. The Journal of Computational Multiphase Flows, 5(1), pp.43-55.

Kim, C.J., Kaviany, M., 1990. A numerical method for phase-change problems, Int. J. Heat and Mass Trans. 33(12), pp.2721-2734.

Kim, C.J., Kaviany, M., 1992. A numerical method for phase-change problems with convection and diffusion, Int. J. Mass Trans. 35(2), pp.457-467.

Kline, S.J. and McClintock, F.A., 1953. Analysis of uncertainty in single-sample experiments. Mechanical Engineering, 75, pp.3-9.

Kolosova, N.V., Panov, V.V., Zatonskiy, M.Y., 1971. On methodology of charting possible areas of vessel icing in Arctic Seas. In article collection: Theoretical and experimental surveys of vessel icing conditions. Leningrad.

Kraj, A.G., 2007. Icing characteristics and mitigation strategies for wind turbines in cold climates (Master thesis). University of Manitoba, Manitoba, Canada.

Kubat, I., Timco, G., 2005. NRC marine icing database. Canadian Hydraulics Centre – National Research Council Canada, IWAIS XI.

Kuhns, I.E., Mason, B.J., The supercooling and freezing of small water droplets falling in air and other gases, in: Proceedings of the Royal Society of London A: Mathematical, Physical and Eng. Sci. 302(1471) (1968), pp. 437-452

Kulinich, S.A., Farzaneh, M., 2009a. Ice adhesion on super-hydrophobic surfaces. Applied Surface Science, 255(18), pp. 8153-8157.

Kulinich, S.A., Farzaneh, M., 2009b. How wetting hysteresis influences ice adhesion strength on superhydrophobic surfaces. Langmuir, 25(16), pp. 8854-8856.

Kulyakhtin, A., 2014. Numerical modelling and experiments on sea spray icing. PhD Thesis, Norwegian University of Science and Technology, Trondheim, Norway.

Kulyakhtin, A., Løset, S., 2011. Sea spray icing: in-cloud evaporation. Semi-analytical and numerical investigations. Proc. of the 14th Intl. Workshop on Atmospheric Icing of Structures.

Kulyakhtin, A., Tsarau, A., 2014. A time-dependent model of marine icing with application of computational fluid dynamics. Cold Reg. Sci. Technol. 104, 33–44.

Kulyakhtin, A., Kulyakhtin, S., Løset, S., 2013. Measurements of thermodynamic properties of ice created by frozen sea spray. Proc. of the Twenty-Third Intl. Offshore and Polar Eng.

Kulyakhtin, A., Shipilova, O., Muskulus, M., 2014. Numerical simulation of droplet impingement and flow around a cylinder using RANS and LES models. J. Fluid and Structures 48, 280-294.

Kulyakhtin, A., Kulyakhtin, S., Løset, S., 2016. The role of the ice heat conduction in the ice growth caused by periodic sea spray. Cold Reg. Sci. Technol. 127, 93-108.

Kulyakhtin, A., Shipilova, O., Libby, B., Løset, S., 2012a. Full-scale 3D CFD simulation of spray impingement on a vessel produced by ship-wave interaction. 21st IAHR Intl. Symposium on Ice, 1129-1141.

Kulyakhtin, A., Kollar, L., Løset, S., Farzaneh, M., 2012b. Numerical simulation of 3D spray flow in a wind tunnel with application of O'Rourke's interaction algorithm and its validation. Proc. of the 21st IAHR Intl. Symposium on Ice.

Lacroix, M., Voller, V.R., 1990. Finite difference solutions of solidification phase change problems: transformed versus fixed grids. Numer. Heat Trans. 17(1), pp.25-41.

Lafuma, A. and Quéré, D., 2003. Superhydrophobic states. Nature materials, 2(7), p.457.

Laforte, J.L., Allaire, M.A.,d Laflamme, J., 1998. State-of-the-art on power line de-icing. Atmospheric Research, 46(1-2), pp.143-158.

Lam, L.S., Hodes, M., Enright, R., 2015. Analysis of galinstan-based microgap cooling enhancement using structured surfaces. Journal of Heat Transfer, 137(9), p.091003.

Lamb, H., Hydrodynamics. Cambridge university press, 1932.

Langham, E.J., Mason, B.J., 1958. The heterogeneous and homogeneous nucleation of supercooled water, in: Proceedings of the Royal Society of London A: Mathematical, Physical and Engineering Sciences (247), pp. 493-504.

Landau, H.G., 1950. Heat conduction in a melting solid. Quart. Appl. Math. 8, pp.81-94.

Landy, M., Freiberger, A., 1967. Studies of ice adhesion: I. Adhesion of ice to plastics. Journal of colloid and interface science, 25(2), pp.231-244.

Lazaridis, A., 1970. A numerical solution of the multidimensional solidification (or melting) problem, Int. J. Heat and Mass Trans. 13, pp.1459-1477.

Le Bot, C., Vincent, S., Arquis, E., 2005. Impact and solidification of indium droplets on a cold substrate. International Journal of Thermal Sciences, 44(3), pp.219-233.

Li, H., Roisman, I.V., Tropea, C., 2011. Water drop impact on cold surfaces with solidification. In AIP Conference Proceedings (Vol. 1376, No. 1, pp. 451-453). AIP.

Lions, J,L., 1969. Quelques m´ethodes de r´esolution pour les´equations non-lin´eaires, Dunod, Paris.

Liu, H., Lavernia, E.J., Rangel, R. 1993. Numerical simulation of substrate impact and freezing of droplets in plasma spray processes. Journal of Physics 26 (11): 1900–1908.

Liu, W., Wang, G.X., Matthys, E.F., 1995. Thermal analysis and measurements for a molten metal drop impacting on a substrate: cooling, solidification and heat transfer coefficient. International Journal of Heat and Mass Transfer, 38(8), pp.1387-1395.

Liu, J., Vu, H., Yoon, S.S., Jepsen, R.A., Aguilar, G., 2010. Splashing phenomena during liquid droplet impact. Atomization and Sprays, 20(4).

Liu, Z., Zhang, X., Wang, H., Meng, S., Cheng, S., 2007. Influences of surface hydrophilicity on frost formation on a vertical cold plate under natural convection conditions. Experimental Thermal and Fluid Science, 31(7), pp.789-794.

Lock, G.S.H., Foster, L.B., 1990. Experiments on the growth of spongy ice near a stagnant point. J. of Glaciology 36, 143-150.

Lopes, P., 2013. Free-surface flow interface and air-entrainment modelling using OpenFOAM (Doctoral dissertation).

Lorenzini, G., Saro, O., 2013. Thermal fluid dynamic modelling of a water droplet evaporating in air. International Journal of Heat and Mass Transfer, 62, pp. 323-335.

Lunkad, S.F., Buwa, V.V., Nigam, K.D.P., 2007. Numerical simulations of drop impact and spreading on horizontal and inclined surfaces. Chemical Engineering Science, 62(24), pp. 7214-7224.

Lozinski, D., Matalon, M., 1993. Thermocapillary motion in a spinning vaporizing droplet, Physics of Fluids A: Fluid Dynamics, 5(7), pp. 1596-1601.

Lozowski, E.P., Gates, E.M., 1991. On the modelling of ice accretion, in: Cheng, K.C., Seki, N. (Eds.), Freezing and melting heat transfer in engineering. New York: Hemisphere, pp. 615-660.

Lozowski, E.P., Makkonen, L., 2005. Fifty years of progress in modelling the accumulations of atmospheric ice on power network equipment, IWAIS XI, Montreal.

Lozowski, E.P., Forest, T.W., Chung, V., Szilder, K., 2002. Study of marine icing: Final report.

Lozowski, E.P., Stallabrass, J.R., Hearty, P.F., 1983. The icing of an unheated, nonrotating cylinder. Part I: A simulation model. J. Climate and Appl. Meteorol. 22, 2053-2062.

Lozowski, E. P., Szilder, K., Makkonen, L., 2000. Computer simulation of marine ice accretion, Philos. Trans. R. Soc. Lond. Ser. A 358, pp. 2811-2845.

Lundqvist, J.E., Udin, I., 1977. Ice accretion on ships with special emphasis on Baltic conditions. Res. Rep. 23.

McDonald, J.E., 1954. The shape and aerodynamics of large rain drops, Journal of Meteorol. 11, pp. 478-494.

Macdonald, O.C., McCartney, H.A., 1987. Calculation of splash droplet trajectories. Agricultural and forest meteorology, 39(2-3), pp. 95-110.

Macklin, W.C., 1962. The density and structure of ice formed by accretion. Quarterly Journal of the Royal Meteorological Society, 88(375), pp. 30-50.

Madejski, J., 1976. Solidification of droplets on a cold surface. International Journal of Heat and Mass Transfer, 19(9), pp.1009-1013.

Makkonen, L., 1984a. Atmospheric icing on sea structures. Cold Reg. Res. Eng. Laboratory, CRREL-MONO-84-2.

Makkonen, L., 1984b. Modeling of ice accretion on wires. J. Climate and Appl. Meteorol. 23, pp. 929-939.

Makkonen, L., 1987. Salinity and growth rate of ice formed by sea spray. Cold Reg. Sci. Technol. pp.163-171.

Makkonen, L., 1988. A model of icicle growth. J. Glaciology, 34, 64-70.

Makkonen, L., 1989. Formation of spray ice on offshore structures. Working group on ice forces, 4th State-of-the-Art Report: CRREL Special Report, pp.89-5.

Makkonen, L., 2000. Models for the growth of rime, glaze, icicles and wet snow on structures. Philosophical Transactions of the Royal Society of London A: Mathematical, Physical and Eng. Sci. 358(1776), pp.2913-2939.

Makkonen, L. Fujii, Y., 1993. Spacing of icicles. Cold Reg. Sci. Technol. 21, 317-322.

Makkonen, L., Brown, R. D., Mitten, P. T., 1991. Comments on “Prediction of vessel icing for near-freezing sea temperatures”. American Meteorol. Soc. pp.565-567.

Majithia, A.K., Hall, S., Harper, L., Bowen, P.J., 2008. Droplet breakup quantification and processes in constant and pulsed air flows. In Proceedings of the 22nd Conference on Liquid Atomization and Spray Systems (ILASS-Europe).

Manservisi, S., Scardovelli, R. A., 2009. Variational approach to the contact angle dynamics of spreading droplets. Comput. Fluids; 38(2), pp. 406–24.

Makkonen, L., 2000. Models for the growth of rime, glaze, icicles and wet snow on structures. Philosophical Transactions of the Royal Society of London A: Mathematical, Physical and Engineering Sciences, 358(1776), pp. 2913-2939

Malgarinos, I., Nikolopoulos, N., Marengo, M., Antonini, C., Gavaises, M., 2014. VOF simulations of the contact angle dynamics during the drop spreading: standard models and a new wetting force model, Advances in Colloid and Interface Science, 212, pp. 1-20.

Mao, T., Kuhn, D.C.S., Tran, H. 1997. Spread and rebound of liquid droplets upon impact on flat surfaces. AIChE Jounal 43 (9), pp. 2169-2179.

Marengo, M., Antonini, C., Roisman, I.V. and Tropea, C., 2011. Drop collisions with simple and complex surfaces. Current Opinion in Colloid & Interface Science, 16(4), pp.292-302.

Marín, A.G., Enríquez, O.R., Brunet, P., Colinet, P., Snoeijer, J.H., 2014. Universality of tip singularity formation in freezing water drops, Phys. Rev. Lett. 113, pp.054301.

Mastanaiah, K., 1976. On the numerical solution of phase change problems in transient non-linear heat conduction, Int. J. Numer. Meth. Eng. 10, pp.833-44.

Mehdizadeh, N.Z., Raessi, M., Chandra, S., Mostaghimi, J., 2004. Effect of substrate temperature on splashing of molten tin droplets. Transactions-American Society of Mechanical Engineers, Journal of Heat Transfer, 126(3), pp. 445-452.

Megaridis, C.M., Hodges, J.T., Xin, J., Day, J.M., Presser, C., 1994. Internal droplet circulation induced by surface-driven rotation. International Journal of Heat and Fluid Flow, 15(5), pp. 364-377.

Ménard, T., Tanguy, S., Berlemont, A., 2007. Coupling level set/VOF/ghost fluid methods: Validation and application to 3D simulation of the primary break-up of a liquid jet. International Journal of Multiphase Flow, 33(5), pp.510-524.

Mertins, H.O., 1968. Icing on fishing vessels due to spray. Marine Observer, 38(221), pp.128-130.

Mikic, B., 1969. On mechanism of dropwise condensation. International journal of heat and mass transfer, vol. 12, no. 10, pp. 1311–1323.

Mishchenko, L., Hatton, B., Bahadur, V., Taylor, J.A., Krupenkin, T. and Aizenberg, J., 2010. Design of ice-free nanostructured surfaces based on repulsion of impacting water droplets. ACS nano, 4(12), pp.7699-7707.

Milne, A.J.B. and Amirfazli, A., 2009. Drop shedding by shear flow for hydrophilic to superhydrophobic surfaces. Langmuir, 25(24), pp.14155-14164.

Minsk, L.D., 1977. Ice accumulation on ocean structures. Cold Reg. Res. Eng. Laboratory, CRREL Rep.77-17.

Minsk, L.D., 1980. Icing on structures. U.S. Army Cold Reg. Res. Eng. Laboratory, CRREL Rep. pp.80-31.

Mintu, S., Molyneux, D., Oldford, D., 2016, State-of-the-Art review of research on ice accretion measurements and modelling. Arctic Technology Conference. Offshore Technology Conference.

Mohammadi, M., 2016. Droplet Impact and Solidification on Solid Surfaces in the Presence of Stagnation Air Flow, Doctoral dissertation, Concordia University.

Mostaghimi, J., Pasandideh-Fard, M., Chandra, S., 2002. Dynamics of splat formation in plasma spray coating process, Plasma Chem. Plasma Process. 22 (1),pp.59–84.

Mukherjee, S., Abraham, J., 2007. Investigations of drop impact on dry walls with a lattice Boltzmann model. Journal of colloid and interface science, 312(2), pp. 341-354.

Mundo, C.H.R., Sommerfeld, M., Tropea, C., 1995. Droplet-wall collisions: experimental studies of the deformation and breakup process. International journal of multiphase flow, 21(2), pp.151-173.

Murry, W.D., Landis, F., 1959. Numerical and machine solutions of transient heat conduction problems involving melting or freezing, J. Heat Trans. 81, pp.106–112.
Meyer, G.H., 1971. A numerical method for two-phase Stefan problems, SIAM J. 8, pp.555-568.
Meyer, G.H., 1973. Multidimensional Stefan problems, SIAM J. Numer. Anal., 10, pp.522–538.
Meyer, G.H., 1975. Heat transfer during fluidized-bed coating, Int. J. Numer. Methods Eng. 9, pp.669-678.
Meyer, G.H., 1977. An application of the method of lines to multidimensional free boundary problems, IMA J. Appl. Math. 20, pp.317-329.
Myers, T.G., Charpin, J.P., 2004. A mathematical model for atmospheric ice accretion and water flow on a cold surface. Int. J. Heat and Mass Trans. 47(25), pp.5483-5500.
Myers, T.G., Hammond, D.W., 1999. Ice and water film growth from incoming supercooled droplets. Int. J. Heat and Mass Trans. 42(12), pp.2233-2242.
Nakakita, K., Nadarajah, S., Habashi, W., 2010. Toward real-time aero-icing simulation of complete aircraft via FENSAP-ICE. J. Aircr., 47 (1), pp. 96–109.
Naterer, G.F., 2011. Multiphase transport processes of droplet impact and ice accretion on surfaces. Cold Reg. Sci. Technol. 65(1), pp.5-12.
Naterer, G.F., 2003. Coupled liquid film and solidified layer growth with impinging supercooled droplets and Joule heating. International Journal of Heat and Fluid Flow, 24(2), pp.223-235.
Nellis, G., Klein, S., 2008. Heat Transfer. Cambridge Press.
Nikolopoulos N, Theodorakakos A, Bergeles G. A., 2007. Numerical investigation of the evaporation process of a liquid droplet impinging onto a hot substrate. International Journal of Heat and Mass Transfer, 50(1), pp. 303-319.
Nourgaliev, R.R., Dinh, T.N., Theofanous, T.G., Joseph, D., 2003. The lattice Boltzmann equation method: theoretical interpretation, numerics and implications. International Journal of Multiphase Flow, 29(1), pp. 117-169.
Noye, J., 1987. Numerical methods for solving the transport equation, in: Noye, J., (Eds.), Numerical modelling: Applications to marine systems, North-Holland Mathematical Studies, pp.195-230.
Obreiter, E., 1987. Physics of the marine ice accretion process: (i) spreading and freezing of salt water drops (ii) mass loss due to splashing on a wet accretion (Master thesis). University of Alberta, Canada.
Omega. In online: https://www.omega.com/prodinfo/thermal_imagers.html
Ono, N., 1974. Studies on the ice accumulation on ships. IV. Low Temp Sci. A, 32, pp.235-242.
Osher, S., Sethian, J.A., 1988. Fronts propagating with curvature-dependent speed: algorithms based on Hamilton-Jacobi formulations. Journal of computational physics, 79(1), pp. 12-49.
Oukach, S., Hamdi, H., El Ganaoui, M. and Pateyron, B., 2012. Thermal effects on the spreading and solidification of a micrometric molten particle impacting onto a rigid substrate. Fluid Dynamics & Materials Processing, 8(2), pp.173-195.

Ou, J., Shi, Q., Wang, Z., Wang, F., Xue, M., Li, W. and Yan, G., 2015. Sessile droplet freezing and ice adhesion on aluminum with different surface wettability and surface temperature. Science China Physics, Mechanics & Astronomy, 58(7), pp.1-8.

Overland, J.E., 1990. Prediction of vessel icing for near-freezing sea temperatures. American Meteorol. Soc. 5, 62-77.

Overland, 1991: Reply to comments on "Prediction of vessel icing for near-freezing sea temperatures". Weather and Forecasting 6, 568-570., 2011: Private communication.

Overland, J.E., Pease, C.H., Preisendorfer, R.W., Comiskey, A.L., 1986. Prediction of vessel icing. J. Climate and Appl. Meteorol. 25, 1793-1806.

Panov, V.V., 1976. Icing of ships. Polar Geography, 2(3), pp.166-186.

Pardeshi, R., Voller, V.R., Singh, A.K., Dutta, P., 2008. An explicit–implicit time stepping scheme for solidification models. Int. J. Heat and Mass Trans. 51(13), pp.3399-3409.

Parent, O., Ilinca, A., 2011. Anti-icing and de-icing techniques for wind turbines: Critical review. Cold Reg. Sci. Technol. 65(1), pp.88-96.

Parrissenti, G., Niro, A., 2015. Numerical solution of a three-phase Stefan problem with high power input, Heat Trans. Eng. 36, pp.611-619.

Pasandideh-Fard, M., Mostaghimi, J., 1996. On the spreading and solidification of molten particles in a plasma spray process: Effect of the Thermal Contact Resistance. Plasma Chemistry and Plasma Processing. vol. 16, no. 1, pp. 83-98.

Pasandideh-Fard, M., Bhola, R., Chandra, S., Mostaghimi, J., 1998. Deposition of tin droplets on a steel plate: simulations and experiments. Int. J Heat Mass Transfer; 41(19), pp. 2929–2945.

Pasandideh-Fard, M., Chandra, S., Mostaghimi, J., 2002. A three-dimensional model of droplet impact and solidification. International Journal of Heat and Mass Transfer, 45(11), pp. 2229-2242.

Pasandideh- Fard, M., Qiao, Y.M., Chandra, S., Mostaghimi, J., 1996. Capillary effects during droplet impact on a solid surface. Physics of Fluids (1994-present), 8(3), pp. 650-659.

Pati, A.R., Behera, A.P., Munshi, B., Mohapatra, S.S., 2017. Enhancement of heat removal rate of high mass flux spray cooling by sea water. Experimental Thermal and Fluid Science, 89, pp.19-40.

Pham, Q.T., 1985. A fast, unconditionally stable finite-difference scheme for heat conduction with phase change, Int. J. Heat and Mass Trans. 28 (11), pp.2079-2084.

Pham, Q.T., 1986. The use of lumped capacitance in the finite-element solution of heat conduction problems with phase change, Int. J. Heat and Mass Trans. 29, pp.285-291.

Phillips, R.J., 1988. Microchannel heat sinks. The Lincoln Laboratory Journal, 1(1), pp.31-48.

Pitter, R.L., Pruppacher, H.R., 1973. A wind tunnel investigation of freezing of small water drops falling at terminal velocity in air. Quarterly Journal of the Royal Meteorological Society, 99(421), pp. 540-550.

Poirier, D., Salcudean, M., 1988. On numerical methods used in mathematical modeling of phase change in liquid metals, J. Heat Transfer, 110(3), pp.562-570.

Polis, M.P., Goodson, R.E., 1976. Parameter identification in distributed systems: A synthesizing overview. 1976: Proc. IEEE, 64(1), pp.45-61.

Pope, S.B., 2000. Turbulent flows. Cambridge University Press, Cambridge.

Prajitno, D.H., Maulana, A., Syarif, D.G., 2016, August. Effect of Surface Roughness on Contact Angle Measurement of Nanofluid on Surface of Stainless Steel 304 by Sessile Drop Method. In Journal of Physics: Conference Series (Vol. 739, No. 1, p. 012029). IOP Publishing.

Price, P.H., Slack, M.R., 1954. The effect of latent heat on numerical solutions of the heat flow equation, British J. Appl. Physics, 5(8), pp.285-287.

Punge, H.J., Kunz, M., 2016. Hail observations and hailstorm characteristics in Europe: A review. Atmospheric Research, 176, pp.159-184.

Rabin, Y., Korin, E., 1993. An efficient numerical solution for the multidimensional solidification (or melting) problem using a microcomputer, Int. J. Heat Mass Trans. 36, pp.673-683.

Ranz, W.E., Marshall, W.R., 1952. Evaporation from drops. Chem. Eng. Prog. 48(3), pp. 141-146.

Rao, P.R., Sastri, V.M.K., 1984. Efficient numerical method for dimensional phase change problems, Int. J. Heat and Mass Trans. 27, pp.2077-2084.

Rashid, T., Khawaja, H.A., Edvardsen, K., 2016. Review of marine icing and anti-/de-icing systems. J. Marine Eng. Technol. 15(2), pp.79-87.

Reznik, S.N., Yarin, A.L., 2002. Spreading of an axisymmetric viscous drop due to gravity and capillarity on a dry horizontal wall. International journal of multiphase flow, 28(9), pp.1437-1457.

Richert, F., 1996. Is rotorcraft icing knowledge transferable to wind turbines. BOREAS III. FMI, Saariselkä, Finland, pp. 366-380.

Ritger, P.D., Rose, N.J., 2000. Differential equations with applications. Courier Corporations.

Roebber, P., Mitten, P., 1987. Modelling and measurement of icing in Canadian waters. Atmos. Environment Ser.

Rose, M.E., 1960. A method for calculating solutions of parabolic equations with a free boundary, Math. Comput. 14, pp.249–56.

Ruiz, O.E., Black, W.Z., 2002. Evaporation of water droplets placed on a heated horizontal surface. Transactions-American Society of Mechanical Engineers, Journal of Heat Transfer, 124(5), pp.854-863.

Rybczynski, W., 1911. Uber die fortschreitende Bewegung einer flussigen Kugel in einem zaben Medium, Bull. Internat. Acad. Sci. Cracovia, Ser. A, No. 1A.

Ryerson, C., 1992. Ship structure icing data collection and instrument performance on USCGC midget research cruise. CRREL report.

Ryerson, C., 1995 Superstructure spray and ice accretion on a large US Coast Guard Cutter. Atmos. Res. 36, pp. 321-337.

Ryerson, C.C., 2009. Assessment of superstructure ice protection as applied to offshore oil operations safety.

Ryerson, C.C., 2011. Ice protection of offshore platforms. Cold Regions Science and Technology, 65(1), pp. 97-110.

Saha, D., Dehghani, S. R., Pope, K., Muzychka, Y., 2016a. The extent of water sheet breakup on a vertical surface. Arctic Technology Conference, Offshore Technology Conference.

Saha, D., Dehghani, S. R., Pope, K., Muzychka, Y., 2016b. Temperature distribution during solidification of saline and fresh water droplets after striking a super-cooled surface. Arctic Technology Conference, Offshore Technology Conference.

Saitoh, T., 1976. An experimental study of the cylindrical and two-dimensional freezing of water with varying wall temperature. Tohoku University Technical Report 41, pp.61-72.

Saitoh, T., 1978. Numerical method for multi-dimensional freezing problems in arbitrary domains. J. Heat Trans. 100, pp.294-299.

Samarskii, A.A., Moiseynko, B.D., 1965. An economic continuous calculation scheme for the Stefan multidimensional problem. USSR Computational Math. Mathematical Physics 5, pp.816-27.

Samarskii A A, Vabishchevich P N, Iliev O P., Churbanov A, 1993. Numerical simulation of convection/diffusion phase change problems – a review, Int. J. Heat Mass Transfer 36, pp. 4095–106.

Sastry, S., 2005. Water: Ins and outs of ice nucleation. Nature, 438(7069), pp. 746-747.

Sawada, T., 1962. Icing on ships and its forecasting. J. of Japanese Society of Snow and Ice. Tokyo, 24, pp.12-14.

Sawada, T., 1966. A method for forecasting ice accretion in the waters off the Kuril Islands. Tokyo, Japan.

Sawada, T., 1968. Ice accretion on ships in northern seas of Japan. J. Meteorol. Soc. Japan. Ser. II, 46(3), pp.250-254.

Schiaffino, S., Sonin, A.A., 1997. Molten droplet deposition and solidification at low Weber numbers. Physics of Fluids, 9(11), pp.3172-3187.

Sébastien, B., 2008. Sea ice risks. Safety Course.

Sghaier, N., Prat, M. and Nasrallah, S.B., 2006. On the influence of sodium chloride concentration on equilibrium contact angle. Chemical Engineering Journal, 122(1-2), pp.47-53.

Shamsundar, N., Sparrow, E.M., 1975. Analysis of multidimensional conduction phase change via the enthalpy model, J. Heat Trans. 97, pp.333–40.

Shamsundar, N., 1978. Moving boundary problems, in D.G. Wilson, A.D. Solomon, P.T. Boggs (eds.), New York: Academic Press, In Wilson et al.

Shan, X., Chen, H., 1993. Lattice Boltzmann model for simulating flows with multiple phases and components. Physical Review E, 47(3), pp.1815.

Shan, X., Doolen, G., 1995. Multicomponent lattice-Boltzmann model with inter particle interaction. Journal of Statistical Physics, 81(1-2), pp. 379-393.

Sharqawy, M.H., Lienhard V, J.H., Zubair, S.M., 2010. Thermophysical properties of seawater: A review of existing correlations and data desalination and water treatment. V.16, pp. 354-380.

Shastri, S.S., Allen, R.M., 1998. Method of lines and enthalpy method for solving moving boundary problems, Int. Communications in Heat and Mass Trans. 25, pp.531–540.
Shellard, H.C., 1974. The meteorological aspects of ice accretion on ships. World Meteorol. Organ., Mar. Sci. Aff., pp.34.
Shekhtman, A.N., 1967. Hydrometeorological conditions of icing on ships. Naue-Issl. Inst., Aeroklimatologii. Teudy No. 45, Gidrometeoizdat. Moscow. 51-63. (In Russian)
Shekhtman, A.N., 1968. The probability and intensity of the icing-up of ocean-going vessels. Moskow Nauk-Issled Inst. Aeroklim, T. Vyp 50, pp. 55-65.
Shellard, H.C., 1974. The meteorological aspects of ice accretion on ships. World Meteorol. Organ., Mar. Sci. Aff., pp.34.
Shreiber, A.A., Podvisotski, A..M., Dubrovski, V.V., 1996. Deformation and breakup of drops by aerodynamic loads, Atomization Sprays, 6(6), pp. 667.
Shukla, R.K., Yadav, S.K., Shete, M.H., Kumar, A., 2015. Numerical modeling of impact and solidification of a molten alloy droplet on a substrate. In Advances in Material Forming and Joining (pp. 307-322). Springer, New Delhi.
Sedev, R.V., Budziak, C.J., Petrov, J.G., Neumann, A.W., 1993. Dynamic contact angles at low velocities. Journal of colloid and interface science, 159(2), pp. 392-399.
Siddhartha, F., Vivek, V. B., Nigam, K.D.P., 2007. Numerical simulations of drop impact and spreading on horizontal and inclined surfaces. Chemical Engineering Science 62 (24), pp. 7214 – 7224.
Sirignano, W.A., 2000. Fluid dynamics and transport of droplets and sprays (Vol. 1). Cambridge: Cambridge university press, pp. 144.
Sˇikalo, Sˇ., Marengo, M., Tropea, C., Ganic, E.N., 2002. Analysis of impact of droplets on horizontal surfaces. Experimental Thermal and Fluid Science 25 (7), pp. 503-510.
Šikalo, Š., Tropea, C., Ganic´, E.N., 2005a. Impact of droplets onto inclined surfaces. Journal of Colloid and Interface Science 286 (2), pp. 661–669.
Šikalo, Š., Tropea, C., Ganic´, E.N. 2005b. Dynamic wetting angle of a spreading droplet. Experimental Thermal and Fluid Science 29 (7): 795–802.
Šikalo, Š., Wilhelm, H.D., Roisman, I.V., Jakirlić, S., Tropea, C., 2005c. Dynamic contact angle of spreading droplets: Experiments and simulations. Physics of Fluids (1994-present), 17(6), pp. 062-103.
Snoeijer, J.H., Brunet, P., 2012. Pointy ice-drops: how water freezes into a singular shape, Am. J. Phys. 80, pp.764–771.
Stallabrass, J.R., 1980. Trawler icing. A compilation of work done at NRC. Mechanical Eng. Rep. MD-56, NRC No. 19372, National Research Council, Ottawa, Canada.
Strub, M., Jabbour, O., Strub, F., Bédécarrats, J.P., 2003. Experimental study and modelling of the crystallization of a water droplet. International journal of refrigeration, 26(1), pp. 59-68.
Sommers, A.D., Napora, A.C., Truster, N.L., Caraballo, E.J., Hermes, C.J., 2017. A semi-empirical correlation for predicting the frost density on hydrophilic and hydrophobic substrates. International Journal of Refrigeration, 74, pp. 311-321.

Son, G., 2003. Efficient implementation of a coupled level-set and volume-of-fluid method for three-dimensional incompressible two-phase flows. Numerical Heat Transfer: Part B: Fundamentals, 43(6), pp.549-565.

Son, G., Hur, N., 2002. A coupled level set and volume-of-fluid method for the buoyancy-driven motion of fluid particles. Numerical Heat Transfer: Part B: Fundamentals, 42(6), pp.523-542.

Song, Y.S., Adler, D., Xu, F., Kayaalp, E., Nureddin, A., Anchan, R.M., Maas, R.L., 2010. U. Demirci, Vitrification and levitation of a liquid droplet on liquid nitrogen. Proceedings of the National Academy of Sciences, 107(10), pp. 4596-4600.

Strotos, G., Gavaises, M., Theodorakakos, A., Bergeles, G., 2008. Numerical investigation on the evaporation of droplets depositing on heated surfaces at low Weber numbers. International Journal of Heat and Mass Transfer, 51(7), pp.1516-1529.

Strotos, G., Aleksis, G., Gavaises, M., Nikas, K.S, Nikolopoulos, N., Theodorakakos, A., 2011. Non-dimensionalisation parameters for predicting the cooling effectiveness of droplets impinging on moderate temperature solid surfaces. International Journal of Thermal Sciences, 50(5), pp. 698-711.

Suli, L., Zhengying, W., Jun, D., Pei, W. and Bingheng, L., 2017. A numerical analysis on the metal droplets impacting and spreading out on the substrate. Rare Metal Materials and Engineering, 46(4), pp.893-898.

Sultana, K.R., Pope, K., Muzychka, Y.S., 2016. Numerical predictions of solidification and water droplet impingement. In Arctic Technology Conference. Offshore Technology Conference.

Sultana, K.R., Dehghani, S.R., Pope, K., Muzychka, Y.S., 2017a. A Review of Numerical Modelling Techniques for Marine Icing Applications, In Cold Regions Science and Technology, Volume 145, 2017, Pages 40-51.

Sultana, K.R., Pope, K., Lam, L.S., Muzychka, Y.S., 2017b. Phase change and droplet dynamics for a free falling water droplet. International Journal of Heat and Mass Transfer, 115, pp.461-470.

Sultana, K.R., Pope, K., Muzychka, Y.S., 2017c. Numerical prediction of transient cooling and phase change of a falling water droplet in sub-zero air temperatures. 2nd Thermal and Fluid Engineering Conference, TFEC2017. Las Vegas, NV, USA.

Sultana, K.R., Dehghani, S.R., Pope, K., Muzychka, Y.S., 2018. Numerical techniques for solving solidification and melting phase change problems, in Numerical Heat Transfer, Part B: Fundamentals, pp.1-17.

Sundin, E., Makkonen, L., 1998. Ice loads on a lattice tower estimated by weather station data. J. Appl. Meteorol. 37, 523-529.

Sussman, M., Puckett, E.G., 2000. A coupled level set and volume-of-fluid method for computing 3D and axisymmetric incompressible two-phase flows. Journal of computational physics, 162(2), pp.301-337.

Suzuki, S., Nakajima, A., Yoshida, N., Sakai, M., Hashimoto, A., Kameshima, Y., Okada, K., 2007. Freezing of water droplets on silicon surfaces coated with various silanes. Chemical Physics Letters, 445(1-3), pp.37-41.

Swaminathan, C.R., Voller, V.R., 1992. A general enthalpy method for modeling solidification processes, Metallurgical transactions B, 23, pp.651-664.

Szilder, K., Lozowski, E.P., 1993a. Stochastic modelling of icicle formation. Proc. of 12th Intl. Conference Offshore Mechanics and Arctic Eng., 59-64.

Szilder, K., Lozowski, E.P., 1993b. An analytical model of icicle growth. Annual Glaciology 19, 141-145.

Szilder, K., Lozowski, E.P., 1995a. Experimental verification of a pendant ice formation model. Proc. Of the 5th Intl. Offshore and Polar Eng. Conf., 469-475.

Szilder, K., Lozowski, E.P., 1995b. Simulation of icicle growth using a three dimensional random walk model. Atmos. Res. 36, 243-249.

Szilder, K., Lozowski, E.P., Gates, E.M., 1988. Some applications of a new, time-dependent cylinder ice accretion model. Atmos. Res. 22(1), pp.41-59.

Tabakova, S., Feuillebois, F., 2004. On the solidification of a supercooled liquid droplet lying on a surface. Journal of colloid and interface science, 272(1), pp. 225-234.

Tabbara, H. and Gu, S., 2012. Modelling of impingement phenomena for molten metallic droplets with low to high velocities. International Journal of Heat and Mass Transfer, 55(7), pp.2081-2086.

Tabata, T., 1969. Studies of ice accumulation, III. Low Temperature Sci. Ser. A, pt. 27, 337-349.

Tabata, T., Iwata, S., Ono, N., Hope, E.R., 1963. Studies of ice accumulation on ships, I. Low Temperature Sci. Ser. A, pt. 21, p. 173-221.

Tacke, K.H., 1985. Discretization of the explicit enthalpy method for planar phase change, Int. J. Numer. Methods Eng. 21, pp.543-554.

Tanner, F.X., 2011. Droplet freezing and solidification. In Handbook of Atomization and Sprays (pp. 327-338). Springer, Boston, MA.

Tanaka, Y., Washio, Y., Yoshino, M., Hirata, T., 2011. Numerical simulation of dynamic behavior of droplet on solid surface by the two-phase lattice Boltzmann method. Computers & fluids, 40(1), pp. 68-78.

Tien, L.C., Churchill, S.W., 1965. Freezing front motion and heat transfer outside an infinite isothermal cylinder, AIChE J. 11, pp.790–793.

Trapaga, G., Szekely, J. 1991. Mathematical modeling of the isothermal impingement of liquid droplets in spraying processes. Metallurgical Transactions B 22 (6), pp. 901-914.

Trawler Icing Research, 1957. British Shipbuilding Research Association, Rep. 221, London, England.

Trapaga, G., Matthys, E. F., Valencia, J. J., Szekely J., 1992. Fluid flow, heat Transfer and solidification of molten metal droplets impinging on substrate: comparison of numerical and experimental results. Metall. Trans., vol. 23B, pp. 701–718.

Tryggvason, G., Bunner, B., Esmaeeli, A., Juric, D., Al-Rawahi, N., Tauber, W., Han, J., Nas, S., Jan, Y.J., 2001. A front-tracking method for the computations of multiphase flow. Journal of Computational Physics, 169(2), pp. 708-759.

Tsilingiris, P., 2008. Thermophysical and transport properties of humid air at temperature range between 0 and 100 c. Energy Conversion and Management, vol. 49, no. 5, pp. 1098–1110, 2008.

Turland, B.D., 1979. A general formulation of the isotherm migration method for reactor accident analysis. Structural Mechanics in Reactor Technol. Transactions B.

Turland, B.D., Wilson, G., 1977. UKAEA (Culham) Report RS (77) N42.
Unverdi, S.O., Tryggvason, G., 1992. A front-tracking method for viscous, incompressible, multi-fluid flows. Journal of computational physics, 100(1), pp. 25-37.
Uwaterloo. Online link: http://www.mhtl.uwaterloo.ca/old/onlinetools/airprop/airprop.html
Varanasi, K.K., Hsu, M., Bhate, N., Yang, W., Deng, T., 2009. Spatial control in the heterogeneous nucleation of water. Applied Physics Letters, 95(9), pp.094101.
Vefsnmo, S., Horjen, I., Løset, S., 1987. Time-dependent numerical model for sea spay icing on marine structures. Proc. of the Intl. Conference Port and Ocean Engineering Under Arctic Conditions, pp. 571-579.
Voller, V.R., 1985. Implicit finite-difference solutions of the enthalpy formulation of Stefan problem, IMA J. Numer. Analysis 5, pp.201-214.
Voller, V.R., 1990. Fast implicit finite-difference method for the analysis of phase change problems, Numer. Heat Trans. B 17, pp.155-169.
Voller, V.R., 1996. An overview of numerical methods for solving phase change problems, in W. Minkowycz (eds.), CRC Press, Volume 1.
Voller, V.R., Brent, A.D., 1990. Modelling the mushy region in a binary alloy, Appl. Math. Modelling 14, pp.320-326.
Voller, V.R., Cross, M., 1981a. Accurate solutions of moving boundary problems using the enthalpy method, Int. J. Heat and Mass Trans. 24, pp.545- 556.
Voller, V.R., Cross, M., 1983. Use of the enthalpy method in the solution of Stefan problems, Int. Conf. Numerical Methods in Thermal Problems. 3, pp.91-101.
Voller, V.R., Cross, M., 1981b. Estimating the solidification/melting times of cylindrically symmetric regions, Int. J. Heat and Mass Trans. 24, pp.1457-62.
Voller, V.R., Peng, S., 1994. An enthalpy formulation based on an arbitrarily deforming mesh for solution of the Stefan problem, Computational Mechanics 14, pp.492-502, Springer-Verlag.
Voller, V.R., Prakash, C., 1987. A fixed grid numerical modelling methodology for convection-diffusion mushy region phase-change problems. International Journal of Heat and Mass Transfer, 30(8), pp.1709-1719.
Voller, V.R., Swaminathan, C.R., Thomas, B.G., 1990. Fixed grid techniques for phase change problems: a review, Int. J. Numer. Methods Eng. 30(4), pp.875-898.
Volkov, R.S., Kuznetsov, G.V., Strizhak, P.A., 2015. Water droplet deformation in gas stream: Impact of temperature difference between liquid and gas, International Journal of Heat and Mass Transfer, 85, pp. 1-11.
Volkov, R.S., Kuznetsov, G.V., Kuibin, P.E.A., Strizhak, P.A., 2016. Features of water droplet deformation during motion in a gaseous medium under conditions of moderate and high temperatures. High Temperature, 5(54), pp. 722-730.
Wang, X., 2008. Convection heat transfer and experimental icing aerodynamics of wind turbine blades. PhD thesis. University of Manitoba, Canada.
Wang, J., Liu, Z., Gou, Y., Zhang, X., Cheng, S., 2006. Deformation of freezing water droplets on a cold copper surface, Sci. China Ser. E 49, pp. 590–600.

Wang, Z., Yang, J., Koo, B., Stern, F., 2009. A coupled level set and volume-of-fluid method for sharp interface simulation of plunging breaking waves. International Journal of Multiphase Flow, 35(3), pp.227-246.

Water density calculator. Online: http://www.csgnetwork.com/h2odenscalc.html (Access on April 2017).

Weeks, W., 2010. On sea ice. University of Alaska Press.

Wierzba, A., 1990. Deformation and breakup of liquid drops in a gas stream at nearly critical Weber numbers, Experiments in Fluids, 9(1), pp. 59-64.

Winslow, A.M., 1967. Numerical solution of the quasilinear poisson equation in a non-uniform triangle mesh, J. Computational Physics1, pp.149-172.

Wise, J.L., Comiskey, A.L., 1980. Superstructure icing in Alaskan waters. US Department of Commerce, National Oceanic and Atmospheric Administration, Environmental Res. Laboratories.

Woodruff, D.P., 1973. The solid-liquid interface, Cambridge University Press.

Wood, S.E., Baker, M.B., Swanson, B.D., 2002. Instrument for studies of homogeneous and heterogeneous ice nucleation in free-falling supercooled water droplets. Review of Scientific Instruments, 73(11), pp. 3988-3996.

World Meteorological Organization, 1962. Precipitation measurements at sea. World Meteorological Organization, Technical note 47.

Wu, J., 1973. Spray in the atmospheric surface layer: Laboratory study. J. Geophysical Res. 78(3), pp.511-519.

Wu, J., 1979. Spray in the atmospheric surface layer: Review and analysis of laboratory and oceanic results. J. Geophysical Res. 84, (C4): 1693-1704.

Wu, X.M., Webb, R.L., 2001. Investigation of the possibility of frost release from a cold surface. Experimental Thermal and Fluid Science, 24(3-4), pp.151-156.

Wu, X., Hu, S., Chu, F., 2016. Experimental study of frost formation on cold surfaces with various fin layouts. Applied Thermal Engineering, 95, pp.95-105.

Wu, X., Dai, W., Xu, W., Tang, L., 2007. Mesoscale investigation of frost formation on a cold surface. Experimental thermal and fluid science, 31(8), pp.1043-1048.

Xu, Q., Li, Z., Wang, J. and Wang, R., 2012. Characteristics of single droplet impact on cold plate surfaces. Drying technology, 30(15), pp.1756-1762.

Yang, G., Guo. K., Li, N., 2011. Freezing mechanism of supercooled water droplet Impinging on metal surfaces. International Journal of Refrigeration 34 (8), pp. 2007-2017.

Yang, X., James, A.J., Lowengrub, J., Zheng, X., Cristini, V., 2006. An adaptive coupled level-set/volume-of-fluid interface capturing method for unstructured triangular grids. Journal of Computational Physics, 217(2), pp.364-394.

Yao, S.C., Schrock, V.E., 1976. Heat and mass transfer from freely falling drops, Trans. ASME J. Heat Transf., pp. 120-126.

Yoo, J., Rubinsky, B., 1983. Numerical computation using finite elements for the moving interface in heat transfer problems with phase transformation, Numerical Heat Trans. 6, pp.209-222.

Yovanovich, M., 1997. Transient spreading resistance of arbitrary isoflux contact areas: development of a universal time function. 32nd AIAA Thermophysics Conference, Atlanta, GA.

Yovanovich, M., Teertstra, P., Culham, J., 1995. Modeling transient conduction from isothermal convex bodies of arbitrary shape. Journal of thermophysics and heat transfer, vol. 9, no. 3, pp. 385–390.

Yuan, Y., Lee, T.R., 2013. Contact angle and wetting properties. In Surface science techniques (pp. 3-34). Springer Berlin Heidelberg.Zakrzewski, W.P., 1986a. Icing of ships. Part I: Splashing a ship with spray. NOAA Tech. Memo., ERL PMEL-66, Pacific marine environmental laboratory, Seattle, WA, 74.

Yue, X., Liu, W., Wang, Y., 2016. Effects of black silicon surface structures on wetting behaviors, single water droplet icing and frosting under natural convection conditions. Surface and Coatings Technology, 307, pp. 278-286.

Zakrzewski, W.P., 1986b. Icing of fishing vessels. Part I: Splashing a ship with spray. Proc. of the 8th IAHR Symposium on Ice, Iowa City.

Zakrzewski, W.P., 1987. Splashing a ship with collision-generated spray. Cold Reg. Sci. Technol. 14(1), pp.65-83.

Zakrzewski, W.P., Lozowski, E.P., 1991. Modelling and forecasting vessel icing, in: Cheng, K.C., Seki, N. (Eds.), Freezing and melting heat transfer in engineering. New York: Hemisphere, pp.

Zarling, J.P., 1980. Heat and mass transfer from freely falling drops at low temperature. CRREL Rep. Cold Reg. Res. Eng. Laboratory.

Zarling, J.P., 1980. Heat and mass transfer from freely falling drops at low temperature. Cold Regions Research and Engineering Laboratory, CRREL Report.

Zhang, X., Min, J., Wu, X., 2016a. Model for aircraft icing with consideration of property-variable rime ice. International Journal of Heat and Mass Transfer, 97, pp.185-190.

Zhang, H., Zhao, Y., Lv, R. and Yang, C., 2016b. Freezing of sessile water droplet for various contact angles. International journal of thermal sciences, 101, pp.59-67.

Zhang, X., Wu, X., Min, J., 2017a. Aircraft icing model considering both rime ice property variability and runback water effect. International Journal of Heat and Mass Transfer, 104, pp.510-516.

Zhang, X., Wu, X., Min, J., 2017b. Freezing and melting of a sessile water droplet on a horizontal cold plate. Experimental Thermal and Fluid Science, 88, pp.1-7.

Zhang, X., Wu, X., Min, J., Liu, X., 2017c. Modelling of sessile water droplet shape evolution during freezing with consideration of supercooling effect. Applied Thermal Engineering, 125, pp.644-651.

Zheng, Y.Z., Li, Q., Zheng, Z.H., Zhu, J.F., Cao, P.L., 2014. Modeling the impact, flattening and solidification of a molten droplet on a solid substrate during plasma spraying. Applied Surface Science, 317, pp. 526-533.

Zienkiewicz, O.C., Parekh, C.J., Wills, A.J., 1973. The application of finite elements to heat conduction problems involving latent heat, Rock Mech. 5, pp.65-76.